2016

Ultrafast Mechanisms of Nonlinear Refraction and Two-photon Photochromism

Peng Zhao
University of Central Florida

ULTRAFAST MECHANISMS OF NONLINEAR REFRACTION AND TWO-PHOTON PHOTOCHROMISM

by

PENG ZHAO
B.S. Measuring and Controlling Technology and Instruments, Tianjin University, 2010
M.S. Electrical Engineering, Case Western Reserve University, 2012

A dissertation submitted in partial fulfillment of the requirements
for the degree of Doctor of Philosophy
in CREOL, the College of Optics and Photonics
at the University of Central Florida
Orlando, Florida

Fall Term
2016

Major Professors: Eric W. Van Stryland and David J. Hagan

ABSTRACT

Derived from a material's third-order nonlinearity, nonlinear refraction (NLR) occurs at any wavelength in any material, and may exhibit noninstantaneous dynamics depending on its physical origins. The main subject of this dissertation is to investigate the underlying mechanisms responsible for the NLR response in different phases of matter, e.g. liquids, gases, and semiconductors, by extensively using our recently developed ultrafast Beam Deflection (BD) technique. An additional subject includes the characterization of a novel two-photon photochromic molecule.

In molecular liquids, the major nonlinear optical (NLO) response can be decomposed into a nearly instantaneous bound-electronic NLR (Kerr effect), originating from the real part the electronic second hyperpolarizability, γ, and noninstantaneous mechanisms due to nuclear motions. By adopting the methodology previously developed for carbon disulfide (CS_2), we have measured the NLO response functions of 23 common organic solvents, providing a database of magnitudes and temporal dynamics of each mechanism, which can be used for predicting the outcomes of any other NLR related experiments such as Z-scan. Also, these results provide insight to relate solvent nonlinearities with their molecular structures as well as linear polarizability tensors. In the measurements of air and gaseous CS_2, coherent Raman excitation of many rotational states manifests as revivals in the transient NLR, from which we identify N_2, O_2 and two isotopologues of CS_2, and unambiguously determine the dephasing rate, and rotational and centrifugal constants of each constituent. Using the revival signal as a self-reference, γ is directly measured for CS_2 molecules in gas phase, which coincides with the γ determined from liquid phase measurements when including the Lorentz-Lorenz local field correction.

In semiconductors, the Kerr effect dominates the NLR in the sub-gap regime. Here, we primarily focus on investigating the dispersion of nondegenerate (ND) NLR, namely the refractive

index change at frequency ω_a due to the presence of a beam at frequency ω_b. The magnitude and sign of the ND-NLR coefficient $n_2(\omega_a;\omega_b)$ are determined for ZnO, ZnSe and CdS over a broad spectral range for different values of nondegeneracy, which closely follows our earlier predictions based on nonlinear Kramers-Kronig relations. In the extremely nondegenerate case, $n_2(\omega_a;\omega_b)$ is positively enhanced near the two-photon absorption (2PA) edge, suggesting applications for nondegenerate all-optical switching. Additionally, $n_2(\omega_a;\omega_b)$ exhibits a strong anomalous nonlinear dispersion within the ND-2PA spectral region, providing a large phase modulation of a femtosecond pulse with bandwidth centered near the zero-crossing frequency.

Another subject of this dissertation is the characterization of a spiro-type two-photon photochromic molecule, in which Förster resonance energy transfer (FRET) is utilized to activate the ring-opening effect from a 2PA-donor chromophore. Evidence of energy transfer is observed via fluorescence measurements of the quantum yield, excitation spectra and anisotropy. The absorption and lifetime of the open form are measured in a dye-doped sol-gel matrix. Transient absorption measurements indicate both ring opening and closing occurs on a several picosecond time scale along with multiple transient photoproducts, from which a high FRET efficiency is measured in agreement with theoretical predictions. This efficient 2PA-FRET photochrome may be implemented into photonic devices such as optical memories. However, with a relatively small open-form absorption cross section and significant ring closing, the photochrome may not be viable for enhancing nonlinear absorption in applications such as optical limiting.

To my family.

ACKNOWLEDGMENTS

Faculty advisors

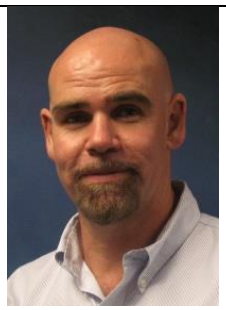	David J. Hagan CREOL, Professor of Optics Dept. of Physics, Professor of Physics Associate Dean for Academic Programs
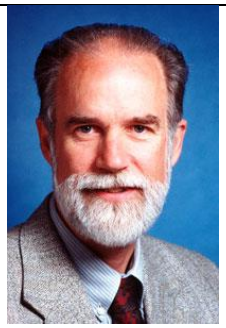	Eric W. Van Stryland CREOL, Professor of Optics Dept. of Physics, Professor of Physics Former Dean Trustee Chair

CREOL Committee Member

	Demetrios N. Christodoulides CREOL, Pegasus Professor of Optics Cobb Family Endowed Chair

External Committee Member

	Florencio Eloy Hernández Dept. of Chemistry, Professor of Chemistry

To explore the fields of nonlinear optics is an absolutely amazing experience. I truly appreciate my advisors Eric W. Van Stryland and David J. Hagan for offering me the opportunity to do research in the NLO group. They have been extremely helpful and supportive in many ways during the four years of my Ph.D. My advisors provide me not only the needed guidance to complete the dissertation work, but also numerous opportunities to attend different academic conferences, which results in great benefits to my career. I would also like to thank my committee members Demetrios N. Christodoulides and Florencio E. Hernandez for their valuable input and great interest to my dissertation research.

I gratefully thank all the former and current members of the NLO group for their help and education, which are indispensable in every detail of this dissertation. First, I particularly thank Trenton Ensley and Matthew Reichert, who taught me most of the essential skills needed in both the experimental work and the theoretical modelling, and in the meantime significantly contributed to my dissertation work on nonlinear refraction measurements of molecular liquids and gases and semiconductors. I would also like to thank Honghua Hu for his initial help on fluorescence measurements of photochromics, Manuel Ferdinandus for his introduction of the Beam Deflection technique, Himansu Pattanaik for the discussions of semiconductor physics. Also, great thanks to other NLO group members whom I have worked with during my Ph.D., including Salimeh Tofighi, Sepehr Benis, Munan Gao, Davorin Peceli, Akbar Ali Syed, Evelyn Strunk, Rajesh Sharma, Jennifer Reed, Brendan Turnbull and Scott Webster.

Many thanks to our collaborators for their valuable contributions. Vladimir Khodorkovsky for synthesizing the composite photochromic molecule PC-1. Raz Gvishi for providing dye-doped sol-gel matrix samples. Mykhailo Bondar and Siarhei Kurhuzenkau for inspiring discussions on organic photophysics.

Finally, I would like to thank my father Linping Zhao, my mother Hongyan Yu and my wife Yan Jun Chen for their continued support, patience inspiration and love over these years.

TABLE OF CONTENTS

LIST OF FIGURES xiv

LIST OF TABLES xxiii

LIST OF ACRONYMS AND ABBREVIATIONS xxiv

CHAPTER 1: INTRODUCTION 1

1.1. Ultrafast Mechanisms of NLR 1

1.2. Two-Photon Photochromism 5

1.3. Dissertation Outline 8

CHAPTER 2: NONLINEAR ABSORPTION AND REFRACTION 10

2.1. Nonlinear Optical Interactions 11

2.1.1. Nonlinear Polarizations 12

2.1.2. Nonlinear Wave Equation 15

2.2. Nonlinear Refraction and Absorption 16

2.2.1. Bound-electronic Nonlinearities 17

2.2.2. Noninstantaneous Nuclear Nonlinearities 22

2.3. Excited-state Nonlinearities 25

CHAPTER 3: EXPERIMENTAL TECHNIQUES 28

3.1. Linear Spectroscopy 28

3.2. Nonlinear spectroscopy 29

3.2.1. Femtosecond Laser and OPA/Gs 30
3.2.2. Z-scan 33
3.2.2.1. Principles 34
3.2.2.2. Dual-arm Z-scan 38
3.2.3. Beam Deflection 41
3.2.3.1. “Prism” Deflection Approximation 45
3.2.3.2. Beam Deflection with GVM and NLA 48
3.2.3.3. Separation of NLR from NLA 53
CHAPTER 4: NONLINEAR RESPONSE FUCTIONS OF ORANNIC SOLVENTS 55
4.1. Physical Origins of NLR 56
4.1.1. Bound-electronic Second Hyperpolarizability 56
4.1.2. Molecular Reorientation 59
4.1.3. Other Noninstantaneous Contributions 62
4.2. Beam Deflection Measurements 64
4.2.1. Temporal Dynamics of NLR 66
4.2.2. Polarization Dependence 69
4.3. Nonlinear Response Functions of Common Solvents 72
4.3.1. Experimental Results 73
4.3.1.1. Benzene Derivatives 74

4.3.1.2. Tetrahedral Alkanes 76

4.3.1.3. Alcohols 77

4.3.1.4. Miscellaneous Families 79

4.3.2. Comparisons of Theory and Experiment 82

4.4. Applications of NLO Response Functions 83

CHAPTER 5: TRANSIENT NONLINEAR REFRACTION OF MOLECULAR GASES[2] 86

5.1. Transient Rotational NLR of Linear Molecules 88

5.1.1. Density Matrix Formulism 89

5.1.2. Nuclear Spin Statistics 94

5.2. Measurements of Air 98

5.3. Measurements of Gaseous CS_2 104

CHAPTER 6: DISPERSION OF NONDEGENERATE NONLINEAR REFRACTION IN SEMICONDUCTORS 109

6.1. Nonlinear Kramers-Kronig Relations 111

6.2. Mechanisms of NLR in Semiconductors 112

6.3. Nondegenerate Beam Deflection Measurements 116

6.3.1. Dispersion of ND-NLR 118

6.3.1.1. ZnO 119

6.3.1.2. ZnSe 121

6.3.1.3. CdS 122

6.3.2. Nondegenerate 3PA Spectra 124
6.4. Strong Anomalous Nonlinear Dispersion 125
6.5. Nondegenerate Figure of Merit 129
CHAPTER 7: TWO-PHOTON PHOTOCHROMISM 132
7.1. Organic Photochromism: Molecules and Dynamics 132
7.2. Two-photon Photochromism via FRET 136
7.2.1. Molecular Structure and Linear Characterizations 137
7.2.2. Theoretical FRET Efficiency 140
7.2.3. Experimental Evidence of FRET 142
7.3. Cumulative Measurements with Sol-gels 145
7.3.1. Thermal Dynamics 146
7.3.2. Open-form Accumulation 147
7.4. Ultrafast Dynamics of Ring Opening and Closing 153
7.4.1. 1PA Ring-opening Dynamics 156
7.4.2. 2PA-FRET Ring-opening Dynamics 160
7.4.3. Ring-closing Dynamics 165
CHAPTER 8: CONCLUSIONS AND FUTURE WORK 169
8.1. NLR of Molecular Liquids and Gases 169
8.2. ND-NLR Dispersion of Semiconductors 171

8.3. Two-Photon Photochromism 172

LIST OF REFERENCES 175

LIST OF FIGURES

Figure 1.1 A survey of literature values reported for CS_2. The letters represents references of [1-16]. 2

Figure 1.2 Reversible photochromic transformation of a chromene. The arrows indicate 1PA/2PA induced ring-opening, and thermal/photo reversing. The images are closed and open form of a dye-doped sol-gel [55]. 6

Figure 2.1 Nonlinear dependence (black) of induced polarization *P* on the driving electric field *E* at (a) small amplitude and (b) large amplitude, as compared to the linear dependence (blue dash). 11

Figure 2.2 (a) energy diagram of a 3-level system; (b) normalized population time evolution of ground and excited states along with the input pulse. 26

Figure 3.1 General configuration of Coherent Legend Elite Duo HE+ system based on chirped pulse amplification. 31

Figure 3.2 Energy output of signal and idler from (a) TOPAS-800 with ~ 1.3 mJ pump at 800nm, and (b) TOPAS-HE with ~ 10 mJ pump at 800nm. 32

Figure 3.3 Schematics of (a) open aperture Z-scan, and beam divergence in close aperture Z-scan using a sample with positive $n2$ (b) after and (c) before the focus. 34

Figure 3.4 Examples of Z-scan: (a) open aperture Z-scan of GaAs data (circles) fit (red) with a two-photon absorption coefficient $\alpha 2$; (b) closed aperture Z-scan of Carbon disulfide (CS_2) fit (red) with a positive nonlinear refraction coefficient $n2$. 36

Figure 3.5 Example of Dual-arm Z-scan measurements of a 1.4 μm thin neat film PE1-DOB-C9 on a 1 mm thick fused silica substrate at wavelength of 1.55 μm: (b) linear absorption spectra with molecular structures on the left; (b) low energy background (LEB) in closed aperture (CA) signal;

(c) open aperture (OA) signal; (d) CA and CA/OA after subtraction of LEB. The film was fabricated by the Jen's group at University of Washington. 40

Figure 3.6 (a) Schematics of Beam Deflection setup; (b) spatial irradiance distribution of the excitation beam (red) and overlapping geometry with the probe beam (blue) at the sample plane; (c) positions of probe beam on segmented quad-cell detector without and with deflection..... 43

Figure 3.7 Beam deflection measurements of a 1 mm thick fused silica with parallel (black) and perpendicularly polarized excitation and probe. 47

Figure 3.8 Normalized Beam Deflection signals using $\lambda b = 2.3$ μm under various GVM: fused silica (black) with $\rho \approx 0$; ZnO (blue) with $\lambda a = 650$ nm ($\rho = 3.7$), and (green) with $\lambda a = 460$ nm ($\rho = 7.8$); (b) the group index dispersion of fused silica (black) and ZnO (red). The experimental data (circles) are fit (lines) with Eq. (3.8)-(3.14). 52

Figure 3.9 (a) Beam Deflection measurements of 0.5 mm thick CdS near the zero-crossing of nondegenerate NLR dispersion, with a large ND-2PA background; (b) simulations of Z-scan using the $n2$ (2.2×10^{-5} cm^2/GW) and $\alpha 2$ (13 cm/GW) fitted from BD measurements in (a). 54

Figure 4.1 (a) Definition of laboratory frame x, y, z and molecular frame x, y, z; linear polarizability tensor with anisotropy. 60

Figure 4.2 Data (circles) and fit (lines) of BD measurement of CS_2 using co-polarized excitation and probe: (a) with WLC probe filter at 700 nm with pulsewidth ~ 200 fs (FWHM); (b) the normalized response function for different nuclear mechanisms; (c) with 52 fs (FWHM) probe pulse from TOPAS-800 at 720nm compressed by a prism compressor; inset shows enlarged signals < 2 ps; (d) logarithmic scale plot of data in (c). 67

Figure 4.3 Data (circles) and fit (lines) of BD measurement of CS_2 for parallel (black), (red) perpendicular, and (blue) magic angle polarizations; (b) reconstruction of perpendicular

polarization measurement using the data from parallel and magic angle polarizations, considering isotropic and reorientational symmetry properties. 71

Figure 4.4 BD measurements (circles) with fits (lines) of benzene, toluene, nitrobenzene, p-xylene, pyridine and o-dichlorobenzene for parallel (black), perpendicular (red), and magic angle (blue) polarizations. 74

Figure 4.5 BD measurements (circles) with fits (lines) of dichloromethane, chloroform and carbon tetrachloride for parallel (black), perpendicular (red), and magic angle (blue) polarizations. 77

Figure 4.6 BD measurements (circles) with fits (lines) of methanol, ethanol, butanol and 1-octanol for parallel (black), perpendicular (red), and magic angle (blue) polarizations. 78

Figure 4.7 BD measurements (circles) with fits (lines) of hexane, cyclohexane, acetone, acetonitrile, butyl salicylate, tetrahydrofuran, dimethyl sulfoxide, dimethylformamide, water and heavy water for parallel (black), perpendicular (red), and magic angle (blue) polarizations. 80

Figure 4.8 Predictions of pulsewidth dependent $n2,\mathrm{eff}$ of (a) CS_2 using parameters in Table 4.2, which is compared to Z-scan measurements in [17], as well as literature values a-r taken from [1-16]; (b-c) predictions of the other 23 solvent molecules using parameters in Table 4.3. 84

Figure 5.1 (a) Nonresonant Raman transition between J, M and J', M' with following selection rule of $\Delta J = \pm 2$, and $\Delta M = 0$; (b) coherent Raman excitation of many rotational states. 90

Figure 5.2 Weighting factor TJ in Eq. (5.13) for (a) $^{14}N_2$, (b) $^{16}O_2$, and (c)$^{12}C^{32}S_2$. 95

Figure 5.3 The calculated normalized refractive index change due to rotational revivals using Eqs. (5.15) and (5.2) for (a) $^{14}N_2$, (b) $^{16}O_2$, and (c) $^{12}C^{32}S_2$. Note the different times scales. 97

Figure 5.4 The excitation and probe crossing geometry in (a) the yz-plane, and (b) displacement in the xz-plane resulting in a deflection in the x-direction at the segmented photodiode. 99

Figure 5.5 (a) Measured (circles) BD signal from air along with fit (violet), which is a sum of both the contribution of N_2 and O_2. (b) and (c) show the first 12 ps of delay, with fits only considering N_2 and O_2, respectively. 100

Figure 5.6 (a) Fourier transform of a BD signal measured out of 300 ps (inset) for air (circles) with the fitting for N_2 (red) and O_2 (blue); (b) the enlarged higher frequency components with fits ignoring (dash) or considering (solid) the effect from centrifugal distortion; (c) the Lorentz linewidth (circles) data of for N_2 (red) and O_2 (blue) in (a) for different Raman transitions start with J, along with exponential decay fits. 101

Figure 5.7 Measured (circles) and fit (lines) polarization dependence of transient NLR of air for parallel (black), perpendicular (red), and magic angle (blue) polarizations. 103

Figure 5.8 Measured (circles) BD signal from gaseous CS_2, along with a fit (red line) considering isotopologue $C^{32}S^{34}S$, centrifugal distortion effect and thermally populated first excited vibrational states $\nu 2$ of $C^{32}S_2$. The inset enlarges the $\Delta E/E$ around the zero, fitted with a single exponential decay (red); (b) ¼, and (c) ½ revival $C^{32}S_2$. (d) shows the ½ revival from $C^{32}S^{34}S$. In (b) the fits in black and blue neglect centrifugal distortion, and the black curve also neglects $\nu 2$ of $C^{32}S_2$.... 105

Figure 5.9 (a) Measured (circles) BD signals about zero delay with fits (lines) for parallel (black), perpendicular (red) and magic angle (blue) polarizations. (b) Enlarged measurement at magic angle. 107

Figure 6.1 (a) Illustrations of nondegenerate NLA processes contributing to NLR in the sub-gap regime; (b) spectral functions for NLA from different mechanisms; (c) calculated degenerate NLR dispersion function $G2$ with total contribution (solid line) decomposed into 2PA, Raman and AC Stark contributions (dashed lines) [45]. 113

Figure 6.2 Calculated ND-NLR (solid lines) and ND-2PA coefficients of ZnO (dashed lines) with excitation photon energy $\hbar\omega b$ of 20% (2), 15% (3) and 10% (4) of the bandgap, as compared to the degenerate case (1). 115

Figure 6.3 Examples of measured BD signals (circles) from ZnO, ZnSe, CdS and fused silica, along with fits (lines) considering GVM 118

Figure 6.4 Measured $n2\omega a;\omega b$ dispersion (red circles) of ZnO, compared to theoretical calculations for nondegenerate (solid lines) and degenerate (dashed lines) $n2$; Shaded region represents errors from the bandwidth of the excitation pulse; degenerate $n2$ data (black squares) is from [41]. 120

Figure 6.5 Measured $n2\omega a;\omega b$ dispersion (red circles) of ZnSe, compared to theoretical calculations for nondegenerate (solid lines) and degenerate (dashed lines) $n2$; Shaded region represents errors from the bandwidth of the excitation pulse; degenerate $n2$ data (black squares) is from [41, 44]. 122

Figure 6.6 Measured $n2\omega a;\omega b$ dispersion (red circles) of CdS, compared to theoretical calculations for nondegenerate (solid lines) and degenerate (dashed lines) $n2$; Shaded region represents errors from the bandwidth of the excitation pulse; degenerate $n2$ data (black squares) is from [41]. 123

Figure 6.7 (a) Examples of ND-3PA signal in ZnSe under different excitation energies, with fits considering GVM; (b) the irradiance dependence of simultaneously measured ΔT and $\Delta E/E$; Comparisons of theory and experiment of ND-3PA spectra for (c) ZnSe and (d) CdS. 125

Figure 6.8 (a) Calculated probe pulsewidth (dash) and $\hbar\omega aT/Eg$ (solid) using Eq. (6.6) at front (black) and back (red) of sample; (b) Converted $n2T$ with different chirping conditions. Inset is the theoretical $n2\omega a;\omega b$ dispersion (black) of ZnO relative to the probe bandwidth (blue); (c)

measured $\Delta E/E$ (black circles), compared to theoretical predictions based on chirping conditions at the front (red dashed) and back (red solid) surface of the sample along with the averaged curve (blue solid). 127

Figure 6.9 Measured FOM of ZnSe in the presence of 2PA for degenerate (black squares) and nondegenerate (red circles) NLR, as compared to theory (solid lines) [41, 45]; FOM in the presence of ND-3PA are based on Isw = 10 GW/cm^2 (green triangles) and Isw = 1 GW/cm^2 (blue stars). The degenerate data is from [44]. The minimum requirements for AOS geometries of a Mach-Zehnder (MZ) interferometer, nonlinear directional coupler (NLDC) and Fabry-Perot (FP) filter are included for comparison..... 130

Figure 7.1 Schematic potential energy curves of general photochromic reaction (only the diabatic process is shown as an example); (b) simplified transformation diagram using molecular triplet state as an analogy. 133

Figure 7.2 Common families of organic photochromic compounds, including both closed- and open-forms reversible transformations [46, 193]..... 134

Figure 7.3 Schematic of 2PA-FRET induced photochromic ring opening mechanism. 136

Figure 7.4 Molecular structures of (a) photochrome, (b) 2PA chromophore and (c) composite molecule PC-1; (d) ORTEP representation of the molecular structure of PC-1 with a distance between C2 and C31 of 6.923 Å [203]; (e) the linear absorption spectra in DCM of PC-1, photochrome, and their subtraction, as compared to that of the pure 2PA chromophore; (f) The absorption spectra in DCM of closed-form PC-1, after UV illumination (closed- and open-form mixture form) and the subtraction between them. 138

Figure 7.5 Linear absorption spectra of (a) blank and (b) dye-doped sol-gels with (1) photochrome, (2) PC-1; (3) shows the visible absorption spectrum of open-form from a PC-1 doped sol-gel. 139

Figure 7.6 (a) Linear absorption spectra of photochrome (red) and M-106 (black), along with the fluorescence spectrum of M-106 (blue); (b) calculated spectral integral function $J\lambda$. 142
Figure 7.7 (a) Fluorescence spectra of PC-1, M-106 and photochrome in DCM; (b) excitation scans of PC-1 (solid) with fixed emission wavelength at 450 nm (black) and 360 nm (blue), in comparison to absorption spectra (dash) of PC-1 (black), M-106 (blue) and photochrome (red). 143
Figure 7.8 (a) Fluorescence anisotropy measurements of PC-1 (blue) and photochrome (red), as compared to the absorption spectrum of PC-1 (black) in dichloromethane. 144
Figure 7.9 (a) Thermal reversing dynamics measured at 460 nm, recovering from two initial conditions: ΔOD=0.9 (black) and ΔOD=0.6 (blue). Both are fitted with triple exponential decay functions using same time constants. (b) thermal reversing of open form after excitation being blocked at 412 s; recovering process is speeded up by illumination of a 532 nm CW beam at 2816 s; (c) normalized ΔOD spectra at 5 s and 9060 s during thermal reversing..... 147
Figure 7.10 (a) Linear absorption spectrum (red) of a sol-gel doped with mixture of M-106 and photochrome with different concentration; (b) measured (black) irradiance dependence of open-form ΔOD of mixed sol-gel at 460 nm and fits (red) using $\varepsilon op = 9700$ $M^{-1}cm^{-1}$ with $\phi = 10$, 20 and 30 %, where the shaded area represents the values of ϕ in between; (c) steady-state accumulation of Nop for different $I0$ and z; (d) accumulation build-up of a Nop averaged over z. 150
Figure 7.11 (a) Measured (black) irradiance dependence of open-form ΔOD of composite sol-gel at 460 nm and fit (red) with the same εop measured in Figure 7.10 (b) and $\phi = 8$, 10 and 12 %; (b) steady-state accumulation of Nop for different $I0$ and z. 151

Figure 7.12 (a) Open-form absorption spectra induced by a same two-photon excitation in sol-gels doped with composite PC-1 and pure photochrome; the quadratic dependence of ΔOD at 460 nm on the excitation energy. 152
Figure 7.13 (a) experimental setup of pump-probe measurements with flowed solutions; (b) measured spectra for a near-UV pump for1PA opening (blue), a visible pump for 2PA-FRET opening (red) and a visible pump for closing (green), as compared to the absorption spectra of closed-form PC-1 (black solid), open-form PC-1 in visible (orange) and closed-form pure photochrome (black dash); the arrow indicates the probe wavelength and bandwidth; (c) measured transmission (normalized to the maximum) of the probe from $Pump_O$ excited PC-1 with various flow rate. 154
Figure 7.14 Measured transient absorption of PC-1 (circles) at 450 nm after one-photon excitation (388 nm) directly applied on photochromic moiety with a temporal delay of (a) 25 ps and (b) a detailed scan within 3 ps with two different pump energies. The fits (red) are applied using a 3-step model [188]. 157
Figure 7.15 energy diagram of the “3-step” reaction model. 158
Figure 7.16 (a) 2PA spectrum of M-106 measured by two-photon induced fluorescence (red circles) and Z-scan (blue square) measurements, along with comparisons to fluorescence anisotropy (blue stars) at emission wavelength of 380nm and linear absorption spectrum (black curve); pump-probe measurements (circles) of M-106 in DCM solution with different excitation energies, along with fits (red lines) with same molecular parameters. 161
Figure 7.17 (a) energy diagram of 2PA-FRET photochromism scheme of PC-1: 2PA of donor moiety followed by FRET and the “3-step” reaction process (see Figure 7.15); a direct comparison of signals (normalized to its concentration) from PC-1 (blue) and M-106 (black) DCM solutions

with identical experimental conditions; (c) measured transient absorption signals of PC-1 (circles) with two different energies, along with fits (red lines) using 2PA-FRET scheme in (a). 164
Figure 7.18 (a) Energy diagram of ring-closing reaction scheme; (b) measured (blue) normalized transmission of an optically induced *trans*-merocyanine solution, showing a transient recovery due to ring-closing; (c) measurement of ring closing dynamics within 4 ps. 166

LIST OF TABLES

Table 2.1 Relations of $\alpha 2$ and $n2$ with $\chi(3)$ for single- and two-beam interaction 19

Table 2.2 Relations of $\alpha 3$ and $n4$ with $\chi(5)$ for single- and two-beam interaction 20

Table 2.3 Definition of nonlinear cross sections for single- and two-beam interactions 21

Table 2.4 Third-order noninstantaneous NLR for single- and two-beam interactions [17, 93] ... 24

Table 4.1 Noninstantaneous NLR response functions due to nuclear motions [17, 73, 125]..... 64

Table 4.2 Fit parameters of the response function of CS_2[a,b] 71

Table 4.3 Fit parameters of nonlinear response function of solvents[a,b] 80

Table 4.4 Reorientational $n2, r$ comparison between theoretical and experimental values[a,b,c] 82

Table 5.1 Symmetries of different wavefunctions upon nuclear interchange [20, 90, 139]..... 94

Table 5.2 Measured rotational and centrifugal distortion constants of N_2 and O_2.[a,b] 103

Table 5.3 Measured rotational and centrifugal distortion constants of $C^{32}S_2$.[a,b] 106

Table 6.1 Measured nondegenerate NLR and NLA coefficients for ZnO.[a] 121

Table 6.2 Measured nondegenerate NLR and NLA coefficients for ZnSe.[a] 122

Table 6.3 Measured nondegenerate NLR and NLA coefficients for CdS.[a] 123

Table 6.4 Measured nondegenerate FOMs in 2PA and 3PA region.[a,b] 131

Table 7.1 Fit parameters of ring-opening transients of photochrome..... 159

Table 7.2 Fit parameters of 2PA-FRET photochromism in PC-1. 165

Table 7.3 Fit parameters of photo-induced ring-closing..... 167

LIST OF ACRONYMS AND ABBREVIATIONS

Acronyms/Units	Descriptions
1PA	One-photon Absorption
2PA	Two-photon Absorption
2PIF	Two-photon Induced Fluorescence
3D	Three Dimensional
3PA	Three-photon Absorption
AC	Alternating Current (Optical)
AOS	All Optical Switching
BBO	Barium Borate
BD	Beam Deflection
CCl_4	Carbon Tetrachloride
CdS	Cadmium Sulfide
$CHCl_3$	Chloroform
CPA	Chirped Pulse Amplified
CS_2	Carbon Disulfide
CW	Continuous Wave
DA	Dual-Arm
DC	Direct Current
DCM / CH_2Cl	Dichloromethane
DFWM	Degenerate Four Wave Mixing
ESA	Excited-State Absorption

ESR	Excited-State Refraction
FOM	Figure Of Merit
FP	Fabry-Perot
FRET	Förster Resonance Energy Transfer
FWHM	Full Width Half Maximum
GM	Göppert-Mayer
GVD	Group Velocity Dispersion
GVM	Group Velocity Mismatch
HeCd	Helium Cadmium
HW1/eM	Half Width 1/e Maximum
KK	Kramers-Kronig
LEB	Low Energy Background
MZ	Mach-Zehnder
ND	Nondegenerate
NLA	Nonlinear Absorption
NLDC	Nonlinear Directional Coupler
NLO	Nonlinear Optical
NLR	Nonlinear Refraction
NOPA	Non-collinear Optical Parametric Amplification
OA&CA	Open & Closed Aperture
OD	Optical Density
OHD	Optical Heterodyne Detection

OKE	Optical Kerr Effect
OPA/G	Optical Parametric Amplifier / Generator
ORTEP	Oak Ridge Thermal Ellipsoid Program
pTHF	Polytetrahydrofuran
RSA	Reverse Saturable Absorption
S/N	Signal to Noise Ratio
SFG	Sum Frequency Generation
SHG	Second Harmonic Generation
SVEP	Slowly Varying Envelope Approximation
THG	Third Harmonic Generation
WLC	White Light Continuum
ZnO	Zinc Oxide
ZnSe	Zinc Selenide

CHAPTER 1: INTRODUCTION

The third-order nonlinearity of materials is responsible for various physical phenomena including two-photon absorption (2PA) and nonlinear refraction (NLR), which alters the material properties, i.e. absorption coefficient and refractive index, by introducing a dependence on the irradiance of the light. Unlike 2PA which occurs instantaneously and requires specific criteria for energy conservation, NLR occurs at any wavelength in any material and sometimes may be accompanied with temporal dynamics depending on its physical origin. Studies of NLR in different phases of material (i.e. gases, liquids and solid-state materials) thus allows us to reveal different aspects of the physical processes responsible for the nonlinear response of materials. In this dissertation, we make extensive use of our recently developed Beam Deflection (BD) technique to explore the ultrafast mechanisms that contribute to NLR in materials of molecular liquids and gases as well as semiconductors.

The second subject is an experimental investigation of a chromene based two-photon photochromic molecule, in which the Förster resonance energy transfer (FRET) has been utilized to activate the photochromic ring-opening effect from 2PA of another chromophore. Transient absorption measurements are performed to resolve the essential parameters required to understand both ring opening and closing reaction schemes, making possible using this 2PA-FRET photochromic molecule for ultrafast photonic applications.

1.1. Ultrafast Mechanisms of NLR

Knowledge of the NLR of liquid solvents is of importance in organic nonlinear spectroscopy, as it helps to understand the results performed on solutions of organic dyes, e.g. to separate the response

of the solute. To quantify NLR, the nonlinear refractive index, n_2, is commonly used for a description for most materials; however, this quantity definition is often abused. n_2 can essentially be treated as a material constant only for bound-electronic NLR (also known as Kerr effect[1]), which originates from the real part of pure electronic second hyperpolarizability. Using n_2 to quantify the refractive index change due to other physical origins, e.g. nuclear motions and cumulative excited-state nonlinearities, creates problem in comparison of literature values. For example, the n_2 of organic solvents has been the subject of numerous experimental measurements, but the results often appear to conflict in value. As an example, liquid-phase carbon disulfide, CS_2, liquid has been extensively studied, and has become one of the most popular nonlinear liquids as a reference material in nonlinear spectroscopy. However, the reported values of n_2 taken from references over the past decades differ from one another over two orders of magnitude depending on the experimental methods, pulsewidths used, and interpretation, as shown in Figure 1.1, where letters represent the measured n_2 values reported in Refs. [1-16].

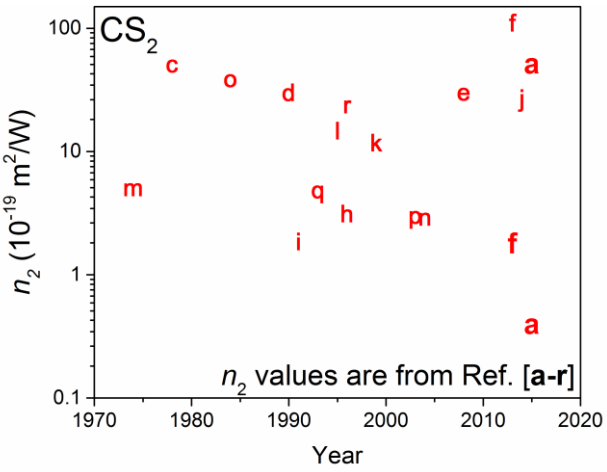

Figure 1.1 A survey of literature values reported for CS_2. The letters represents references of [1-16].

1. In this dissertation, Kerr effect is specifically defined to represent bound-electronic NLR. It should be noted it has also been used for other "long-lived" nonlinearities in other literatures.

In molecular liquids, this is in part because the nuclear nonlinearity of organic solvents results in noninstantaneous contributions to the NLR, making n_2 not a simple number, rather than an effective NLR coefficient, $n_{2,\mathrm{eff}}$, that depends on experimental conditions such as pulsewidth used. An example is the optically-induced molecular reorientation. As discussed in 4.1.2. , a linearly polarized optical field can induce a dipole by polarizing the molecule, making the molecule align towards the field direction. This changes the net orientation (angularly averaged) of the molecular liquid from its initial random distribution, resulting in a change in the refractive index. Different from the instantaneous bound-electronic response, molecular nuclear motion is a dynamic effect due to inertia, which imposes different NLR for different pulsewidths. With our recent study of carbon disulfide (CS_2), we developed a methodology to decompose the nonlinear optical (NLO) response into four different response functions, namely an instantaneous NLR which originates from the purely bound-electronic hyperpolarizability, and three strong noninstantaneous mechanisms due to nuclear motions including collision, libration and reorientation [17, 18]. Polarization-resolved BD measurements separate bound-electronic NLR from the nuclear contributions, allowing us to determine the total NLO response function. The usefulness to have the response function is that we can use it to predict the outcomes of other NLO experiments such as the pulsewidth dependent n_2 measured by Z-scan [17], as discussed in 4.4.

Following the methodology developed for CS_2 [17], we have characterized the NLO response functions of another 23 widely used organic solvents in CHAPTER 4: . Much like for CS_2, the knowledge of the response function will allow prediction of any other NLR measurements on the material, thereby truly establishing self-consistent references for various NLR applications.

Also, the response functions will provide insight to build up the relations between solvent molecular structures and nonlinear refractive properties, which will enhance our understanding on the physical origins of molecular liquid nonlinearities.

Further investigations of solvent nonlinearities are conducted by performing gas-phase BD measurements. The NLO response of molecular gases under intense laser fields, i.e. femtosecond pulses, has long been studied [19, 20]. The knowledge of NLR transients of gases is important in applications such as pulse compression [21], high harmonic generation [22], attosecond pulse shaping [23, 24], control of filamentation [25-28] and separation of molecular isotopologues [29]. For molecules with anisotropic polarizabilities, the major mechanisms that cause NLR in dilute gases are the bound-electronic response, and the noninstantaneous rotational response that originates from the net alignment of the molecular ensemble. As pointed out CHAPTER 5: , our particular interest of study NLR of solvents in gas phase is that the electronic second hyperpolarizability, γ, is directly measured without the need for the nonlinear local-field correction [30-32] that may be required in liquid phase. The measured γ in gas phase is important to compare theoretical models that are usually performed for isolated molecules [33]. Additionally, the direct comparison of γ measured in both liquid and gas phases will help to complete our understanding of Lorentz-Lorenz local field theory, which is crucially meaningful in nonlinear optics where the correction factor due to the impact of the local field is much larger than that in the linear case.

We also investigate NLR in direct-gap semiconductors, in which the optical Kerr effect is the dominant optical nonlinearity in the sub-gap regime [30, 31, 34]. Owing to its ultrafast response, the Kerr effect has been exploited for various ultrafast applications including Kerr-lens mode locking [35], optical limiting [36, 37] and soliton propagation [38, 39]. The degenerate NLR dispersion in semiconductors has been extensive studied both theoretically and experimentally

with single-beam techniques such as Z-scan [40-44]; however, the dispersion of nondegenerate (ND) NLR, namely the refractive index change at frequency ω_a due to the presence of a beam at frequency ω_b, is much less explored than for the degenerate case. While the theory for ND-NLR dispersion has been established in Ref. [45] based on the Kramers-Kronig (KK) transformation, a complete experimental confirmation is still missing particularly in the extremely nondegenerate case and within spectral regions where 2PA is present. The Beam Deflection technique provides the capability of measuring the dispersion of ND-NLR coefficient $n_2(\omega_a;\omega_b)$ with an extraordinary ability to discriminate a large nonlinear absorption (NLA) background. As we will present in CHAPTER 6: , we have measured the $n_2(\omega_a;\omega_b)$ dispersion along with the nondegenerate 2PA and 3PA coeffieient for three direct-gap semiconductors, i.e. ZnO, ZnSe and CdS, which allows us to give a universal scaling of ND-NLR for many materials.

From the application perspective, a great interest of ND-NLR comes from the expectation that $n_2(\omega_a;\omega_b)$ should exhibit substantial enhancement over its degenerate counterpart. This is borne out by our previous observation of the orders of magnitude enhancement of the ND-2PA coefficient $\alpha_2(\omega_a;\omega_b)$. In the extremely ND case. An enhanced NLR suggests the benefit of nondegenerate operating schemes for photonic devices such as for all-optical switching.

1.2. Two-Photon Photochromism

Photochromism usually refers to a photo-initiated reversible transformation process within a single chemical species between two isomeric forms having distinguishable absorption spectra. It is essentially a photochemical process, in which the incident photon can induce changes of atomic arrangement [46]. Historically, *photochromism* simply means light-induced change of color, first proposed by Hirshberg in the 1950s [47], and has since become a commonly known name because

of the commercialization of photochromic spectacles that darken in the sun and recover their transparency at low light levels [48]. Although the first a few applications were mainly based on inorganic materials, such as transition or rare earth metal elements doped single crystals (i.e.$Bi_{12}GeO_{20}$, $Bi_{12}SiO_{20}$ and BTPbO) [49], research work has been heavily focused on organic photochromic materials and their photonic applications. Owing to the large and long-lived colored form in the visible spectrum, organic photochromic molecules, such as naphthopyrans, have been adopted commercially in plastic ophthalmic lenses to provide adaptive transitions to sunlight [50-54]. Figure 1.2 shows an example of the reversible transformation of a typical photochromic spirocompound, chromene. The molecule in closed form contains a twisted ring structure, which only absorbs in ultraviolet (UV) spectral range. Upon activation by UV excitation, the chemical bond cleavage between the sprio-carbon and oxygen atoms leads to an open-ring form. This is followed by *cis-trans* isomerization, resulting in an extended conjugation of π-electron system that exhibits broadband absorption in visible. The colored species usually have a long lifetime up to hours and thermally fade back to the initial transparent state. However, back transfer process can also be induced by photo excitation in visible spectrum, which is also known as photochemical ring-closing. The images in Figure 1.2 show the appearances of transparent closed-form and the colored open-form chromene molecules after doped into a sol-gel matrix [55].

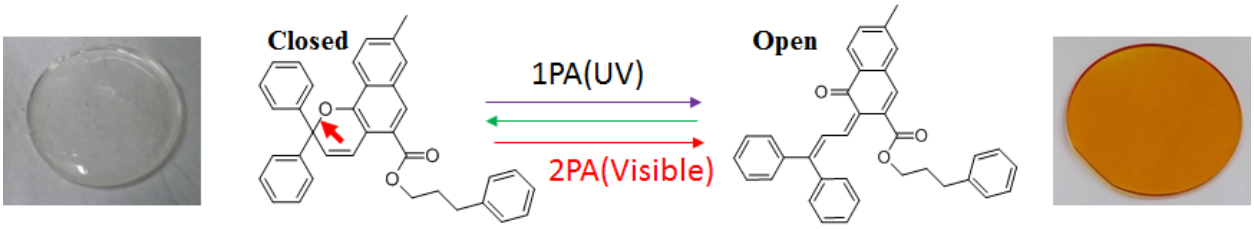

Figure 1.2 Reversible photochromic transformation of a chromene. The arrows indicate 1PA/2PA induced ring-opening, and thermal/photo reversing. The images are closed and open form of a dye-doped sol-gel [55].

Photochromism of Spiro-type compounds have also received great interest for ultrafast photonic applications such as optical memory and switching [56-61], since the photo induced ring opening and closing usually completes within a few or tens of picoseconds. It has been shown these photochromic transformations are accompanied by different transient photoproducts, which may have different temporal dynamics and absorptions. Therefore, the knowledge of the transient ring opening/closing properties such as the quantum yields, reaction time constants and absorption cross sections, are important for developing photonic devices based on photochromic molecule.

As shown in Figure 1.2, the ring opening can also be induced by 2PA in visible spectrum, which leads to various NLO applications utilizing the photochromic effect. For example, two-photon photochromic molecules have been applied to make high-density 3D optical storages. This arises from the advantages of high spatial selectivity of 2PA excitation, as well as the long lifetime of photochromic open form [56-58, 60-62]. Another potential application is to enhance NLA with the open-form absorption. Activated by 2PA, the initial transparent (closed form) molecules start to absorb at the same wavelength as 2PA excitation due to ring opening, possibly resulting in a strong and broadband NLA. Since the ring opening occurs fast in only picoseconds time scale, the photochromic molecule may become a good candidate for making optical limiters in visible spectral range with a truly broadband.

However, most photochromes are not optimized to have large 2PA cross sections (i.e. < 10 GM), which makes two-photon photochromism inefficient for practical applications. To overcome this limitation, we synthesized a novel bifunctional composite photochromic molecule by covalently linking a chromene with a carbazole 2PA chromophore via a carboxyl bridge in an inter-orthogonal configuration without perturbing the electronic distribution of each individual moiety.

Due to the Förster resonance energy transfer (FRET) coupling between the donating 2PA chromophore with the photochromic acceptor, the efficiency of overall two-photon photochromism can be greatly enhanced. In this dissertation, we have performed extensive characterizations on both linear and nonlinear properties of this composite molecule, and resolved the essential parameters for both photochromic ring opening and closing reactions, making possible to implement this composite molecule for practical applications. Additionally, we also investigate the viability of using photochromic molecules for optical limiting application.

1.3. Dissertation Outline

CHAPTER 2: provides the basic theoretical background and formalism of nonlinear interactions needed for this dissertation, particularly focusing on both instantaneous and noninstantaneous NLA and NLR. CHAPTER 3: introduces the laser and parametric devices as well as the nonlinear spectroscopic techniques used in the experimental work of this dissertation. This includes discussions on the principles of Z-scan in 3.2.2. and Beam Deflection in 3.2.3. . CHAPTER 4: starts with introducing the methodology to determine the nonlinear response functions of molecular liquids using the Beam Deflection technique. The measured results of 24 widely used organic solvents are presented with their fitting parameters. CHAPTER 5: provides a detailed formalism describing the rotational nonlinearity of gas-phase molecules. The transient NLR is measured in ambient air and gaseous CS_2. CHAPTER 6: presents studies of the ND-NLR dispersion of direct-gap semiconductors, i.e. ZnO, ZnSe and CdS, where the nondegenerate enhancement and the strong anomalous dispersion are emphasized. The intriguing possibility of improving the figure-of-merit of all-optical switching is discussed. CHAPTER 7: includes an overview of the work done on

charactering the two-photon photochromic molecule studied, including its linear, nonlinear, thermal as well as transient properties. CHAPTER 8: gives conclusions of this dissertation and discusses possible future research.

CHAPTER 2: NONLINEAR ABSORPTION AND REFRACTION

Within the scope of light-matter interactions, the realm of nonlinear optics (NLO) occurs in materials when the intensity of the light beam is sufficiently strong. A group of new phenomena arises from nonlinear interactions such as generating a coherent beam with new frequencies, or manipulating the transmission, polarization or phase of one beam with another beam. This leads to the development of various NLO devices including widely frequency-tunable parametric amplifier/generators (OPA/OPG) [63] and NLA/NLR based all-optical control, e.g. for optical communication [38, 64-69]. Measurements of the nonlinearities of materials also usually help us understand the fundamental aspects of the underlying physical processes [7, 11, 41, 70-76]. For example, the frequency spectrum of the response is closely related to the electronic energy levels as well as their transition dipole moments, and the temporal response function is useful for separation of the physical origins of the various nonlinearities, e.g. electronic and nuclear contributions.

This chapter provides a basic classical approach for describing the nonlinear interaction between light and matter, where, similar to linear optics, macroscopic nonlinear susceptibilities are used to quantify the interactions at a phenomenological level. In this work, we will primarily focus on deriving two particular phenomena, two-photon absorption (2PA) and nonlinear refraction (NLR), originating from the third-order bound-electronic nonlinearities. Among the higher-order effects, only the three-photon absorption terms from the fifth-order susceptibility are discussed. To describe the noninstantaneous NLR due to nuclear contributions, the treatment using the nonlinear response function is introduced. In addition, cumulative nonlinearities such as excited-state absorption (ESA) will also be discussed briefly.

2.1. Nonlinear Optical Interactions

Nonlinear optical behavior arises from higher-order material responses of the incident electric field $\vec{\boldsymbol{E}}(t)$. In dielectric materials, the negative and positive charges, electrons and nuclear ions, are bound together, which move in opposite directions when the electric field is applied. This results in an induced polarization $\vec{\boldsymbol{P}}(t)$, which oscillates according to the driving field. In the ultraviolet and visible spectrum where the frequency is high ($> 10^{13}$ Hz), the motion of the electrons is particularly significant, as the nuclear ions have much larger mass. Therefore, the optical properties mainly originate from bound electrons in this spectral region.

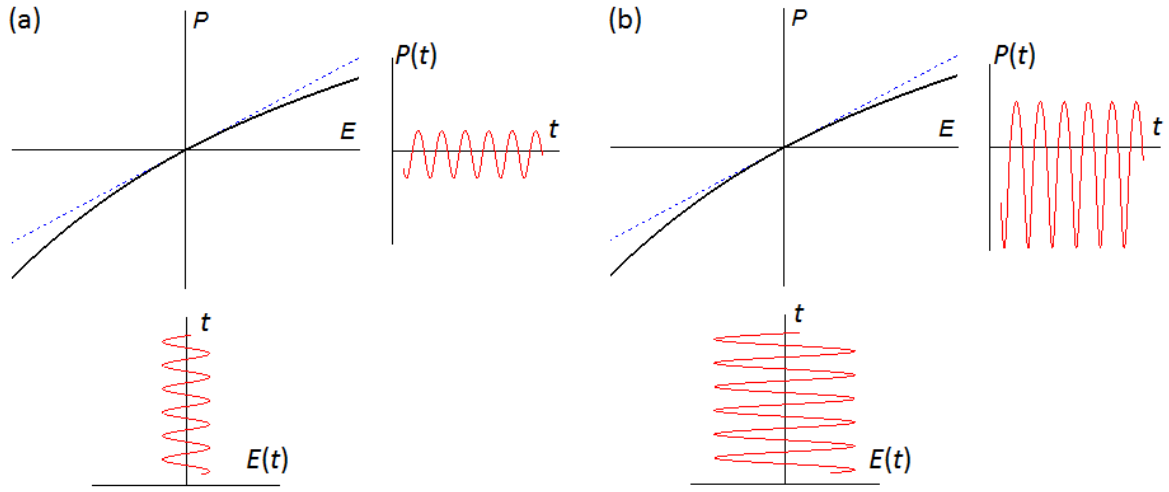

Figure 2.1 Nonlinear dependence (black) of induced polarization *P* on the driving electric field *E* at (a) small amplitude and (b) large amplitude, as compared to the linear dependence (blue dash).

The anharmonic oscillator model [30-32], provides a mechanical analogy to help visualize the material responses that result in nonlinear optical phenomena. An electron is attached to its nuclei with anharmonic potentials, where the restoring force is nonlinearly dependent on the electron's displacement x from its mean position. Driving by $\vec{\boldsymbol{E}}(t)$ at frequency ω, the motion of the

electron is governed by the equation of motion for an anharmonic oscillator, from which we can relate x, or the magnitude of the induced polarization $P = Nex$, with a power series expansion of E, the magnitude of $\vec{\boldsymbol{E}}(t)$, where N is the density of electric dipoles and e is the charge of the electron. This nonlinear dependence is illustrated in Figure 2.1, where the induced polarization follows the sinusoidal oscillation of the driving field at small amplitude, but becomes significantly distorted at larger amplitude, indicating the nonlinear response of the material. The interesting facts come from the Fourier analysis of $P(t)$ in Figure 2.1(b). Besides the fundamental frequency ω, the spectrum of $P(t)$ also contains substantial components at 2ω, 3ω as well as at zero frequency, which corresponding to nonlinear processes such as second- and third-harmonic generation and optical rectification [31, 32]. However, it also includes nonlinear terms at ω which is the primary subject of this dissertation.

2.1.1. Nonlinear Polarizations

A more rigorous formulation of the constitutive relation between $\vec{\boldsymbol{P}}(t)$ and the driving field $\vec{\boldsymbol{E}}(t)$ utilizes material's macroscopic linear and nonlinear susceptibilities $\boldsymbol{\chi}^{(n)}(t)$ [31, 34, 77, 78]:

$$\begin{aligned}\vec{\boldsymbol{P}}_i(t) = \varepsilon_0 \int_{-\infty}^{\infty} \boldsymbol{\chi}_{ij}^{(1)}(t-t')\,\vec{\boldsymbol{E}}_j(t')dt' \\ + \varepsilon_0 \iint_{-\infty}^{\infty} \boldsymbol{\chi}_{ijk}^{(2)}(t-t', t-t'')\vec{\boldsymbol{E}}_j(t')\vec{\boldsymbol{E}}_k(t'')dt'dt'' \\ + \varepsilon_0 \iiint_{-\infty}^{\infty} \boldsymbol{\chi}_{ijkl}^{(3)}(t-t', t-t'', t-t''')\vec{\boldsymbol{E}}_j(t')\vec{\boldsymbol{E}}_k(t'')\vec{\boldsymbol{E}}_l(t''')dt'dt''dt''' \\ + \cdots,\end{aligned} \tag{2.1}$$

where ε_0 is the vacuum permittivity, $\vec{\boldsymbol{P}}_i(t)$ induced at time t is calculated from a summation of convolutions of different orders of $\boldsymbol{\chi}^{(n)}(t)$ with mixed optical fields exerted at different times (i.e. t', t'' and t''') which may or may not have the same frequency. *i*, *j*, *k* and *l* represent the polarization directions. For instantaneous nonlinear responses, i.e. bound-electronic nonlinearities, the integrals vanish except at time $t = t' = t'' = t''' = \cdots$. It must be noted that the effect due to the optical magnetic field is neglected as it is usually weak. Also, Eq. (2.1) assumes spatially local nonlinearity, i.e. the induced polarization only occurs at the point where the electric field is applied.

An alternative description, perhaps more widely used for bound-electronic nonlinearities with mixed monochromatic waves, is the frequency domain susceptibility tensor, e.g. $\boldsymbol{\chi}^{(2)}_{ijk}(\omega; \omega_a, \omega_b)$. By applying Fourier transforms, the convolutions of Eq. (2.1) in the time domain become products in the frequency domain as:

$$\begin{aligned}\mathbf{P}_i(\omega) = {} & \varepsilon_0 \boldsymbol{\chi}^{(1)}_{ij}(\omega)\mathbf{E}_j(\omega) \\ & + \varepsilon_0 \int_{-\infty}^{\infty}\int \boldsymbol{\chi}^{(2)}_{ijk}(\omega; \omega_a, \omega_b)\mathbf{E}_j(\omega_a)\mathbf{E}_k(\omega_b)\delta(\omega - \omega_a - \omega_b)d\omega_a d\omega_b \\ & + \varepsilon_0 \int_{-\infty}^{\infty}\iint \boldsymbol{\chi}^{(3)}_{ijkl}(\omega; \omega_a, \omega_b, \omega_c)\mathbf{E}_j(\omega_a)\mathbf{E}_k(\omega_b)\mathbf{E}_l(\omega_c)\delta(\omega - \omega_a - \omega_b - \omega_c)d\omega_a d\omega_b d\omega_c \\ & + \cdots,\end{aligned} \tag{2.2}$$

where $\mathbf{P}(\omega)$ and $\mathbf{E}(\omega)$ are the Fourier transforms of the time domain polarization and electric field. ω is the mixed frequency $\omega_a + \omega_b + \omega_c + \cdots$, where the energy conservation is ensured by Dirac delta functions, e.g. for the second-order nonlinearity, $\omega = \omega_a + \omega_b$.

The convenience to use frequency domain susceptibility tensors is the fact that this results in superpositions of input monochromatic waves, which corresponds to different nonlinear phe-

nomena [30-32, 78]. For example, we may define the input electric field as a combination of monochromatic plane waves, which may be at different frequencies ω_n and polarization directions indicated by subscript *i*,

$$\vec{\boldsymbol{E}}_i(z,t) = \sum_{i,n}\left(\frac{1}{2}\mathcal{E}_i(\omega_n)e^{i(\boldsymbol{k}\cdot\boldsymbol{z}-\omega_n t)} + c.c.\right)\vec{\boldsymbol{e}}_i \tag{2.3}$$

where $\mathcal{E}_i$ is the complex electric field amplitude with a factor of ½ due to the definition, $\boldsymbol{k}$ is the wavevector, $\boldsymbol{z}$ is the propagation direction vector, $\vec{\boldsymbol{e}}_i$ is the unit vector along with polarization direction and $c.c.$ indicates the complex conjugate terms. A similar definition is applied for $\vec{\boldsymbol{P}}_i(z,t)$, i.e.

$$\vec{\boldsymbol{P}}_i(z,t) = \sum_{i,n}\left(\frac{1}{2}\mathcal{P}_i^{(\mathrm{n})}(\omega)e^{i(\boldsymbol{k}_{\mathbf{NL}}\cdot\boldsymbol{z}-\omega_n t)} + c.c.\right)\vec{\boldsymbol{e}}_i, \tag{2.4}$$

with $\mathcal{P}_i(\omega_n)$ and $\boldsymbol{k}_{\mathbf{NL}}$ as its complex amplitude and wavevector. The Fourier transform in the time domain of Eq. (2.3) yields

$$\mathbf{E}_i(\omega) = \sum_{i,n}\frac{1}{2}\left(\mathcal{E}_i(\omega)\delta(\omega-\omega_n)e^{i\mathbf{k}\cdot\mathbf{z}} + \mathcal{E}_i^*(\omega)\delta(\omega+\omega_n)e^{-i\mathbf{k}\cdot\mathbf{z}}\right)\vec{\boldsymbol{e}}_i. \tag{2.5}$$

By substituting Eq. (2.4) and (2.5) in to (2.2), we can generally relate the complex amplitudes of the n^{th}-order $\mathcal{P}_i^{(\mathrm{n})}(\omega)$ with each $\mathcal{E}_i(\omega_n)$ as

$$\mathcal{P}_i^{(\mathrm{n})}(\omega) = \varepsilon_0 \sum_{\alpha_1\ldots\alpha_n}\sum_{\omega_n} K\chi^{(\mathrm{n})}_{(i;\alpha_1\ldots\alpha_n)}(\omega;\omega_a\ldots\omega_n)\mathcal{E}_{\alpha_1}(\omega_a)\ldots\mathcal{E}_{\alpha_n}(\omega_n), \tag{2.6}$$

where $\Sigma_{\alpha_1\ldots\alpha_n}\Sigma_{\omega_n}$serve as summations for all sets of possible polarizations and frequencies respectively. K is a numerical factor as a result of intrinsic permutation symmetry, i.e. the order for multiplying $\mathcal{E}_{\alpha_n}(\omega_n)$ is permutable (or indistinguishable). To know the corresponding physical phenomena of each induced nonlinear polarization, a wave equation needs to be solved using

$\mathcal{P}_i^{(\mathrm{n})}(\omega)$ as a driving source (or perturbation), which give the evolution of the generated eigenmode fields as a result of nonlinear interaction in the material.

2.1.2. Nonlinear Wave Equation

To examine how the induced nonlinear polarizations modify the incident field as a plane wave $\vec{\boldsymbol{E}}_i(z,t)$ is propagating through the medium, we start with the wave equation derived from Maxwell equations [31, 79, 80]

$$\frac{\partial^2 \vec{\boldsymbol{E}}_i(z,t)}{\partial z^2} - \frac{1}{c^2}\frac{\partial^2 \vec{\boldsymbol{E}}_i(z,t)}{\partial t^2} = \mu_0 \frac{\partial^2 \vec{\boldsymbol{P}}_i(z,t)}{\partial t^2}, \tag{2.7}$$

where μ_0 is the vacuum permeability, and $c = 1/\sqrt{\mu_0 \varepsilon_0}$ is the speed of light. The complex amplitude of $\vec{\boldsymbol{P}}_i(z,t)$, defined in Eq. (2.6), is rewritten in terms of a linear and a nonlinear term as: $\mathcal{P}_i^{(\mathrm{n})}(\omega) = \mathcal{P}_i^{(1)}(\omega) + \mathcal{P}_i^{\mathrm{NL}}(\omega)$. $\mathcal{P}_i^{(1)}(\omega) = \varepsilon_0 \chi_{ii}^{(1)}(\omega;\omega)\mathcal{E}_i(\omega)$ is related with linear optical properties of the material, i.e. $\sqrt{1+\chi_{ii}^{(1)}(\omega;\omega)} = n(\omega) + i\kappa(\omega)$, where $\kappa(\omega)$ is the imaginary part of the complex refractive index, which is related to the one-photon absorption coefficient $\alpha_1 = 2\kappa\omega/c$. By replacing $\mathcal{P}_i^{(1)}(\omega)$ with the complex index of refraction and substituting Eq. (2.3), Eq. (2.7) can be simplified to only include $\mathcal{P}_i^{\mathrm{NL}}(\omega)$ as its driving term. Furthermore, the slowly varying envelope approximation (SVEA) is applied for both $\mathcal{E}_i(\omega)$ and $\mathcal{P}_i^{\mathrm{NL}}(\omega)$, which facilitates ignoring the second-order derivatives for both space and time. Together these approximations yield

$$i2k\left(\frac{\partial \mathcal{E}_i}{\partial z} + \frac{n}{c}\frac{\partial \mathcal{E}_i}{\partial t} + \frac{\alpha_1}{2}\mathcal{E}_i\right)e^{ikz} = -\mu_0\omega\left(i2\frac{\partial \mathcal{P}_i^{\mathrm{NL}}}{\partial t} + \omega\mathcal{P}_i^{\mathrm{NL}}\right)e^{ik_{NL}z}. \tag{2.8}$$

Assuming continuous waves (CW) or slowly varying amplitudes and the absence of linear absorption, the second and third terms on the left hand side of Eq. (2.8) vanish. Combining the phase terms to $e^{i(k_{NL}-k)z}$, the SVEA nonlinear wave equation becomes

$$\frac{\partial \mathcal{E}_i(\omega)}{\partial z} = i\frac{\omega}{2nc\varepsilon_0}\mathcal{P}_i^{\mathrm{NL}}(\omega)e^{i(k_{NL}-k)z}. \tag{2.9}$$

This is a formalism to solve the evolution of an eigenmode field generated from $\mathcal{P}_i^{\mathrm{NL}}(\omega)$ driving interactions. It must be noted that Eq.(2.9) becomes an exact differential equation when the wavevector of the nonlinear polarization matches that of the generated output field ($k_{NL} = k$). This is also known as the phase matching condition, when the two fields add constructively through propagation in z. For example, for effects due to a quadratic nonlinear polarization, e.g. $\mathcal{P}_i^{(1)}(\omega_I) = K\varepsilon_0\chi_{ijk}^{(21)}(\omega_I;\omega_p,\omega_s)\mathcal{E}_j(\omega_p)\mathcal{E}_k^*(\omega_s)$, a variety of frequency mixing phenomena occur such as second-harmonic generation (SHG), sum- and difference-frequency mixing associated parametric amplification, optical rectification and electro-optic (Pockel cell) effect [78], where the phase matching condition, i.e. $k_P = k_I + k_s$, needs to be satisfied. The application of Eq. (2.9) for higher order processes, e.g. third-order nonlinearities, will be discussed in the next section.

2.2. Nonlinear Refraction and Absorption

The cubic polarizations arises from a material response at the third power of the electric field amplitude, which governs frequency mixing phenomena such as third-harmonic generation (THG) and general four-wave mixing [31, 34, 77, 78]. Of particular interest in this work, we focus on the induced nonlinear polarizations that return the same frequency (or same wavevector) as the incident field, where the phase matching condition is automatically satisfied. This leads to a modification of the amplitude or phase of the incident beam itself that is proportional to the irradiance of

the light. One is nonlinear refraction (NLR), also known as the optical Kerr effect, which is the key mechanism of many nonlinear phenomena, e.g. self-focusing [81], soliton propagation [38, 39, 82-84] and phase conjugate reflection [85]. Also, the third-order nonlinear polarizations gives rise to some effects which essentially show the quantum nature such as two-photon absorption (2PA) [86-88] and stimulated Raman scattering [89, 90]. Nonlinear spectroscopy, e.g. determining the 2PA spectrum, will reveal electronic energy levels of the material that usually cannot be accessed via linear spectroscopy [88, 91], i.e. 1PA spectra.

Different from Kerr nonlinearities that have nearly-instantaneous response due to its electronic nature, for molecules there are other mechanisms, e.g. vibrational and rotational nuclear motions, which can also give local irradiance dependent NLR but with a temporal response on timescales of hundreds of femtoseconds to tens of picoseconds [17, 73, 75, 92-94]. As discussed later, we provide a general formalism to describe noninstantaneous NLR due to nuclear motions.

2.2.1. Bound-electronic Nonlinearities

Within the scope of our experimental conditions, we will derive the third-order NLR and NLA imposed on the incident beam polarized in $\vec{\boldsymbol{e}}_x$ at frequency ω_a, due to its irradiance (single beam), and due to the presence of a collinear propagating second beam at ω_b, with either parallel ($\vec{\boldsymbol{e}}_x$) or perpendicular ($\vec{\boldsymbol{e}}_y$) polarization. Here, we use $\vec{\boldsymbol{e}}_x$ for ω_b in the following derivation. From Eq.(2.6), the induced third-order polarization that returns the same frequency and direction as the incident beam is

$$\mathcal{P}_x^{(3)}(\omega_a) = \frac{3}{4}\varepsilon_0\chi_{xxxx}^{(3)}(\omega_a;\omega_a,-\omega_a,\omega_a)|\mathcal{E}_x(\omega_a)|^2\mathcal{E}_x(\omega_a) + \frac{3}{2}\varepsilon_0\chi_{xxxx}^{(3)}(\omega_a;\omega_a,-\omega_b,\omega_b)|\mathcal{E}_x(\omega_b)|^2\mathcal{E}_x(\omega_a). \quad (2.10)$$

The numerical factor K defined Eq.(2.6) is $\frac{3}{4}$ and $\frac{3}{2}$ for one- and two-beam interactions, respectively, due to intrinsic permutation symmetry, where the latter case is 2× larger. This factor of 2 is critical to consider in interpretation of experimental results for consistency between one- and two-beam experiments, e.g. Z-scan and Beam Deflection measurements as discussed in 3.2. . Also, the overall nonlinear wavevector due to three electric fields, $k_{NL} = k_a$, automatically matches the wavevector on the left-hand side of Eq.(2.9). Therefore, we can substitute Eq. (2.10) into Eq.(2.9) and on the left-hand side replace the amplitude of electric field by $\mathcal{E}_x(\omega_a, z) = \sqrt{\frac{2}{\varepsilon_0 n_a c} I_x(\omega_a, z)}e^{i\Delta\phi_x(\omega_a,z)}$, where $I_x(\omega_a, z)$ is the irradiance and $\Delta\phi_x(\omega_a, z)$ is the induced non-linear phase change. We thus can equalize the real and imaginary components in Eq.(2.9) and arrive at

$$\frac{\partial I_x(\omega_a)}{\partial z} = -\alpha_1 I_x(\omega_a) - \alpha_{2,\parallel}(\omega_a;\omega_a)I_x^2(\omega_a) - 2\alpha_{2,\parallel}(\omega_a;\omega_b)I_x(\omega_b)I_x(\omega_a), \quad (2.11)$$

$$\frac{\partial \Delta\phi_x(\omega_a)}{\partial z} = k_{0,a}n_{2,\parallel}(\omega_a;\omega_a)I_x(\omega_a) + 2k_{0,a}n_{2,\parallel}(\omega_a;\omega_b)I_x(\omega_b), \quad (2.12)$$

where $k_{0,a}$ is the wavenumber in vacuum, , α_2 and n_2 are defined as 2PA coefficient and nonlinear refractive index respectively, which are related to the imaginary and real part of the third-order susceptibility as given in Table 2.1. The factor of 2 in both two-beam terms is by definition, which accounts for the numerical factor K defined in Eq. (2.10) due to permutation and ensures consistency between single- and two-beam definitions of α_2 and n_2. Eqs. (2.11) and (2.12) can be solved individually to give the amplitude and phase change of the electric field after propagation

through the material, as long as the thickness is less than the Rayleigh ranges of both beams and the nonlinear induced phase distortion does not propagate within the sample to produce irradiance changes on either beam. This is also known as external interaction [81].

Table 2.1 Relations of α_2 and n_2 with $\chi^{(3)}$ for single- and two-beam interactions

	2PA coefficient	Nonlinear refractive index
Single beam	$\alpha_{2,\parallel}(\omega_a;\omega_a)=\frac{3}{2}\frac{\omega_a\mu_0}{n_a^2}\chi^{(3)}_{I,xxxx}(\omega_a;-\omega_a,\omega_a,\omega_a)$	$n_{2,\parallel}(\omega_a;\omega_a)=\frac{3}{4}\frac{1}{n_a^2\varepsilon_0 c}\chi^{(3)}_{R,xxxx}(\omega_a;-\omega_a,\omega_a,\omega_a)$
Nondegenerate	$\alpha_{2,\parallel}(\omega_a;\omega_b)=\frac{3}{2}\frac{\omega_a\mu_0}{n_a n_b}\chi^{(3)}_{I,xxxx}(\omega_a;\omega_a,\omega_b,-\omega_b)$	$n_{2,\parallel}(\omega_a;\omega_b)=\frac{3}{4}\frac{1}{n_a n_b\varepsilon_0 c}\chi^{(3)}_{R,xxxx}(\omega_a;\omega_a,\omega_b,-\omega_b)$
Cross-polarized	$\alpha_{2,\perp}(\omega_a;\omega_a)=\frac{3}{2}\frac{\omega_a\mu_0}{n_a^2}\chi^{(3)}_{I,xxyy}(\omega_a;\omega_a,\omega_a,-\omega_a)$	$n_{2,\perp}(\omega_a;\omega_a)=\frac{3}{4}\frac{1}{n_a^2\varepsilon_0 c}\chi^{(3)}_{R,xxyy}(\omega_a;\omega_a,\omega_a,-\omega_a)$
Cross-polarized & nondegenerate	$\alpha_{2,\perp}(\omega_a;\omega_b)=\frac{3}{2}\frac{\omega_a\mu_0}{n_a n_b}\chi^{(3)}_{I,xxyy}(\omega_a;\omega_a,\omega_b,-\omega_b)$	$n_{2,\perp}(\omega_a;\omega_b)=\frac{3}{4}\frac{1}{n_a n_b\varepsilon_0 c}\chi^{(3)}_{R,xxyy}(\omega_a;\omega_a,\omega_b,-\omega_b)$

Bound-electronic NLR and NLA can also arises from higher-order nonlinearities. Although the susceptibilities become significantly smaller when going towards higher orders [31], some effects are still observable in experiments such as three-photon absorption (3PA) from the imaginary part of $\chi^{(5)}$[74, 86, 95]. Within the scope of single- and two-beam interaction geometries, similar with Eq. (2.10), the fifth-order nonlinear polarizations that return the same frequency and direction as the incident beam are

$$\begin{aligned}\mathcal{P}_x^{(5)}(\omega_a)=&\frac{5}{8}\varepsilon_0\chi^{(5)}_{xxxxxx}(\omega_a;\omega_a,-\omega_a,\omega_a,-\omega_a,\omega_a)|\mathcal{E}_x(\omega_a)|^4\mathcal{E}_x(\omega_a)\\&+\frac{15}{8}\varepsilon_0\chi^{(5)}_{xxxxxx}(\omega_a;\omega_a,\omega_b,-\omega_b,\omega_b,-\omega_b)|\mathcal{E}_x(\omega_b)|^4\mathcal{E}_x(\omega_a),\end{aligned}\tag{2.13}$$

where the second term (two-beam interaction in an excite-probe geometry) has a numerical factor that is 3× larger the first term, which again is from permutation symmetry and needs to be considered for consistency between single- and three-input experiments. Similarly, we can substitute Eq. (2.13) into Eq.(2.9) replace the electric field with irradiance and phase change, which yields;

$$\frac{\partial I_x(\omega_a)}{\partial z} = -\alpha_{3,\parallel}(\omega_a;\omega_a,\omega_a)I_{\mathrm{x}}^3(\omega_a) - 3\alpha_{3,\parallel}(\omega_a;\omega_b,\omega_b)I_{\mathrm{x}}^2(\omega_b)I_x(\omega_a), \tag{2.14}$$

$$\frac{\partial \Delta\phi_x(\omega_a)}{\partial z} = k_{0,a}n_{4,\parallel}(\omega_a;\omega_a,\omega_a)I_{\mathrm{x}}^2(\omega_a) + 3k_{0,a}n_{4,\parallel}(\omega_a;\omega_b,\omega_b)I_{\mathrm{x}}^2(\omega_b), \tag{2.15}$$

where α_3 and n_4 are defined as 3PA coefficient and higher order nonlinear refractive index respectively, which are related to the imaginary and real part of the fifth-order susceptibility given in Table 2.2. Similar to the $\chi^{(3)}$ case, the factor 3 in both two-beam terms make single- and multiple-beam input experiments consistent. The interaction of cross-polarized beams can be derived in similar a manner.

Table 2.2 Relations of α_3 and n_4 with $\chi^{(5)}$ for single- and two-beam interaction

	$\alpha_{3,\parallel}$	$n_{4,\parallel}$
Single beam $(\omega_a;\omega_a,\omega_a)$	$\frac{5}{2}\frac{\omega_p}{\varepsilon_0^2 n_a^3 c^3}\chi^{(5)}_{I,xxxxxx}(\omega_a;\omega_a,\omega_a,-\omega_a,\omega_a,-\omega_a)$	$\frac{5}{4}\frac{1}{\varepsilon_0^2 n_a^3 c^2}\chi^{(5)}_{R,xxxxxx}(\omega_a;\omega_a,\omega_a,-\omega_a,\omega_a,-\omega_a)$
Two beams $(\omega_a;\omega_a,\omega_b)$	$\frac{5}{2}\frac{\omega_p}{\varepsilon_0^2 n_a n_b^2 c^3}\chi^{(5)}_{I,xxxxxx}(\omega_a;\omega_a,\omega_b,-\omega_b,\omega_b,-\omega_b)$	$\frac{5}{4}\frac{1}{\varepsilon_0^2 n_a n_b^2 c^2}\chi^{(5)}_{R,xxxxxx}(\omega_a;\omega_a,\omega_b,-\omega_b,\omega_b,-\omega_b)$

Strictly speaking, n_2, α_2 and the susceptibilities are all macroscopic parameters which give the properties of the actual "sample" used in the experiment. When dealing with organic molecules, measurements performed in solution form is common. Then, different molecular densities, *N*, will result in different macroscopic parameters. Therefore, it is more meaningful to define microscopic parameters, e.g., the nonlinear cross sections, which conventionally written in units of

"Göppert-Mayer" (GM), 1GM = 10^{-50} cm^4 s photon^{-1} molecule^{-1}[96]. The relations between 2PA (δ_{2PA}), 3PA (δ_{3PA}) and NLR (δ_{NLR}) cross sections with corresponding nonlinear coefficients are tabulated in Table 2.3 for both single-beam and nondegenerate multiple input-beam interactions.

Table 2.3 Definition of nonlinear cross sections for single- and two-beam interactions

	δ_{2PA}	δ_{3PA}	δ_{NLR}
Single-beam	$\frac{\alpha_2(\omega_a;\omega_a)\hbar\omega_a}{N}$	$\frac{\alpha_3(\omega_a;\omega_a,\omega_a)(\hbar\omega_a)^2}{N}$	$\frac{k_{0,a}n_2(\omega_a;\omega_a)\hbar\omega_a}{N}$
Two-beam nondegenerate	$\frac{\alpha_2(\omega_a;\omega_b)\hbar\omega_b}{N}$	$\frac{\alpha_3(\omega_a;\omega_b,\omega_b)(\hbar\omega_b)^2}{N}$	$\frac{k_{0,a}n_2(\omega_a;\omega_b)\hbar\omega_b}{N}$

Effectively, NLA and NLR can be treated as modifications of the linear absorption and refraction. For an excite-probe geometry, these changes are attributed to a strong excitation beam at ω_b, and the self-nonlinearity from the weak probe (ω_a) itself is negligible. Considering only third- and fifth-order effects, the changes in refractive index and absorption are

$$\Delta n(\omega_a) = 2n_2(\omega_a;\omega_b)I(\omega_b) + 3n_4(\omega_a;\omega_b,\omega_b)I^2(\omega_b), \tag{2.16}$$

$$\Delta\alpha(\omega_a) = 2\alpha_2(\omega_a;\omega_b)I(\omega_b) + 3\alpha_3(\omega_a;\omega_b,\omega_b)I^2(\omega_b), \tag{2.17}$$

This approach generalizes the problem and is not only applicable to bound-electronic nonlinearities, but other physical origins of NLR and NLA such as noninstantaneous NLR from nuclear responses of the molecule. As discussed later, by evaluating the resulting modifications on its linear properties, we are able to define effective NLR coefficient.

2.2.2. Noninstantaneous Nuclear Nonlinearities

For materials with a noninstantaneous response, e.g. due to nuclear vibrational and rotational motions, from Eq. (2.1), the third-order component of the induced polarization is

$$\vec{\boldsymbol{P}}_{n,i}^{(3)}(t) = \varepsilon_0 \iiint_{-\infty}^{\infty} \boldsymbol{\chi}_{n,ijkl}^{(3)}(t-t', t-t'', t-t''')\vec{\boldsymbol{E}}_j(t')\vec{\boldsymbol{E}}_k(t'')\vec{\boldsymbol{E}}_l(t''')dt'dt''dt'''. \tag{2.18}$$

In early work of Hellwarth et al [97], the Born-Oppenheimer approximation was employed to separate the third-order nonlinear optical response from contributions of bound-electrons ($\boldsymbol{\chi}_e^{(3)}$) and nuclei ($\boldsymbol{\chi}_n^{(3)}$), where the interacting optical frequency is well below any electronic resonances. This greatly simplifies the expression of the susceptibility compared to [98]. As described in [97, 99], the nuclear nonlinearity takes the form

$$\boldsymbol{\chi}_n^{(3)}(t-t', t-t'', t-t''') = \boldsymbol{\chi}_n^{(3)}(t-t')\delta(t-t'')\delta(t'-t'''). \tag{2.19}$$

Substituting this into Eq. (2.18), it reduces to a single temporal integral over t'

$$\vec{\boldsymbol{P}}_{n,i}^{(3)}(t) = \varepsilon_0 \int_{-\infty}^{\infty} \boldsymbol{\chi}_{n,ijkl}^{(3)}(t-t')\vec{\boldsymbol{E}}_j(t')\vec{\boldsymbol{E}}_k(t)\vec{\boldsymbol{E}}_l(t')dt', \tag{2.20}$$

where the integrand involves a product of only two complex electric fields, which for a single-beam interaction contains two second-harmonic terms $\frac{1}{4}\left(\mathcal{E}(t')^2 e^{i2\omega t} + \mathcal{E}(t')^2 e^{-i2\omega t}\right)$, integrating to zero, and the "irradiance" term $\frac{1}{2}|\mathcal{E}(t')|^2$. By substituting into Eq. (2.20) with suppression of frequency and polarization arguments, the time dependent complex amplitude of $\vec{\boldsymbol{P}}_{n,i}^{(3)}(t)$ becomes

$$\mathcal{P}_n^{(3)}(t) = \frac{1}{2}\varepsilon_0 \int_{-\infty}^{\infty} \chi_n^{(3)}(t-t')\mathcal{E}(t)|\mathcal{E}(t')|^2 dt'. \tag{2.21}$$

For two-beam interactions, we are particularly interested in a nondegenerate excite-probe geometry with an excitation beam at ω_b and probe beam at ω_a. This greatly simplifies problems such as the two-beam coupling effects in the degenerate case [31]. Evaluating the two-field products within the integrand of Eq. (2.20) results in terms rapidly oscillating at $2\omega_a$, $2\omega_b$ and $(\omega_a - \omega_b)$, which again will be integrated to zero. The only surviving term is the "irradiance" term of excitation, $\frac{1}{2}|\mathcal{E}_b(t')|^2$, where the subscript represents the frequency, which gives the complex amplitude of $\vec{\boldsymbol{P}}_n^{(3)}(t)$ that affects the probe beam due to the presence of the excitation as

$$\mathcal{P}_{n,a}^{(3)}(t) = \frac{1}{2}\varepsilon_0 \int_{-\infty}^{\infty} \chi_n^{(3)}(t-t')\mathcal{E}_a(t)|\mathcal{E}_b(t')|^2 dt'. \tag{2.22}$$

It must be noted that for a noninstantaneous nuclear nonlinearity, the induced nonlinear polarizations of single- and two-beam interactions have the same numerical factor $K = \frac{1}{2}$, while a factor of 2 appeared in the bound-electronic nonlinearities, as shown in Eq. (2.10). This strongly depends on the approximation made in Eq.(2.19) where the temporal integral is simplified to only include two electric fields. Physically, it can also be explained since the factor 2 is due to the moving interference pattern in the two-beam interaction, which is now moving too fast for noninstantaneous nuclear response to follow [17, 93]. Substituting either Eq. (2.21) or (2.22) into Eq. (2.9) with phase matching ($k_{NL} = k_a$) yields

$$\frac{\partial \mathcal{E}_a(t)}{\partial z} = i\frac{\omega}{4nc} \int_{-\infty}^{\infty} \chi_n^{(3)}(t-t')\mathcal{E}_a(t)\left|\mathcal{E}_{a,b}(t')\right|^2 dt'. \tag{2.23}$$

Since $\chi_n^{(3)}(t-t')$ is real as $\vec{\boldsymbol{P}}_{n,i}^{(3)}$ and $\vec{\boldsymbol{E}}$ are real in Eq. (2.20), the nuclear nonlinearity only results in a phase change of $\mathcal{E}_a(t)$ as it propagates through the material in *z*. This nuclear nonlinearity is induced noninstantaneously by either another beam $|\mathcal{E}_b(t')|^2$ or by itself $|\mathcal{E}_a(t')|^2$. Much

like Eq. (2.12), the complex field amplitude can be decomposed into a phase change and irradiance term under the external self-action approximation. We then arrive at

$$\frac{\partial \Delta\phi_a}{\partial z} = k_0 \int_{-\infty}^{\infty} R(t-t') I_{a,b}(t') \mathrm{d}t', \tag{2.24}$$

where $R(t)$, in terms of susceptibility, is the response function for noninstantaneous NLR.

Together with the refractive index change due to the bound-electronic nonlinearity, the overall $\Delta n(t)$ along with the response functions in both single- and two-beam interactions are summarized in Table 2.4. Note in the single beam case, it is worth defining an effective NLR coefficient $n_{2,\mathrm{eff}}$, $n_{2,\mathrm{eff}} = \langle \Delta n(t) \rangle / \int I(t) \mathrm{d}t$, where $\langle \Delta n(t) \rangle$ is the refractive index change weighted by the temporal profile of the irradiance, as explicitly discussed in Refs. [17, 93]. This integral averages out the temporal dynamics of the material response, and may correspond to the results measured in single-beam experiment such as Z-scan.

Table 2.4 Third-order noninstantaneous NLR for single- and two-beam interactions [17, 93]

	Single-beam $(\omega_a; \omega_a)$	Two-beam $(\omega_a; \omega_b)$
$R(t)$	$\frac{2\chi_n^{(3)}(t)}{4n_a^2 \varepsilon_0 c}$	$\frac{2\chi_n^{(3)}(t)}{4n_a n_b \varepsilon_0 c}$
$\Delta n(t)$	$n_2(\omega_a; \omega_a) I_a(t) + \int_{-\infty}^{\infty} R(t-t') I_a(t') \mathrm{d}t'$	$2n_2(\omega_a; \omega_b) I_b(t) + \int_{-\infty}^{\infty} R(t-t') I_b(t') \mathrm{d}t'$
$n_{2,\mathrm{eff}}$	$n_2(\omega_a; \omega_a) + \frac{\int_{-\infty}^{\infty} I_a(t) \int_{-\infty}^{\infty} R(t-t') I_a(t') \mathrm{d}t' \, \mathrm{d}t}{\int_{-\infty}^{\infty} {I_a}^2(t) \mathrm{d}t}$	$n_2(\omega_a; \omega_b)$

2.3. Excited-state Nonlinearities

The absorption and refraction of a material can be changed due to level population redistribution, which also known as excited-state nonlinearities. Organic molecules sometimes display excited-state absorption (ESA) and refraction (ESR), and in semiconductors this originates from induced free carriers. In contrast to nonresonant bound-electronic nonlinearities from induced higher-order nonlinear polarizations, real linear absorption processes are involved in these population related nonlinearities [32, 100, 101].

To demonstrate how population redistribution affects nonlinear transmission (i.e. NLA or linear absorption saturation), we introduce a simple 3-level system as shown in Figure 2.2(a). At the wavelength of the incident light, the linear absorption coefficient $\alpha = \sigma_{01}N_0$, where σ_{01} and N_0 are ground state absorption cross section and population (density), respectively. The excited-state, with population N_1, can also absorb at the same wavelength with cross section σ_{12}. τ_{21} and τ_s are relaxation time constants from the higher excited-state N_2 to N_1 and from N_1 to N_0, respectively. It is useful to examine the time evolution of the population densities as an optical pulse passing through the material. As an example shown in Figure 2.2(b), N_1 simply builds up as a time integration of the pulse when the pulsewidth is much less than τ_s and in the meantime, N_0 depletes. Typically, if $\tau_{21} \ll \tau_s$ there is essentially no accumulation of N_2. Sufficient N_1 populated by the front-side of the incoming pulse can effectively act as a "ground" state to subsequently linearly absorb the back-side of the pulse with a different linear absorption cross section σ_{12}. Note that the populations are normalized to the initial ground-state population. Therefore, the higher the fluence (energy per unit area) of the input pulse, the more the excited-state population, and the more the change in linear transmission.

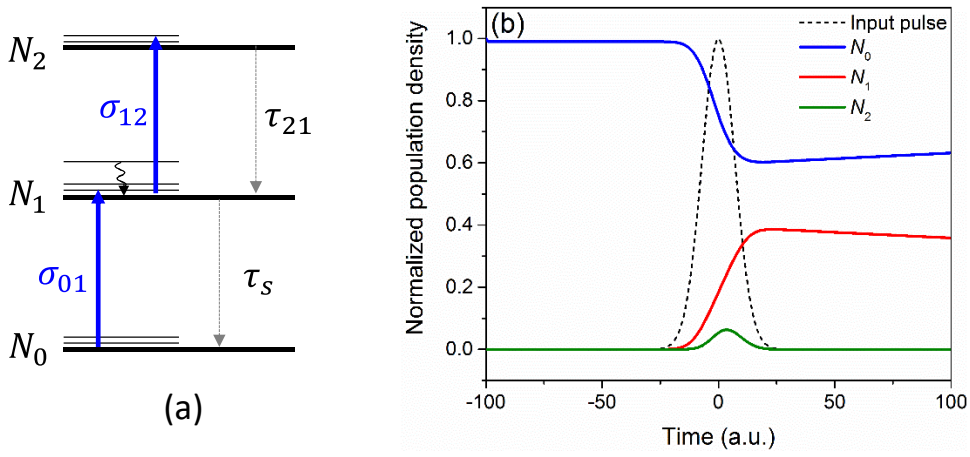

Figure 2.2 (a) energy diagram of a 3-level system; (b) normalized population time evolution of ground and excited states along with the input pulse.

The propagation of irradiance along the material and population changes can be described by a set of significantly simplified rate equations as;

$$\frac{dI(t)}{dz} = -\sigma_{01}N_0(t)I(t) - \sigma_{21}N_1(t)I(t),$$

$$\frac{dN_1(t)}{dt} = \sigma_{01}N_0(0)\frac{I(t)}{\hbar\omega}, \tag{2.25}$$

$$\frac{dN_0(t)}{dt} = -\sigma_{01}N_0(0)\frac{I(t)}{\hbar\omega},$$

where we neglect population of N_2 due to its fast relaxation, and as well as relaxations from N_1 to N_0 since they take long compared to the pulsewidth. The stimulated emission terms are also ignored since in realistic molecular systems the initial absorption is usually associated with absorption into a rovibronic band which then rapidly relaxes to the lower energy state where ESA occurs. We also assume negligible ground-state depletion i.e. constant $N_0(0)$. Applying temporal integration from 0 to t on both sides of the second and third equations in Eq. (2.25), we first obtain $N_0(t) = N_0(0) - \frac{\sigma_{01}N_0(0)}{\hbar\omega}F(t)$ and $N_1(t) = \frac{\sigma_{01}N_0(0)}{\hbar\omega}F(t)$, where $F(t) = \int_0^t I(t)\,dt$ is the fluence. Substituting these into Eq. (2.25) and integrating on both sides yields

$$\frac{dF(t)}{dz} = -\sigma_{01}N_0(0)F(t) + \int_0^t \left(\frac{\sigma_{01}^2 N_0(0)}{\hbar\omega} - \frac{\sigma_{21}\sigma_{01}N_0(0)}{\hbar\omega}\right)F(t)dF(t), \qquad (2.26)$$

where the partial integration rule is used to change $dt \rightarrow dF(t)$, which gives

$$\frac{dF(t)}{dz} = -\sigma_{01}N_0(0)F(t) - \sigma_{01}N_0(0)\frac{(\sigma_{21} - \sigma_{01})}{2\hbar\omega}F^2(t). \qquad (2.27)$$

With $\sigma_{21} > \sigma_{01}$, this NLA process is referred to reverse saturable absorption (RSA), in which the absorption loss of increases with increasing of input, much like the results from pure electronic 2PA. Therefore, it is not surprising to see Eq. (2.27) displays analogy to the "single-beam" term in Eq. (2.11), but with quadratic dependence on fluence instead of irradiance as for 2PA. It must be noted that different from 2PA which is a real $\chi^{(3)}$ process, RSA is sequential linear absorption process, or $\chi^{(1)}$: $\chi^{(1)}$. With $\sigma_{21} < \sigma_{01}$, the NLA becomes a saturation process, resulting in an increase of transmission with increase of input. Due to the long lifetime of N_1, the NLA remains even after the pulse, which can be detected by another incoming pulse in an excite-probe experiment.

This 3-level model may become insufficient to describe population dynamics for more complicated systems e.g. intersystem crossing occurs to form molecular triplet states. A five-level model is needed to account for this effect. Another example is photochromic system which involves many intermediate state transients with different absorption and lifetime, as discussed with more details in CHAPTER 7:

CHAPTER 3: EXPERIMENTAL TECHNIQUES

This chapter provides an introduction to experimental techniques used within the scope of this work. Linear optical properties are mainly characterized by absorption and fluorescence measurements, which provide basic information of the material and help determine the strategy in successive nonlinear studies. Nonlinear spectroscopy experiments usually require intense light sources i.e. from pulsed laser systems, and results should offer quantitative determinations of both NLA spectra and NLR dispersion. Sometimes time-resolved measurements, e.g. using excite-probe, is needed to give the ultrafast temporal dynamics which usually helps reveal the underlying physical origins of the nonlinearities. In this dissertation, an emphasis is placed on our recently developed Beam Deflection technique [18], which is heavily used to study the ultrafast NLR and NLA for different phases of matter including liquids, molecular gases and semiconductors.

3.1. Linear Spectroscopy

The chromatic dispersion of the linear index of refraction and absorption spectrum are the linear properties for the materials studied in this work. In most cases, the dispersion of the linear refraction of the materials of interest, i.e. solvents and semiconductors, is determined from a fit of experimental results from the literature using Sellmeier equations [102]. The absorption spectrum is determined from transmission measurements using a Cary 500 spectrophotometer. It should be noted that for organic solutions, a differential measurement from solution and solvent is required to separate the linear absorption spectrum of the organic dye itself (solute). The measured transmission (T) is related with the sample's optical density (OD) by $T = 10^{-\mathrm{OD}}$, where OD is directly proportional to the molecule's molar absorptivity ε ($\mathrm{cm^{-1}\,M^{-1}}$), molar concentration, or molarity C

(M) and sample thickness L (cm), by $\mathrm{OD} = \varepsilon CL$. Traditionally, the units of M is mol/L. Typically, ε or C can be derived from linear absorption measurements by knowing either one of them.

3.2. Nonlinear spectroscopy

Various experimental techniques have been developed for measuring NLO responses, which usually have their own advantages and limitations. For example, single-beam techniques such as nonlinear transmission [103] and Z-scan [104, 105] cannot provide temporal dynamics of nonlinearities as two-beam techniques do, but their simplicity usually leads to better absolute calibration. However, temporal response is sometimes essential for interpreting the results to determine the contributing mechanisms to the nonlinearities. Overall, precise determination of nonlinear coefficients (e.g. n_2 and α_2) is still challenging, as the reported values from most nonlinear techniques are still accompanied with ~ 20-30% absolute errors contributed from irradiance calibration, i.e. pulse energy, spatial profile and pulsewidth, as well as fitting errors, i.e. data noise.

NLA is usually more straightforward to measure than NLR, which simply can be derived from transmission changes by energy measurements. On the other hand, NLR requires the techniques to be sensitive to both magnitude and sign of the phase change in the wave-front of the beam. One way to measure this nonlinearly induced phase change can be directly through interferometric techniques [7, 14, 106]. There are also several indirect methods: the induced birefringence method such as Optical Kerr Effect (OKE) [71, 73, 75, 107] and the transient grating method such as degenerate four wave mixing (DFWM) [72, 108], both of which require optical heterodyne detection (OHD) in order to tell the sign of the phase change.

Another approach to measure NLR is based on modelling the spatial energy redistribution upon propagation after the sample, where the sample serves as a nonlinear phase mask. This usually puts stringent requirements on the spatial beam profile of the input beams, e.g. Gaussian beams, in order to facilitate precise modelling of the beam propagation with the added nonlinear phase. But some techniques utilizing this approach have shown substantial advantages over others. For example, they are capable of measuring both magnitude and sign of NLR without the need of OHD, and in the meantime offers interferometric sensitivity [105, 109, 110]. This is because the nonlinear propagation is essentially a self-interference (or diffraction) process, which results in wave front reconstruction and spatial energy redistribution. Also, it is much simpler experimentally and less sensitive to environmental perturbation compared to conventional interferometry. In the spectral region where NLA is present, both NLA and NLR can be simultaneously measured. But to separate one from the other in a valid way, the experimental parameters have to be carefully designed. This approach stands as the basic principle for Z-scan and Beam Deflection techniques, which will be discussed in detail.

3.2.1. Femtosecond Laser and OPA/Gs

The nonlinear measurements of this dissertation mainly use a commercial chirped pulse amplified (CPA) Ti:sapphire femtosecond laser system, Coherent model Legend Elite Duo HE+. The system produces 12 mJ pulse energy at wavelength ~ 800 nm with a bandwidth of ~ 28 nm, which supports a pulse duration as short as 35 fs. Although the repetition rate is tunable, the measurements have been done using 1kHz. The basic configuration of this system is shown in Figure 3.1. The seed is

generated from the Vitara-T oscillator, which has a Ti:sapphire gain medium pumped by a continuous wave (CW) diode laser that is intra-cavity doubled at 532 nm. Through Kerr lens mode-locking, the oscillator outputs 500 mW pulses with 80 MHz repetition rate at a wavelength of 800nm with a bandwidth ~ 80 nm (FWHM). The seed pulse is then sent to a pair of gratings to stretch to picosecond pulses to prepare for amplification. The first stage is a regenerative amplification cavity where a Ti:sapphire crystal is pumped on both sides by a Q-switched Nd:YLF laser (Evolution 45) frequency doubled to 527 nm with 20 mJ output energy at a 1kHz repetition rate. After being amplified ~ 5 times, i.e., 5 passes, the pulse is dumped out of the cavity by a synchronized Pockels cell with ~ 7 mJ pulse energy. It is then passed through another Ti:sapphire gain medium pumped by another Evolution model (HE) with 45 mJ. With just a single pass, the pulse energy is doubled to ~ 14 mJ. Then it goes through a grating compressor with ~ 85% efficiency to compress to a final output of ~ 12mJ with ~ 35fs pulsewidth (FWHM).

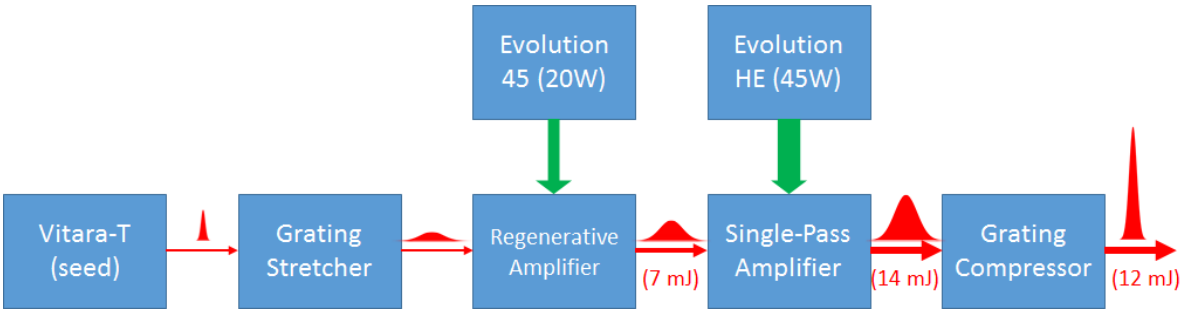

Figure 3.1 General configuration of Coherent Legend Elite Duo HE+ system based on chirped pulse amplification.

To provide broadly tunable sources for nonlinear spectroscopy, ~ 10 mJ is directly split out from the output of the laser to pump a Light Conversion Optical Parametric Amplifier/Generator (OPA/G) system TOPAS-HE, and then ~ 1.3 mJ from the remaining 2 mJ is split out to pump another OPA/G, TOPAS-800. The two OPA/Gs are operated based on different principles.

The TOPAS-800 is one of the earliest models from light Conversion, which utilizes parametric down conversion in a $\chi^{(2)}$ medium to generate the broadband superfluorescence as the seed source. This principle has been replaced by white-light continuum (WLC) generation in the latest femtosecond system (e.g. TOPAS-C, -Prime and -HE), but still remains popular for picosecond systems (e.g. TOPAS-800-ps). In our TOPAS-800-fs, only one single barium borate (BBO) crystal is used to support all the processes via 5 passes: the input 800 nm beam is split into three beam, namely main pump (96%), pre-amp pump (2%) and seed pump (2%). The seed pump goes through the BBO in the 1st pass to generate broadband superfluorescence via parametric down conversion. The generated superfluorescence co-propagating with the rest of the seed goes through the BBO another two times (2nd and 3rd passes) to get amplified/generated at particular wavelengths for signal/idler, depending on the crystal angle. Then the signal/idler overlaps with the pre-amp pump at the crystal to get further amplified in the 4th pass. The amplified signal/idler finally overlaps with the main pump on the crystal to finish the OPA/G process. The remaining pump beam is blocked by a movable notch filter at the output.

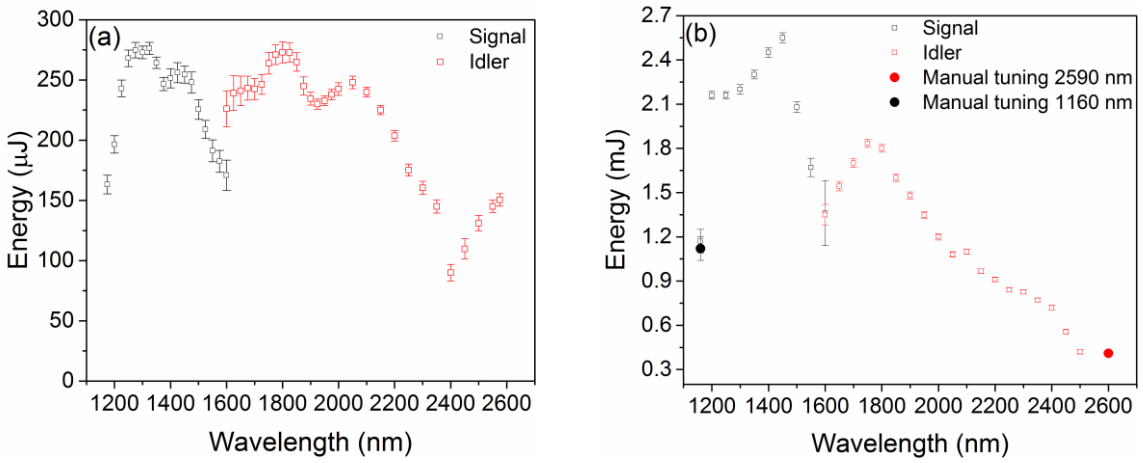

Figure 3.2 Energy output of signal and idler from (a) TOPAS-800 with ~ 1.3 mJ pump at 800nm, and (b) TOPAS-HE with ~ 10 mJ pump at 800nm.

The high energy TOPAS-HE uses WLC generation to produce the seed in one BBO crystal, which follows pre- and main- and high power amplification processes but in separate BBO crystals. This greatly simplifies the alignment of the instrument compared to the old model, i.e. TOPAS-800. In the TOPAS-HE, the input 800 nm beam is split into a high-power pump (~ 90-95%), main pump, pre-amp pump and seed pump. The seed pump is focused on a 5 mm sapphire plate to generate WLC which is then chirped using a ZnSe plate to temporally separate different frequencies. Then the WLC is overlapped with the pre-amp pump in the first BBO crystal with an angle to generate signal/idler in a non-collinear optical parametric amplification (NOPA) manner, which results in a spatially separated beam pattern, namely amplified signal, SFG of signal and pump, pump, SFG of idler and pump, and generated idler. A beam block only allows the amplified signal to go through at a particular wavelength determined by the pre-amp delay as well as the crystal angle, which is then overlapped with the main pump at a second BBO crystal to get further amplified. After an expanding telescope, the signal overlaps with the high energy pump at the third BBO to reach the final energy. The typical energy output of the TOPAS-800 (with frequency mixture stages) and TOPAS-HE is shown in Figure 3.2.

3.2.2. Z-scan

The Z-scan technique was invented in 1989 [104, 105], which was followed by several expansions such as two-color Z-scan [111], eclipsing Z-scan [110], Z-scan for thick samples [112] and more recently Dual-arm Z-scan [109, 113]. It has been a simple technique but has become extremely popular in nonlinear spectroscopy for studying various materials, as it only needs a single beam which gives both NLA and NLR (including sign) with interferometric sensitivity. The original Z-

scan translates a “thin” sample through the focus of a Gaussian beam, and the energy of the transmitted beam in the far field is measured with and without a partially closed aperture.

3.2.2.1. Principles

As shown in Figure 3.3(a), by collecting all the transmitted energy, the open aperture (OA) Z-scan measures NLA. This includes instantaneous multiphoton absorption, e.g. 2PA and 3PA, as well as cumulative ESA and any other NLA process. Since the absorption depends on irradiance/fluence, i.e. Eq. (2.11), (2.13) and (2.27), the transmission change is maximized at focus of the beam where the irradiance/fluence is the highest. With a known spatial profile of the laser beam, i.e. Gaussian TEM_{00}, the fit of transmission change upon scanning the sample through focus gives a determination of the NLA coefficient, e.g. α_2 or σ_{12}.

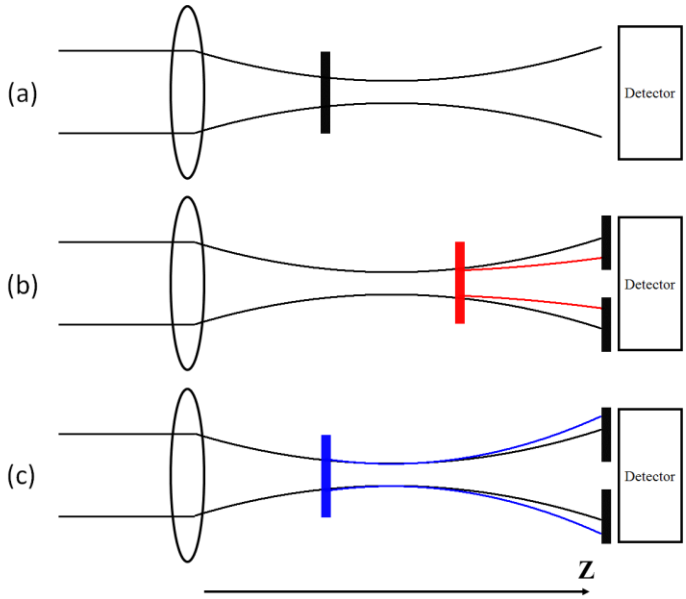

Figure 3.3 Schematics of (a) open aperture Z-scan, and beam divergence in close aperture Z-scan using a sample with positive n_2 (b) after and (c) before the focus.

As mentioned previous, Z-scan measures NLR by modelling the spatial energy redistribution upon propagation to the detector placed in the far field after the sample. This is done by putting an aperture centered on the beam in the far field where the beam is diverged after focus. Without any sample, the aperture is partially closed to only allow ~ 33% of the input energy to transmit through, which makes the transmitted energy still sensitive to NLR induced spatial energy redistribution at the plane of the closed aperture (CA) but averages over beam spatial inhomogeneities. The experiment is demonstrated in Figure 3.3(b) and (c) for a nonlinear medium with positive n_2. In the case of a TEM_{00} Gaussian beam, the nonlinear phase mask due to self-nonlinearity follows its spatial Gaussian profile (see Eq. (2.12)), where the refractive index change at the center is larger than in the wings, which modifies the wavefront much like a positive lens, giving a self-focusing effect. Therefore, by comparing the parameters without the sample (linear parameters), with placing the sample before the original focus, self-focusing will increase the divergence, resulting in a larger spot size at the aperture decreasing the transmitted energy. Placing the sample after the original focus, self-focusing will decrease the divergence, resulting in a smaller spot size at the aperture increasing the transmitted energy. By scanning the sample in "Z", the signal of CA will sharply switch from decreased transmission to increased transmission when crossing the focus ($Z = 0$). This becomes the opposite with a self-defocusing nonlinearity due to negative n_2.

Figure 3.4 (a) gives an example of an OA Z-scan signal from a 0.5 mm thick GaAs wafer at a wavelength of 1550 nm, where the minimum transmission at focus is due to 2PA. By fitting the signal, the degenerate α_2 at 1550 nm can be determined as 15 cm/GW. Figure 3.4 (b) gives an example of a CA Z-scan signal from liquid carbon disulfide (CS_2) filled in a 1 mm pass length quartz cuvette. Since no NLA is present at the wavelength of 1550 nm, the CA signal is only contributed by NLR. The valley-peak shape before ($Z < 0$) and after ($Z > 0$) focus indicates $n_2 >$

0. The fit gives $n_2 = 2.0 \times 10^{-15}$ cm^2/W, which is due to the contribution from both CS_2 and the walls of the quartz cuvette. It must be noted that the CA signal may be distorted if NLA is present at the wavelength of measurement (see Figure 3.5 (d)), because it contaminates the spatial energy distribution upon propagation. In this case, we can simply fit the CA signal for NLR with a known NLA from OA signal. However, it has been found that dividing signals from CA by OA (CA/OA) yields results similar to the CA signal obtained as if the sample only has NLR. This is the approach of Z-scan for separating NLR from NLA, which may fail in the case of measuring a small magnitude n_2 with a large NLA background, as discussed in more detail in 3.2.3.3. .

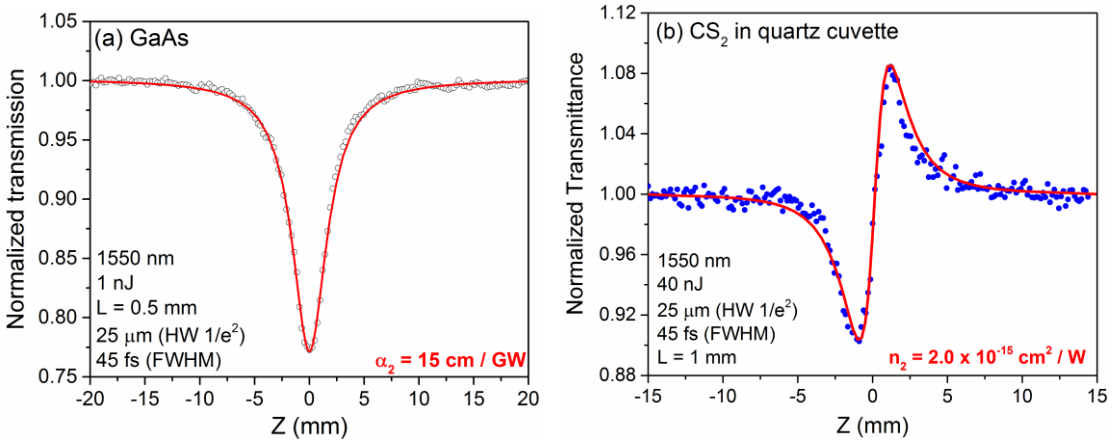

Figure 3.4 Examples of Z-scan: (a) open aperture Z-scan of GaAs data (circles) fit (red) with a two-photon absorption coefficient α_2; (b) closed aperture Z-scan of Carbon disulfide (CS_2) fit (red) with a positive nonlinear refraction coefficient n_2.

The modeling of Z-scan (particularly CA) signals requires calculations of two main processes given a particular sample position Z: calculating the complex electric field right at the sample output plane $\widetilde{\mathcal{E}_{\text{out}}} = \mathcal{E}_{\text{out}} e^{i\Delta\phi}$ in terms of amplitude and phase change; calculating the complex electric field at the aperture plane $\widetilde{\mathcal{E}_{\text{Ap}}}$ using Fresnel diffraction propagation. Although $\widetilde{\mathcal{E}_{\text{out}}}$ can be calculated from numerical propagation through the sample, analytical solutions of the output

irradiance $I_{\text{out}} = \frac{1}{2}\varepsilon_0 nc|\mathcal{E}_{\text{out}}|^2$ and NLR induced phase change $\Delta\phi_{\text{NL}}$ can be separately derived from Eq. (2.11) and (2.12), which again is under the approximation of external self-action [81]. This is also known as the "thin" sample approximation, which requires a nearly constant irradiance across the sample thickness *L*. Usually it will be satisfied if the sample thickness *L* is less than the Rayleigh range (z_0) of a TEM$_{00}$ Gaussian beam, and in the meantime the self-lensing effect from NLR is negligible within the sample. With any input irradiance distribution $I_{\text{in}}(r, z, t)$ of a TEM$_{00}$ Gaussian beam, the analytical solutions of I_{out} and $\Delta\phi_{\text{NL}}$ can be derived from Eq. (2.11) and (2.12) with and without the presence of linear absorption

$$I_{\text{out}} = \begin{cases} \dfrac{I_{\text{in}}}{1 + \alpha_2 L I_{\text{in}}}, & \alpha_1 = 0 \\ \dfrac{\alpha_1 I_{\text{in}} e^{-\alpha_1 L}}{\alpha_1 + \alpha_2 I_{\text{in}}(1 - e^{-\alpha_1 L})}, & \alpha_1 \neq 0 \end{cases},$$

$$\Delta\phi_{\text{NL}} = \begin{cases} k_0 n_2 \dfrac{\ln[1 + \alpha_2 L I_{\text{in}}]}{\alpha_2}, & \alpha_1 = 0 \\ k_0 n_2 \dfrac{(-\alpha_1 L + \ln[e^{\alpha_1 L}(\alpha_1 + \alpha_2 I_{\text{in}}) - \alpha_2 I_{\text{in}}])}{\alpha_2}, & \alpha_1 \neq 0 \end{cases}, \tag{3.1}$$

where ln[] is the natural logarithm function, and the argument on radial dimension, sample position in "Z" and time (r, z, t) is suppressed but should be applied to I_{in}, I_{out} and $\Delta\phi_{\text{NL}}$. From Eq. (3.1), the amplitude $\mathcal{E}_{\text{out}}$ can be calculated from $\sqrt{\frac{2I_{\text{out}}(r,z,t)}{\varepsilon_0 nc}}$. To derive the total phase shift $\Delta\phi(r, z, t)$ of $\widetilde{\mathcal{E}_{\text{out}}}$, $\Delta\phi_{\text{NL}}(r, z, t)$ is added with the phase change from the radius of curvature and Gouy shift [114], which yields

$$\Delta\phi(r,z,t) = \Delta\phi_{NL}(r,z,t) + \frac{k_0 r^2}{2\left(z + \frac{z_0^2}{z}\right)} + \tan^{-1}\left(\frac{z}{z_0}\right). \quad (3.2)$$

With knowledge of $\widetilde{\mathcal{E}_{\text{out}}}$, $\widetilde{\mathcal{E}_{\text{Ap}}}$ can be found by performing a Fresnel diffraction of a radially symmetric beam

$$\widetilde{\mathcal{E}_{Ap}}(r_a,z,t,d') = \frac{2\pi}{i\lambda d'}\exp\left[\frac{i\pi r_a^2}{\lambda d'}\right]\int_0^\infty r dr \widetilde{\mathcal{E}_{out}}(r,z,t)\exp\left[\frac{i\pi r^2}{\lambda d'}\right]J_0\left[\frac{i\pi r r_a}{\lambda d'}\right], \quad (3.3)$$

where r_a is the radial variable at the plane of the CA, $d' = d - z$ is the distance from the sample position Z to the detector (d is the distance between beam focus and CA) and exp[] and J_0[] are the exponential and Bessel function of the first kind, respectively. Now, by integrating the corresponding irradiance over space and time, the transmitted energy can be found for both CA and OA Z-scans.

It must be noted that Z-scan measures the temporally averaged transmittance, and the n_2 fit from the above theory treats the nonlinearities as instantaneous (i.e. from bound-electron). For other origins of nonlinearity, e.g. molecular nuclear reorientations, n_2 essentially becomes pulse-width dependent, and Z-scan results in an effective $n_{2,\text{eff}}$ defined in Table 2.4.

3.2.2.2. Dual-arm Z-scan

The dual-arm Z-scan technique was initially developed to measure the nonlinearity of organic dyes (solute) which are dissolved in a solvent [109]. For most solvents, 2PA does not exist in the visible and near infrared (IR) spectral regions of interest, but they do contribute to the overall n_2 of solutions along with the solute. In the conventional Z-scan, sequential measurements are performed on the solution and pure solvent, and a subtraction between them is needed to separate the solute

contribution. The problem with subtracting two sequentially measured Z-scans is the resultant large noise floor due to the uncorrelated noise between signals of solution and solvent. For low concentration solutions, the signal from solute may be completely buried within the noise. Similar difficulties occur for the characterization of thin-film nonlinearities, in which the NLR contribution from the much thicker substrate needs to be subtracted.

The dual-arm (DA) Z-scan is designed to overcome this problem. By duplicating the conventional Z-scan with identical optical paths, this added arm allows us to measure the solution cuvette (or coated substrate) and solvent cuvette (bare substrate) simultaneously in one scan. Since the beams in the two arms are split from one single beam, the same noise sources lead to noise correlation such that they can be subtracted and cancelled for each laser shot. Compared to sequential measurements, this yields an increase in the signal-to-noise ratio (S/N), which allows us to determine the nonlinearities of solutes with low concentration (or thin films). The DA Z-scan is particularly beneficial to improve the S/N in CA signals and therefore increase the sensitivity for NLR characterization. An important noise source is beam pointing instability, which is always present in CA signals. With "dual" identical arms, the movements of the two beams on each CA are synchronized such that the subtraction effectively eliminates this effect. The alignment and calibration procedures for the DA Z-scan have been discussed in detail in [91, 113].

Figure 3.5 gives an example of a DA Z-scan signal of a 1.4 μm thick PE1-DOB-C9 neat film at a wavelength of 1.55 μm. Due to limitations of homogeneity and optical quality, a large Z-scan background signal usually exists for thin films even with very small energy (< 1 nJ) where no nonlinear signal from the thin film itself is observable. Therefore a low energy background (LEB) and its subtraction is necessary to reveal the actual Z-scan profile, as shown in Figure 3.5 (b) for CA signal. Sometimes the LED background is smoothed (i.e. using Savitzky-Golay filter)

before subtraction to avoid introducing undesired noise. In this measurement, the minimum beam waist and pulsewidth are determined as 28 μm (HW1/e^2 M) and 70 fs (FWHM) respectively. The fit of the OA signal gives $\alpha_2 = (4.8 \pm 1)$ cm/GW, and the fit of the CA and CA/OA signals corresponds to $n_2 = -(310 \pm 60) \times 10^{-15}$ cm^2/W.

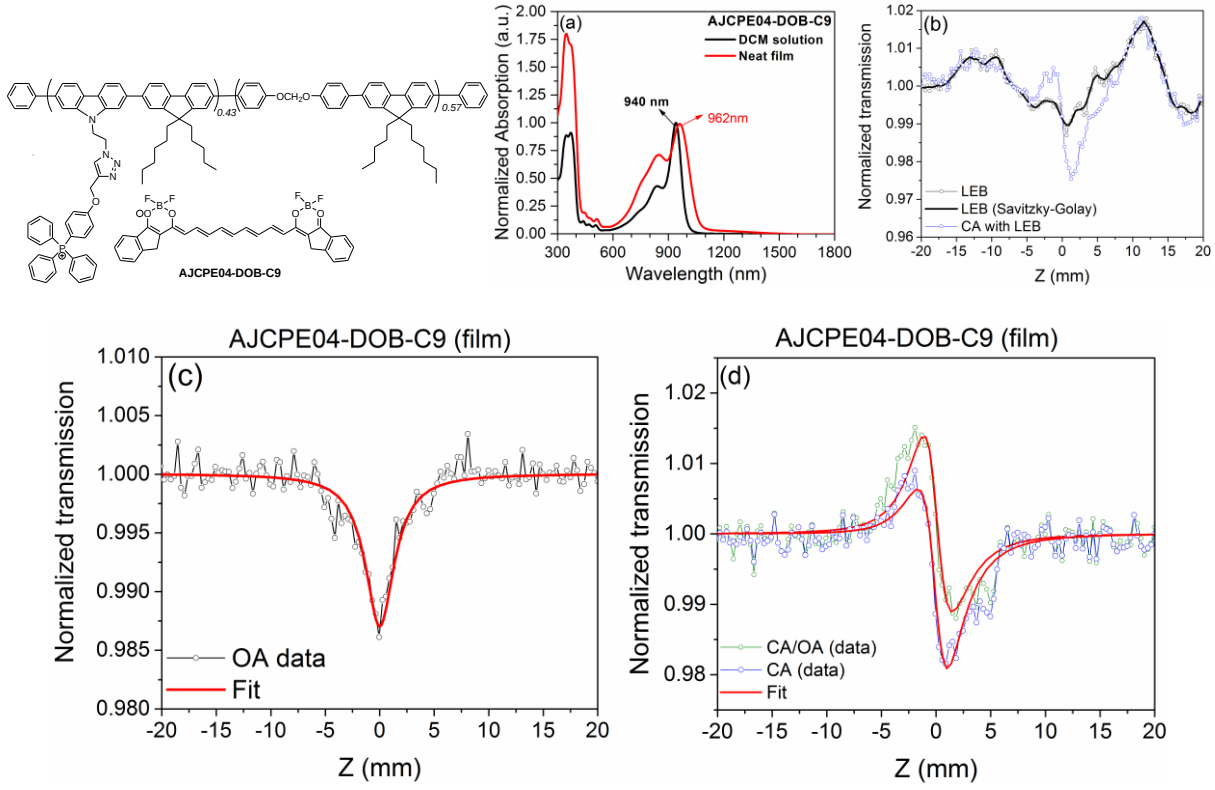

Figure 3.5 Example of Dual-arm Z-scan measurements of a 1.4 μm thin neat film PE1-DOB-C9 on a 1 mm thick fused silica substrate at wavelength of 1.55 μm: (b) linear absorption spectra with molecular structures on the left; (b) low energy background (LEB) in closed aperture (CA) signal; (c) open aperture (OA) signal; (d) CA and CA/OA after subtraction of LEB. The film was fabricated by the Jen's group at University of Washington.

A typical noise floor for the DA Z-scan is about 0.2% standard deviation of the normalized transmission as reported in [109], which corresponds to a detectable phase change of $\sim\lambda/1000$. This sensitivity is significantly dependent on the actual laser beam instability, i.e. energy, pulse-

width and beam pointing fluctuations, as well as the calibration quality for noise correlation between the dual arms, i.e. energy, beam waist and sample position in Z. Since in the regular experimental setup two individual detectors with separate photodiodes and amplifiers are used each of the two arms for either OA or CA, the subtraction between them has been done manually as a part of the procedure for data processing. The electrical noise inherited from the mismatch between electronic components, e.g. photodiodes and amplifiers, are not correlated thus cannot be cancelled by subtracted. By implementing a commercial balanced amplified detector, the subtraction is performed by an internal differential amplifier directly from two well-matched photodiodes, which further improves the sensitivity of the DA Z-scan by 3-5×.

As a single beam technique, Z-scan offers great simplicity with interferometric sensitivity, which makes it advantageous for absolutely calibrated measurements. But since single beam technique only give temporally averaged results, the underlying ultrafast mechanisms contributing to NLR and NLA are usually not directly explored, unless performing some systematic studies of pulsewidth and energy dependence [17, 115]. In the next section we describe a complementary experimental method that does yield the temporal response while giving an even better sensitivity to nonlinear refraction.

3.2.3. Beam Deflection

One of the main interests of this dissertation is to explore the ultrafast mechanisms of NLR in various materials, which requires excitation and probe pulses to measure temporal dynamics, as well as the magnitude and sign of NLR. Beam Deflection (BD) is a recently developed technique which is heavily used in this dissertation work to characterize the ultrafast NLR (and NLA) for

various materials [17, 18, 70]. The BD method is similar to the photo thermal beam deflection technique [116, 117], in which the deflection originates from an index gradient caused by a thermal nonlinearity. In BD, femtosecond excitation pulses are used to create such index gradient via ultrafast NLR, which deflects a pulsed probe beam coming at a variable temporal delay, and therefore NLR can be characterized by measuring the deflection of the probe. Since BD is an excite-probe technique, it gives the response dynamics of the nonlinear medium.

Experimentally, the strong excitation pulse at ω_b creates an index change $\Delta n = 2n_2(\omega_a;\omega_b)I_b(\boldsymbol{r})$ that follows its spatial irradiance distribution $I_b(\boldsymbol{r})$, here TEM_{00} Gaussian, as shown in Figure 3.6. $n_2(\omega_a;\omega_b)$ is the nondegenerate NLR coefficient defined in Table 2.1. The probe pulse at ω_a is focused to a spot size ~ 3-5× smaller than that of the excitation beam and is spatially displaced to the Gaussian wings of the excitation beam where the index gradient is nearly linear and maximized. This deflects the probe by a small angle which is measured using a position sensitive segmented detector by taking the difference of the energy falling on the left and right halves, $\Delta E = E_{left} - E_{right}$, or $(E_1 + E_3 - E_2 - E_4)$, and normalized to the total energy $E = E_1 + E_2 + E_3 + E_4$. The BD signal, $\Delta E/E$, is directly proportional to $n_2(\omega_a;\omega_b)$, with its sign corresponding to the deflection direction. BD maintain the basic functionality of the excite-probe technique with a regular photodiode, as the transmission change in E is proportional to the NLA (e.g. 2PA).

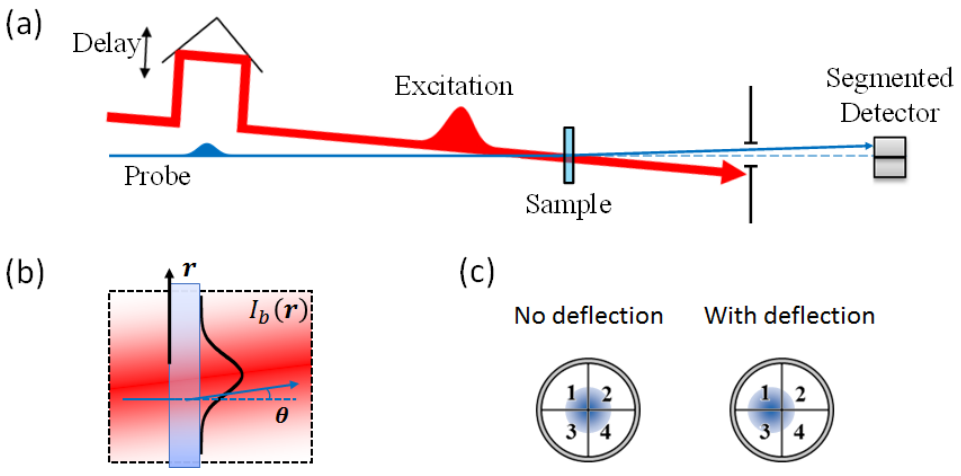

Figure 3.6 (a) Schematics of Beam Deflection setup; (b) spatial irradiance distribution of the excitation beam (red) and overlapping geometry with the probe beam (blue) at the sample plane; (c) positions of probe beam on segmented quad-cell detector without and with deflection.

The experimental setup is quite straightforward as a NLR technique, and BD holds several advantages over other methods. First, the excite-probe configuration allows BD to measure transient NLR which is not possible in single-beam techniques such as Z-scan. To tell the sign of NLR, BD does not require OHD as is needed in OKE and DFWM, which makes BD relatively simpler. By varying the angle between polarization direction of excitation and probe, BD gives the polarization dependence of NLR, e.g. determining $\chi^{(3)}_{xxyy}$ as opposed to $\chi^{(3)}_{xxxx}$which is not available in other techniques measuring induced birefringence such as OKE which measures the induced birefringence. In the study of ultrafast NLR of molecular liquids (see CHAPTER 4:) and gases (see CHAPTER 5:), the polarization dependence significantly helps separate the bound-electronic from nuclear contributions. By varying the wavelengths of excitation and probe, BD measures

nondegenerate (ND) nonlinearities, which enables our study on the dispersion of ND-NLR in semiconductors (see CHAPTER 6:). Also, BD shows better separation of NLR and NLA than Z-scan for large NLA, as discussed in 3.2.3.3. .

Another advantage of BD is its unprecedented sensitivity. As previously demonstrated from a measurement of 1mm thick fused silica, the noise floor (standard deviation) of $\Delta E/E$ results in a nonlinearly induced phase change of 0.3 mrad, corresponding to an optical path length change of $\lambda_a/20{,}000$, where λ_a is the wavelength of probe [18]. Much like Z-scan, this interferometric sensitivity originates from the nature of the approach of how BD measures NLR: characterizing spatial energy redistribution (of probe) upon propagation after passing through a nonlinear phase mask at the sample. The difference is that in BD this nonlinear phase mask is created by the excitation pulse via cross-phase modulation, while in the Z-scan, the phase mask is induced by the beam itself through a self-nonlinearity. Also, BD measures the spatial energy redistribution using a Quad-cell detector, while Z-scan is made sensitive to NLR by a partially closed aperture. Another factor contributing to the high sensitivity is the advanced electronic equipment used in BD. ΔE from a Quad-cell detector is a differential signal. Much like the balanced photodiode detector in a Dual-arm Z-scan, the shot-to-shot common-mode noise is suppressed. Also, BD operates with a lock-in amplifier with an externally modulated excitation, which improves the S/N for measuring the nonlinear effects.

Based on the reasons given above, the methodology of modeling the BD experiment will be similar to that discussed for the Z-scan (see 3.2.2.1.). Provided a particular temporal delay τ_d between the excitation and probe pulses, it requires rigorous calculations of two main processes: calculating the complex electric field right at the exit plane of the sample, i.e. amplitude of the phase change; then calculating the complex electric field at the quad-cell detector plane using

Fresnel diffraction propagation. But under certain experimental conditions, this calculation can be greatly simplified by treating the nonlinear phase mask as a thin prism, and the spatial energy redistribution at the quad-cell is basically derived from a deflection of the probe [18].

3.2.3.1. "Prism" Deflection Approximation

This approximation is valid if the BD measurement satisfies the following conditions: no NLA is present at the wavelength of measurement; the sample is placed at the beam waist of the probe, and the probe spot size $w_{0,a}$ is much smaller than the excitation w_b such that the probe sees a nearly linear index gradient induced by the excitation; the wavelengths of excitation (λ_b) and probe (λ_a) are nearly degenerate with negligible group velocity mismatch (GVM), and their propagation directions are nearly collinear, meaning no significant spatial and temporal walk-off; the sample thickness L is much less than the Rayleign range ($z_0 = k_0 w_0^2/2$) of both excitation and probe such that the irradiance of excitation is nearly uniform across the sample; the induced phase change is small such that the probe spatial profile upon propagating to the detector still remains nearly Gaussian. Assuming all the conditions above are satisfied, the refractive index change is generally written as

$$\Delta n_a(x, y, t) = \Delta n(t) \exp\left(-2\frac{x^2 + y^2}{w_b^2}\right) \tag{3.4}$$

where the exp() represents the spatial Gaussian profile of the excitation beam with x and y as horizontal and vertical positions; $\Delta n(t)$ is the induced index change given by the convolution with the material's response function and excitation irradiance, as defined in Table 2.4. For a probe with $w_{0,a} \ll w_b$ placed at the excitation waist with $x = w_b/2$ and $y = 0$, it experiences a horizontal deflection, and for a thin sample this angle is

$$\theta(x,y,t) = \int_0^L \nabla[\Delta n_a(x,y,t)]\, dz \approx \nabla[\Delta n_a(x,y,t)]L = \frac{2L}{w_b\sqrt{e}}\Delta n(t), \qquad (3.5)$$

from which the centroid displacement of a Gaussian probe beam upon propagating of distance d to reach detector is $\Delta x = \frac{2L}{w_b\sqrt{e}}\Delta n(t)d$. With some additional approximations as discussed in [18], ΔE and E can be calculated by integrating the probe irradiance at the detector over the appropriate limits of x, y, t, which yields

$$\frac{\Delta E_a(\tau_d)}{E_a} = \frac{2\sqrt{2}}{\sqrt{\pi e}}\frac{w_{0,a}}{w_b}\cdot k_{0,a}L\langle\Delta n(\tau_d)\rangle, \qquad (3.6)$$

where $\langle\Delta n(\tau_d)\rangle = \int_{-\infty}^{\infty}\Delta n(t)I_a(t-\tau_d)dt \,/\, \int_{-\infty}^{\infty} I_a(t-\tau_d)dt$. Although numerous approximations have been made thus far to reach Eq. (3.6), an analytical expression for the BD signal is always useful to get insight of the effect by varying the experimental parameters. For example, the signal is inversely proportional to w_b because a small excitation spot size leads to larger index gradient, and it is proportional to $w_{0,a}$ because a larger probe beam waist corresponds to longer z_0 less diffraction, giving a smaller spot size on the detector in the far field, making the position detector more sensitive to centroid displacement.

Since no restriction has been made on $\Delta n(t)$ so far, Eq. (3.6) can be applied for both instantaneous (electronic) and noninstantaneous nonlinearities. In this dissertation, it has been used to model the BD signals of molecular gases in a relative measurement [18, 93, 118, 119]. A full numerical approach, introduced in in 3.2.3.2. , is used for all the other measurements including the NLO response function of solvents and nondegenerate NLR of semiconductors. For bound-electronic NLR, $\Delta n(t) = 2n_2(\omega_a;\omega_b)I_b(t)$ is substituted into Eq. (3.6), which yields

$$\frac{\Delta E_a(\tau_d)}{E_a} = \frac{2\sqrt{2}}{\sqrt{e\pi}} \frac{w_{0,a}}{w_b} k_{0,a} L \frac{2n_2(\omega_a;\omega_b) I_{0,b}}{\sqrt{1+\tau_b^2/\tau_a^2}} \exp\left(-\frac{\tau_d^2}{\tau_a^2+\tau_b^2}\right). \quad (3.7)$$

where τ_a and τ_b are the pulsewidths (HW1/eM) of probe and excitation pulses respectively; $I_{0,b}$ is the on-axis peak irradiance of the excitation beam. For instantaneous NLR, the profile of $\Delta E/E$ is simply the cross-correlation of excitation and probe pulses, and it is directly proportional to $n_2(\omega_a;\omega_b)$, resolving both magnitude and sign.

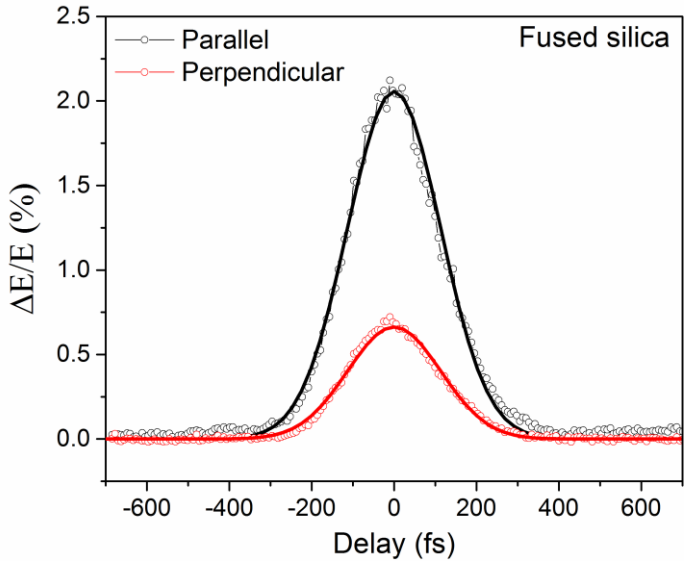

Figure 3.7 Beam deflection measurements of a 1 mm thick fused silica with parallel (black) and perpendicularly polarized excitation and probe.

BD measurements of a 1 mm thick fused silica sample are shown in Figure 3.7 with both parallel (black) and perpendicularly polarized excitation and probe. The excitation is at a wavelength of 1250nm generated from the signal beam of a TOPAS-HE pumped by a femtosecond Coherent laser system, which is then spectrally filtered by a 10 nm (FWHM) bandpass filter, resulting in a pulsewidth ~ 150 fs (FWHM) at the sample. Before the bandpass filter, a portion of the excitation is split off and focused in to a 5 mm thick sapphire plate to generate a WLC, which

is filtered at 1150 nm with a 10 nm bandpass filter to use as a probe with pulsewidth ~ 220 fs (FWHM). The sample is placed at the minimum beam waist of the probe, $w_{0,a} = 123$ mm, where 25 mJ excitation is focused to a beam size of $w_b = 468$ mm. Since bound-electronic NLR dominates for fused silica, the $\Delta E/E$ simply follows the cross-correlation of the two pulses, as indicated by Eq. (3.6). A fit based on the experimental parameters gives $n_{2,\parallel} = 0.33 \times 10^{-19}$ m^2/W for parallel case and $n_{2,\perp} = 0.11 \times 10^{-19}$ m^2/W for perpendicular case. These numbers are ~ 30% larger than literature values [41, 120], probably due to the errors in the energy measurements, or the filtered WLC probe does not have a perfect Gaussian TEM$_{00}$ mode. But relatively $n_{2,\parallel}/n_{2,\perp} = 2.9$ is close to the theoretical ratio for isotropic medium under Kleinman symmetry [31, 32].

3.2.3.2. Beam Deflection with GVM and NLA

When GVM and NLA are not negligible, e.g. nondegenerate measurements within the 2PA spectral region, the "prism" deflection approximation, i.e. Eq. (3.6) is not applicable. Then we need to start with the two general procedures, as discussed previously. First is to calculate the complex electric field of the delayed probe at the exit plane of the sample $\widetilde{\mathcal{E}_{\text{out}}}(x, y, t, \tau_d)$. Then the complex electric field of the probe at quad-cell detector plane $\widetilde{\mathcal{E}_{\text{QD}}}(x_d, y_d, t, \tau_d)$ can be calculated using Fresnel diffraction propagation to a distance d

$$\widetilde{\mathcal{E}_{\text{QD}}}(x_d, y_d, t, \tau_d) = \frac{e^{ik_{0,a}d}}{i\lambda_a d} e^{i\frac{k_{0,a}(x_d^2+y_d^2)}{2d}} \mathcal{F}\left[\widetilde{\mathcal{E}_{\text{out}}}(x, y, t, \tau_d) e^{i\frac{k_{0,a}(x^2+y^2)}{2d}}\right], \quad (3.8)$$

where $\mathcal{F}[]$ represents the two-dimensional spatial Fourier transform, i.e.

$$\mathcal{F}\left[\widetilde{\mathcal{E}_{\mathrm{out}}}(x,y,t,\tau_d)e^{i\frac{k_{0,a}(x^2+y^2)}{2d}}\right]$$
$$=\iint_{-\infty}^{\infty}\widetilde{\mathcal{E}_{\mathrm{out}}}(x,y,t,\tau_d)e^{i\frac{k_{0,a}(x^2+y^2)}{2d}}e^{i\frac{k_{0,a}(xx_d+yy_d)}{d}}dxdy, \tag{3.9}$$

which may also be evaluated numerically using techniques such as FFT []. Then we can integrate the irradiance distribution of $\widetilde{\mathcal{E}_{\mathrm{QD}}}$ over space and time to find out the energy falling on each half of the segments, i.e. $\Delta E_a(\tau_d)$ and $E_a(\tau_d)$.

In this dissertation, we are interested in $\widetilde{\mathcal{E}_{\mathrm{out}}}$ from third- and fifth-order interactions with the excitation. To account for GVM, we follow the methodology developed by Negres et al. [121], and start with the nonlinear wave equation with SVEP, i.e. Eq. (2.8) and (2.9), involving third- and fifth-order polarizations as driving terms which oscillating at the same frequency of the probe ω_a

$$\left(\frac{\partial\mathcal{E}_a}{\partial z}+\frac{n_{g,a}}{c}\frac{\partial\mathcal{E}_a}{\partial t}\right)=i\frac{\omega}{2n_a c\varepsilon_0}\left(\mathcal{P}^{(3)}(\omega_a)+\mathcal{P}^{(5)}(\omega_a)\right), \tag{3.10}$$

where $\mathcal{E}_a$ is the amplitude of complex field of probe, $n_{g,a}$ is the group index of the sample at the probe frequency ω_a. Here, the group velocity dispersion (GVD) and linear absorption are neglected. Now substitute the two-beam term in Eq. (2.10) and (2.13) to replace $\mathcal{P}^{(3)}(\omega_a)$ and $\mathcal{P}^{(5)}(\omega_a)$, and then replace the complex susceptibility, i.e. $\chi^{(3)}_{xxxx}(\omega_a;\omega_a,\omega_b,-\omega_b)$ and $\chi^{(5)}_{xxxxxx}(\omega_a;\omega_a,\omega_b,-\omega_b,\omega_b,-\omega_b)$ by the corresponding nonlinear coefficients using relations in Table 2.1 and Table 2.2, which together yield

$$i\left(\frac{\partial \mathcal{E}_a}{\partial z}+\frac{n_{g,a}}{c}\frac{\partial \mathcal{E}_a}{\partial t}\right)$$

$$=-\Bigg(2k_{0,a}n_2(\omega_a;\omega_b)+i\alpha_2(\omega_a;\omega_b)+3\,k_{0,a}n_4(\omega_a;\omega_b,\omega_b)I_b(t) \tag{3.11}$$

$$+\,i\frac{3}{2}\alpha_3(\omega_a;\omega_b,\omega_b)I_b(t)\Bigg)I_b(t)\mathcal{E}_a.$$

Following [121], the normalized parameters are introduced for time $T=\left(t-z/v_{g,b}\right)/\tau_b$, delay $T_d=\tau_d/\tau_b$ and space $Z=z/L$, which leads to changes in spatial and temporal derivatives on the left-hand side of Eq. (3.11) to be $\frac{\partial}{\partial z}=\frac{1}{L}\frac{\partial}{\partial Z}-\frac{1}{v_{g,b}\tau_b}\frac{\partial}{\partial T}$ and $\frac{\partial}{\partial t}=\frac{1}{\tau_b}\frac{\partial}{\partial T}$ respectively, where $v_{g,b}$ is the group velocity of the excitation pulse. Note the term associated with n_4 is ignored as it is out of the scope of this experimental study. Therefore, we can rewrite Eq. (3.11) as

$$i\left(\frac{\partial \mathcal{E}_a}{\partial Z}+\rho\frac{\partial \mathcal{E}_a}{\partial T}\right)$$

$$=-\Bigg(2k_{0,a}n_2(\omega_a;\omega_b)+i\alpha_2(\omega_a;\omega_b) \tag{3.12}$$

$$+\,i\frac{3}{2}\alpha_3(\omega_a;\omega_b,\omega_b)I_b(T)\Bigg)I_b(T)L\mathcal{E}_a,$$

where $\rho=\left(n_{g,a}-n_{g,b}\right)L/(c\tau_b)$ is the GVM parameter, related to the temporal walk-off between excitation and probe pulses. Assuming a temporally Gaussian excitation pulse, i.e. $I_b(T)=I_{0,b}e^{-T^2}$, and assuming the input probe field is $\mathcal{E}_{0,a}e^{-\frac{1}{2}\left(\frac{T-T_d}{\tau_a/\tau_b}\right)^2}$, we can analytically solve Eq. (3.12) for the probe field $\mathcal{E}_a(1,T)$ at the back surface of the sample ($Z=1$):

$$\mathcal{E}_a(1,T) = \mathcal{E}_{0,a}\exp\Bigg(-\frac{(T-T_d-\rho)^2}{2(\tau_a/\tau_b)^2} + \frac{i}{\rho}\int_{T-\rho}^{T}\Big\{2k_a n_2(\omega_a;\omega_b) + i\alpha_2(\omega_a;\omega_b) + i\frac{3}{2}\alpha_3(\omega_a;\omega_b,\omega_b)I_b(T)\Big\}LI_b(T)dT\Bigg). \tag{3.13}$$

Treating $n_2(\omega_a;\omega_b)$, $\alpha_2(\omega_a;\omega_b)$ and $\alpha_3(\omega_a;\omega_b,\omega_b)$ as invariant w.r.t. T , meaning the spectral dependence of these quantities are negligible within the bandwidth of the pulses, $\mathcal{E}_a(1,T)$ can be further simplified to

$$\mathcal{E}_a(1,T) = \mathcal{E}_{0,a}\exp\Bigg(-\frac{(T-T_d-\rho)^2}{2(\tau_a/\tau_b)^2} + \frac{i\sqrt{\pi}}{2\rho}LI_{b,0}\big\{(2k_a n_2 + i\alpha_2)\big(\mathrm{erf}(T) - \mathrm{erf}(T-\rho)\big)\big\} - \frac{3\sqrt{2\pi}}{8\rho}LI_{b,0}^2\alpha_3\Big\{\mathrm{erf}\big(\sqrt{2}T\big) - \mathrm{erf}\Big(\sqrt{2}(T-\rho)\Big)\Big\}\Bigg). \tag{3.14}$$

To add the transverse spatial Gaussian distribution in (x,y), normalized spatial parameters are introduced by normalizing (x,y) to the beam waist of the excitation w_b, i.e. $(X,Y) = \left(\frac{x}{w_b},\frac{y}{w_b}\right)$. At the Gaussian wings of the excitation where the index gradient is maximized, the normalized offset of the probe becomes $\Delta X = 1/2$. Using the center of the probe beam as the origin of (X,Y), the complex field of the probe at the exit plane of the sample is

$$\mathcal{E}_a(X,Y,1,T) = \mathcal{E}_{0,a} e^{-\frac{(X^2+Y^2)}{w_a^2/w_b^2}} \exp\left(-\frac{(T-T_d-\rho)^2}{2(\tau_a/\tau_b)^2}\right.$$

$$+\frac{i\sqrt{\pi}}{2\rho} L I_{b,0} e^{-2\left(\left(X+\frac{1}{2}\right)^2+Y^2\right)} \{(2k_a n_2 + i\alpha_2)(\mathrm{erf}(T) - \mathrm{erf}(T-\rho))\} \quad (3.15)$$

$$\left.-\frac{3\sqrt{2\pi}}{8\rho} L I_{b,0}^2 e^{-4\left(\left(X+\frac{1}{2}\right)^2+Y^2\right)} \alpha_3 \left\{\mathrm{erf}\left(\sqrt{2}T\right) - \mathrm{erf}\left(\sqrt{2}(T-\rho)\right)\right\}\right),$$

which gives both amplitude and phase change of the probe electric field and can be substituted in to Eq. (3.8) and (3.9) to replace $\widetilde{\mathcal{E}_{\mathrm{out}}}$ and proceed to all the following calculations using normalized parameters and eventually transfer from $\Delta E(T_d)/E(T_d)$ to $\Delta E(\tau_d)/E(\tau_d)$. Similar derivations can be made for noninstantaneous NLR, which will be discussed in 4.2. .

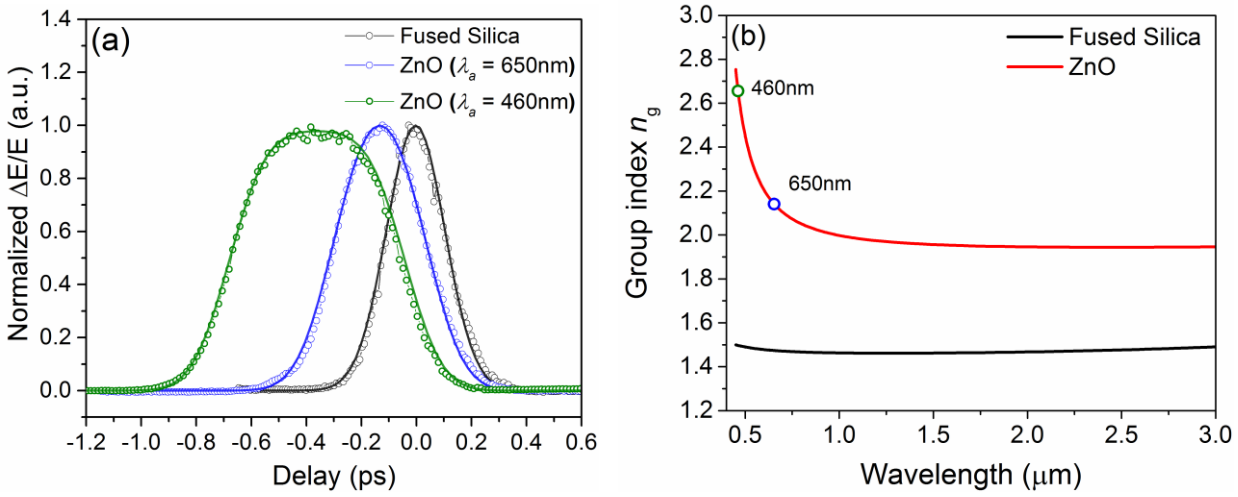

Figure 3.8 Normalized Beam Deflection signals using $\lambda_b = 2.3$ μm under various GVM: fused silica (black) with $\rho \approx 0$; ZnO (blue) with $\lambda_a = 650$ nm ($\rho = 3.7$), and (green) with $\lambda_a = 460$ nm ($\rho = 7.8$); (b) the group index dispersion of fused silica (black) and ZnO (red). The experimental data (circles) are fit (lines) with Eq. (3.8)-(3.14).

Examples of how GVM affects measured BD signals ($\Delta E/E$) along with the material's group index dispersion are shown in Figure 3.8, in which fused silica and ZnO were measured with excitation $\lambda_b = 2.3$ μm and probe at $\lambda_a = 650$ and 460 nm. For fused silica, the GVM between excitation and probe pulses is negligible (i.e. ρ = 0.03 at 650 nm [122]), since its group

index is nearly dispersionless in this spectral range. $\Delta E/E$ again simply follows the cross correlation of the two pulses. In ZnO, since the group index grows dramatically for shorter wavelength near its bandgap [122], where the temporal walk-off between excitation and probe within the sample becomes obvious. $\Delta E/E$ is broadened towards negative delays where the probe comes prior to excitation but travels at a slower group velocity such that the faster excitation pulse catches up and walks through the probe over a distance less than L. It is worth pointing out GVM may result in a slightly different profile of the 3PA signal compared to 2PA or NLR. This can be seen from Eq. (3.14) where a factor of $\sqrt{2}$ in the error function, erf (), of the 3PA term, leads to a slightly faster growth (or decay) of GVM signal on the edges.

3.2.3.3. Separation of NLR from NLA

As discussed earlier, BD is capable of simultaneously characterizing both transient NLR and NLA within one self-consistent measurement. Experimentally, NLA and NLR are separately measured from the total signal $E(\tau_d)$ and normalized deflection signal $\Delta E(\tau_d)/E(\tau_d)$ from a quad-cell detector respectively. The analysis based on Eq. (3.8)-(3.14) can be applied to extract the corresponding nonlinear coefficients. Since the deflection signal originates from spatial energy redistribution upon propagation, the contamination from NLA is inevitable, i.e. in Z-scan. This comes from a nonuniform nonlinear absorption imposed by the Gaussian irradiance profile of the excitation beam. Instead of a phase gradient induced by NLR, NLA will introduced an attenuation gradient, i.e. larger absorption near the center and less at the Gaussian wings, which effectively reshapes the probe beam to laterally translate its centroid towards the wing. Therefore, the $\Delta E(\tau_d)$ from NLA contributions will always look like a negative NLR (i.e., shifts the beam toward the wings),, as

shown in [70]. Unlike the NLR contribution which is almost independent of propagation distance d (see Eq. (3.6)), the $\Delta E(\tau_d)$ from NLA decreases as increasing of d due to the diverging of the beam. This indicates that the BD technique may have excellent potential to measure small NLR signals with a large NLA background, as the contamination from NLA will diminish in the far field. A preliminary demonstration is shown in Figure 3.9 (a), where the $n_2(\omega_a;\omega_b)$ of CdS is measured along with $\alpha_2(\omega_a;\omega_b)$. This has been done using excitation at $\lambda_b = 2.3$ μm and probe at $\lambda_a = 570$ nm, which is associated with the zero-crossing of the nondegenerate NLR dispersion, as discussed in more detail in CHAPTER 6: . The fits give a small value of n_2 (2.2×10^{-5} cm^2/GW) and a large α_2 (13 cm/GW) background. Using an arbitrary irradiance, the Z-scan simulations based on these values are shown in Figure 3.9 (b), which displays a nearly symmetric valley-peak-valley structure in the CA/OA signal. This is an indication that n_2 is too small and becomes over-whelmed with such a large 2PA background. In this case, BD shows the capability of separating small NLR signals (including the sign) from large NLA, which would be very difficult to do with Z-scan.

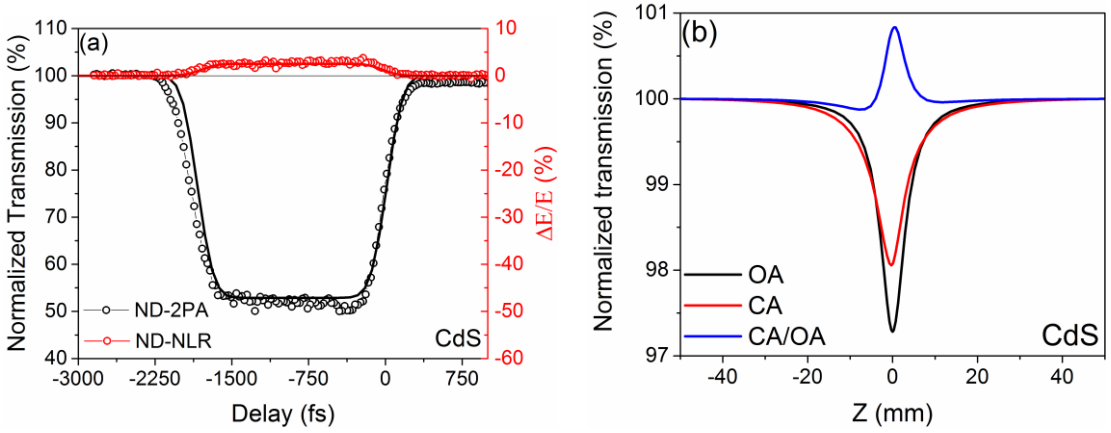

Figure 3.9 (a) Beam Deflection measurements of 0.5 mm thick CdS near the zero-crossing of nondegenerate NLR dispersion, with a large ND-2PA background; (b) simulations of Z-scan using the n_2 (2.2×10^{-5} cm^2/GW) and α_2 (13 cm/GW) fitted from BD measurements in (a).

CHAPTER 4: NONLINEAR RESPONSE FUCTIONS OF ORANNIC SOLVENTS

Knowledge of the nonlinear optical (NLO) properties of organic solvents is critical in organic NLO applications, of which the nonlinear refraction (NLR) and its temporal dynamics is of great importance particularly in the visible and near-IR spectral window where the solvent is nearly transparent. First, since most NLO characterizations of organic dyes are performed in solutions where the solute is dissolved in solvents, knowing the solvent nonlinearities helps to interpret the results, i.e. to separate out the response of the solute. Also, the study of solvents nonlinearity provides insight into the structure-property relations of the molecules themselves, which will help to enhance our understanding on the origins of molecular liquids nonlinearity.

As mentioned in 1.3. , measurements of n_2 of commonly used organic solvents in the liquid phase have been the subject of numerous studies using techniques such as Z-scan, but the results often appear to conflict in value depending on the experimental methods, pulsewidths used, or interpretations [1]. This is because besides the nearly instantaneous bound-electronic NLR, the induced nuclear motions in the liquid phase often result in different noninstantaneous contributions, which usually complicates the molecular NLR response function as discussed in 2.2.2. This sometimes makes the experimental results, i.e. $n_{2,\text{eff}}$ defined in Table 2.4, dependent upon the pulsewidths used. To fully understand and solve this problem, we recently developed a methodology to study the nonlinear response of solvents using the polarization-resolved Beam Deflection technique [17, 18]. With carbon disulfide (CS_2) as the example material, the overall NLO response is decomposed into an instantaneous bound-electronic NLR, and three major noninstantaneous mechanisms due to collisional, librational and rotational nuclear motions. It has also been shown

that knowledge of the full set of NLO response functions of CS_2 allows us to predict the outcomes of other NLO experiments on CS_2 such as DFWM, as well as the pulsewidth dependent $n_{2,\mathrm{eff}}$ measured by Z-scan [17].

In this Chapter, we utilize our Beam Deflection (BD) technique and the methodology developed in [17] to measure the NLO response functions of another 23 widely used organic solvents. First, we will introduce the physical origins of NLR for molecular liquids, and how the polarization-resolved BD measurements help to separate electronic and nuclear responses. Then the measured NLR response functions from selected solvents will be presented with tentative explanations from the standpoint of their molecular structures. Using these response functions, the effective nonlinear refractive index ($n_{2,\mathrm{eff}}$) is predicted for different pulsewidths. Finally, we show several examples of BD measurements on solutions of organic dyes, in which the solute response is separated from the solvent background.

4.1. Physical Origins of NLR

In this section, the physical origins of a solvent's NLR response are discussed, in which bound-electronic $n_{2,\mathrm{el}}$ is related to the induced electronic dipoles on a microscopic level, and noninstantaneous response function $R(t)$ due to the induced nuclear motions is clarified by introducing the magnitude $n_{2,\mathrm{m}}$ and normalized response function $r_m(t)$ for each particular mechanism.

4.1.1. Bound-electronic Second Hyperpolarizability

As discussed in 2.1. , light interacts with matter via an induced electronic polarization $\vec{\boldsymbol{P}}$ with both linear and nonlinear components. To describe the response of material in a macroscopic view, $\vec{\boldsymbol{P}}$

is related with the external driving fields $\vec{\boldsymbol{E}}$ by linear and nonlinear susceptibilities $\boldsymbol{\chi}^{(n)}$ in Eq. (2.1). In a microscopic view, light interacts with matter by inducing a dipole moment $\vec{\boldsymbol{\mu}}$ on each of the atoms or molecules. In molecular liquids with initial random orientation, the macroscopic polarization can be written as a sum of orientationally averaged dipole moments $\vec{\boldsymbol{P}} = N\langle\vec{\boldsymbol{\mu}}\rangle$, which provides a connection between microscopic and macroscopic quantities.

Conventionally, $\vec{\boldsymbol{\mu}}$ can be expanded as a power series as $\vec{\boldsymbol{\mu}} = \overrightarrow{\boldsymbol{\mu_0}} + \boldsymbol{\alpha}\vec{\boldsymbol{E}}_{\mathbf{loc}} + \boldsymbol{\beta}\vec{\boldsymbol{E}}_{\mathbf{loc}}^{\mathbf{2}} + \boldsymbol{\gamma}\vec{\boldsymbol{E}}_{\mathbf{loc}}^{\mathbf{3}} + \cdots$, where $\overrightarrow{\boldsymbol{\mu_0}}$ is the permanent dipole moment, $\boldsymbol{\alpha}$ is the linear polarizability, $\boldsymbol{\beta}$ is the first hyperpolarizability and $\boldsymbol{\gamma}$ is the second hyperpolarizability which is associated with the effects induced by a term third-order in the field, i.e. NLR and 2PA. Note $\vec{\boldsymbol{E}}_{\mathbf{loc}}$ is known as the local field, which should be distinguished from the applied field (or Maxwell field) $\vec{\boldsymbol{E}}$. In condensed matters, e.g. liquids, each molecule interacts with their neighbors by a dipole field $\vec{\boldsymbol{E}}_{\mathbf{d}}$ that is induced by $\vec{\boldsymbol{E}}$. Therefore the total field that effectively acts on each molecule is $\vec{\boldsymbol{E}}_{\mathbf{loc}} = \vec{\boldsymbol{E}} + \vec{\boldsymbol{E}}_{\mathbf{d}}$. Although precise calculation of $\vec{\boldsymbol{E}}_{\mathbf{d}}$ is difficult for materials with complicated symmetries or intermolecular interactions, for isotropic media the Lorentz-Lorenz treatment provides an approach by considering a spherical cavity with dipole charges [30, 31], which gives $\vec{\boldsymbol{E}}_{\mathbf{d}} = \frac{1}{3\varepsilon_0}\vec{\boldsymbol{P}}$. By equalizing the polarizations derived from microscopic and macroscopic quantities within the scope of linear optics, we have

$$\vec{\boldsymbol{P}} = \varepsilon_0\boldsymbol{\chi}^{(\mathbf{1})}\vec{\boldsymbol{E}} = N\boldsymbol{\alpha}\vec{\boldsymbol{E}}_{\mathbf{loc}} = N\boldsymbol{\alpha}\left(\vec{\boldsymbol{E}} + \frac{1}{3\varepsilon_0}\vec{\boldsymbol{P}}\right) \tag{4.1}$$

which leads to the Clausius-Mossotti relation [31]. Further substitution within Eq. (4.1) results in

$$\vec{\boldsymbol{E}}_{\mathbf{loc}} = \left(\frac{\epsilon_r + 2}{3}\right)\vec{\boldsymbol{E}} \approx \left(\frac{n^2 + 2}{3}\right)\vec{\boldsymbol{E}} \tag{4.2}$$

where ϵ_r is the relative permittivity. With zero linear absorption, $\epsilon_r = n^2$. There $\vec{\boldsymbol{E}}_{\mathbf{loc}}$ appears to be enhanced over $\vec{\boldsymbol{E}}$ by a factor of $f^{(1)} = \left(\frac{n^2+2}{3}\right)$, which is often considered in calculations of (hyper) polarizabilities from experimentally measured susceptibilities, i.e. $\chi^{(1)} = \varepsilon_0^{-1} N\langle\alpha\rangle \left(\frac{n^2+2}{3}\right)$. For solvents, this enhancement factor is relatively small for linear optical properties, i.e. 1.4× for linear refractive index of 1.5. But this local field enhancement could become considerably larger for nonlinear optical properties. As derived in [30, 31], in the absence of linear absorption $\chi^{(3)}$is related with $\langle\gamma\rangle$ by

$$\begin{aligned}&\chi^{(3)}(\omega_a + \omega_b, +\omega_c; \omega_a, \omega_b, \omega_c) = \varepsilon_0^{-1} f^{(\mathbf{3})} N\langle\gamma\rangle \\ &= \varepsilon_0^{-1}\left(\frac{n^2(\omega_a + \omega_b, +\omega_c) + 2}{3}\right)\left(\frac{n^2(\omega_a) + 2}{3}\right)\left(\frac{n^2(\omega_b) + 2}{3}\right)\left(\frac{n^2(\omega_b) + 2}{3}\right) N\langle\gamma\rangle,\end{aligned} \tag{4.3}$$

where $f^{(\mathbf{3})}$is defined as the Lorentz-Lorenz third-order local field factor. For single beam and nondegenerate two-beam experiments, we can relate $\langle\gamma\rangle$ to experimentally measured bound-electronic $n_{2,\mathrm{el}}$ via $\chi^{(3)}$ using Table 2.1

$$n_{2,el}(\omega_a; \omega_a) = \frac{3}{4}\frac{N}{n_a^2 \varepsilon_0^2 c}\left(\frac{n^2(\omega_a) + 2}{3}\right)^4 \mathrm{Re}[\langle\gamma\rangle], \tag{4.4}$$

$$n_{2,el}(\omega_a; \omega_b) = \frac{3}{4}\frac{N}{n_a n_b \varepsilon_0^2 c}\left(\frac{n^2(\omega_a) + 2}{3}\right)^2\left(\frac{n^2(\omega_b) + 2}{3}\right)^2 \mathrm{Re}[\langle\gamma\rangle], \tag{4.5}$$

For solvents with a linear index of refraction ~ 1.5, the local field enhancement factor is ~ 4× which is much larger than for the linear case. One way to examine the validation of Lorentz-Lorenz local field theory is to compare γ values determined in both liquid and gas phases. Since in dilute gases $f^{(\mathbf{3})} \sim 1$, γ is directly measured without the need for local field correction, as discussed in 5.3. .

4.1.2. Molecular Reorientation

Besides bound-electronic NLR ($n_{2,\mathrm{el}}$) that originates from the pure electronic second hyperpolarizability, there are other noninstantaneous mechanisms contributing to the refractive index change. Following the methodology used in [17, 73, 75, 106], these contributions have been treated as linearly independent, and the total nonlinear response function $R(t)$ defined in (2.24) becomes

$$R(t) = \sum_m n_{2,m} r_m(t), \tag{4.6}$$

where $n_{2,m}$ is the nonlinear refractive index for the noninstantaneous mechanism "m", which governs the magnitude, and $r_m(t)$ is the corresponding normalized response function, $\int_{-\infty}^{\infty} r_m(t)\mathrm{d}t = 1$, which governs the temporal dynamics. In liquid phase solvents, the physical origins of these noninstantaneous responses of NLR are usually from light induced nuclear motions such vibration and rotation, which occur on the time scale of hundred femtoseconds to tens of picoseconds.

The molecular reorientation effect is an important nuclear nonlinearity for molecules having spatial anisotropic polarizabilities. This first starts from the linear dipole moment induced by the incident light $\overrightarrow{\boldsymbol{\mu_1}} = \boldsymbol{\alpha}\vec{\boldsymbol{E}}_{\mathbf{loc}}$. Depending on the initial orientation of the molecule, $\overrightarrow{\boldsymbol{\mu_1}}$ may not have the same direction as $\vec{\boldsymbol{E}}_{\mathbf{loc}}$, which produces a torque $\vec{\boldsymbol{\tau}} = \overrightarrow{\boldsymbol{\mu_1}} \times \vec{\boldsymbol{E}}_{\mathbf{loc}}$ on the molecule causing it to rotate towards the direction of $\vec{\boldsymbol{E}}_{\mathbf{loc}}$. This torque comes from a derivative of the energy, $\bar{V} = -\bar{\mathcal{P}} \cdot \bar{E}_{\mathrm{loc}}$, where $\bar{\mathcal{P}}$ is the induced polarization in molecular frame as defined later. The molecular alignment is through the optical field interacting with the induced first-order dipole moment, which is able to change direction along with the fast oscillating field, making $\vec{\boldsymbol{\tau}}$ always point the same direction. If a permanent dipole moment $\overrightarrow{\boldsymbol{\mu_0}}$ exists for the molecule, interacting with the permanent dipole moment $\overrightarrow{\boldsymbol{\mu_0}}$, the produced torque will change sign over each half optical cycle, giving an

averaged zero effect. But it should be noted that molecules with a $\overrightarrow{\boldsymbol{\mu_0}}$ should be able to be aligned by a DC (or terahertz) field [123, 124].With the orientation of the molecules now different from their initial distribution, for molecules with anisotropic polarizabilities the incident field will see a change in the index of refraction due to the optically induced transient change in the angularly averaged $\langle\alpha(t)\rangle$, where the transient refractive index $n(t)$ is related with the transient $\langle\alpha(t)\rangle$ by

$$n^2(t) = \epsilon_r = 1 + \chi^{(1)} = 1 + \frac{N\langle\alpha(t)\rangle}{\varepsilon_0} \tag{4.7}$$

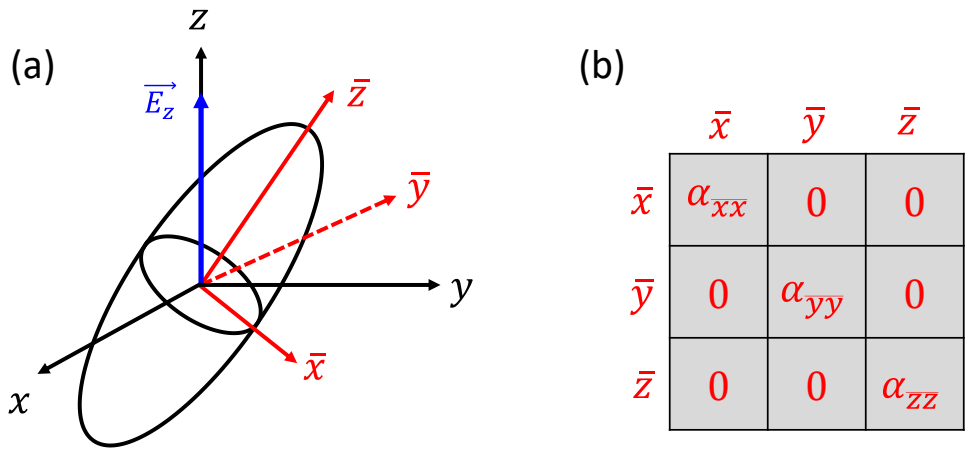

Figure 4.1 (a) Definition of laboratory frame (x, y, z) and molecular frame $(\bar{x}, \bar{y}, \bar{z})$; linear polarizability tensor with anisotropy.

Since the solvent molecule studied in this work is not necessarily to be linear, here we need to consider a general case where the molecule has anisotropic polarizabilities $\alpha_{\bar{x}\bar{x}} \neq \alpha_{\bar{y}\bar{y}} \neq \alpha_{\bar{z}\bar{z}}$ in its molecular frame $(\bar{x}, \bar{y}, \bar{z})$, as illustrated in Figure 4.1 (a). The applied electric field is defined as $\vec{\boldsymbol{E}}_{\mathbf{loc}}(z,t) = \left(\frac{1}{2}\mathcal{E}_z e^{i(k\cdot z-\omega t)} f^{(1)} + c.c.\right)\vec{\boldsymbol{e}}_z$, along the z-axis in the laboratory frame (x, y, z). To calculate the induced polarization magnitude $\mathcal{P}$ in (x, y, z), we need to first calculate the polarization in the molecular frame $\bar{\mathcal{P}}$ by transferring $\vec{\boldsymbol{E}}_{\mathbf{loc}}(z,t)$ to $(\bar{x}, \bar{y}, \bar{z})$, then $\bar{\mathcal{P}}$ needs to be projected

back to the laboratory frame to give $\mathcal{P}$. In principle, Euler transformation can be used to relate the different coordinate systems. Therefore, the induce polarization $\mathcal{P}_z$ in the same direction ($\vec{\boldsymbol{e}}_z$) of the incident light can be derived as

$$\mathcal{P}_z = N\langle \alpha_{\bar{x}\bar{x}} \sin^2\theta \cos^2\psi + \alpha_{\bar{y}\bar{y}} \sin^2\theta \sin^2\psi + \cos^2\theta\, \alpha_{\bar{z}\bar{z}} \rangle \mathcal{E}_z \left[f^{(1)}\right]^2, \tag{4.8}$$

where θ is the angle between $\bar{\boldsymbol{z}}$ and $\boldsymbol{z}$, ψ is the angle between $\bar{\boldsymbol{x}}$ and the projection of $\boldsymbol{z}$ on the $\bar{x}, \bar{y}$ plane. The angle ϕ between $\bar{\boldsymbol{x}}$ and $\boldsymbol{x}$ will not affect $\mathcal{P}_z$ but will be needed for polarizations induced in the perpendicular direction, i.e. $\mathcal{P}_x$ and $\mathcal{P}_y$. At the initial state, the molecules are randomly distributed in angle. The ensemble averaging in spherical coordinates gives $\int_0^{\pi/2}\int_0^{2\pi}\int_0^{2\pi} \sin\theta\, d\theta d\psi d\phi$, gives $\langle\alpha\rangle = \frac{1}{3}\left(\alpha_{\bar{x}\bar{x}} + \alpha_{\bar{y}\bar{y}} + \alpha_{\bar{z}\bar{z}}\right)$. Substituting $\langle\alpha\rangle$ into Eq. (4.7) and (4.8) results in a linear refractive index n_0 and linear (first-order in $\mathcal{E}_z$) polarization $\mathcal{P}_z^L$.

Upon perturbation from an applied optical field, $\mathcal{P}_z$ deviates from $\mathcal{P}_z^L$ with a nonlinear contribution due to changes in $\langle\alpha\rangle$. In liquids, two processes need to be considered in order to describe the molecular reorientation [32]: the alignment energy from the torque $\bar{V} = -\bar{\mathcal{P}} \cdot \bar{E}_{\mathrm{loc}}$, and the thermal agitation that tends to return system to a molecular random distribution, which together form an angular probability of $\exp(-\bar{V}/k_B T)$, where k_B is the Boltzmann constant and T is the temperature. The ensemble averaging in Eq. (4.8) thus becomes

$$\mathcal{P}_z = N \frac{\int_0^{\pi/2}\int_0^{2\pi}\int_0^{2\pi} \alpha(\theta,\psi,\phi) \exp\left(-\frac{\bar{V}}{k_B T}\right) \sin\theta\, d\theta d\psi d\phi}{\int_0^{\pi/2}\int_0^{2\pi}\int_0^{2\pi} \exp\left(-\frac{\bar{V}}{k_B T}\right) \sin\theta\, d\theta d\psi d\phi} \mathcal{E}_z \left[f^{(1)}\right]^2, \tag{4.9}$$

where $\alpha(\theta,\psi,\phi) = \alpha_{\bar{x}\bar{x}} \sin^2\theta \cos^2\psi + \alpha_{\bar{y}\bar{y}} \sin^2\theta \sin^2\psi + \cos^2\theta\, \alpha_{\bar{z}\bar{z}}$. For small reorientational angle, $\exp(-\bar{V}/k_B T) \approx 1 + \frac{1}{4}\alpha(\theta,\psi,\phi)\mathcal{E}_z^2 \left[f^{(1)}\right]^2$, where the first term simply results in $\mathcal{P}_z^L$,and the second term gives the nonlinear polarization which is third-order in the electric field

$$\mathcal{P}_z^{NL} = N\left[f^{(1)}\right]^4 \mathcal{E}_z \frac{\left(\alpha_{\overline{xx}}^2 + \alpha_{\overline{yy}}^2 + \alpha_{\overline{zz}}^2 - \alpha_{\overline{xx}}\alpha_{\overline{yy}} - \alpha_{\overline{xx}}\alpha_{\overline{yy}} - \alpha_{\overline{xx}}\alpha_{\overline{zz}}\right)}{45k_BT} \mathcal{E}_z^2 \qquad (4.10)$$

From this third-order nonlinear polarization, we should be able to define the NLR coefficient for the noninstantaneous reorientational effect. To be consistent with our previous definition, i.e. $n_{2,m}$ in Eq. (4.6), we start by comparing Eq. (4.10) and (2.22), and define a nuclear third-order susceptibility as

$$\chi_{re}^{(3)}(t) = \frac{2N}{\varepsilon_0}\left[f^{(1)}\right]^4 \frac{\left(\alpha_{\overline{xx}}^2 + \alpha_{\overline{yy}}^2 + \alpha_{\overline{zz}}^2 - \alpha_{\overline{xx}}\alpha_{\overline{yy}} - \alpha_{\overline{xx}}\alpha_{\overline{yy}} - \alpha_{\overline{xx}}\alpha_{\overline{zz}}\right)}{45k_BT} r_r(t), \qquad (4.11)$$

where the normalized response function $r_r(t)$ from Eq. (4.6) is added in the end of the equation to account for the noninstantaneous dynamics from hindered rotation processes. Following [17], $r_r(t)$ simply takes the form of exponential rising and falling terms, as defined in Table 4.1.

Now we are able to relate $\chi_{re}^{(3)}(t)$ with the response function $R(t)$ using Table 2.4, from which the nonlinear refractive index $n_{2,r}$ for reorientational effect is

$$n_{2,r} = \frac{N}{n_0^2\varepsilon_0^2 c}\left[f^{(1)}\right]^4 \frac{\left(\alpha_{\overline{xx}}^2 + \alpha_{\overline{yy}}^2 + \alpha_{\overline{zz}}^2 - \alpha_{\overline{xx}}\alpha_{\overline{yy}} - \alpha_{\overline{xx}}\alpha_{\overline{yy}} - \alpha_{\overline{xx}}\alpha_{\overline{zz}}\right)}{45k_BT} \qquad (4.12)$$

which provides a theoretical value calculated from linear polarizability tensors, which we can expand to compare to our experimental values of different solvents measured using Beam Deflection, as discussed in 4.3.2. .

4.1.3. Other Noninstantaneous Contributions

Other than the reorientational effect, there are other induced nuclear motions giving changes in the refractive index with different magnitudes and response dynamics. For the needs of the data analysis, we will briefly introduce the other three major nuclear mechanisms contributing to NLR,

namely libration, collision and vibration, with their response function listed in Table 4.1. More details on their physical origins are discussed in [17, 73, 125]. Libration is referred to as an oscillatory rocking motion initiated by the torque applied by the external field, which usually starts in the first several hundreds of femtosecond and decays faster than the reorientational effect. This effect will only be of importance in dense media since the 'rocking' comes from interactions with near neighbor molecules, i.e. the rotation starts but gets interrupted by neighboring molecules. The librational response function is modeled using a quantum harmonic oscillator (see Table 4.1). Since it is a random Gaussian process, the response is inhomogeneously broadened [71], which is described by an antisymmetrized Gaussian distribution function [126], $g(\omega)$, in which ω_0 and σ are the center frequency and bandwidth, respectively. Since libration arises from same torque as reorientation, they share the same polarization dependence, as discussed in 4.2.2. . Additionally, the field-induced dipole will reradiate an electric field, which will affect its neighboring molecules by distorting their polarizability, thus giving refractive index change. This is referred to collision-induced NLR, which has been modeled using an exponential rise and decay in its response function [73]. Different from orientation and libration, the collision mechanism has an isotropic polarization dependence, as discussed in 4.2.2. .

Vibrational motion is another nuclear mechanism that alters the linear polarizability of the molecule. In our experiment, it can be excited by a broadband femtosecond pulse through the stimulated Raman effect. But this requires that the corresponding vibrational mode must be Raman active, and the excitation pulse is shorter than the vibrational period (so that the spectrum of the excitation pulse overlaps the vibration spectrum). The response function of NLR from nuclear vibration takes the form of a damped oscillation at frequency ω_v with a decay constant $\tau_{f,v}$.

Table 4.1 Noninstantaneous NLR response functions due to nuclear motions [17, 73, 125]

	$n_{2,m}$	$r_m(t)$[a,b]
Reorientation	$n_{2,r}$	$r_d(t) = C_d\left(1 - e^{-\frac{t}{\tau_{r,d}}}\right)e^{-\frac{t}{\tau_{f,d}}}\Theta(t)$
Libration	$n_{2,l}$	$r_l(t) = C_l e^{-\frac{t}{\tau_{f,l}}}\Theta(t)\int_0^\infty \frac{\sin(\omega t)}{\omega}\left(e^{-\frac{(\omega-\omega_0)^2}{2\sigma^2}} - e^{-\frac{(\omega+\omega_0)^2}{2\sigma^2}}\right)\mathrm{d}\omega$
Collision	$n_{2,c}$	$r_c(t) = C_c\left(1 - e^{-\frac{t}{\tau_{r,c}}}\right)e^{-\frac{t}{\tau_{f,c}}}\Theta(t)$
Vibration	$n_{2,v}$	$r_v(t) = C_v \sin(\omega_v t)\, e^{-\frac{t}{\tau_{f,v}}}\Theta(t)$

[a] $\Theta(t)$ is the Heaviside (step) function;
[b] $C_m = (\tau_{r,m} + \tau_{f,m})/\tau_{f,m}^2$ is a normalization constant.

4.2. Beam Deflection Measurements

In this section, we present the methodology of using the Beam Deflection (BD) technique to measure the nonlinear response function of liquid phase solvents. The measurements from carbon disulfide is used as a demonstration. Since electronic and different nuclear nonlinearities have different temporal response, early work using OKE differentiate their contributions simply from the induced transient birefringence at different delays [73, 125], which requires both excitation and probe pulses shorter than the nuclear response time of the molecule. Different from OKE, the signal of BD $\Delta E/E$ is directly proportional to n_2 (see Eq. (3.7)) which gives the magnitude, sign and temporal dynamics of NLR. More importantly, this enables us to vary the polarizations of excite and probe to take advantage of different tensor symmetries of bound-electronic and reorientational NLR, which results in better separation of the two without having to use extremely short pulses, as discussed in 4.2.2.

The previous modeling of the BD signal $\Delta E/E$ in section 3.2.3. is given based on bound-electronic NLR and NLA, but it is straightforward to expand it for noninstantaneous responses. In Eq. (3.11), we simply replace $2n_2(\omega_a;\omega_b)I_b(t)$ on the right-hand side to be the "two-beam" Δn in Table 4.1, which includes both electronic $n_2(\omega_a;\omega_b)$ as well as the total nuclear response function $R(t)$ that convolved with the excitation irradiance $I_b(t)$ gives:

$$i\left(\frac{\partial \mathcal{E}_a}{\partial z}+\frac{n_{g,a}}{c}\frac{\partial \mathcal{E}_a}{\partial t}\right)=-\left(2k_{0,a}n_{2,el}I_b(t)+\int_{-\infty}^{\infty}R(t-t')I_b(t')\mathrm{d}t'\right)\mathcal{E}_a, \tag{4.13}$$

where NLA terms are ignored as they are negligible at the wavelengths of our experiments. Similar to the procedure in Eq. (3.12)-(3.15), we follow [17, 121] to introduce normalized variables and solve the differential equation assuming temporally Gaussian pulses, which yields

$$\begin{aligned}\mathcal{E}_a(1,T)=\mathcal{E}_{0,a}\exp\Bigg(&-\frac{(T-T_d-\rho)^2}{2(\tau_a/\tau_b)^2}\\&+\frac{i\sqrt{\pi}}{2\rho}Lk_aI_{b,0}\Bigg\{2n_{2,el}\big(\mathrm{erf}(T)-\mathrm{erf}(T-\rho)\big)\\&+\int_{T-\rho Z}^{T}\int_{-\infty}^{\infty}R(T''-T')e^{-T'^2}\mathrm{d}T'\,\mathrm{d}T''\Bigg\}\Bigg),\end{aligned} \tag{4.14}$$

After adding the normalized transverse spatial Gaussian distribution as we did in Eq. (3.15), we can proceed to the Fresnel propagation in Eq. (3.8) and (3.9) to derive the BD signal, $\Delta E/E$, for transient NLR of solvents.

4.2.1. Temporal Dynamics of NLR

Here we present the BD measurements of the response function of liquid carbon disulfide as a demonstration of the methodology in [17]. The experimental setup utilized the Coherent laser system as introduced in 3.2.1. . In this experiment, BD experiments are performed using 800 nm, ~ 100 fs (FWHM) pulses with an energy of ~ 6.7 μJ as the excitation directly from a Ti:sapphire amplified system at a repetition rate of 1 kHz. A portion of the excitation is used to generate a white-light continuum (WLC) by focusing into 1 cm quartz cuvettes filled with water, which is then spectrally filtered by narrow bandpass interference filters ($\Delta\lambda$ ~10 nm) at 700 nm to use as the probe. The excitation and probe are focused to radii of 290 μm and 40 μm respectively at the sample. The deflection signal of the probe is detected by a quad-segmented Si photodiode (OSI QD50-0-SD) placed 25 cm behind the sample. For the conditions of these experiments, this is in the far field. The wavelength of the excitation and probe are chosen to be slightly nondegenerate within the transparency window of the organic solvents to avoid artifacts common in degenerate experiments [127]; however, the wavelengths are close enough to keep the reduction of temporal resolution caused by GVM to a minimum. The BD measurements on CS_2 (Sigma-Aldrich, ≥ 99 %) used in a 1 mm path length quartz cuvette and the contribution from the cuvette are measured separately under identical conditions and subtracted.

Figure 4.2 (a) shows the measured BD signal, $\Delta E/E$, of the liquid CS_2 by varying the temporal delay of co-polarized excitation and probe pulses. The observed dynamics are similar with early reported results in [17, 121], with an instantaneous contribution at zero delay followed by noninstantaneous responses decaying in a multi-exponential manner. The normalized response functions for noninstantaneous components used to interpret this data is shown in Figure 4.2 (b), taking into account the three nuclear mechanisms, which consist of a slower decaying (> 1 ps)

response due to diffusive reorientation, a fast rising and rapidly damped intermediate component due to librational motion and a relatively small response due to collisional-induced molecular polarizability. The total contribution (red) is simply taken by summing of the three responses, which gives a maximum ~ 130 fs after zero delay. However, the temporal resolution is limited to the width of the cross-correlation ~ 220 fs of excitation and probe pulses, so the prominent peak from the total nuclear contribution at ~ 130 fs is totally overwhelmed within the instantaneous contribution of bound-electronic NLR .

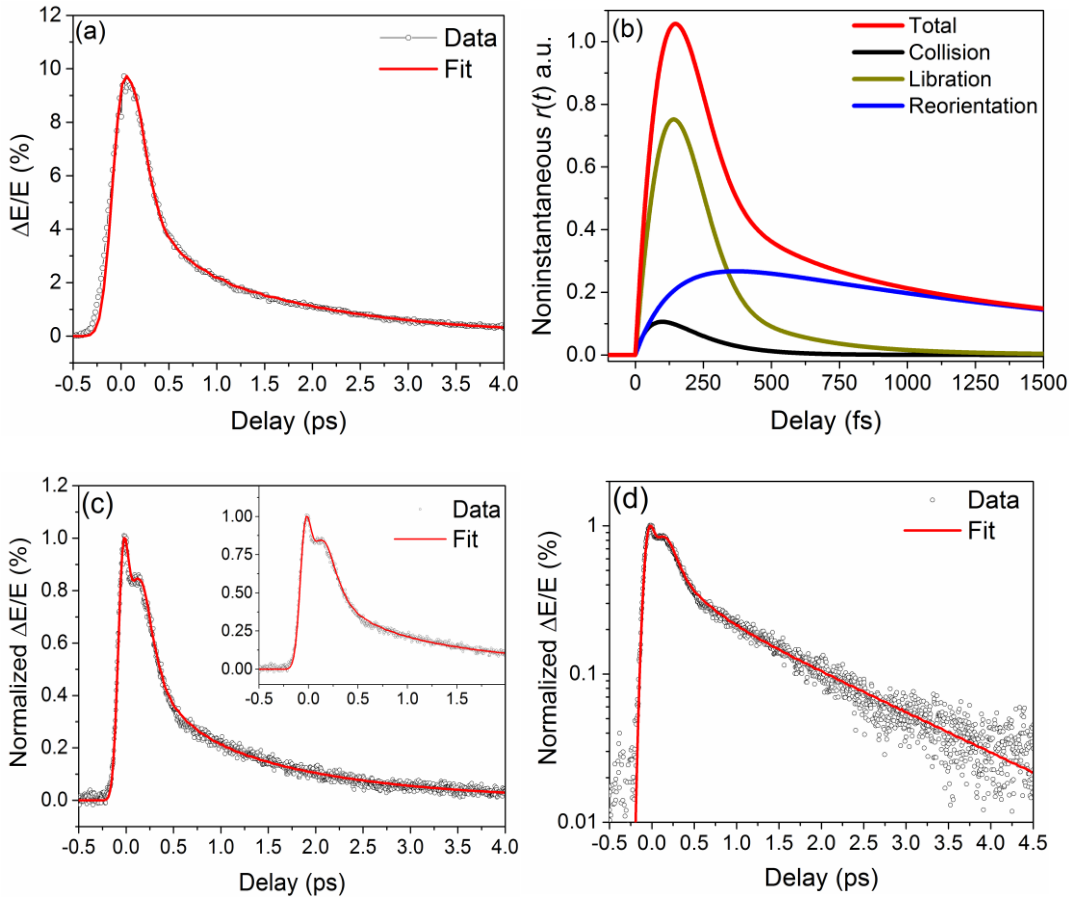

Figure 4.2 Data (circles) and fit (lines) of BD measurement of CS_2 using co-polarized excitation and probe: (a) with WLC probe filter at 700 nm with pulsewidth ~ 200 fs (FWHM); (b) the normalized response function for different nuclear mechanisms; (c) with 52 fs (FWHM) probe pulse from TOPAS-800 at 720nm compressed by a prism compressor; inset shows enlarged signals < 2 ps; (d) logarithmic scale plot of data in (c).

To achieve better time resolution, another BD measurement of CS_2 is performed by taking the signal beam at wavelength 1440 nm from TOPAS-800 (OPA), which is then frequency doubled to 720 nm to use as the probe. A typical pulse compressor is built by using two fused silica prisms to compress the probe pulse to 52 fs. Using excitation at a wavelength of 800 nm with a pulsewidth of 100 fs (FWHM). The resultant BD measurement (see Figure 4.2 (c)) now shows a maximum at zero delay due to the instantaneous NLR due to bound-electrons, which is followed by a prominent shoulder at exactly 130 fs corresponding to the maximum of total nuclear response discussed in Figure 4.2 (b). The data is fit using same response functions as used in Figure 4.2 (a) but with short pulses. On a logarithmic scale shown in Figure 4.2 (d), the difference in the relaxation time constants between librational and reorientational responses becomes more distinct than on a linear scale. Comparing to the measurement in Figure 4.2 (a) using a filtered WLC probe, the data in Figure 4.2 (c) shows a larger noise floor which may be due to the larger pointing instability of the probe beam from the TOPAS-800.

Although the differences can be observed in the time domain which distinguish various NLR mechanisms to a certain extent, the precise determination of the magnitudes of $n_{2,m}$, rising/falling time constants and other parameters associated with each response function in Table 4.1 is still challenging. The analysis of the polarization dependence in BD measurements provides a prescription for separating electronic NLR from large reorientational contributions.

4.2.2. Polarization Dependence

As discussed in 4.1. , bound-electronic NLR originates from the pure electronic second hyperpolarizability, which is a real $\chi^{(3)}$ effect, while the molecular reorientation alters the angular distribution, resulting in a change in the ensemble averaged linear polarizability $\langle\alpha\rangle$. The two different physical origins leads to different tensor symmetry properties, which can be used in Beam Deflection measurements to give a better separation between electronic and nuclear NLR [18, 93].

For the bound-electronic nonlinearity, n_2 is related with the corresponding $\chi^{(3)}$ in Table 2.1. For the two-beam case, the ratio of n_2 between co- and cross-polarized beams gives $n_{2,\parallel}/n_{2,\perp} = \chi^{(3)}_{R,xxxx}/\chi^{(3)}_{R,xxyy}$. Since the materials we are studying are mostly isotropic, Kleinman symmetry leads to $\chi^{(3)}_{R,xxxx}/\chi^{(3)}_{R,xxyy} = 1/3$ [31, 32]. Therefore, the results from BD measurements with parallel ∥ and perpendicular ⊥ polarizations between excitation and probe shows $n^{iso}_{2,\parallel}/n^{iso}_{2,\perp} = 3$ for nonlinearities with isotropic tensor symmetry, e.g. fused silica in Figure 3.7.

The reorientational nonlinearities have a different symmetry property. Similar to Eq. (4.12), where we derive the reorientational $n^{re}_{2,\parallel}$ for co-polarized two-beam interactions, to derive $n^{re}_{2,\perp}$ of cross-polarized beams, a derivation can also be made following Eq. (4.7)-(4.8). Here the polarization in the molecular frame $\bar{\mathcal{P}}(\bar{x},\bar{y},\bar{z})$ needs to project to the perpendicular direction of the input in the laboratory frame, i.e. to calculate $\mathcal{P}_x$ or $\mathcal{P}_y$ in Eq. (4.8). As shown in [32], the ratio for reorientational nonlinearities follows $n^{re}_{2,\parallel}/n^{re}_{2,\perp} = -2$. Different from isotropic NLR, $n^{re}_{2,\perp}$ is not only smaller, but changes sign. But this "-2" ratio cannot be explained in a very intuitive way: if the polarization of the probe is parallel with the excitation along the *z*-axis, the torque induced by excitation will cause molecules to align towards the *z*-axis, therefore the molecules initially align from both the *x*- and *y*-axes and will contribute to an increase of $\langle\alpha\rangle$ (positive $n^{re}_{2,\parallel}$ from both *x*-

and *y*-polarized molecules); if the polarization of the probe is along the *x*-axis, which is perpendicular to the excitation (*z*-axis), as the torque-induced reorientation occurs, only the molecules initially aligned along the *x* axis will contribute to a decrease of $\langle\alpha\rangle$ (negative $n_{2,\perp}^{re}$ from *x*-axis).

Now the tensor symmetry properties can be applied for BD measurements of solvents to model the transient response measured at any angle θ between the polarizations of excitation and probe. Derived from the index ellipsoid [31], a small index change satisfies $\Delta n(\theta) = \Delta n_{\parallel}\cos^2(\theta) + \Delta n_{\perp}\sin^2(\theta)$. In liquid solvents, bound-electronic and collision-induced NLR follow isotropic tensor symmetry, which together give Δn^{iso}, and on the other hand librational and reorientational give Δn^{re}. Considering their symmetry properties, the total refractive index change that is experienced by a probe with polarization at θ w.r.t. the excitation is

$$\Delta n(\theta) = \Delta n_{\parallel}^{iso}\left(\cos^2(\theta) + \frac{1}{3}\sin^2(\theta)\right) + \Delta n_{\parallel}^{re}\left(\cos^2(\theta) - \frac{1}{2}\sin^2(\theta)\right), \qquad (4.15)$$

which gives the polarization dependent NLR. The contribution from isotropic nonlinearities are always positive, it decreases from $\Delta n_{\parallel}^{iso}$ at $\theta = 0$ to $\frac{1}{3}\Delta n_{\parallel}^{iso}$ at $\theta = 90°$. But the reorientational nonlinearities change sign from $\Delta n_{\parallel}^{re}$ at $\theta = 0$ to $-\frac{1}{2}\Delta n_{\parallel}^{re}$ at $\theta = 90°$, and the switching point is the magic angle $\theta = 54.7°$, where the reorientational contribution becomes zero, leaving the total index change only contributed by isotropic nonlinearities, i.e. $\Delta n(54.7) = \frac{5}{9}\Delta n_{\parallel}^{iso}$. $\theta = 54.7°$ is the 3-D equivalent of 45° in 2D and is the angle made by the diagonal of a cube.

The polarization BD measurements in Figure 4.3 (a) are performed using identical experimental conditions as the measurement in Figure 4.2 (a), by simply rotating the polarization of the probe to be perpendicular and at magic angle w.r.t the excitation beam polarization. Compared to the parallel case in Figure 4.2 (a), the perpendicular polarization data shows a positive n_2 around

zero delay mainly due to bound-electronic NLR, which then rapidly becomes negative and decays at longer delays due to the librational and reorientational response decays. At the magic angle, both librational and reorientational contributions are zero, so the measured $\Delta E/E$ nearly follows the cross-correlation of the excitation and probe pulses. But there is a small noninstantaneous component, which we attribute to the collision-induced mechanism [128-130]. Knowing the symmetry properties, one can also reconstruct one of the polarization measurement from the other two. For example, the perpendicular polarization measurement can be reconstructed by $\frac{3}{2}\Delta n_{\text{magic}} - \frac{1}{2}\Delta n_{\parallel}$, as shown in Figure 4.3 (b).

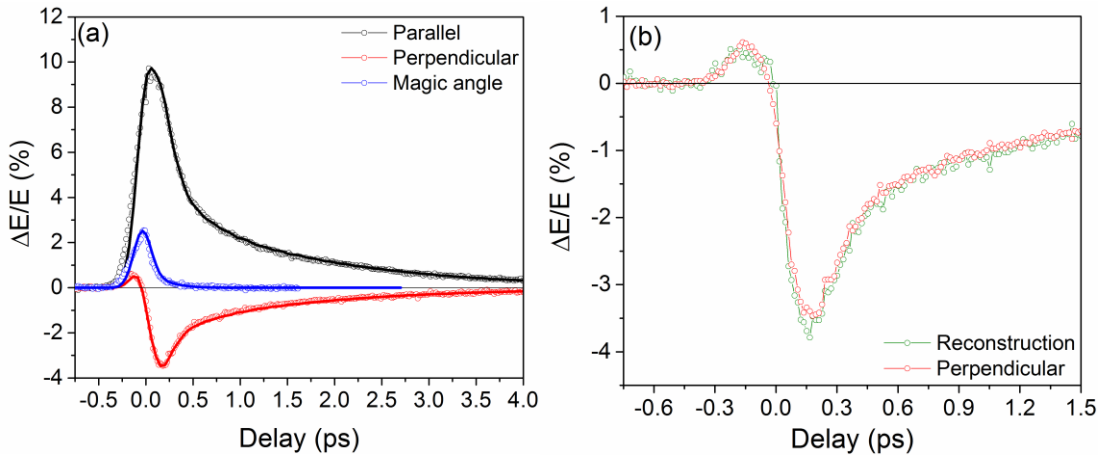

Figure 4.3 Data (circles) and fit (lines) of BD measurement of CS_2 for parallel (black), (red) perpendicular, and (blue) magic angle polarizations; (b) reconstruction of perpendicular polarization measurement using the data from parallel and magic angle polarizations, considering isotropic and reorientational symmetry properties.

Table 4.2 Fit parameters of the response function of CS_2[a,b]

Mechanism	$n_{2,m}$	$\tau_{r,m}$ (fs)	$\tau_{f,m}$ (fs)
Electronic	1.5	Instantaneous	
Collisional	0.8	150 ± 50	140 ± 50
Librational	7.2	*	450 ± 100
Reorientational	18	150 ± 50	1610 ± 50

[a] $n_{2,m}$ are given in the units of 10^{-19} m^2/W;
[b] $\omega_0 = 8.5 \pm 1.0$ ps^{-1}, $\sigma = 5 \pm 1$ ps^{-1}.

The polarization dependence determined from BD measurements allows unambiguous determination of the NLO response function of each mechanism. First, based on the BD signal at the magic angle, bound-electronic and collisional NLR can be resolved by fitting the slightly asymmetric cross-correlation signal. Then the parallel and perpendicular results can be used together to fit the librational and reorientational responses. For CS_2, the NLO response functions are resolved for each mechanism and the fit parameters are shown in Table 4.2. Errors in $n_{2,m}$ (~20%) are estimated from the irradiance uncertainty. Here, we do not fit the vibrational component since the bandwidth of the excitation pulse does not overlap with the first vibrational transition.

4.3. Nonlinear Response Functions of Common Solvents

Using polarization-resolved Beam Deflection and the methodology we developed with the work on liquid CS_2 [17], we embark on the characterizations of the NLO response functions for many commonly used organic solvents with the purpose to establish self-consistent references for various NLO applications. Thus far, we have studied another 23 widely used solvents, which are selected from different families including benzene derivatives, alkanes, halo-alkanes, alcohols, ketones, nitriles, esters, ethers, formamides and others. These 23 solvents are benzene, nitrobenzene, toluene, dichlorobenzene, xylene, dichloromethane, chloroform, carbon tetrachloride, hexane, cyclohexane, methanol, ethanol, butanol, 1-octanol, acetone, acetonitrile, butyl salicylate, tetrahydrofuran, pyridine, dimethyl sulfoxide, dimethylformamide, water and heavy water.

In this section, the experimental results from BD measurements with polarization dependence are presented. The fit parameters for the full response function of each solvent are summa-

rized in Table 4.3, which are closely related with the molecular structures of the solvents themselves. The comparison between measured values of reorientational $n_{2,r}$ and theoretical values calculated from linear polarizability tensors in Eq. (4.12) is also given.

4.3.1. Experimental Results

The BD measurements on selected solvents are all conducted using 1 mm path length quartz cuvettes using identical experimental conditions as for the CS_2 experiments measured via the filtered WLC probe as shown in Figure 4.3 (a). Therefore, CS_2 with known parameters stands as a reference material to ensure the system is properly aligned and calibrated during the measurements from one material to another. All the solvents are measured using ~ 20 μJ of excitation pulse energy. It should be noted that the contribution from the cuvette is more significant in most solvents than for CS_2 due to their smaller nonlinearities, which must be measured separately and subtracted.

4.3.1.1. Benzene Derivatives

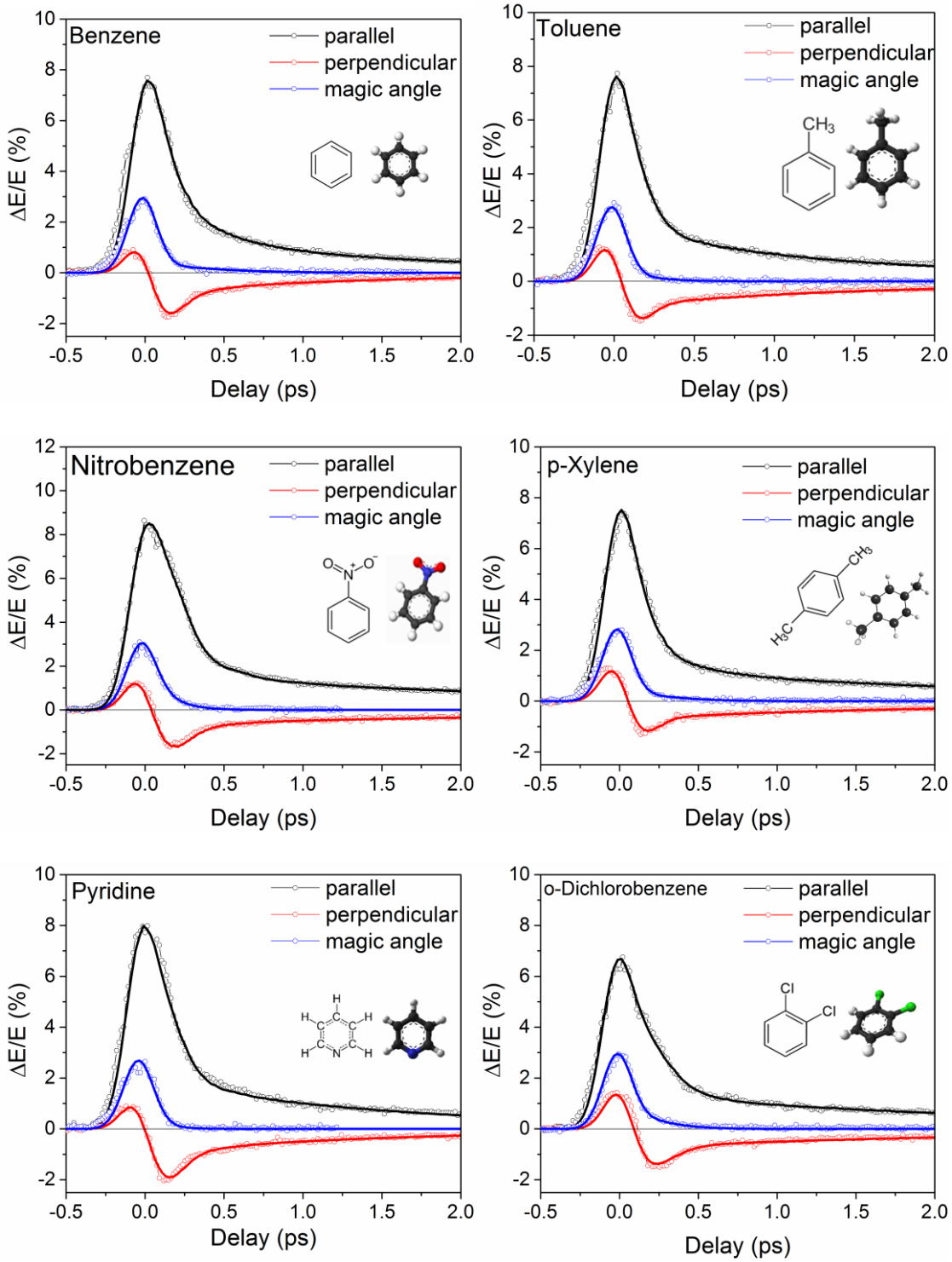

Figure 4.4 BD measurements (circles) with fits (lines) of benzene, toluene, nitrobenzene, p-xylene, pyridine and o-dichlorobenzene for parallel (black), perpendicular (red), and magic angle (blue) polarizations.

The results from benzene derivatives in Figure 4.4 show very similar NLR temporal dynamics. Basically, the molecules with large anisotropy in their polarizabilities usually have large $n_{2,l}$ and $n_{2,r}$ (see Table 4.3), resulting in a universal temporal dynamics, i.e. in the parallel polarized case, an instantaneous response is followed by a quickly damped librational response, and then the slow exponential decaying response from molecular reorientation dominates for longer delays. In this case, the benzene is a cyclic molecule with aromaticity, which results in a planar structure such that the polarizabilities parallel to the plane of the benzene ring is much larger than that in the perpendicular direction [131], as shown later in Table 4.4. On the other hand, cyclohexane is also a cyclic molecule with six carbon atoms, but they are combined with single bonds without π electrons, and are free to rotate. Different from benzene, cyclohexane naturally has a twisted structure, e.g. chair or boat conformations, which leads to a small anisotropy in polarizability [131]. As shown in Figure 4.7 with fit parameter in Table 4.3, the measured $n_{2,l}$ and $n_{2,r}$ for cyclohexane is much smaller than for benzene.

From the derivatives we have studied, the benzene moiety plays a significant role in the overall nonlinearity of the molecule, but effects from certain substitutions are also considerable. For example, the overall effects from methyl-group substitutions, i.e. toluene and p-xylene are very small, with the fit parameters showing the same values of $n_{2,el}$ and slightly larger $n_{2,r}$. This indicates methyl substitutions introduce negligible electronic interaction, but slightly increase the polarizability anisotropy as agrees with theory [131]. For derivatives with heavier substitutions i.e. nitrobenzene and o-dichlorobenzene, the reorientational NLR response is significantly altered. In o-dichlorobenzene, a significant difference appears in the changes of the resonance frequency and bandwidth of the librational motion. In nitrobenzene, $n_{2,r}$ becomes much larger, and its associated diffusive reorientational lifetime is also longer. Measurements with long delays may be required

to more precisely resolve this long decay time constant. However, the values of $n_{2,el}$ measured from both derivatives do not differ from benzene, indicating less electronic interaction. A smaller $n_{2,el}$ is measured when benzene includes an ester group substitution, i.e. butyl salicylate, as shown in Figure 4.7 with fit parameters in Table 4.3. This may be because the ester- and hydrocarbon (ortho) groups are closely patterned, resulting in shared electrons which significantly changes the electronic structure of benzene. To understand the effects of benzene substitutions on the bound-electronic NLR, rigorous analysis of the electronic structure and calculations of the second hyperpolarizabilities may be needed [33, 132, 133].

4.3.1.2. Tetrahedral Alkanes

The BD measurements of dichloromethane, chloroform and carbon tetrachloride are shown in Figure 4.5 with their polarization dependence. These three molecules all have similar tetrahedral geometries but with different numbers of H (or Cl) atoms, which will affect their nonlinear responses in both electronic and nuclear NLR. First, the asymmetrical structure in dichloromethane (CH_2Cl_3) and chloroform ($CHCl_3$) leads to anisotropic polarizabilities, from which the librational and reorientational NLR are measured in BD experiments shown as the typical noninstantaneous contribution that decays in several picoseconds. These reorientational related responses become zero in carbon tetrachloride (CCl_4), which is a highly symmetric molecule with absolutely zero polarizability anisotropy, i.e. $\alpha_{\overline{xx}} = \alpha_{\overline{yy}} = \alpha_{\overline{zz}}$, which results in $n_{2,r} = 0$ based on Eq. (4.12).

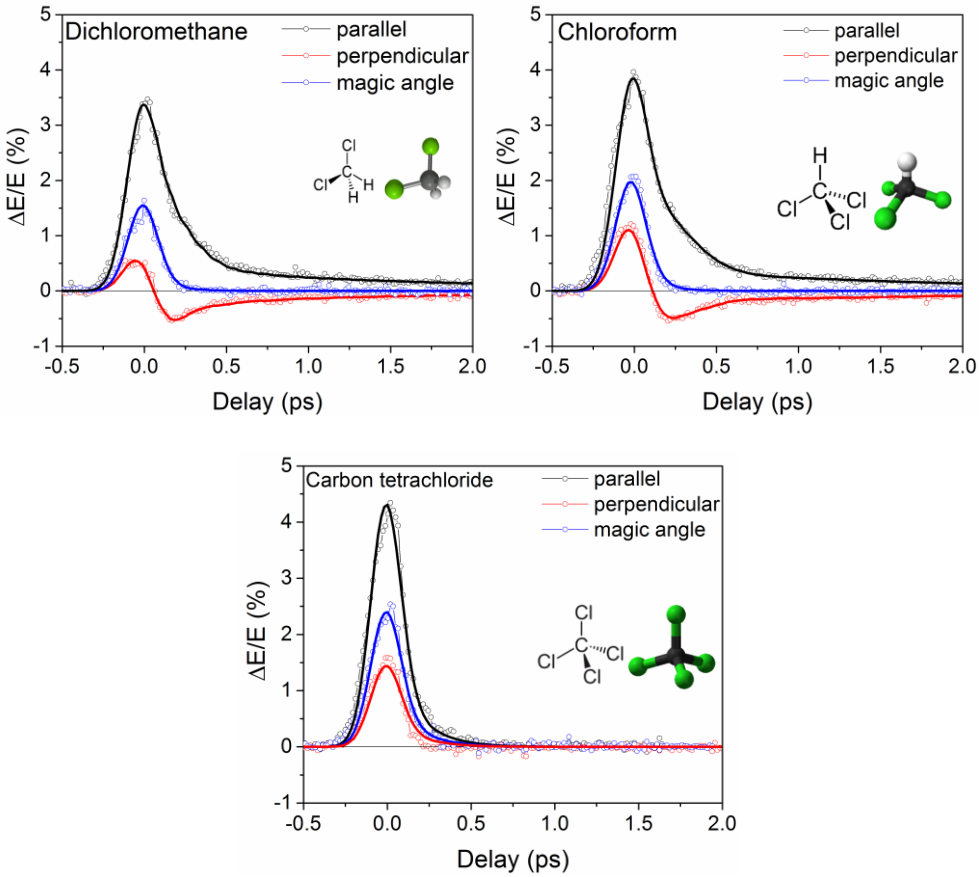

Figure 4.5 BD measurements (circles) with fits (lines) of dichloromethane, chloroform and carbon tetrachloride for parallel (black), perpendicular (red), and magic angle (blue) polarizations.

Comparing the electronic NLR, we found the measured $n_{2,el}$ increases as we increase the number of C–Cl bonds, i.e. $n_{2,el}(\mathrm{CCl_4}) > n_{2,el}(\mathrm{CHCl_3}) > n_{2,el}(\mathrm{CH_2Cl_2})$. One of the reason may be the bond hyperpolarizability of C–Cl is higher than that of C–H [134].

4.3.1.3. Alcohols

Interestingly, the alcohols are all asymmetric molecules, but they do not show an obvious reorientational response on the time scale of the pulsewidth, as shown in Figure 4.6. A small librational response is barely resolved by utilizing the large impact of the reorientational symmetry parallel

and perpendicular results. This is because alcohols are single-bond molecules without conjugation, so the polarizability along the molecular axis is not significantly larger than along other directions [131], leading to a small anisotropy. For example, as shown in Table 4.4, the $n_{2,r}$ calculated from the polarizability tensor of ethanol using Eq. (4.12) is ~ 8× smaller than for dichloromethane and ~ 24× smaller than for benzene. The BD measured results of other solvents are shown in Figure 4.7, with all the fit parameters for each NLO response function summarized in Table 4.3.

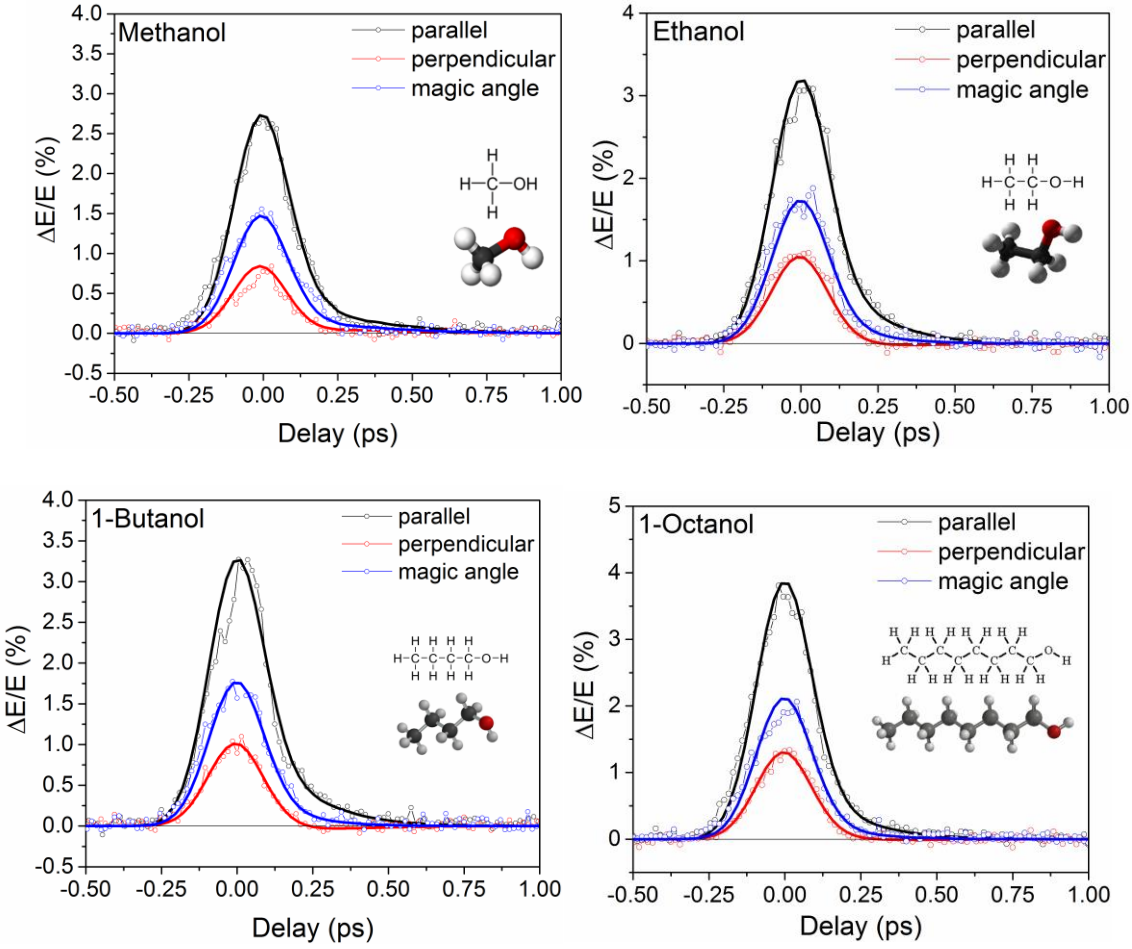

Figure 4.6 BD measurements (circles) with fits (lines) of methanol, ethanol, butanol and 1-octanol for parallel (black), perpendicular (red), and magic angle (blue) polarizations.

4.3.1.4. Miscellaneous Families

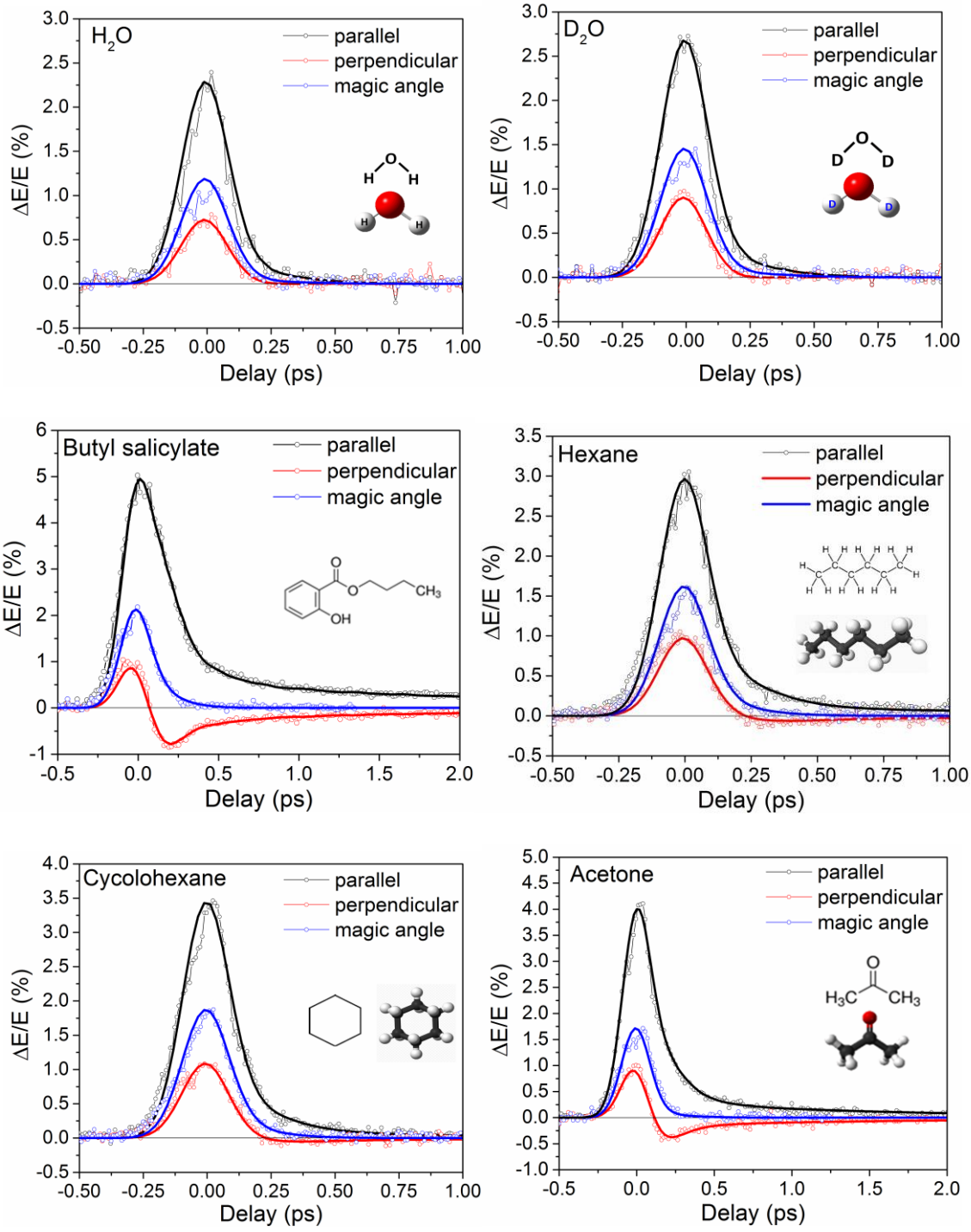

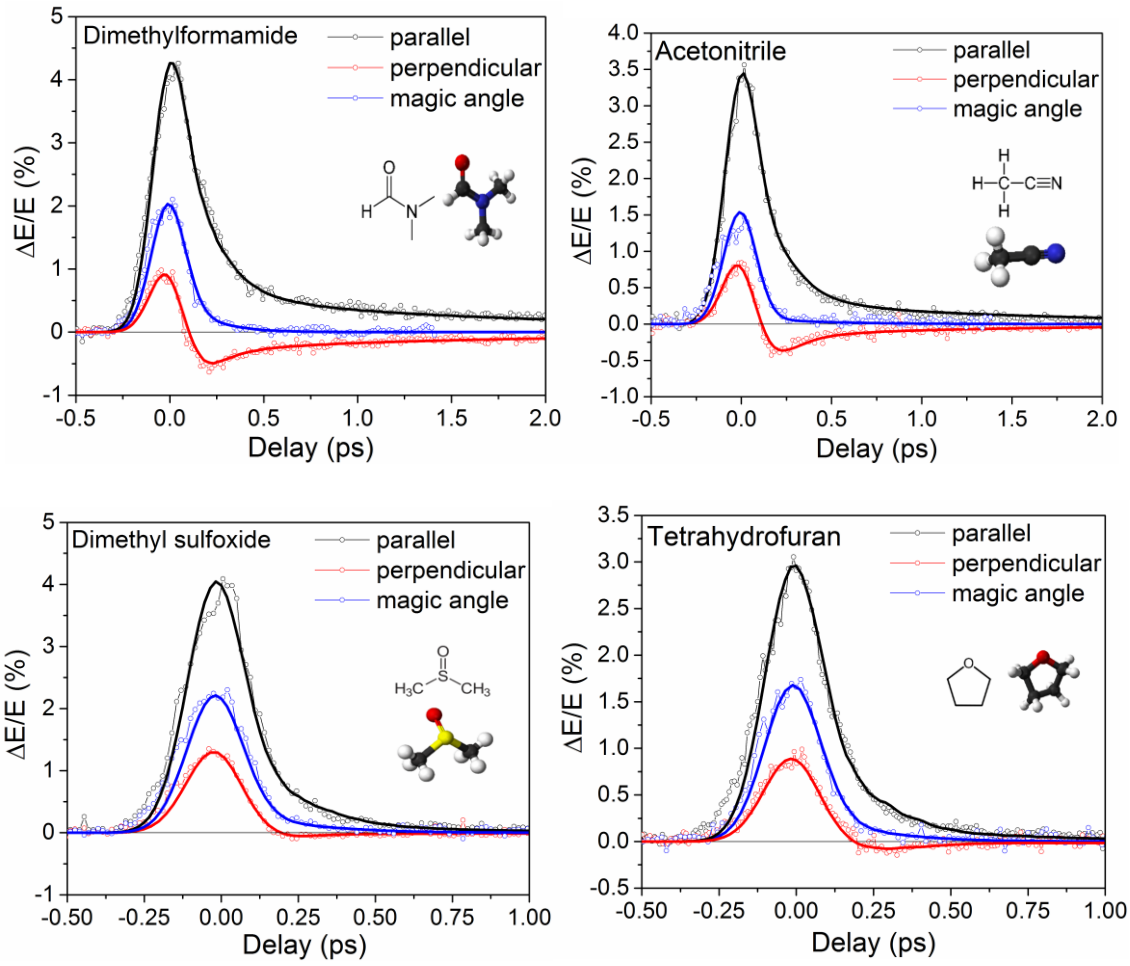

Figure 4.7 BD measurements (circles) with fits (lines) of hexane, cyclohexane, acetone, acetonitrile, butyl salicylate, tetrahydrofuran, dimethyl sulfoxide, dimethylformamide, water and heavy water for parallel (black), perpendicular (red), and magic angle (blue) polarizations.

Table 4.3 Fit parameters of nonlinear response function of solvents[a,b]

	$n_{2,el}$	$n_{2,c}$	$\tau_{r,c}$ / $\tau_{f,c}$	$n_{2,l}$	ω_0 / σ	$\tau_{f,l}$	$n_{2,r}$	$\tau_{r,r}$ / $\tau_{f,r}$
Toluene	0.60	0.12	250±100 / 200±100	1.2	11±2 / 8±2	350±100	3	250±50 / 2100±500
Nitrobenzene	0.60	0.35	200±100 / 100±50	1.7	5±2 / 9±2	400±100	5	100±50 / 3500±500
Benzene	0.60	0.25	250±100 / 200±100	1.2	11±2 / 8±2	250±100	2.3	100±50 / 1500±400
p-Xylene	0.62	0.2	250±100 / 200±100	1.1	11±2 / 6±2	350±100	3.3	250±100 / 2600±500

	$n_{2,el}$	$n_{2,c}$	$\tau_{r,c}$ / $\tau_{f,c}$	$n_{2,l}$	ω_0 / σ	$\tau_{f,l}$	$n_{2,r}$	$\tau_{r,r}$ / $\tau_{f,r}$
Pyridine	0.60	0.05	250±100 100±50	1.5	12±2 8±2	350±100	3.1	250±100 1800±500
Dichloro-methane	0.3	0.05	200±50 100±50	0.4	7±2 4±2	250±100	0.75	100±50 1800±500
Chloroform	0.41	0.08	100±50 100±50	0.4	5±2 2±1	250±100	0.75	250±100 1800±500
Carbon tetrachloride	0.48	0.2	100±50 150±50	0	N/A N/A	N/A	0	N/A N/A
o-Dichloroben-zene	0.60	0.3	200±50 200±50	1	3±1 10±2	150±50	3.2	100±50 2500±500
Acetone	0.4	0.05	100±50 150±50	0.3	5±2 6±2	200±100	0.45	100±50 1500±500
Dimethylforma-mide	0.4	0.15	100±50 150±100	0.4	8±2 6±2	350±100	1.1	100±50 2000±500
Acetonitrile	0.35	0.05	100±50 150±50	0.25	5±2 6±2	200±100	0.4	100±50 1800±500
Dimethyl sulfoxide	0.45	0.13	400±100 150±50	0.14	4±2 6±2	250±100	0.1	100±50 2500±500
Tetrahydrofuran	0.32	0.1	200±100 150±50	0.12	4±2 8±2	350±100	0.08	100±50 2000±1000
Hexane	0.32	0.1	200±100 100±50	0.08	3±1 5±2	150±50	0.2	200±50 2000±1000
Cyclohexane	0.35	0.1	200±100 100±50	0.07	5±2 4±2	350±100	0.07	200±100 1500±500
Butyl salicylate	0.38	0.25	200±100 100±50	0.7	5±2 9±2	450±100	1.3	100±50 2500±500
1-Octanol	0.4	0.06	200±100 100±50	0.03	2±1 2±1	150±100	0	N/A N/A
1-Butanol	0.33	0.06	200±100 100±50	0.05	3±1 2±1	150±100	0	N/A N/A
Ethanol	0.32	0.06	200±100 100±50	0.04	4±2 6±2	150±100	0	N/A N/A
Methanol	0.28	0.1	200±100 200±100	0.04	14±2 2±1	350±100	0	N/A N/A
D_2O	0.28	0.05	200±100 150±100	0.04	2±1 2±1	100±50	0	N/A N/A
H_2O	0.25	0.03	200±100 150±100	0.04	2±1 2±1	100±100	0	N/A N/A

*$n_{2,m}$ are given in the units of 10^{-19} m^2/W; $\tau_{r,m}$ and $\tau_{f,m}$ are given in units of fs; $\omega_0$and σ are given in units of ps^{-1}.

4.3.2. Comparisons of Theory and Experiment

The NLO response function of solvents measured from BD experiments provides NLR coefficients due to both electronic and reorientational origins, which are useful to compare to the values predicted by theoretical models. First, from the measured $n_{2,el}$, the derived electronic second hyperpolarizability $\langle\gamma\rangle$ from Eq. (4.5) with a Lorentz-Lorenz local field correction factor serves as a comparison of $\langle\gamma\rangle$ measured in the gas phase, which will be discussed with more details in 5.3. . Here, the comparison between measured reorientational $n_{2,r}$ and theoretical values calculated from the polarizability tensor using Eq. (4.12) is shown in Table 4.4 for selected solvents.

Table 4.4 Reorientational $n_{2,r}$ comparison between theoretical and experimental values[a,b,c]

Solvents	$\alpha_{\overline{xx}}$	$\alpha_{\overline{yy}}$	$\alpha_{\overline{zz}}$	$f^{(3)}$	$n_{2,or}$ theory	$n_{2,or}/f^{(3)}$ theory	$n_{2,r}$ experiment
CS_2	6.2	6.2	16.8	5.3	54.3	10.2	18
Benzene	7.1	13.7	13.7	3.8	11.7	3.0	2.3
p-Xylene	9.8	17.3	20.2	4.0	16.9	4.3	3.3
o-dichlorobenzene	10.0	16.6	20.7	4.6	20.4	4.4	3.2
Pyridine	6.4	12.0	13.2	4.1	12.2	3.0	3.1
Toluene	8.2	15.1	17.2	4.0	15.5	3.8	3.0
Nitrobenzene	8.6	14.7	19.8	4.5	23.7	5.2	5.0
Dichloromethane	5.6	6.7	9.3	3.3	3.7	1.1	0.75
Chloroform	7.5	10.5	10.5	3.4	2.5	0.73	0.75
Acetone	5.4	7.9	7.9	2.7	1.6	0.6	0.45
Acetonitrile	4.3	4.3	6.4	2.6	1.7	0.65	0.4
Cyclohexane	10.5	13.3	13.4	3.3	1.5	0.45	0.07
Ethanol	4.9	5.4	6.3	2.8	0.5	0.18	0
Methanol	2.9	3.6	4.5	2.5	0.9	0.37	0

[a] $n_{2,r}$ are given in the units of 10^{-19} m^2/W;
[b] $\alpha_{\overline{xx}}$, $\alpha_{\overline{yy}}$ and $\alpha_{\overline{zz}}$ values from [131, 135, 136]are given in the units of 10^{-40} Fm^2;
[c] Theoretical $n_{2,or}$ is calculated from Eq. (4.12), and the experimental $n_{2,r}$ is from Table 4.3.

The values of polarizability tensors in three dimensions, i.e. $\alpha_{\overline{xx}}$, $\alpha_{\overline{yy}}$ and $\alpha_{\overline{zz}}$ are taken from [131, 135, 136] and converted from Gaussian to SI units, where their definition of orientations w.r.t. the principle axes of the molecular structures are given. The number density in Eq. (4.12) is calculated by $N = N_A \cdot \rho / M_A$, where ρ the room temperature density, M_A is the molar mass of the molecule and N_A is the Avogadro's number. As shown in Table 4.4, the theoretical values without taking into account the Lorentz-Lorenz local field correction factor, i.e. $n_{2,or}/f^{(3)}$ results in better agreement with experimental measurements.

4.4. Applications of NLO Response Functions

With the knowledge of the NLO response function of solvents, we are able to predict the effective NLR coefficient, $n_{2,\text{eff}}$, defined in Table 2.4 for single beam experiments such as Z-scan, where the index change is averaged temporally over the pulse irradiance [17]. This results in a pulsewidth dependence of $n_{2,\text{eff}}$. The NLO response function of solvents also helps interpret experimental results from solution measurements, where the NLR signals contributed from both solvent and organic dyes need to be separated.

Based the NLO response functions from Beam Deflection measurements, the pulsewidth dependence of $n_{2,\text{eff}}$ for 24 solvents are calculated. In Figure 4.8 (a), the prediction for CS_2 is compared to experimental results from Z-scan measurements with the pulsewidth varied over three orders of magnitude [17], i.e. from 30 fs up to ~ 25 ps. The prediction from BD measured NLO response functions with parameters in Table 4.2 shows good agreement without any fitting parameters, which further validates the measurements. For short pulses (< 50 fs), only the bound-electronic nonlinearity contributes significantly ($n_{2,\text{eff}} \cong n_{2,el}$) due to its nearly instantaneous nature.

The noninstantaneous nuclear nonlinearities, particularly librational and reorientational responses, can increase or even dominate $n_{2,\text{eff}}$ for longer pulsewidths. The pulsewidth dependence of $n_{2,\text{eff}}$ also helps us to understand the large discrepancies in the literature reported n_2 values of CS2 [1-16], discussed previously in Figure 1.1. By plotting $n_{2,\text{eff}}$ w.r.t. the pulsewidth used in the particular experiment, the prediction greatly reduces the scatter of the data.

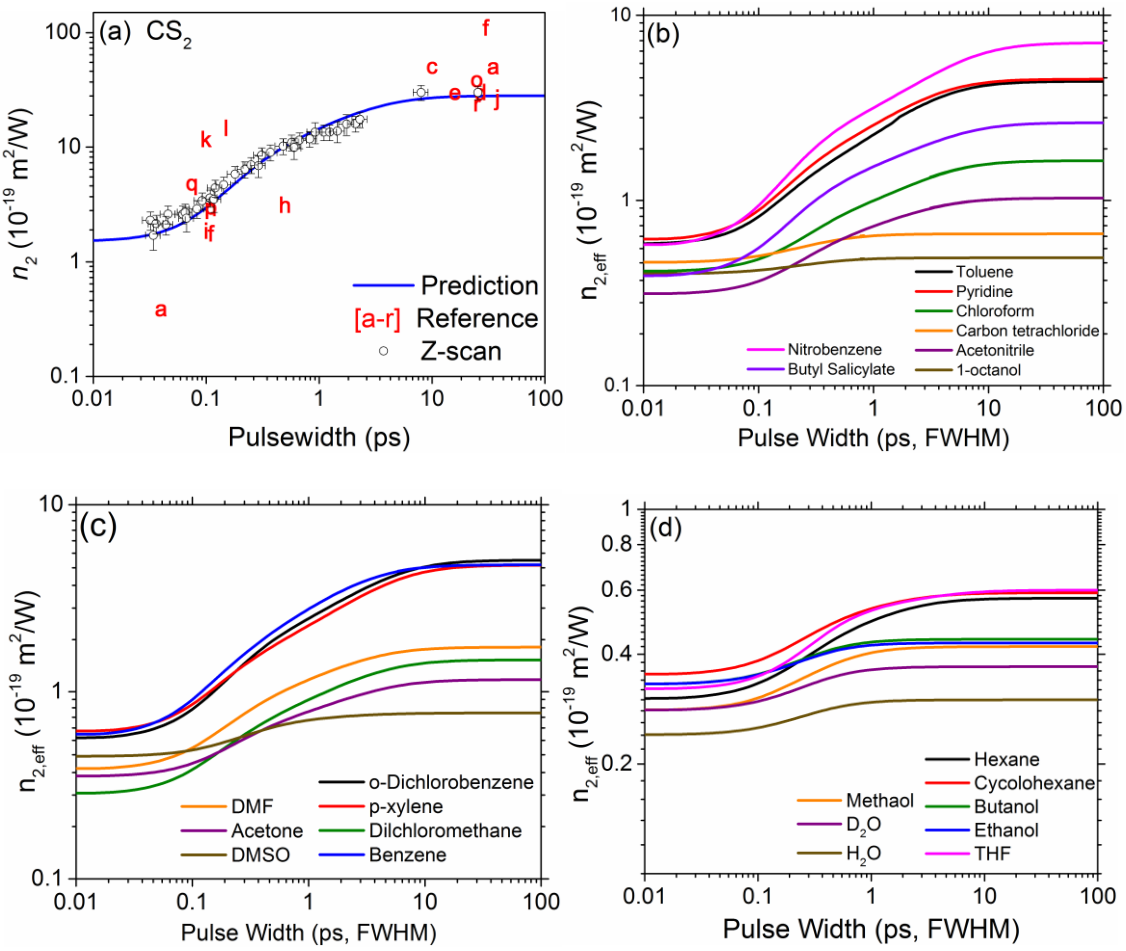

Figure 4.8 Predictions of pulsewidth dependent $n_{2,\text{eff}}$ of (a) CS_2 using parameters in Table 4.2, which is compared to Z-scan measurements in [17], as well as literature values a-r taken from [1-16]; (b-c) predictions of the other 23 solvent molecules using parameters in Table 4.3.

Based on the same methodology, we calculate the pulsewidth dependence of $n_{2,\mathrm{eff}}$ for the other 23 solvent molecules using $n_{2,\mathrm{eff}}$ BD measured NLO response with parameters in Table 4.3. The $n_{2,\mathrm{eff}}$ of the benzene derivatives at longer pulsewidths (>10 ps) increases nearly ~ 8× over the short pulse limit, primarily owing to their large $n_{2,l}$ and $n_{2,r}$. Carbon tetrachloride and alcohols with zero or negligible reorientational nonlinearities do not show a considerable increase of $n_{2,\mathrm{eff}}$ for longer pulsewidths. Other NLO experiments such as Z-scan can be used to verify such predictions from BD measurements.

CHAPTER 5: TRANSIENT NONLINEAR REFRACTION OF MOLECULAR GASES[2]

A molecular gas with an anisotropic polarizability exhibits nonlinear refraction (NLR) that originates from a nearly instantaneous bound-electronic response and a noninstantaneous response from field-induced molecular rotation [20, 93, 118, 137, 138]. The NLO response of gas phase molecules is significantly different from its liquid phase for both nuclear and bound-electronic contributions. First, the strong intermolecular interactions in liquids hinders the induced rotation, giving an overdamped response that returns (exponentially decays) to equilibrium without oscillating, as discussed in 4.1.2. . But in dilute gases where the damping (i.e. librational and collisional contributions) is small, the induced rotation after impulsive alignment is able to continue to rotate at frequencies depending on the quantized rotational energies, and the transient refractive index change, $\Delta n(t)$, can be derived from the net alignment of the molecular ensemble. With many rotational modes being excited in phase with a short pulse, the net alignment of rotating molecules results in $\Delta n(t)$ "pulses", which is also known as rotational revivals, as discussed in 5.1. [21, 72, 139]. Additionally, the Lorentz-Lorenz local field in the liquid phase causes an enhancement factor $f^{(3)}$ to $n_{2,el}$, which becomes negligible ($f^{(3)} = 1$) for dilute gases [31, 32]. Gas phase measurements thus allow us to directly measure the second hyperpolarizability, γ, of isolated molecules without the need for local-field correction, which is important to compare to theoretical models [33]. This also allows a direct γ comparison of solvent molecules measured in liquid and gas phases [17, 93].

[2]This work is collaborated with Matthew Reichert. Some of the results are also included in Ref. [140].

Several time-resolved techniques based on the excite-probe type geometry have been applied to measure transient NLR of molecular gases, where an excitation pulse induces rotation of the molecules, and another pulse coming at a variable delay probe the transient phase shift, or $\Delta n(t)$, of the molecular ensemble. One of the earliest experimental studies used OKE to measure the rotational revivals in gaseous CS_2, where the measured revival period showed good agreement with theory [19, 20]. A more recent work applied DFWM measurements on a very low density CS_2 gas. The results resolve the rotational and centrifugal distortion constants with very high precision [72]. The transient phase change can also be measured via interferometric techniques[106], where a reference pulse is usually needed to interfere with the probe. More recently, Milchberg et al. developed a single-shot technique which windows one of the revivals with a picosecond pulse [76, 139, 141]. Therefore, this technique is less sensitive to environmental perturbations than traditional interferometry. Alternatively, the time-resolved coulomb explosion imaging measures the angular distribution of the velocities of the ions induced by an optical pulse, from which the molecular alignment can be derived [142, 143]. But this technique does not provide information on Kerr nonlinearities such as the bound-electronic NLR.

In this chapter, we apply our Beam deflection (BD) technique to measure the transient NLR of gas-phase CS_2 and major constituents (N_2 and O_2 mixture) of ambient air [93]. Much like the previous application in solvent measurements, BD holds several advantages over other techniques. First, unlike the OKE and DFWM, BD gives both magnitude and sign of the refractive index change without the need of OHD [17]. With the polarization dependence (see 4.2.2.), BD separates the bound-electronic response from rotational revivals, allowing unambiguous determination of the electronic second hyperpolarizability. Similar with other techniques, BD also measures the

rotational revivals up to many periods, resolving the rotational constants, dephasing rate, and allows reconstruction of the rotational Raman spectrum using a Fourier transform.

5.1. Transient Rotational NLR of Linear Molecules

As discussed in 4.1.2. , for molecules with anisotropic polarizabilities, the nonlinear refraction due to molecular rotation is due to changes in the ensemble averaged linear polarizability $\langle\alpha\rangle$, which is related to refractive index in Eq. (4.7). Following the same geometries in Figure 4.1, $\langle\alpha\rangle$ seen by an incident beam polarized along $\vec{\boldsymbol{e}}_z$ is $\langle\alpha_{\overline{xx}}\sin^2\theta\cos^2\psi + \alpha_{\overline{yy}}\sin^2\theta\sin^2\psi + \cos^2\theta\,\alpha_{\overline{zz}}\rangle$, which is reduced to $\langle(\alpha_{\overline{zz}} - \alpha_{\overline{xx}})\cos^2\theta + \alpha_{\overline{xx}}\rangle$ for a linear molecule, with $\alpha_{\overline{zz}}$ parallel and $\alpha_{\overline{xx}} = \alpha_{\overline{yy}}$ perpendicular to the molecular axis respectively. Here $\Delta\alpha = \alpha_{\overline{zz}} - \alpha_{\overline{xx}}$ is known as the polarizability anisotropy. Substituting these values of $\langle\alpha\rangle$ into Eq. (4.7) yields

$$n^2(t) = 1 + \frac{N}{\varepsilon_0}(\Delta\alpha\langle\cos^2\theta(t)\rangle + \alpha_{\overline{xx}}), \tag{5.1}$$

where $\langle\cos^2\theta(t)\rangle$ is known as the transient degree of alignment, which is $1/3$ for randomly distributed molecules, i.e. at $t \to 0$ or ∞. Upon perturbation from the incident pulse, the degree of alignment deviates from the equilibrium value of $1/3$, which results in the transient $\Delta n(t)$ due to molecular rotation. Assuming a small change in refractive index, $n(t)^2 - n(0)^2 = \big(n_0 + \Delta n_{rot}(t)\big)^2 - n_0^2 \cong 2n_0\Delta n_{rot}(t)$, which leads to

$$\Delta n_{rot}(t) = \frac{N\Delta\alpha}{2\varepsilon_0 n_0}\left(\langle\cos^2\theta(t)\rangle - \frac{1}{3}\right). \tag{5.2}$$

Therefore, $\Delta n_{rot}(t)$ is directly proportional to the change in the angularly averaged degree of alignment, i.e. $\left(\langle\cos^2\theta(t)\rangle - \frac{1}{3}\right)$, and calculation of the time evolution of $\langle\cos^2\theta(t)\rangle$ after the impulsive alignment is the key to describe the transient NLR from molecular rotation.

5.1.1. Density Matrix Formulism

The rotational states are essentially quantized, and the energy associated with the eigenstates $|J, M\rangle$ are usually defined as $\mathrm{E}_J = hcBJ(J+1) - hcDJ^2(J+1)^2$, where J and M (projection of J onto the laboratory frame $\boldsymbol{z}$ in Figure 4.1 (a)) are rotational quantum numbers which denotes the polynominal degrees of spherical harmonic wavefunctions [144]. B and D are known as rotational and centrifugal distortion constants derived from the moment of inertia [144].

Upon a nonreasonant excitation from an optical pulse with sufficient bandwidth, a transition is induced between the initial state $|J, M\rangle$ and an adjacent state $|J', M'\rangle$ via stimulated Raman scattering [20]. Since it is a two-photon transition process between two states with definite parity, the selection rule follows $J' - J = \pm 2$, and $M' - M = 0$ for a linear molecule [20, 139], as shown in Figure 5.1. This process essentially imposes a certain phase relation, or coherence, between two rotational eigenstates within one single molecule, and this coherence become manifest in the temporal behavior of the resulting superposition which evolves at the corresponding Raman frequency, i.e. $\omega_{JJ'} = \frac{\mathrm{E}_{J'} - \mathrm{E}_J}{\hbar} \approx 2hcB(2J+3)$. This coherence decays depending upon intermolecular events such as collisions, which is usually characterized by a dephasing time constant T_2.

This two-quantum coherence produced by stimulated Raman transitions can be viewed as an interaction between an electromagnetic (EM) field with an induced dipole moment $\overrightarrow{\boldsymbol{\mu_1}}$, from which the energy potential is derived. It should be distinguished from one-quantum coherence between $|J\rangle$ and $|J+1\rangle$ created in polar molecules through an electromagnetic field interacting with a permanent dipole moment $\overrightarrow{\boldsymbol{\mu_0}}$, i.e. using a terahertz (THz) field that is resonant with a rotational transition frequency [123, 124].

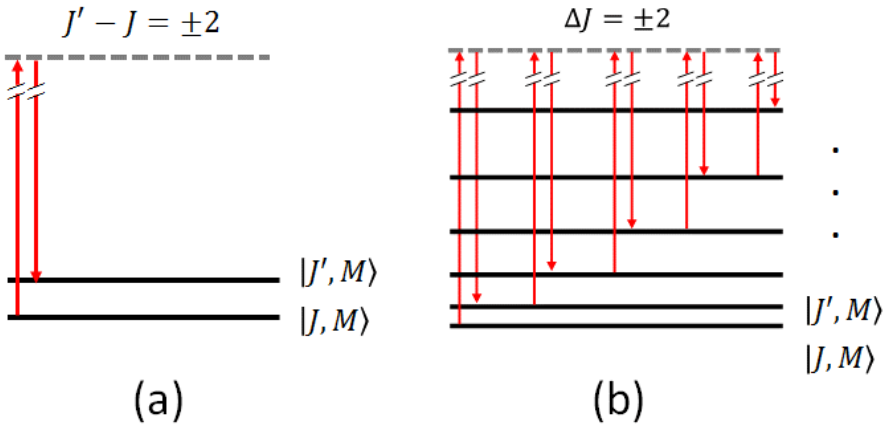

Figure 5.1 (a) Nonresonant Raman transition between $|J, M\rangle$ and $|J', M'\rangle$ with following selection rule of $\Delta J = \pm 2$, and $\Delta M = 0$; (b) coherent Raman excitation of many rotational states.

In real measurements, many molecules are involved and they initially do not start with the same rotational state. Upon a short pulse excitation, multiple Raman transitions occur simultaneously, producing many superpositions in phase, as shown in Figure 5.1 (b). In the case that we do not have knowledge to track the evolution of each molecule in a precise manner, the density matrix formulism needs to be used to describe the "system" (mixed states) in a statistical sense [31, 145]. Here, we define the elements of the density matrix of the system as ρ_{mn} to describe the Raman transitions between two levels, where the sub-indices m and n are meant to run over all the rotational eigenstates, i.e. $|J, M\rangle$.

$$\hat{\rho} = \begin{bmatrix} \rho_{mm} & \rho_{mn} \\ \rho_{nm} & \rho_{nn} \end{bmatrix} \tag{5.3}$$

where the diagonal element, i.e. ρ_{mm}, gives the probability of the "system", or the probability distribution of all eigenstates. The off-diagonal elements, i.e. ρ_{nm}, give the coherence between two eigenstates, which is zero for the initial unperturbed system and will be nonzero if the system is in a superposition of states after Raman excitation. To evaluate the time evolution of the density matrix after Raman excitation, we follow

$$\frac{d\rho}{dt} = -\frac{i}{\hbar}\left[\hat{H}, \hat{\rho}\right], \tag{5.4}$$

where [,] denotes the commutator, i.e. $\left[\hat{H}, \hat{\rho}\right] = \hat{H}\hat{\rho} - \hat{\rho}\hat{H}$; $\hat{H}$ is the total Hamiltonian with the perturbation originating from the interaction of the induced dipole moment $\overrightarrow{\boldsymbol{\mu_1}}$ with the electric field $\vec{\boldsymbol{E}}(t)$

$$\hat{H} = \begin{bmatrix} \mathrm{E}_m & -\overrightarrow{\boldsymbol{\mu_d}} \cdot \vec{\boldsymbol{E}}(t) \\ -\overrightarrow{\boldsymbol{\mu_d}} \cdot \vec{\boldsymbol{E}}(t) & \mathrm{E}_n \end{bmatrix}, \tag{5.5}$$

where E_m and E_n are eigenenergies of two unperturbed rotational states, and $\overrightarrow{\boldsymbol{\mu_d}}$ denotes the off-diagonal element of the dipole operator $\widehat{\boldsymbol{\mu_1}}$. From previous discussion, $\widehat{\boldsymbol{\mu_1}}$ is associated with the projected polarizability operator as

$$\widehat{\boldsymbol{\mu_1}} = \begin{bmatrix} 0 & \overrightarrow{\boldsymbol{\mu_d}} \\ \overrightarrow{\boldsymbol{\mu_d}} & 0 \end{bmatrix} = \widehat{\langle\alpha\rangle}\vec{\boldsymbol{E}}(t) = \left(\widehat{\langle\cos^2\theta\rangle}\Delta\alpha + \hat{\delta}\alpha_{\overline{xx}}\right)\vec{\boldsymbol{E}}(t), \tag{5.6}$$

where $\hat{\delta}$ is the unity matrix. Therefore, $\overrightarrow{\boldsymbol{\mu_d}}$ can be derived by evaluating the off-diagonal elements, i.e. $\Delta\alpha\left\langle m\middle|\widehat{\langle\cos^2\theta\rangle}\middle|n\right\rangle\vec{\boldsymbol{E}}(t)$. Substituting Eqs. (5.3) and (5.5) into the right-hand side of Eq. (5.4) yields

$$\frac{d\rho}{dt} = \frac{i}{\hbar}\begin{bmatrix} -\overrightarrow{\boldsymbol{\mu_d}} \cdot \vec{\boldsymbol{E}}(\rho_{mn} - \rho_{nm}) & (\mathrm{E}_n - \mathrm{E}_m)\rho_{mn} - \overrightarrow{\boldsymbol{\mu_d}} \cdot \vec{\boldsymbol{E}}(\rho_{mm} - \rho_{nn}) \\ (\mathrm{E}_m - \mathrm{E}_n)\rho_{nm} - \overrightarrow{\boldsymbol{\mu_d}} \cdot \vec{\boldsymbol{E}}(\rho_{nn} - \rho_{mm}) & -\overrightarrow{\boldsymbol{\mu_d}} \cdot \vec{\boldsymbol{E}}(\rho_{nm} - \rho_{mn}) \end{bmatrix} \tag{5.7}$$

Here, we particularly focus on the time evolution of off-diagonal elements, i.e. ρ_{mn}, which corresponds to the coherence built in two eigenstates. Replacing $\overrightarrow{\boldsymbol{\mu_d}}$ based on Eq. (5.6), we obtain

$$\frac{d\rho_{mn}}{dt} = \frac{i}{\hbar}\left((\mathrm{E}_n - \mathrm{E}_m)\rho_{mn} - \Delta\alpha\left\langle m\middle|\widehat{\langle\cos^2\theta\rangle}\middle|n\right\rangle|E(t)|^2(\rho_{mm} - \rho_{nn})\right), \tag{5.8}$$

where the first term can be written in terms of the Raman frequency $\omega_{nm} = -(E_n - E_m)/\hbar$, and we need to phenomenologically add the dephasing rate $\Gamma_2 = 1/T_2$, which together gives

$$\frac{d\rho_{mn}}{dt} = -i\omega_{nm}\rho_{mn} - \Gamma_2\rho_{mn} - \frac{i}{\hbar}\Delta\alpha\langle m|\widehat{\langle\cos^2\theta\rangle}|n\rangle|E(t)|^2(\rho_{mm} - \rho_{nn}). \quad (5.9)$$

To solve this differential equation, we assume ρ_{mm} and ρ_{nn} do not depend on t, as the Raman excitation usually will not introduce significant population change [146, 147], which holds true even with the irradiance close to the ionization threshold. So the solution of the time-dependent "coherence" element $\rho_{mn}(t)$ becomes

$$\rho_{mn}(t) = \frac{i}{2\hbar}\Delta\alpha\langle m|\widehat{\langle\cos^2\theta\rangle}|n\rangle\left(\rho_{mm}^{(0)} - \rho_{nn}^{(0)}\right)\int_{-\infty}^{t}|\mathcal{E}(t')|^2 e^{-i(\omega_{nm}+i\Gamma_2)(t-t')}dt', \quad (5.10)$$

where $\rho_{mm}^{(0)}$ represents the diagonal elements of the unperturbed density matrix and $\mathcal{E}$ denotes the envelop of the excitation pulse, which derives from the temporal integral of $|E(t)|^2 \approx |\mathcal{E}(t)|^2/2$ with carrier frequency suppressed within the integrand [139].

Again, assuming negligible population changes [146, 147], the Raman excitation simply introduces coherence between eigenstates, and the resultant superposition system can be written as the summation of initial eigensystem $\hat{\rho}^{(0)}$ and the induced coherence $\hat{\rho}^{(1)}$

$$\hat{\rho}(t) = \hat{\rho}^{(0)} + \hat{\rho}^{(1)}(t) = \begin{bmatrix}\rho_{mm} & 0\\ 0 & \rho_{nn}\end{bmatrix} + \begin{bmatrix}0 & \rho_{mn}(t)\\ \rho_{nm}(t) & 0\end{bmatrix}, \quad (5.11)$$

from which we can calculate the expectation value of any physical observables, e.g. the degree of alignment $\langle\cos^2\theta\rangle$. To do this, we use $\langle\cos^2\theta(t)\rangle = \mathrm{tr}\left[\hat{\rho}(t)\widehat{\langle\cos^2\theta\rangle}\right]$, where tr [ ] denotes the trace operation.

$$\langle\cos^2\theta(t)\rangle = \frac{1}{3} + \rho_{mn}(t)\langle n|\widehat{\langle\cos^2\theta\rangle}|m\rangle + \rho_{nm}(t)\langle m|\widehat{\langle\cos^2\theta\rangle}|n\rangle, \quad (5.12)$$

where $1/3$ results from the first term in Eq. (5.11) $\mathrm{tr}\left[\hat{\rho}^{(0)}\widehat{\langle\cos^2\theta\rangle}\right]$ at thermal equilibrium. Now we can specify the rotational eigenstate to be $|m\rangle = |J, M\rangle$ and $|n\rangle = |J-2, M\rangle$. The diagonal

element of $\hat{\rho}$ becomes $\rho_{JJ}^{(0)}$, which follows a J dependent Boltzmann distribution [20, 139]. By substituting Eq. (5.10) into (5.12) and employing the ensemble averaging, we obtain

$$\begin{aligned}\langle\cos^2\theta(t)\rangle - \frac{1}{3} \\ = -\frac{\Delta\alpha}{\hbar}\sum_{J,M}\left\langle J,M\middle|\langle\widehat{\cos^2\theta}\rangle\middle|J-2,M\right\rangle^2\left(\rho_{JJ}^{(0)}\right. \\ \left.-\rho_{J-2,J-2}^{(0)}\right)\mathrm{Im}\left\{\int_{-\infty}^{t}|\mathcal{E}(t')|^2 e^{-i(\omega_{J,J-2}+i\Gamma_2)(t-t')}dt'\right\},\end{aligned} \tag{5.13}$$

which gives the transient change in the degree of alignment. Finally, the transient refractive index change $\Delta n(t)$ can be calculated by substituting Eq. (5.13) into (5.2).

Considering the rotational eigenstates take the forms of spherical harmonics [145], the angular averaging makes the square of the matrix element on the right-hand side reduce to

$$\sum_{J,M}\left\langle J,M\middle|\langle\widehat{\cos^2\theta}\rangle\middle|J-2,M\right\rangle^2 = \sum_{J,M}\frac{(J^2-M^2)((J-1)^2-M^2)}{(2J-1)^2(2J+1)(2J-3)}. \tag{5.14}$$

Since there is no coupling M due to the interaction symmetry about the molecular axis, after summing over M Eq. (5.14) can be further reduced to $\sum_J \frac{2}{15}\frac{J(J-1)}{2J-1}$, which simplifies Eq. (5.13) to

$$\langle\cos^2\theta(t)\rangle - \frac{1}{3} = -\Delta\alpha\sum_J T_J\mathrm{Im}\left\{\int_{-\infty}^{t}|\mathcal{E}(t')|^2 e^{-i(\omega_{J,J-2}+i\Gamma_2)(t-t')}dt'\right\}, \tag{5.15}$$

where $T_J = \frac{2}{15\hbar}\frac{J(J-1)}{2J-1}\left(\rho_{JJ}^{(0)} - \rho_{J-2,J-2}^{(0)}\right)$, is essentially the weighting factor for a molecule initially in a particular rotational state with quantum number J.

5.1.2. Nuclear Spin Statistics

As discussed previously, the diagonal element $\rho_{JJ}^{(0)}$ of $\hat{\rho}$ follows a J dependent Boltzmann distribution [20, 139], which gives the initial occupation probability as

$$\rho_{JJ}^{(0)} = \frac{g_J e^{-\frac{E_J}{k_B T}}}{\sum_0^\infty g_J(2J+1)e^{-\frac{E_J}{k_B T}}}, \tag{5.16}$$

where g_J is known as the statistical weight for even and odd J states, which depends on the nuclear spin statistics [20, 90, 139]. To facilitate the calculation in Eq. (5.15), the g_J must be known first for the molecules of interest.

Table 5.1 Symmetries of different wavefunctions upon nuclear interchange [20, 90, 139]

Molecules	S	$\hat{\imath}\psi_e$	$\hat{\imath}\psi_v$	$\hat{\imath}\psi_r$	$\psi_{n,sym}$	$\psi_{n,asym}$	$\frac{g_{J,even}}{g_{J,odd}}$
$^{14}N_2$	1 (Boson)	$\psi_e(\Sigma_g^+)$	ψ_v	$\psi_{r,even}$ $-\psi_{r,odd}$	6	3	$\frac{2}{1}$
$^{16}O_2$	0 (Boson)	$-\psi_e(\Sigma_g^-)$	ψ_v	$\psi_{r,even}$ $-\psi_{r,odd}$	1	0	$\frac{0}{1}$
$^{12}C^{32}S_2$	0 (Boson)	$\psi_e(\Sigma_g^+)$	ψ_v	$\psi_{r,even}$ $-\psi_{r,odd}$	1	0	$\frac{1}{0}$

Following [90], the total wavefunction of the molecule may be written as $\psi_{total} = \psi_e\psi_v\psi_r\psi_n$, where the subscripts e, v, r and n indicate electronic, vibrational, rotational and nuclear, respectively. The molecular rotation can be treated as a spatial nuclear interchange operator $\hat{\imath}$, which makes the coordinates change sign, i.e . $\hat{\imath}\psi_{total}(\bar{x},\bar{y},\bar{z}) = \psi_{total}(-\bar{x},-\bar{y},-\bar{z})$. For symmetric molecules where the particles upon interchange are indistinguishable, the Pauli exclusion principle [90, 145] must be satisfied: any particles with integer spin quantum number (Bosons),

e.g. $S = 0, 1, 2 \ldots$, ψ_{total} must remain symmetric upon nuclear interchange, i.e. $\hat{\imath}\psi_{total} \rightarrow \psi_{total}$; any particles with half-integer spin quantum number, e.g. $S = 1/2, 3/2, \ldots$, ψ_{total} becomes anti-symmetric upon nuclear interchange, i.e. $\hat{\imath}\psi_{total} \rightarrow -\psi_{total}$. To satisfy this condition, each constituent wavefunction must be evaluated separately by $\hat{\imath}$. Within the scope of this dissertation, we present the results for the most abundant isotopologues of $^{14}N_2$, $^{16}O_2$, and $^{12}C^{32}S_2$.

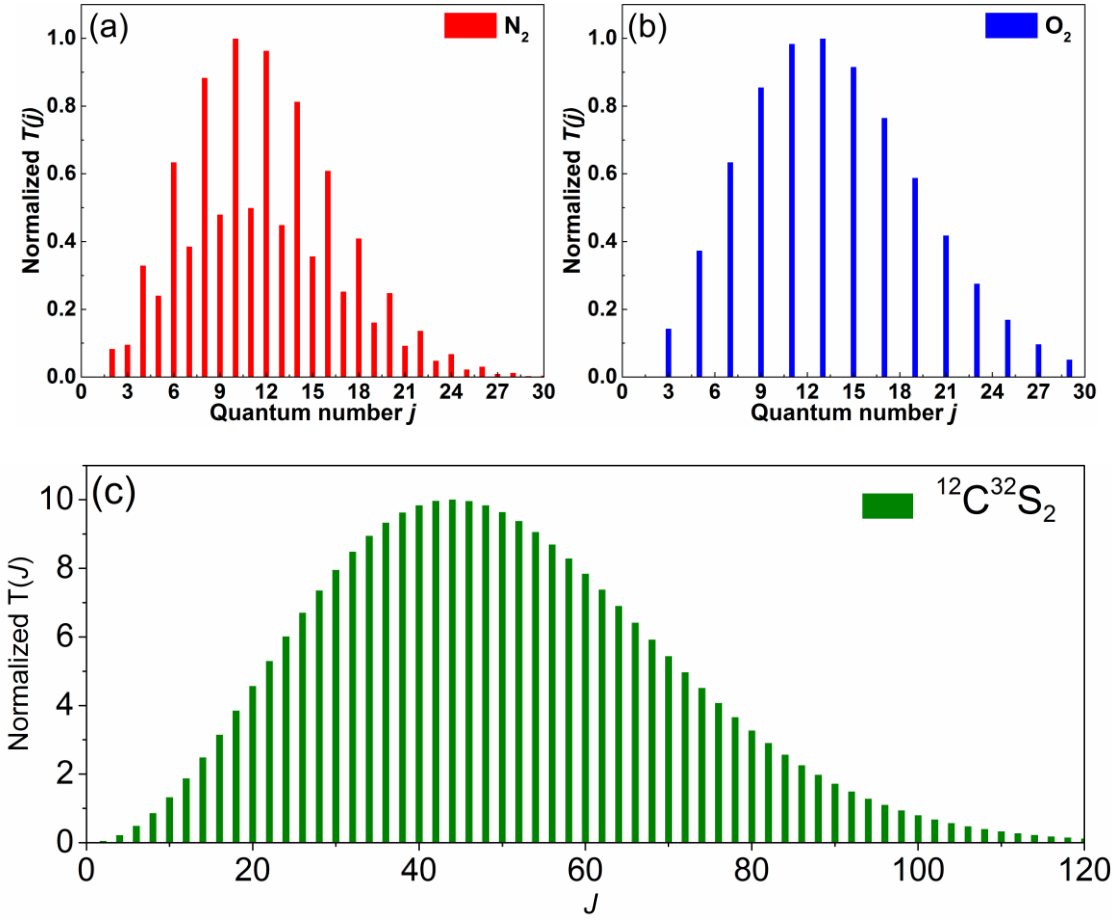

Figure 5.2 Weighting factor T_J in Eq. (5.13) for (a) $^{14}N_2$, (b) $^{16}O_2$, and (c)$^{12}C^{32}S_2$.

Since electrons are rigidly attached to their nuclei, the symmetry of the electronic wavefunction defined in $(\bar{x}, \bar{y}, \bar{z})$ determines the sign change upon nuclear interchange. For a molecule

with Σ_g^+ as the ground state, e.g. N_2, and CS_2, $\hat{\imath}\psi_e \rightarrow \psi_e$, while molecules with a Σ_g^- ground electronic state such as O_2, this results in $\hat{\imath}\psi_e \rightarrow -\psi_e$. The ground-state vibrational wavefunction is usually defined in terms of the bond separation, which usually remains the same upon nuclear interchange, i.e. $\hat{\imath}\psi_v \rightarrow \psi_v$. Gaseous CS_2 has a thermally excited percentage of population in the excited vibrational states, which may have a different symmetry from that of the ground state, as discussed in 5.3. . The rotational wave functions are known to be symmetric and antisymmetric upon nuclear interchange for even and odd J states, respectively. The nuclear wavefunction can be either symmetric or antisymmetric upon interchange, and the number of each is related to the spin quantum number of nuclei, which is given by $(2S+1)(S+1)$ for symmetric states and $(2S+1)S$ for antisymmetric states [148]. The sign changes of each wavefunction of $^{14}N_2$, $^{16}O_2$, and $^{12}C^{32}S_2$ are summarized in Table 5.1. Since interchanging nuclei, i.e. ^{14}N, ^{16}O and ^{32}S, are bosons, $\hat{\imath}\psi_{total} \rightarrow \psi_{total}$ needs to be satisfied. For N_2, this makes the statistical weight of even J states twice that of odd J states. For O_2, only odd J states contribute, while for $^{12}C^{32}S_2$ only even J states contribute. Knowing g_J, the weighting factor T_J can be calculated for $^{14}N_2$, $^{16}O_2$, and $^{12}C^{32}S_2$ as shown in Figure 5.2, where the envelop follows the Boltzmann distribution and the ratio of the contributing J states is governed by spin statistics.

With knowledge of the weighting factors T_J of each even and odd rotational J state, we are able to calculate the transient refractive index change $\Delta n(t)$ from changes in the degree of alignment, i.e. using Eqs. (5.15) and (5.2). Figure 5.3 calculates $\Delta n(t)$ in molecular gases, i.e. $^{14}N_2$, $^{16}O_2$, and $^{12}C^{32}S_2$, after a short pulse excitation at zero delay. Since a short pulse with sufficient bandwidth is able to produce many coherences, which start out in phase and evolve together at their corresponding Raman frequencies, i.e. $\omega_{J,J-2}$. This manifests in Eq. (5.15) that the ensemble

averaged degree of alignment becomes a sum of sinusoids. Because of the Raman frequencies are nearly equally spaced (equal if ignoring centrifugal distortion effect), the sinusoids interfere, resulting in periodic beats, or "revivals" in the degree of alignment. An analogy could be drawn with the principle of mode-locked lasers, where the phase-locked longitudinal modes result in optical pulses [114, 149, 150]. Here, phase-locked rotational coherences (superpositions) give transient refractive index pulses. The rotational revivals may occur at half- or quarter-multiples of the full revival period $T_{rev} = (2cB)^{-1}$ [140]. In between events, the rotational coherences walk out of phase resulting in an isotropic ensemble.

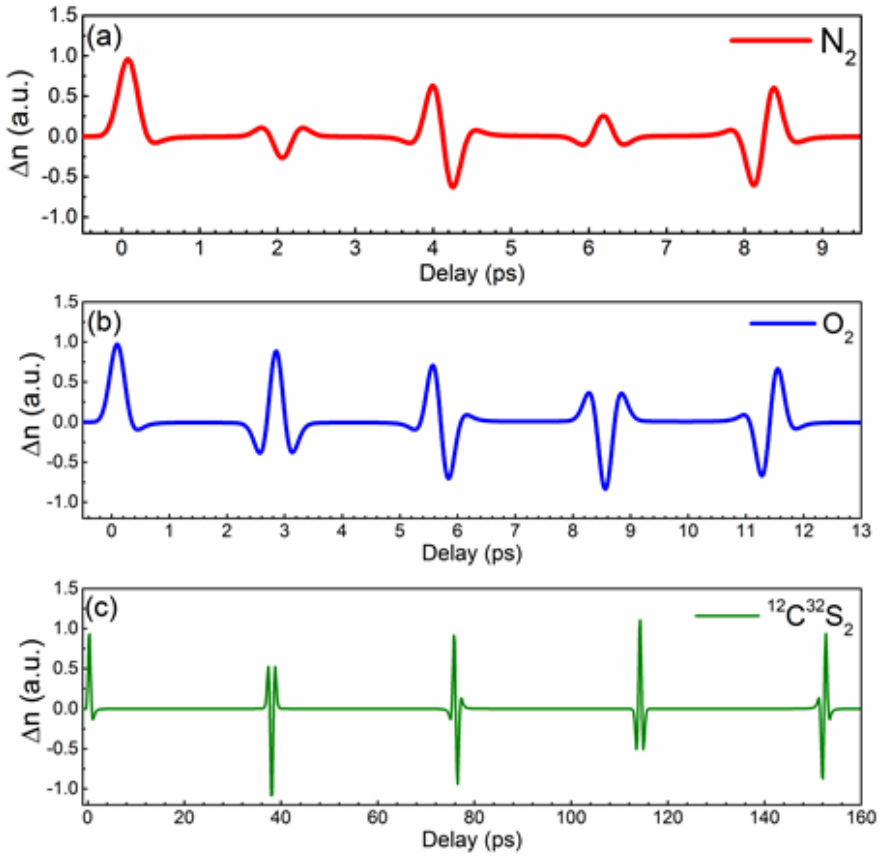

Figure 5.3 The calculated normalized refractive index change due to rotational revivals using Eqs. (5.15) and (5.2) for (a) $^{14}N_2$, (b) $^{16}O_2$, and (c) $^{12}C^{32}S_2$. Note the different times scales.

The magnitude and sign of each revival is closely related with the spin statistics through the weighting factor T_J. For example, both even and odd rotational J states contribute equally to the ½ and full revivals, but give the opposite sign for the ¼ and ¾ revivals. This effect can be seen by comparing the ¼ revivals of $^{16}O_2$ (~ 3ps) with only odd J states, and $^{12}C^{32}S_2$ (~ 40ps) with only even J states. For the ¼ revival of $^{14}N_2$, the contributions from even and odd J states partially cancel each other, which ends up looking an "even J states" signal with a smaller magnitude than that of $^{12}C^{32}S_2$.

5.2. Measurements of Air

To measure the transient NLR of molecular gases induced by a short pulse, we utilize our polarization-resolved Beam Deflection (BD) technique [18, 69, 93]. The principle of the BD experiment has been discussed in 3.2.3. . Because the interaction length in the gas phase sample is long, the requirement of the beam-crossing geometry is more critical than for that in liquid solvent measurements (see 4.2.). Figure 5.4 shows the three dimensional geometry for the beam overlap, where the beams cross one another in the vertical yz-plane, in Figure 5.4 (a), and are displaced in the horizontal xz-plane, in Figure 5.4 (b). This was done to maximize the probe deflection in the x-direction and prevent the cancelation of the deflection by horizontally crossing (x-) at different regions along the length of overlap. The crossing angle between excitation and probe beams is always kept small (< 1°) to maximize the interaction length.

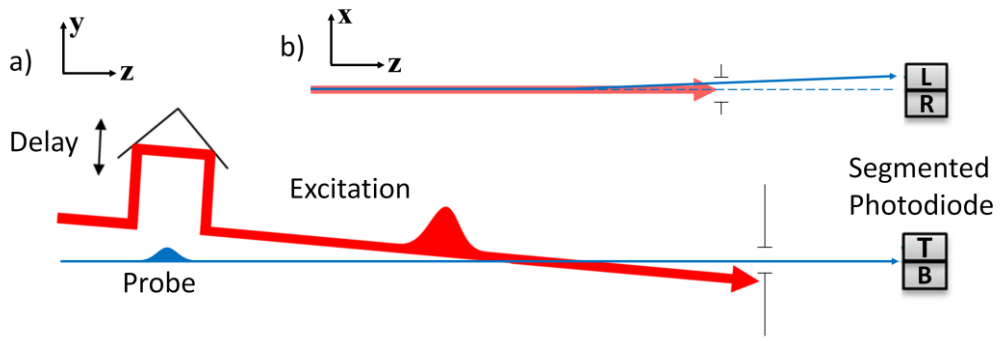

Figure 5.4 The excitation and probe crossing geometry in (a) the yz-plane, and (b) displacement in the xz-plane resulting in a deflection in the x-direction at the segmented photodiode.

Another problem arising from the long interaction lengths in gaseous samples is that the "Prism" deflection approximation discussed in 3.2.3.1. is no longer valid, making absolutely calibrated measurements difficult. One of tasks in our experiment is to measure the bound-electronic NLR, i.e. the second hyperpolarizability $\langle\gamma\rangle$ of the molecular ensemble. To do this, we perform relative measurements using the well-known values of the polarizability anisotropy $\Delta\alpha$ measured from gas phase Raman spectroscopy, as a self-reference. From Eqs. (3.6), (4.5), (5.2) and (5.13), one can show

$$\frac{\Delta n_{el}}{\Delta n_{rot}} \propto \frac{\langle\gamma\rangle}{(\Delta\alpha)^2} \tag{5.17}$$

Therefore, by evaluating the relative magnitudes of the bound-electronic and molecular rotational contributions at different temporal delays of the BD signal $\Delta E/E$, $\langle\gamma\rangle$ can be precisely determined. One of the benefits from this relative measurement is the experimental uncertainties in the interaction length, number density, and excitation irradiance that affect absolute measurements are suppressed.

We first study ambient air. The excitation beam in the BD setup is directly taken from Coherent system (see 3.2.1.) at a wavelength of 800 nm at a repetition rate of 1 kHz. A portion of

the excitation beam (~ 0.8 μJ) is split out and focused into a 1 cm cuvette filled with water to generate a white-light continuum (WLC), from which the probe is spectrally filtered at 650 nm with a 40 nm bandwidth (FWHM) spike filter. A polarizer is used to ensure linear polarization of the probe, and a half-wave plate controls the angle of its polarization with respect to that of the excitation. A delay stage with delay variable up to 2 ns is used for the excitation pulses. To convert the stage position to temporal delay, it is important to take into account down to six decimals of the refractive index of air, i.e. $n_{0,e} = 1.000275$ using the dispersion in [151]. The excitation and probe beams are focused to spot sizes w_e = 177 μm and $w_{0,p}$ = 60 μm, and have pulse widths τ_e = 83 fs and τ_p = 265 fs (FWHM), respectively. Most data is measured with 330 μJ of excitation energy. This corresponds to a peak irradiance of < 9 TW/cm^2, which is nearly an order of magnitude less than previously reported measurements [139] and well below the filamentation threshold [141, 152].

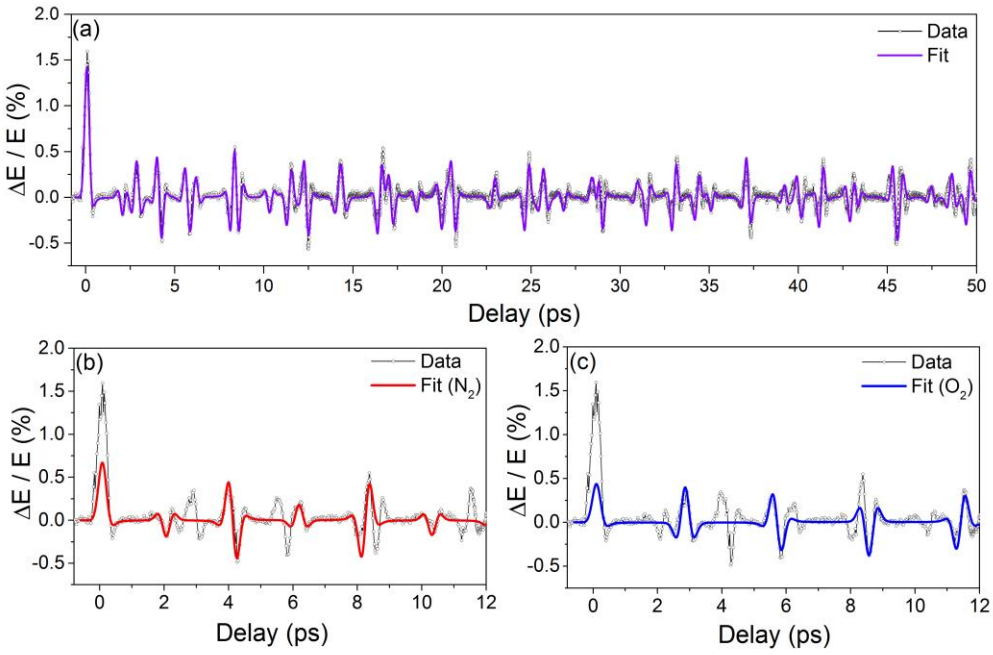

Figure 5.5 (a) Measured (circles) BD signal from air along with fit (violet), which is a sum of both the contribution of N_2 and O_2. (b) and (c) show the first 12 ps of delay, with fits only considering N_2 and O_2, respectively.

Figure 5.5 (a) shows the measured BD signal of the ambient air using co-polarized excitation and probe, along with a theoretical fit calculated from (3.6), (5.2) and (5.13) considering both N_2 and O_2 weighted by their relative atmospheric concentrations at 1 atm. We therefore obtain a good determination of the ratio $\Delta\alpha(O_2)/\Delta\alpha(N_2)$ since they are measured at the same time, which agrees well with the values in Ref. [138]. The total BD signal for the gaseous mixture can be decomposed into the contributions from each molecular species. For example, Figure 5.5 (b) and (c) show the first 12 ps of delay of the measured air signal which contains the first revival periods of both molecules, as compared to theoretical calculations only considering N_2 (red) and O_2 (blue) respectively. The transient at 6 ps arises from the ½ revival of O_2 and the ¾ revival of N_2, and at about 4 ps, only N_2 contributes to the BD signal.

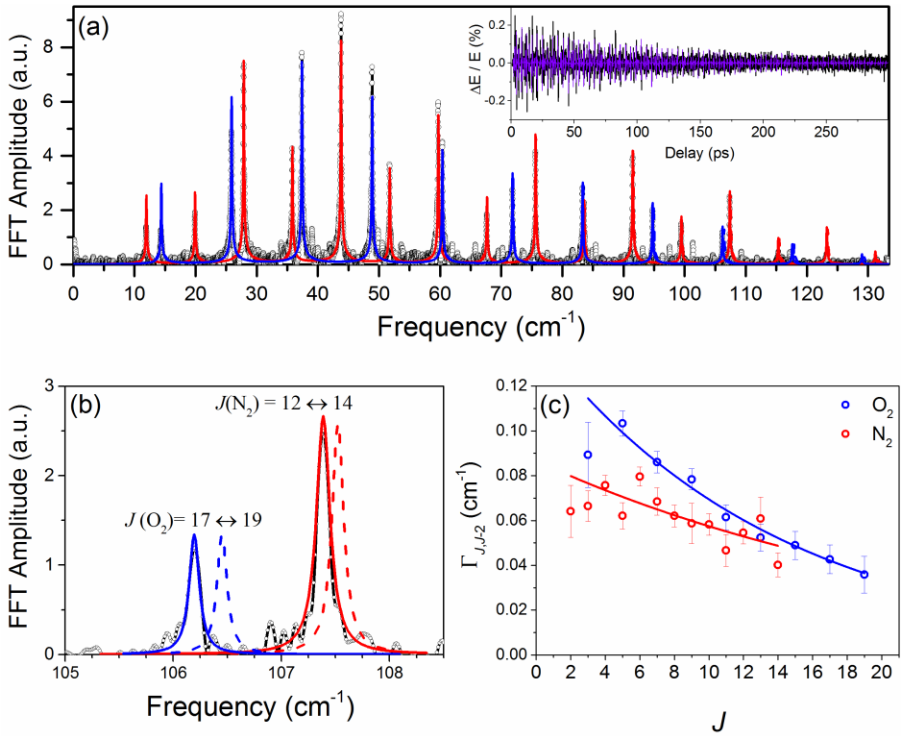

Figure 5.6 (a) Fourier transform of a BD signal measured out of 300 ps (inset) for air (circles) with the fitting for N_2 (red) and O_2 (blue); (b) the enlarged higher frequency components with fits ignoring (dash) or considering (solid) the effect from centrifugal distortion; (c) the Lorentz linewidth (circles) data of for N_2 (red) and O_2 (blue) in (a) for different Raman transitions start with J, along with exponential decay fits.

Another BD measurement of air is performed out to 300 ps of delay (inset), from which the rotational Raman spectrum is obtained through its Fourier transform along with the fits only considering N_2 (red) and O_2 (blue), as shown in Figure 5.6 (a). The center frequency of each peak corresponds to the Raman transition frequency, which is determined by the rotational quantum number J as well as the rotational constant B. The linewidth is related with the dephasing rate Γ_2 defined in Eq. (5.15), from which we fit with a Lorentz broadening corresponding to the time constant of $T_2 \sim 155$ ps. Comparing to the weighting factor T_J of N_2 and O_2 in Figure 5.2 (a) and (b), we found the intensity distribution of this frequency spectrum is simply a consequence of the thermal distribution as well as nuclear spin statistics. For example, the intensity of adjacent peaks in the N_2 spectrum follows the 2:1 ratio of even to odd J states, while only odd J states contribute in the O_2 spectrum.

In the frequency range between 105 cm^{-1} to 110 cm^{-1} in Figure 5.6 (a), Raman transitions between higher rotational states occurs, i.e. $J(12) \rightarrow J(14)$ in N_2 and $J(17) \rightarrow J(19)$ in O_2, where, the measured center frequencies are not as evenly spaced as that for lower rotational transitions. As shown in Figure 5.6 (b), the theoretical predictions (dash) with a B that fits lower J transitions start to deviate from the experiments (circles). This is because at higher rotational states the centrifugal deformation lengthens the bond, which increases the moment of inertia and effective results in a smaller B [144]. To account for this nonlinear J dependence of Raman transition frequency, the centrifugal distortion constant D needs to be included, as defined in 5.1.1. . The values of B and D from fitting (solid) in Figure 5.6 (b) are given in Table 5.2 for N_2 and O_2, which is compared to a Raman scattering measurement in [153]. Interestingly, linewidths $\Gamma_{J\rightarrow J+2}$ also shows some J dependence. As shown in Figure 5.6 (c), $\Gamma_{J\rightarrow J+2}$ decreases in an exponential manner

for higher J levels. Since the linewidth simply reflects the dephasing rate due to collisions, this dependence may indicate that the higher rotational states are more resilient to collisions events, as discussed in [72, 154].

Table 5.2 Measured rotational and centrifugal distortion constants of N_2 and O_2.[a,b]

Molecules	$\Delta\alpha$	B (this work)	B [153]	D (this work)	D [153]
$^{16}N_2$	0.77[138]	1.9896(2)	1.989574(12)	5.9(6)	5.76(3)
$^{16}O_2$	1.21[138]	1.4377(2)	1.437682(9)	5.1(5)	4.852(12)

[a] $\Delta\alpha$, B and D are given in the units of 10^{-40} Fm^2, cm^{-1} and 10^{-6} cm^{-1} respectively.
[b] The number in parenthesis indicates the uncertainties in the last reported digits.

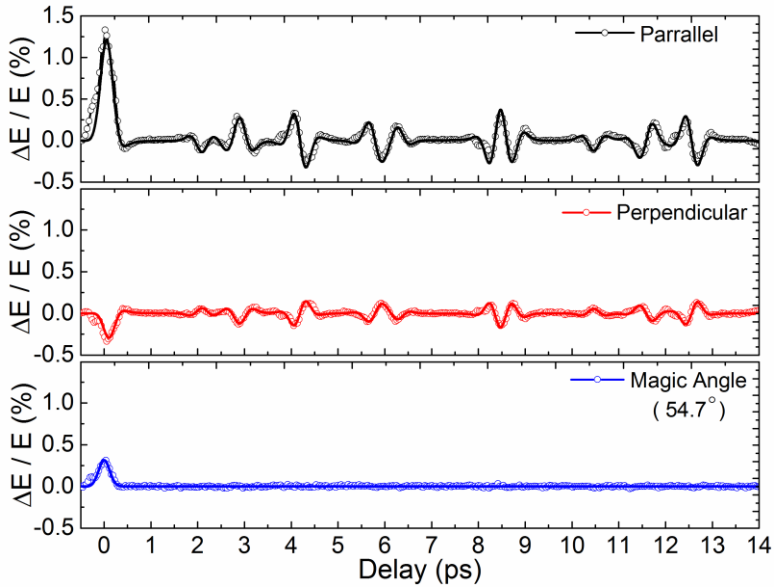

Figure 5.7 Measured (circles) and fit (lines) polarization dependence of transient NLR of air for parallel (black), perpendicular (red), and magic angle (blue) polarizations.

Similar to the study we have done with solvents in 4.2.2. , the polarization dependence has been measured for transient NLR of air with parallel, perpendicular and magic angle polarizations

of excitation and probe. Figure 5.7 shows the BD data for these polarization angles and fits considering the symmetry properties for isotropic and reorientational nonlinearities, i.e. Eq. (4.15). Particularly at the magic angle, the NLR transients from rotational revivals are completely suppressed, with only the bound-electronic response at zero delay. Based on the values of $\Delta\alpha$ of N_2 and O_2 shown in Table 5.2, we use the signal magnitude from the rotational revivals as a self-reference to calibrate our irradiance (see Eq. (5.17)), and measure $n_{2,el}$(air) = (10 ± 2) × 10^{-24} m^2/W using a number density of air N = 2.5 × 10^{19} cm^{-3} [155]. This also gives an averaged value of the second polarizability of air $\langle\gamma_{air}\rangle$ = (1.25 ± 0.20) × 10^{-62} C^4m^4/J^3, which agrees with the sum of γ from individual species in Ref. [132] weighted by their number density, i.e. 0.78γ(N_2) + 0.21γ(O_2) + 0.01γ(Ar) = (0.98 ± 0.10) × 10^{-62} C^4m^4/J^3.

5.3. Measurements of Gaseous CS_2

Measurements of gaseous CS_2 are performed by partially filling a 10 cm borosilicate cell with liquid CS_2 such that the upper portion of the cell is filled with gaseous CS_2. The cell windows are heated to ~ 50 °C with a Thorlabs GCH25-75 cell heater to prevent condensation. In this experiment, we use an OPA (Light Conversion, HE-TOPAS) to generate the 1250 nm wavelength excitation pulse. A portion of the excitation is used to generate a WLC in a 5 mm sapphire plate. A probe is prepared from the spectrally filtered WLC at 950 nm wavelength (FWHM 10 nm). The probe and excitation beams are focused to spot sizes of 90 μm and 468 μm, and have pulsewidths (FWHM) of 137 fs and 120 fs respectively. The excitation energy is 62 μJ, giving a peak irradiance of 140 GW/cm^2.

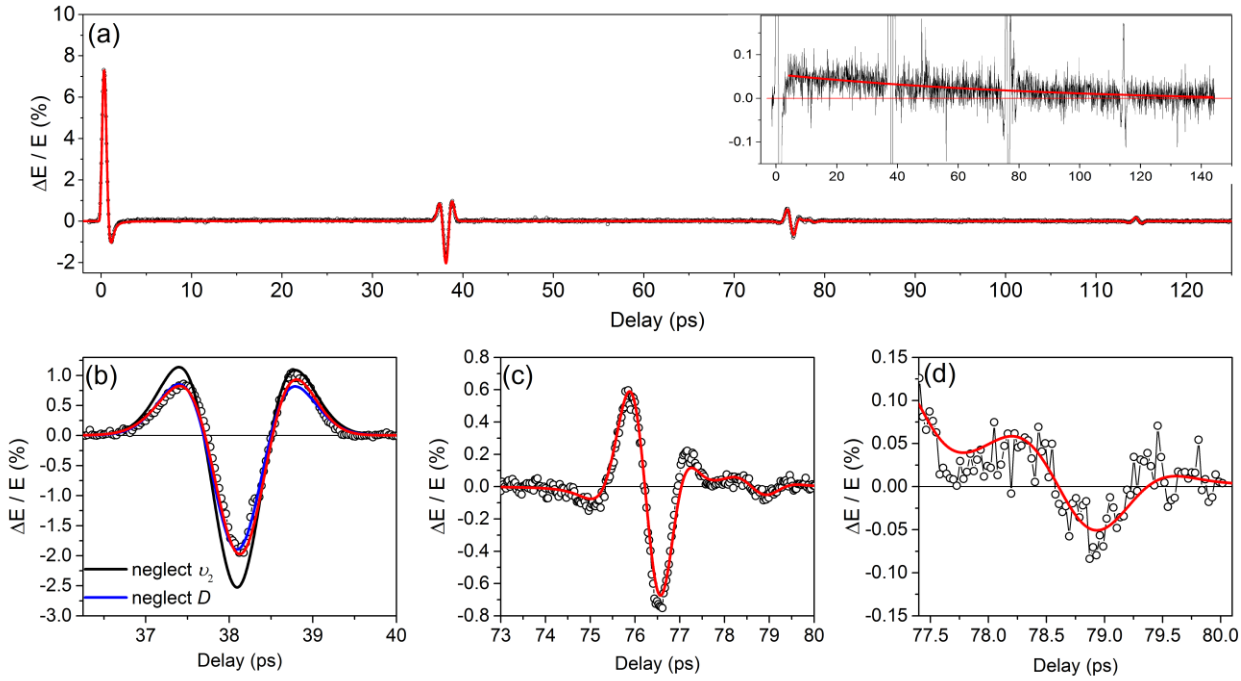

Figure 5.8 Measured (circles) BD signal from gaseous CS_2, along with a fit (red line) considering isotopologue $C^{32}S^{34}S$, centrifugal distortion effect and thermally populated first excited vibrational states ν_2 of $C^{32}S_2$. The inset enlarges the $\Delta E/E$ around the zero, fitted with a single exponential decay (red); (b) ¼, and (c) ½ revival $C^{32}S_2$. (d) shows the ½ revival from $C^{32}S^{34}S$. In (b) the fits in black and blue neglect centrifugal distortion, and the black curve also neglects ν_2 of $C^{32}S_2$.

Figure 5.8 shows the BD measurement for gaseous CS_2 up to the first ¾ revival, as the first full revival (~ 152.4 ps) is below the noise floor. Figure 5.8 (c) shows the ½ revival of CS_2 about 76 ps, with an additional feature at a slightly longer delay (~79 ps), which is enlarged in Figure 5.8 (d). This signal is from the second most common sulfur isotopologue $C^{32}S^{34}S$. Since $C^{32}S^{34}S$ lacks nuclear exchange symmetry, both even and odd rotational states J are equally contributing, giving a zero ¼ and ¾ revival [72]. The ½ revival signal of $C^{32}S^{34}S$ comes slightly later than $C^{32}S_2$ due to the greater moment of inertia (or smaller rotational constant). Based on this feature we measure a relative abundance of (9 ± 3) %, which agrees with the natural abundance of 8.6 % [72]. Additionally, a closer examination of $\Delta E/E$ around the noise floor (see inset of Figure 5.8 (a)), the signal appears a sharp rise at zero delay followed by a single exponential decay (T_1~ 90 ps). This

contribution offsets all the revivals. Similar phenomenon has been observed in [124, 156-158], which is attributed to population relaxation of excited rotational state. In the current simulation, we ignore this effect, i.e. assuming ρ_{mm} and ρ_{nn} are constants when solving Eq. (5.9), and only consider the transient changes in off-diagonal terms (coherence effect) of the density matrix. It is a good approximation as a Raman excitation usually only moves small amount of population to higher rotational states [147].

Table 5.3 Measured rotational and centrifugal distortion constants of $C^{32}S_2$.[a,b]

Molecules	$\Delta\alpha$[138]	B (this work)	B [72]	D (this work)	D [72]
$C^{32}S_2$	10.53	0.10942(10)	0.1091271(6)	0.010(5)	0.01173(1)
$C^{32}S_2(\nu_2)$	10.53	0.10957(10)	0.10930(1)[c] 0.10938(1)[d]	0.010(5)	0.01111(17)[c] 0.01157(13)[d]
$C^{32}S^{34}S$	10.53	0.10617(10)	0.1059086(7)	0.010(5)	0.01105(12)

[a] $\Delta\alpha$, B and D are given in the units of 10^{-40} Fm^2, cm^{-1} and 10^{-6} cm^{-1} respectively.
[b] The number in parenthesis indicates the uncertainties in the last reported digits.
[c] Lower energy rotational states in ν_2
[d] Higher energy rotational states in ν_2

Owing to the sensitivity of the BD technique, there is additional information that can be extracted from this measurement. First, the asymmetric revival signal is a signature of the centrifugal distortion effect. For example, as shown in Figure 5.8 (b) of ¼ revival, the magnitude of the signal at 38.8 ps is larger than that at 37.4 ps, where a theoretical calculation without taking into account centrifugal distortion is shown in blue for comparison. Assuming all $C^{32}S_2$ molecules are in the ground vibrational state, we found the magnitude of the ½ and ¼ revival signals cannot be fit simultaneously. For example, if the fit matches the amplitude of the signals at zero delay and at the ½ revival, the ¼ revival magnitude will clearly be overestimated, as shown in the black curve

in Figure 5.8 (b). This is because at room temperature ~ 15 % of the $C^{32}S_2$ molecules are in the first excited vibrational state, i.e. the doubly-degenerate bending mode at ν_2 = 397 cm^{-1} [72]. Although this vibrational frequency is less than the bandwidth of our excitation pulse, it is a not Raman active mode and has not been excited. However, it does affect our results, because for molecules with a doubly-degenerate bending motion parallel to the axis of rotation, the vibrational wavefunction of $\psi_v(\nu_2)$ may become asymmetric upon nuclear interchange, while the wavefunctions of molecules with bending motion perpendicular to the axis of rotation, $\psi_v(\nu_2)$ are symmetric upon nuclear interchange, as discussed in 5.1.2. . Both cases will give the same sign for the ½ revival signal but have opposite signs and cancel for the ¼ and ¾ revivals. Assuming they have equal population, we can conclude that $C^{32}S_2(\nu_2)$ will not contribute to the ¼ and ¾ revival, but will add up for the ½ revival along with the ground vibrational state of $C^{32}S_2$. Considering all these $C^{32}S_2$ molecular vibration/rotation populations, we are able to fit the rotational and centrifugal distortion constants, as summarized in Table 5.3.

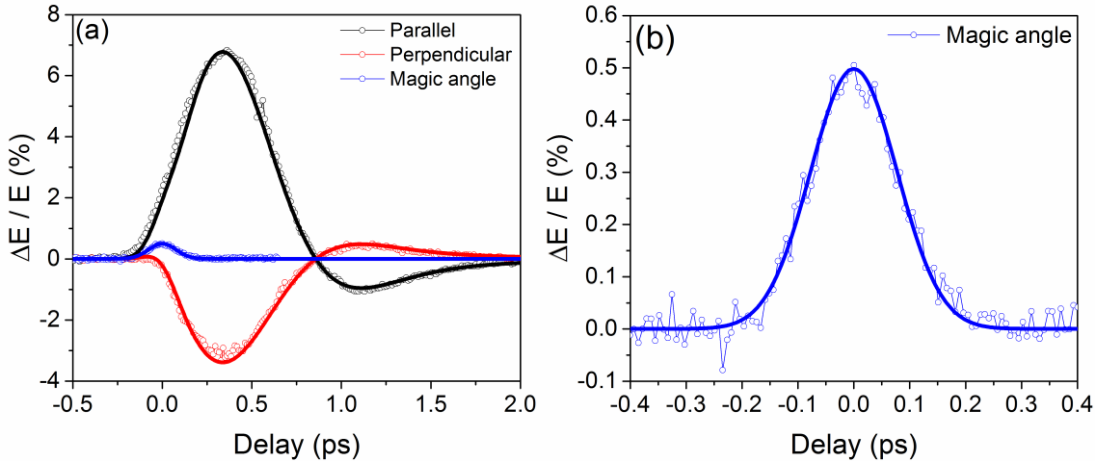

Figure 5.9 (a) Measured (circles) BD signals about zero delay with fits (lines) for parallel (black), perpendicular (red) and magic angle (blue) polarizations. (b) Enlarged measurement at magic angle.

Figure 5.9 shows the BD signals from CS_2 about zero delay for parallel, perpendicular, and magic angle polarizations, along with fits. Using the known value of $\Delta\alpha$ given in [138], we fit the measurement at the magic angle for the bound-electronic nonlinearity to find $\langle\gamma_{\mathrm{gas}}\rangle$ = (19 ± 4) × 10^{-62} C^4m^4/J^3 ((15 ± 4) × 10^{-37} esu) [119]. This ability to determine γ is of interest for theoretical purposes to compare calculated values of γ, which are typically performed for isolated molecules [132, 133]. Additionally, the Lorentz-Lorenz local field correction factor $f^{(3)}$ = 5.35 in liquid phase CS_2, yields $\langle\gamma_{\mathrm{liquid}}\rangle$ = (1.7±0.3)×10^{-61} $C^4m^4J^{-3}$ ((1.4±0.3)×10^{-36} esu), obtained based on $n_{2,el}$ = (1.15±0.3)×10^{-19} m^2/W from our liquid CS_2 Z-scan measurements at the wavelength of 1064 nm [17], which coincides with $\langle\gamma\rangle$ measured in the gas phase within the error bars. Therefore, assuming local field theory [31, 32] is correct, gas and liquid phase CS_2 have the same value of second hyperpolarizability The ongoing gas-phase measurements on the other organic solvents will provide more comparisons of $\langle\gamma\rangle$ to their liquid phase counterparts, which should indicate how local field theory works for other molecules including polar molecules.

CHAPTER 6: DISPERSION OF NONDEGENERATE NONLINEAR REFRACTION IN SEMICONDUCTORS

As introduced in 1.1. , the optical Kerr effect, originating from the bound-electronic NLR, dominates the refractive nonlinearities in the sub-gap regime in semiconductors. The resulting in a refractive index change, Δn, is directly proportional to the irradiance with the coefficient n_2 [30, 31, 34]. Being exploited in numerous applications as previously discussed, Kerr effect, of our particular interest, is used for all-optical switching (AOS) [64, 65, 67, 68, 159], where a transmission of the signal beam can be modulated by a control beam. For example, actual devices have been developed in waveguide geometries such as nonlinear directional couplers [160], Mach-Zehnder interferometers [65, 161] or resonant cavities [162-164], Precise knowledge of the magnitude, sign, and dispersion of n_2 of semiconductors is needed for the design and prediction of AOS devices.

In general, NLR is related to nonlinear absorption (NLA) via a Kramers-Kronig (KK) transformation of the nondegenerate (ND) NLA spectrum [165, 166]. This theory has been extensively used for prediction of n_2 of various solids [41, 45, 167]. For a single beam at frequency ω, Z-scan measurements of this nonlinear refractive index, denoted by $n_2(\omega;\omega)$, have shown excellent agreement with predictions of this theory [42, 43, 105]. However, the ND-NLR, namely the refractive index change at frequency ω_a due to the presence of a beam at frequency ω_b, of coefficient $n_2(\omega_a;\omega_b)$, is much less explored, particularly for the extremely nondegenerate case (i.e. $\hbar\omega_a \gg \hbar\omega_b$) and for spectral regions where 2PA is present.

Previously, orders of magnitude enhancement of two-photon absorption (2PA), of coefficient $\alpha_2(\omega_a;\omega_b)$, has been observed using extremely nondegenerate photon pairs. Such enhancement has been utilized in applications including mid-infrared pulse detection [168], 3D IR imaging

[169] and observation of two-photon gain [170]. Linked by KK relations, the nondegenerate enhancement of 2PA translates into enhancement of $n_2(\omega_a;\omega_b)$ [45, 171], which suggests the use of semiconductors for applications such as nondegenerate AOS. The enhanced $n_2(\omega_a;\omega_b)$ lowers the switching energy required for various device geometries [66]. Traditional AOS devices with degenerate or nearly degenerate signal and control beams operate best below or near half the bandgap energy, E_g, to avoid loss from 2PA [160, 164, 172]. This excludes certain materials to be used for efficient Kerr effect based AOS at wavelengths of interest such as the telecommunication band. Nondegenerate operating schemes for AOS have the potential to overcome such limitations, as it tailors the nonlinearities, and, in principle, allows any signal wavelength below the bandgap to be used without the presence of 2PA. In the extremely nondegenerate case, the theory predicts that when $\hbar\omega_a \to E_g$, the positively enhanced $n_2(\omega_a;\omega_b)$ becomes anomalously dispersive and rapidly switches sign from a large positive value to a large negative value over a very narrow spectral range, i.e., ~10 nm [171]..

In this chapter, we present an extensive experimental study of the dispersion of ND-NLR for three direct-gap semiconductors (ZnO, ZnSe and CdS) using our Beam Deflection (BD) technique [18]. Here, using very different excitation and probe wavelengths, the dispersion of the ND-NLR is measured over the sub-gap region, along with ND-2PA or nondegenerate three-photon absorption (ND-3PA). We observe the resonance enhancement of NLR and the rapid anomalous nonlinear dispersion near the bandgap. The results are compared to theoretical predictions from the KK transformation of [41, 45]. We also define a nondegenerate figure of merit (FOM) for AOS in both ND-2PA and ND-3PA regimes and compare theory and experiment showing potential advantages with respect to the degenerate case.

6.1. Nonlinear Kramers-Kronig Relations

As a consequence of causality in any linear system, a dispersion relation governs the real and imaginary parts of the frequency-domain complex response function via Hilbert transform pairs [173]. In optical systems, this principle results in the Kramers-Kronig transformation, which relates the real and imagery parts of the linear susceptibility $\chi^{(1)}$ by

$$\mathrm{Re}\left[\chi^{(1)}(\omega)\right] = \frac{1}{\pi}\wp \int_{-\infty}^{\infty} \frac{\mathrm{Im}\left[\chi^{(1)}(\omega)\right]}{\omega'^2 - \omega^2} d\omega' , \tag{6.1}$$

where $\wp$ donates the Cauchy principle value of the complex integral. We can rewrite this relation by replacing the susceptibility with refractive index $n(\omega) = 1 - \mathrm{Re}\left[\chi^{(1)}(\omega)\right]/2$, and absorption coefficient $\alpha(\omega) = \omega \mathrm{Re}\left[\chi^{(1)}(\omega)\right]/c$, which yields

$$n(\omega) - 1 = \frac{c}{\pi}\wp \int_{0}^{\infty} \frac{\alpha(\omega)}{\omega'^2 - \omega^2} d\omega', \tag{6.2}$$

where c is the speed of light. By invoking the reality condition, the limits of the integral can be made to only involve positive frequencies ($\omega \geq 0$).

To include nonlinear effects, we introduce nondegenerate perturbations on the refractive index $\Delta n = 2n_2(\omega_a; \omega_b)I_b$ and absorption $\Delta\alpha = 2\alpha_{NL}(\omega_a; \omega_b)I_b$ due to the presence of an excitation optical field at frequency ω_b with irradiance I_b. After subtracting the linear components and dividing out I_b, we derive the KK transformation that relates ND-NLR with ND-NLA [41, 45]

$$n_2(\omega_a; \omega_b) = \frac{c}{\pi} P \int_{0}^{\infty} \frac{\alpha_{\mathrm{NL}}(\omega; \omega_b)}{\omega^2 - \omega_a^2} d\omega, \tag{6.3}$$

where α_{NL} is the total NLA coefficient. Note that the degenerate NLR $n_2(\omega_b; \omega_b)$ can be evaluated by performing the integral and then taking $\omega_a = \omega_b$. As discussed in [41, 45, 165-167], this

method of using KK with the ND-NLA linearizes the problem since the change in absorption is linear in the probe irradiance.

6.2. Mechanisms of NLR in Semiconductors

In semiconductors, the major physical mechanisms of $\alpha_{\mathrm{NL}}(\omega_a;\omega_b)$ consist of 2PA, electronic Raman and the optical (AC) Stark effect, which together can be viewed as the overall change of absorption of a material due to the presence of an excitation beam at ω_b. As graphically illustrated in Figure 6.1 (a), ND-2PA describes simultaneous absorption of both photons of frequency ω_a and ω_b, which requires $\hbar\omega_a + \hbar\omega_b \geq E_g$. Stimulated Raman scattering leads to simultaneous absorption and emission of photons at ω_a and ω_b, respectively, where $|\hbar\omega_a - \hbar\omega_b| \geq E_g$ is required. The optical (AC) Stark effect, also referred to as virtual band blocking [41], can be viewed as saturation of linear absorption for $\hbar\omega_a \geq E_g$, caused by virtual carriers generated by a strong beam at ω_b. Therefore, it results in a negative NLA, meaning decrease of absorption.

The nondegenerate NLA spectra of 2PA, Raman and AC Stark effect were formulated previously based on a two-parabolic band model using perturbation theory [41, 45], which gives the overall NLA coefficient

$$\alpha_{\mathrm{NL}}(\omega_a;\omega_b) = K\frac{\sqrt{E_p}}{n_a n_b E_g^3} F_2\left(\frac{\hbar\omega_a}{E_g};\frac{\hbar\omega_b}{E_g}\right), \tag{6.4}$$

where E_p is the Kane energy parameter, and n_a and n_b are the linear refractive indices at the respective frequencies, K is a material-dependent parameter, which is ~ 3100 cm GW^{-1} eV$^{5/2}$ from an experimental best fit in [37, 174]. F_2 is known as the spectral function, which is explicitly formulated in Table I in [45] for each mechanism. As an example, Figure 6.1 (b) plots F_2 from each mechanism, i.e. 2PA, Raman and AC Stark effect, by vary ω_a with $\hbar\omega_b/E_g$ fixed at 0.4. The

resultant total spectral function is simply the summation of each contribution, which can also be found in Fig. 3 in [41]. Below the bandgap, i.e. $\hbar\omega_a < E_g$, only 2PA contributes to NLA. Above the bandgap, the overall NLA stays positive as a result of positive contributions from 2PA and Raman, and negative contribution from AC Stark effect.

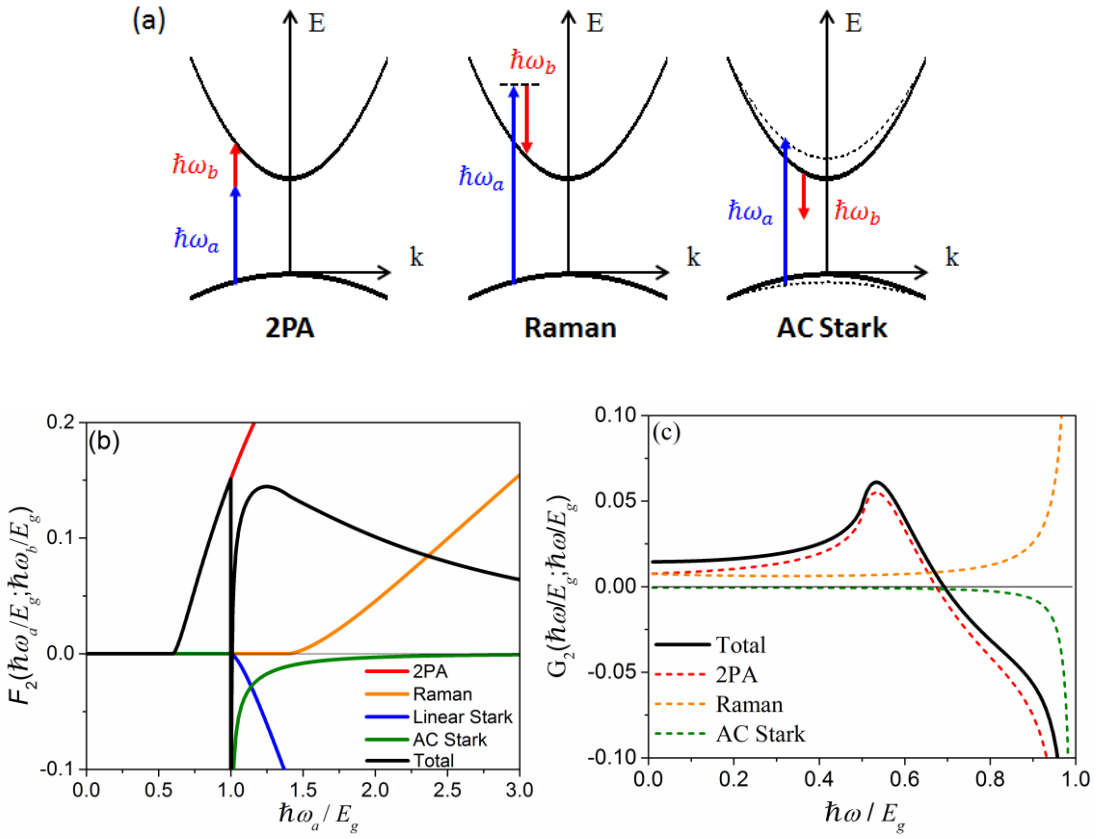

Figure 6.1 (a) Illustrations of nondegenerate NLA processes contributing to NLR in the sub-gap regime; (b) spectral functions for NLA from different mechanisms; (c) calculated degenerate NLR dispersion function G_2 with total contribution (solid line) decomposed into 2PA, Raman and AC Stark contributions (dashed lines) [45].

Based on Eq. (6.4), the nondegenerate $n_2(\omega_b;\omega_b)$ dispersion can be calculated via the KK transformation. Following [41, 45], this results in

$$n_2(\omega_a;\omega_b) = \frac{\hbar cK}{2}\frac{\sqrt{E_p}}{n_a n_b E_g^4} G_2\left(\frac{\hbar\omega_a}{E_g};\frac{\hbar\omega_b}{E_g}\right), \tag{6.5}$$

where G_2 is the dimensionless dispersion function as explicitly defined for each corresponding NLA mechanism in [41, 45]. Note K may vary by a factor of ~ 2 from one semiconductor to another due to the simplicity in the assumption of the band structure [37, 41, 45]. This simple theory results in a generality making it possible to predict NLR of various solids given the bandgap, Kane energy, linear index and optical frequencies.

In Figure 6.1 (c), the dispersion function G_2 for degenerate ($\omega_a = \omega_b$) NLR is calculated from [41, 45], which is independent of materials and therefore represents the universal nonlinear dispersion of semiconductors. The total G_2 is decomposed into contributions from 2PA, Raman, and AC Stark effect. Of these, 2PA contributes the most in the spectral region well below the bandgap, which grows from low frequencies to a maximum near $E_g/2$ (onset of 2PA) and then becomes anomalously dispersive and ultimately turns negative as $\hbar\omega$ approaches the bandgap. Experimentally, this dispersion for degenerate NLR has been verified by extensive measurements using Z-scan [41].

With highly nondegenerate photon pairs, the two-photon transition rate is greatly enhanced due to intermediate-state resonance enhancement (ISRE) of the small photon energy with the intraband self-transition and the larger photon energy with the interband transition [171, 175, 176]. This directly results in the enhancement of 2PA. For example, with same two-photon transition energy, we have previously measured 270× enhancement of $\alpha_2(\omega_a; \omega_b)$ over the degenerate counterpart in ZnSe using photons with a ratio of energies of 12 [171]. Based on the ND-2PA spectrum derived from a two-band model, the ND-NLR dispersion can be calculated via a KK transformation from Eq. (6.5). Figure 6.2 shows the calculated $n_2(\omega_a; \omega_b)$ and $\alpha_2(\omega_a; \omega_b)$ of ZnO by varying $\hbar\omega_a$ from 0 to E_g with the excitation photon energy ($\hbar\omega_b$) fixed at 20 % (1.9 μm), 15 %

(2.5 μm) and 10 % (3.8 μm) of the bandgap. The degenerate spectra of $n_2(\omega_a;\omega_a)$ and $\alpha_2(\omega_a;\omega_a)$ are also shown for comparison.

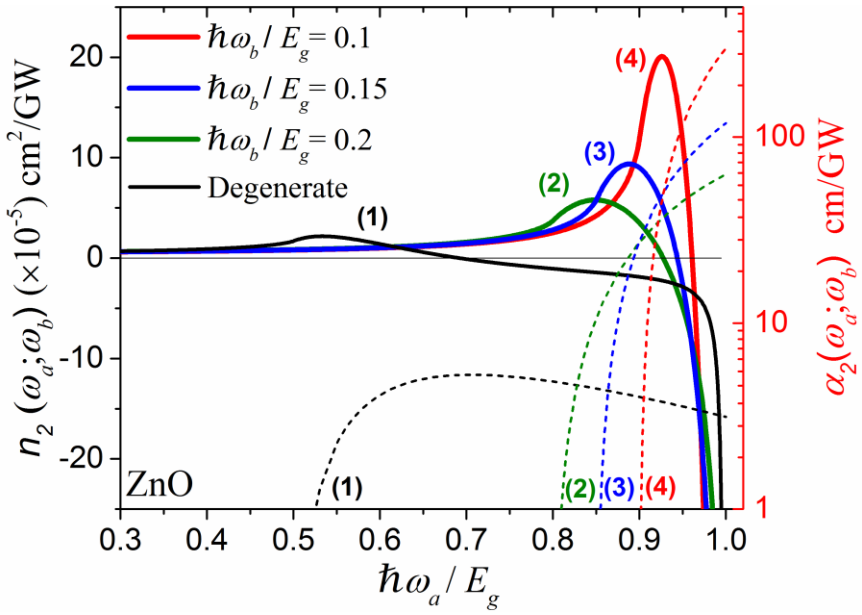

Figure 6.2 Calculated ND-NLR (solid lines) and ND-2PA coefficients of ZnO (dashed lines) with excitation photon energy $\hbar\omega_b$ of 20% (2), 15% (3) and 10% (4) of the bandgap, as compared to the degenerate case (1).

Linked by KK relation, the $n_2(\omega_a;\omega_b)$ starts with positive values for low ω_a and grows to a maximum near the ND-2PA resonance ($\hbar\omega_a = E_g - \hbar\omega_b$). Then $n_2(\omega_a;\omega_b)$ becomes anomalously dispersive and ultimately switches to negative as $\hbar\omega_a$ approaches the bandgap. Associated with ISRE of ND-2PA, $n_2(\omega_a;\omega_b)$ is positively enhanced near $\hbar\omega_a = E_g - \hbar\omega_b$, and the increase of nondegeneracy ($\hbar\omega_a/\hbar\omega_b$) results in larger enhancement. In the extremely nondegenerate case, with $\hbar\omega_b$ only ~10 % of E_g, the maximum $n_2(\omega_a;\omega_b)$ is enhanced by ~30× over its zero-frequency limit ($\hbar\omega_a = 0$), and ~ 9× larger than the maximum for the degenerate case. However, the nondegenerate NLR changes sign and is not as enhanced as the ND-2PA.

Another interesting effect arises from the extremely ND-NLR is a very steep anomalous dispersion near the bandgap, where $n_2(\omega_a;\omega_b)$ can switch sign over a very narrow spectral range. For example, with $\hbar\omega_b = 0.1E_g$, $n_2(\omega_a;\omega_b)$ changes from 11×10^{-5} cm^2/GW to -11×10^{-5} cm^2/GW by varying $\hbar\omega_a$ from 3.1 eV (400 nm) to 3.2 eV (388 nm). This rapid anomalous nonlinear dispersion provides a large modulation for a femtosecond pulse with bandwidth centered near the zero crossing frequency. This may enable other applications such as nonlinear pulse shaping. However, it should be noted that the ND-2PA is also greatly enhanced in this same spectral region. Picosecond pulses with narrow bandwidth might be required to resolve such rapid anomalous dispersion experimentally. However, one can also directly observe this nonlinear dispersion using a linearly chirped femtosecond pulse with its bandwidth centered near the zero crossing frequency of $n_2(\omega_a;\omega_b)$. This is similar to time-wavelength spectroscopy [177-180], as discussed in detail in 6.4. .

6.3. Nondegenerate Beam Deflection Measurements

To experimentally measure ND-NLR of semiconductors, we utilize our Beam Deflection technique with implementing a white-light continuum (WLC) as probe to obtain the with wavelength tunability [17, 69, 93, 95]. The principle of BD is introduced previous in 3.2.3. . The BD signal, $\Delta E/E$, is again directly proportional to $n_2(\omega_a;\omega_b)$, and the transmission change in E is proportional to the NLA (i.e. 2PA). By choosing different wavelengths of excitation and probe, BD measures the magnitudes and signs of both nondegenerate NLR and NLA as well as their temporal dynamics. These measurements also make possible the determination of the material FOM.

In this work, the Coherent Legend Elite Duo HE+ system operating at 1 kHz repetition rate is used to pump an OPA (TOPAS-800) to generate the excitation pulses from the idler beam at a

wavelength of λ_b = 2.3 μm with ~ 150 nm bandwidth (FWHM), which is then focused to a beam waist of w_b = 210 μm (HW1/e^{2}M) at the sample. The WLC probe is obtained by focusing another beam from the Ti:sapphire laser system into a 1 cm quartz cuvette filled with water, which is then spectrally filtered using narrow bandpass interference filters (10-25 nm FWHM) to select desired wavelengths in the range of λ_b = 430-750 nm. The measured beam waist of the probe for different wavelengths at the sample varies from w_b = 30-50 μm (HW1/e^{2}M). The beam crossing angle is kept $< 2°$. The linear polarization of the excitation and probe beams was maintained using polarizers and for most experiments was set to be parallel to each other; however, we also used crossed polarizations for some cases where noted. The deflection of the probe induced by the excitation pulse is detected using a quad-segmented Si photodiode (OSI QD50-0-SD) placed in the far field after the sample. Both ΔE and E are detected via a lock-in amplifier (Stanford Research Systems, SR830) at the 285 Hz modulation frequency of an optical chopper in the excitation beam. While this technique is in principle absolutely calibrated [17, 18], the relative errors between different wavelengths and samples can be reduced by comparing to a standard reference. In this work, all BD measurements of the semiconductors studied were conducted relative to the results obtained from a 1 mm thick fused silica sample using n_2 = 2.5×10^{-16} cm^2/W [120].

Since the nondegenerate excitation and probe pulse have significantly different group velocities inside of sample and NLR may be accompanied by NLA at certain wavelength, the analysis of BD in 3.2.3.2. is applied which considers both GVM and NLA. As discussed previously, the group velocity dispersion (GVD) and linear absorption are neglected here. Particularly, we use Eq. (3.14) is used to fit BD signal $\Delta E/E$ to extract corresponding nonlinear coefficients, in which with a fixed $\hbar\omega_b$, $\alpha_2(\omega_a;\omega_b)$ is nonzero only if $\hbar\omega_a \geq (E_g - \hbar\omega_b)$. For $(E_g - \hbar\omega_b) > \hbar\omega_a \geq$

$(E_g - 2\hbar\omega_b)$, the dominant NLA becomes ND-3PA, of coefficient $\alpha_3(\omega_a; \omega_b, \omega_b)$, with two photons from the excitation and one from the probe [181].

6.3.1. Dispersion of ND-NLR

Examples of measured BD signals with fits are shown in Figure 6.3, where ZnO, ZnSe and CdS along with a 1 mm thick fused silica are measured under identical beam overlapping geometries with excitation ($\hbar\omega_b$ = 0.54 eV) and filtered WLC probe ($\hbar\omega_a$ = 1.9 eV). The respective beam radii are 210 μm and 35 μm in this particular experiment.

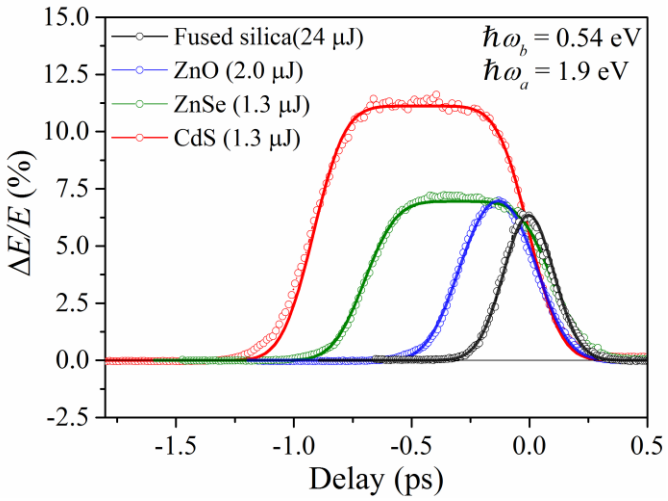

Figure 6.3 Examples of measured BD signals (circles) from ZnO, ZnSe, CdS and fused silica, along with fits (lines) considering GVM

For fused silica, the GVM between excitation and probe pulses is negligible (ρ = 0.03 [122]), therefore $\Delta E/E$ simply follows the cross correlation of the two pulses. For semiconductor samples, GVM becomes a significant factor in interpreting the measured signals, as discussed in Figure 3.8. For example, in ZnSe and CdS, the temporal walk-off between excitation and probe

within the sample results in a broadened $\Delta E/E$ towards negative delays where the probe comes prior to excitation but travels at a slower group velocity such that the faster excitation pulse catches up and walks through the probe over a distance less than L. The corresponding fits (solid lines) for each material take into account GVM using Eq. (3.14), where ρ = 3.7, 8.9 and 10.2 for ZnO [182], ZnSe [183] and CdS [184], respectively. There is a slight mismatch between experiment and fit for CdS around 1.2 ps (backside of sample), possibly due to the broadened probe pulse width after propagating through the material, as GVD is neglected in the analysis [121].

6.3.1.1. ZnO

The measured dispersion of $n_2(\omega_a;\omega_b)$ for ZnO is shown in Figure 6.4 as red circles, along with the theoretical calculations for both nondegenerate (red curve) and degenerate (black curve) cases. Errors in $n_2(\omega_a;\omega_b)$ are mainly from irradiance uncertainties as well as experimental noise in $\Delta E/E$, and those in $\hbar\omega_a/E_g$ originate from the bandwidth of the probe. In all these measurements, $\hbar\omega_b$ is fixed to ~ 16 % of the bandgap, and the WLC probe is filtered at several wavelengths from 750 nm to 440 nm to map out the dispersion of $n_2(\omega_a;\omega_b)$. With $\hbar\omega_a/E_g$ < 0.68 ($\lambda_a \geq$ 600 nm), both 2PA and 3PA are not possible, since $\hbar\omega_a + 2\hbar\omega_b < E_g$, and no NLA is observed, giving values of $n_2(\omega_a;\omega_b)$ close to the zero-frequency limit. For $\hbar\omega_a/E_g$ = 0.69 and 0.72 (570 nm and 550 nm), nondegenerate 3PA (ND-3PA) occurs, and we measure $n_2(\omega_a;\omega_b)$ along with $\alpha_3(\omega_a;\omega_b,\omega_b)$. Significantly larger $n_2(\omega_a;\omega_b)$ is measured in the 2PA spectral region of $\hbar\omega_a/E_g$ = 0.82 – 0.90 (λ_a = 480 – 440 nm) owing to the ISRE. Near the onset of 2PA (i.e. at λ_a = 480 nm), $n_2(\omega_a;\omega_b)$ is measured ~ 6× larger than the degenerate n_2 (black squares) at 1.06 μm measured via Z-scan near its zero-frequency limit [41].

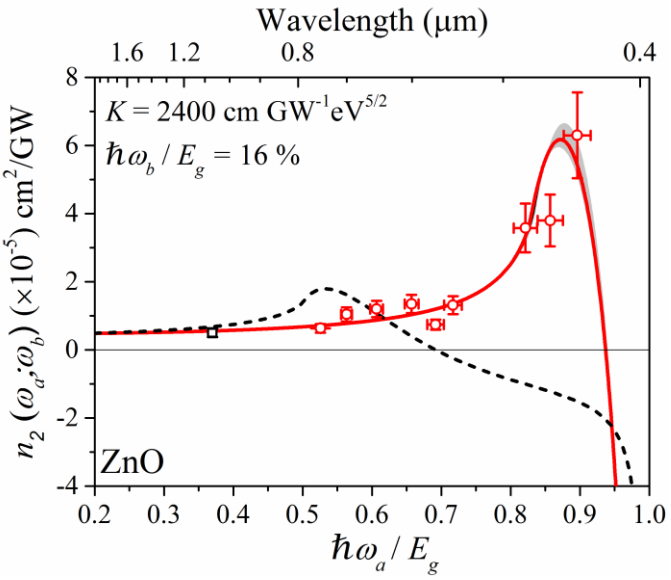

Figure 6.4 Measured $n_2(\omega_a;\omega_b)$ dispersion (red circles) of ZnO, compared to theoretical calculations for nondegenerate (solid lines) and degenerate (dashed lines) n_2; Shaded region represents errors from the bandwidth of the excitation pulse; degenerate n_2 data (black squares) is from [41].

The greatest nondegenerate enhancement in ZnO is measured at λ_a = 440 nm, where $n_2(\omega_a;\omega_b)$ is more than one order-of-magnitude larger than the zero-frequency limit [41] and ~ 3× larger than the maximum of the calculated degenerate n_2. But it should be noted that at the wavelength where $n_2(\omega_a;\omega_b)$ reaches its maximum enhancement, ND-2PA is also greatly enhanced. Using K = 2400 cm GW^{-1} eV$^{5/2}$ in Eq. (6.5), gives good agreement with the measured ND-NLR. Additionally, the dependence of $n_2(\omega_a;\omega_b)$ on the polarization of the probe with respect to that of the excitation is also investigated for selected probe wavelengths. For λ_a = 550 and 600 nm, we measure that with perpendicularly polarized waves, $n_2(\omega_a;\omega_b)$ becomes 3.2× and 2.7× smaller respectively than for the parallel polarization case. All the measured nondegenerate NLR and NLA coefficients for ZnO are summarized in Table 6.1.

Table 6.1 Measured nondegenerate NLR and NLA coefficients for ZnO.[a]

λ_a(nm)	$n_2(\omega_a;\omega_b)$	$\alpha_2(\omega_a;\omega_b)$	$\alpha_3(\omega_a;\omega_b,\omega_b)$
440	6.3 ± 1.4	2.7 ± 0.6	
460	3.8 ± 0.9	0.5 ± 0.11	
480	3.6 ± 0.8	0.3 ± 0.07	
550	1.3 ± 0.3		1.6 ± 0.4
570	0.7 ± 0.15		< 0.8
600	1.4 ± 0.3		
650	1.2 ± 0.25		
700	1.0 ± 0.22		
750	0.6 ± 0.15		

[a] n_2, α_2 and α_3 are given in the units of 10^{-5} cm^2/GW, cm/GW and 10^{-3} cm^3/GW^2 respectively.

6.3.1.2. ZnSe

In the measurements of ZnSe, with $\hbar\omega_b$ ~ 20 % of the bandgap, the increase of $n_2(\omega_a;\omega_b)$ is also observed as $\hbar\omega_a$ increases towards the 2PA resonance as shown in Figure 6.5. For longer wavelengths (λ_a = 750 – 600 nm), ND-NLR is accompanied by ND-3PA. The data of degenerate n_2 dispersion (black squares) of ZnSe is taken from previous measurements using WLC Z-scan [44] for comparison. In the spectral region where $\hbar\omega_a$ is above 70 % of the bandgap, degenerate n_2 becomes negative, as opposed to the positively enhanced nondegenerate $n_2(\omega_a;\omega_b)$ at similar probe wavelengths. A remarkable agreement is found between theoretical calculations and experimental results from both BD and WLC Z-scan measurements when using the same K = 3900 cm GW^{-1} eV$^{5/2}$, indicating the consistency of the theory in both degenerate and nondegenerate cases. This K value is similar to the previously reported K = ~4000 as the experimental best fit for ZnSe [41, 45]. For λ_a = 600 and 750 nm, with perpendicularly polarized waves, $n_2(\omega_a;\omega_b)$ is measured to be 3.7× and 2.4× smaller respectively than the values measured with parallel polarizations. Note that the theoretical model assuming a two-parabolic band structure cannot account for this effect [45], but the ratios measured for ZnSe may be used to compare to the theory considering a more

realistic band structure such as Kane's model [176, 181]. All the measured nondegenerate NLR and NLA coefficients for ZnO are summarized in Table 6.2.

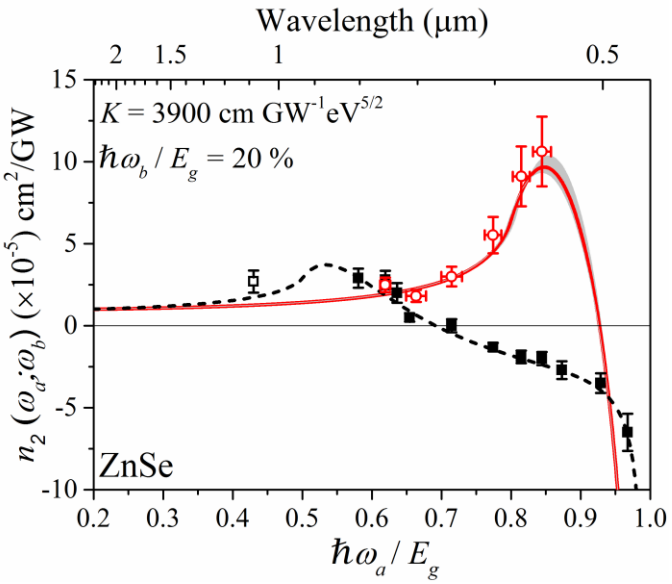

Figure 6.5 Measured $n_2(\omega_a;\omega_b)$ dispersion (red circles) of ZnSe, compared to theoretical calculations for nondegenerate (solid lines) and degenerate (dashed lines) n_2; Shaded region represents errors from the bandwidth of the excitation pulse; degenerate n_2 data (black squares) is from [41, 44].

Table 6.2 Measured nondegenerate NLR and NLA coefficients for ZnSe.[a]

λ_a(nm)	$n_2(\omega_a;\omega_b)$	$\alpha_2(\omega_a;\omega_b)$	$\alpha_3(\omega_a;\omega_b,\omega_b)$
550	10.6 ±2.5	12.5 ± 2.8	
570	9.1 ± 2.0	3.1 ± 0.7	
600	5.5 ± 1.2		63.8 ± 16.0
650	2.9 ± 0.6		38.0 ± 9.5
700	1.8 ± 0.4		25.8 ± 6.5
750	2.5 ± 0.6		38.4 ± 9.6

[a] n_2, α_2 and α_3 are given in the units of 10^{-5} cm^2/GW, cm/GW and 10^{-3} cm^3/GW^2 respectively.

6.3.1.3. CdS

Figure 6.6 shows the measured $n_2(\omega_a;\omega_b)$ of CdS with $\hbar\omega_b$ ~ 23% of the bandgap, along with the theoretical calculations with K = 3900 cm GW^{-1} eV$^{5/2}$. Besides the nondegenerate enhancement of n_2, the anomalous dispersion after the maximum, as well as the associated sign change, are also

resolved with a probe wavelength very close to the bandgap (λ_a = 570 nm and 550nm). At λ_a = 570 nm, the measured deflection and transmission signals are shown in Figure 3.9, which results in a small value of n_2 (2.2×10^{-5} cm^2/GW) with a large 2PA (13 cm/GW) background. In agreement with theory, λ_a = 570 nm is near the zero-crossing frequency of predicted $n_2(\omega_a;\omega_b)$ dispersion. All the measured nondegenerate NLR and NLA coefficients for CdS are summarized in Table 6.3.

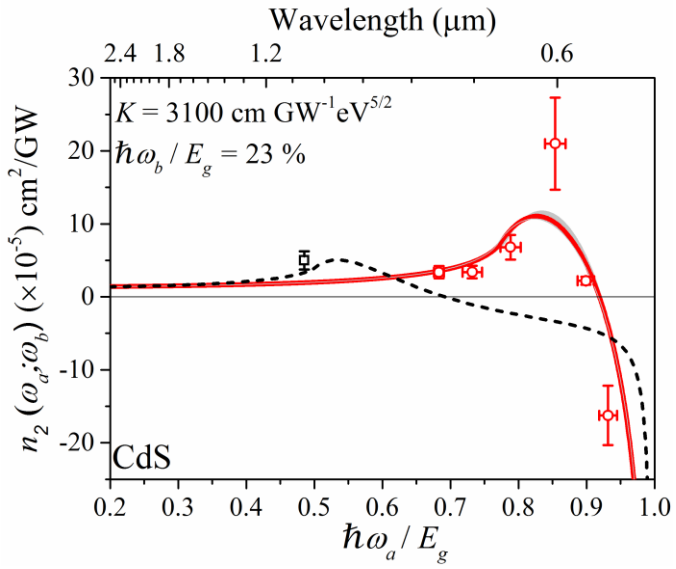

Figure 6.6 Measured $n_2(\omega_a;\omega_b)$ dispersion (red circles) of CdS, compared to theoretical calculations for nondegenerate (solid lines) and degenerate (dashed lines) n_2; Shaded region represents errors from the bandwidth of the excitation pulse; degenerate n_2 data (black squares) is from [41].

Table 6.3 Measured nondegenerate NLR and NLA coefficients for CdS.[a]

λ_a(nm)	$n_2(\omega_a;\omega_b)$	$\alpha_2(\omega_a;\omega_b)$	$\alpha_3(\omega_a;\omega_b,\omega_b)$
550	10.6 ±2.5	12.5 ± 2.8	
570	9.1 ± 2.0	3.1 ± 0.7	
600	5.5 ± 1.2		63.8 ± 16.0
650	2.9 ± 0.6		38.0 ± 9.5
700	1.8 ± 0.4		25.8 ± 6.5
750	2.5 ± 0.6		38.4 ± 9.6

[a] n_2, α_2 and α_3 are given in the units of 10^{-5} cm^2/GW, cm/GW and 10^{-3} cm^3/GW^2 respectively.

6.3.2. Nondegenerate 3PA Spectra

Just below the 2PA edge, ND-3PA should dominate the NLA, where we measure $\alpha_3(\omega_a;\omega_b,\omega_b)$ simultaneously with $n_2(\omega_a;\omega_b)$, as shown in Table 6.3 for ZnO, ZnSe and CdS respectively. These results are useful to compare to theoretical calculations of ND-3PA spectra for zinc-blende semiconductors, as introduced in [95]. Examples of measured ND-3PA signals for ZnSe with different excitation energies are shown in Figure 6.7 (a), where we use excitation ($\hbar\omega_b$ = 0.54 eV) and filtered WLC probe ($\hbar\omega_a$ = 1.65 eV). The respective beam radii are 210 μm and 45 μm in this particular experiment. To extract $\alpha_3(\omega_a;\omega_b,\omega_b)$, GVM is considered in the fits using Eq. (3.14). Since NLR and 3PA are simultaneously measured for each energy, Figure 6.7 (b) plots the percentage changes for both total transmission (NLA) and $\Delta E/E$ (NLR) in logarithmic scale, where the slopes from linear fits reveal their different irradiance dependence, i.e. linear for NLR and quadratic for ND-3PA, as indicated previously in Eqs. (2.16) and (2.17). Figure 6.7 (c) and (d) show the measured ND-3PA spectra of ZnSe and CdS, which are compared with theoretical calculations based on third-order perturbation theory and Kane's band structure [95] with a small scaling factor, i.e. 1.8× for ZnSe and 0.8× for CdS. We found good agreement between experiment and theory in both spectral dependence and magnitude, where ND-3PA is significantly larger than its degenerate counterpart due to ISRE.

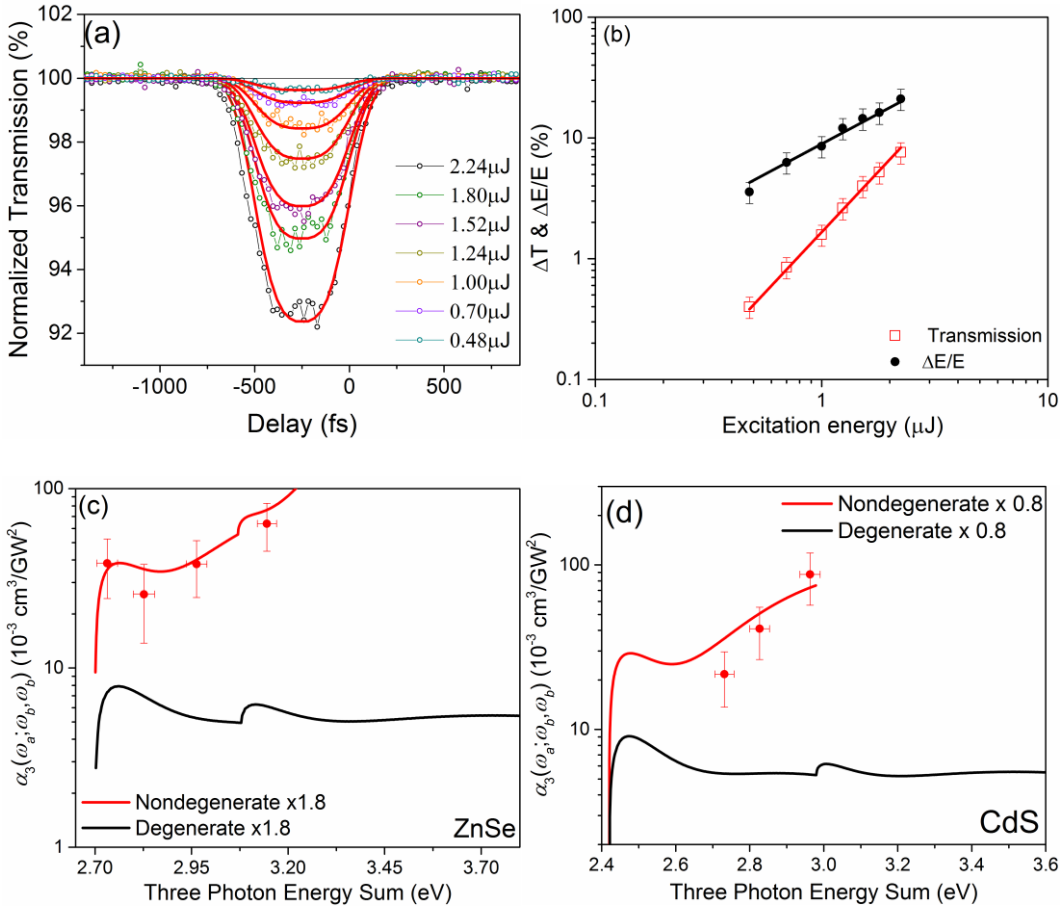

Figure 6.7 (a) Examples of ND-3PA signal in ZnSe under different excitation energies, with fits considering GVM; (b) the irradiance dependence of simultaneously measured ΔT and $\Delta E/E$; Comparisons of theory and experiment of ND-3PA spectra for (c) ZnSe and (d) CdS.

6.4. Strong Anomalous Nonlinear Dispersion

Limited by the large bandwidth of femtosecond pulses, the frequency resolution is insufficient to directly measure the absolute value of n_2 near the bandgap in the extremely nondegenerate case (e.g. ZnO in Figure 6.4), as the theory predicts a rapid anomalous nonlinear dispersion followed by a sign change in a very narrow spectral range. Here we utilize a methodology similar to time-wavelength spectroscopy [177-180] to resolve this strongly dispersive NLR.

In ZnO measurements with the same excitation of 2.3 μm, the WLC probe is filtered at a center wavelength of 430 nm to 10 nm (FWHM) bandwidth, the pulsewidth of the coming probe

pulse τ_a is determined to be ~ 500 fs (FWHM) from the cross-correlation in fused silica using the same BD setup. After propagating through the ZnO sample with a thickness of L = 0.53 mm, the probe pulse is further chirped, resulting in a pulsewidth broadening as well as changes in the instantaneous frequency due to presenting GVD [149]. Here the instantaneous probe frequency with a linear chirp is defined as

$$\omega_a(t) = \omega_{0,a} - \frac{2at}{\tau_G} \tag{6.6}$$

where $\omega_{0,a}$ is the carrier frequency of the probe (here at 430 nm), τ_G is the pulsewidth of the probe field (HW^1⁄$_e$M), a is the chirping parameter. Assuming the probe pulse is linearly up-chirped, with lower frequencies arriving before higher frequencies, a is estimated as 14 for the initial input pulse based on the measured pulsewidth and spectrum. To take into account the effect from GVD, we introduce a quadratic spectral phase $e^{i\frac{k_2}{2}L(\omega-\omega_{0,a})^2}$, where k_2 = 4158 fs^2/mm is the GVD parameter calculated from the second order derivative of the linear refractive index dispersion of ZnO in [182], i.e. $k_2 = \frac{\lambda_a^3}{2\pi c}\frac{d^2n(\lambda_a)}{d\lambda_a^2}$. This results in probe pulse is broadened to be ~ 660 fs (FWHM) at the back surface of sample, which corresponds to a = 20.5 assuming the same spectral bandwidth.

As predicted by theory [45, 95], the probe spectrum covers the zero-crossing frequency of $n_2(\omega_a;\omega_b)$ (422 nm), as shown in the inset of Figure 6.8 (b). Since the probe is linearly up-chirped, higher and lower frequency components will see a negative and positive n_2, respectively. As shown in Figure 6.8 (c), the measured $\Delta E/E$ of ZnO is greatly different from the signals shown in Figure 6.3, where the dispersion of $n_2(\omega_a;\omega_b)$ over the bandwidth of the probe is negligible. Around zero delay, the excitation temporally overlaps the rising edge of the probe pulse (lower frequency) at the front surface of the sample, giving a positive signal. A negative signal is observed

at a delay of ~ – 2.5 ps, where the excitation pulse overlaps with the falling edge of the probe (higher frequency) at the back surface of the sample. For delays in between, the excitation and probe completely walk through each other within the sample, giving an averaged small positive signal from all frequency components.

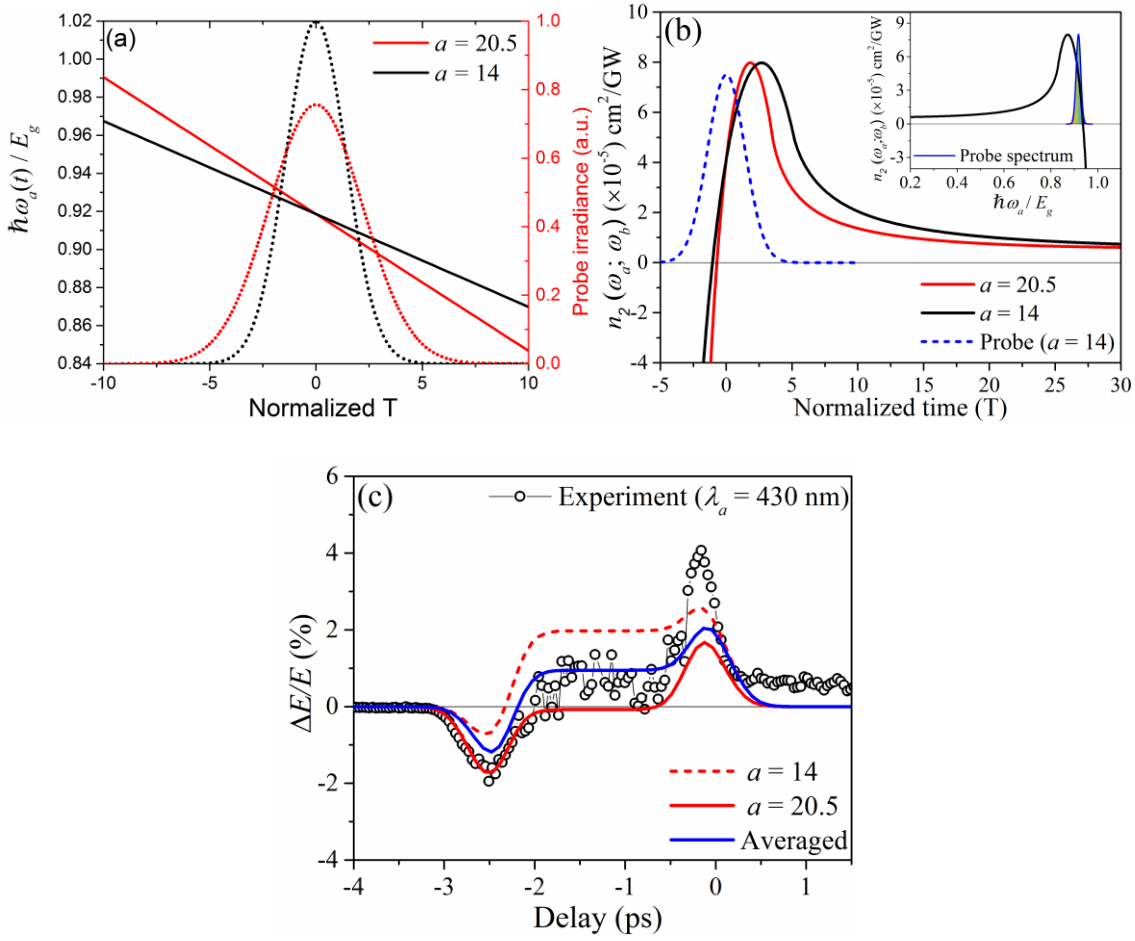

Figure 6.8 (a) Calculated probe pulsewidth (dash) and $\hbar\omega_a(T)/E_g$ (solid) using Eq. (6.6) at front (black) and back (red) of sample; (b) Converted $n_2(T)$ with different chirping conditions. Inset is the theoretical $n_2(\omega_a;\omega_b)$ dispersion (black) of ZnO relative to the probe bandwidth (blue); (c) measured $\Delta E/E$ (black circles), compared to theoretical predictions based on chirping conditions at the front (red dashed) and back (red solid) surface of the sample along with the averaged curve (blue solid).

To investigate this transient NLR quantitatively, the $n_2(\omega_a;\omega_b)$ dispersion is converted to a time-domain quantity $n_2(T)$ via the instantaneous probe frequency, where T is the normalized time defined in Eq. (3.12). $n_2(T)$ is calculated by first transfer Eq. (6.6) in to $\hbar\omega_a(T)/E_g$, as shown in Figure 6.8 (a), which is then substituted into Eq. (6.5). Figure 6.8 (b) shows $n_2(T)$ for the two different chirps at the front (red dashed) and back (red solid) surface of the sample, where the temporal profile of the probe (blue dashed) is also plotted for comparison.

Clearly, Eq. (3.14) is not applicable for predicting $\Delta E/E$ in this experiment because $n_2(\omega_a;\omega_b)$ in Eq. (3.13) cannot be assumed to be constant in the integral of *T*. But the variation of $\alpha_2(\omega_a;\omega_b)$ is negligible within the same spectral (temporal) range. For extremely ND-NLR, this anomalous dispersion is very steep within the instantaneous frequency (or temporal profile) of the probe, so that we can take a first-order approximation to obtain a linear dependence of n_2 on $\omega_a(t)$ (or *T*), giving $n_2(\omega_a;\omega_b) = n_2(T) = n_{2,0} + n_{2,1}T$. By substituting this into Eq. (3.13), the output probe field with ND-2PA becomes

$$\begin{aligned}\mathcal{E}_a = \mathcal{E}_{0,a}\exp\Bigg(&-\frac{(T-T_d-\rho)^2}{2(\tau_a/\tau_b)^2}\\ &+\frac{i\sqrt{\pi}}{2\rho}LI_{b,0}\{(2k_a n_{2,0}+i\alpha_2)(\mathrm{erf}(T)-\mathrm{erf}(T-\rho))\}\\ &+\frac{i}{\rho}k_a n_{2,1}LI_{b,0}\{e^{-(T-\rho)^2}-e^{-T^2}\}\Bigg),\end{aligned} \tag{6.7}$$

where $n_{2,0}$ and $n_{2,1}$ are derived from a linear fit of $n_2(T)$ at T = 0. Figure 6.8 (c) also shows theoretical predictions of $\Delta E/E$ calculated from Eq. (6.7) for an initial probe chirp of a = 14 (red dashed) and that after the sample of a = 20.5 (red solid). The averaged curve between the two cases (blue solid) leads to a better agreement of the shape of the NLR transients. Note an even better

agreement can be achieved by varying $n_{2,0}$ and $n_{2,1}$ as fitting parameters. Therefore, we confirm the theoretical prediction of the anomalous dispersive sign switching of extremely nondegenerate n_2 near the bandgap, which provides a large nonlinear modulation of a femtosecond pulse.

6.5. Nondegenerate Figure of Merit

Owing to the large enhancement of NLR, the nondegenerate operating scheme can be implemented into Kerr-effect based photonic devices such as AOS, where the signal beam, with $\hbar\omega_a$ close to the bandgap, can be modulated with an infrared control beam at $\hbar\omega_b$. With a larger $n_2(\omega_a;\omega_b)$, the switching irradiance of the control beam, I_{sw}, can be significantly reduced for a required nonlinear phase change $\Delta\phi = 2k_a n_2(\omega_a;\omega_b)I_{sw}L$. In practice, the nonlinear loss terms imposed by ND-2PA and ND-3PA should satisfy $2\alpha_2(\omega_a;\omega_b)I_{sw}L < 1$ and $3\alpha_3(\omega_a;\omega_b,\omega_b)I_{sw}^2L < 1$, respectively [66, 185], from which FOMs are defined by the absolute value of the ratio of $\Delta\phi$ and loss terms as

$$FOM_{2PA} = \frac{4\pi}{\lambda_a}\left|\frac{n_2(\omega_a;\omega_b)}{\alpha_2(\omega_a;\omega_b)}\right|, \tag{6.8}$$

$$FOM_{3PA} = \frac{8\pi}{3\lambda_a}\left|\frac{n_2(\omega_a;\omega_b)}{\alpha_3(\omega_a;\omega_b,\omega_b)I_{sw}}\right|, \tag{6.9}$$

where a factor of 2 is added to be consistent with other definitions (i.e. $\mathrm{FOM_{2PA}} = \left|\mathrm{Re}\left(\chi^{(3)}\right)/\mathrm{Im}\left(\chi^{(3)}\right)\right|$ [88]). For different AOS geometries, both FOMs need to be larger than 4π for a Mach-Zehnder (MZ) interferometer [66], 8π for a nonlinear directional coupler (NLDC) [41, 166] and $2/\sqrt{3}$ for a Fabry-Perot (FP) filter [172, 186]. Table 6.4 summarizes measured nondegenerate $\mathrm{FOM_{2PA}}$ and $\mathrm{FOM_{3PA}}$ for ZnO, ZnSe, and CdS based on the definitions of Eqs. (6.8) and (6.9). It should be noted that the most enhanced n_2, measured with a probe at 440 nm, 550 nm,

and 600 nm in ZnO, ZnSe, and CdS respectively, do not result in the largest FOM. This is because in the spectral region where nondegenerate enhancement of NLR is maximized, the enhancement of 2PA is even larger, leading to a smaller $\mathrm{FOM}_{2\mathrm{PA}}$ [171]. The largest FOM values measured in the 2PA spectral region are either near the onset of 2PA (i.e. 480 nm in ZnO and 570 nm in ZnSe) or near the bandgap with a negative n_2 (i.e. 550 nm in CdS).

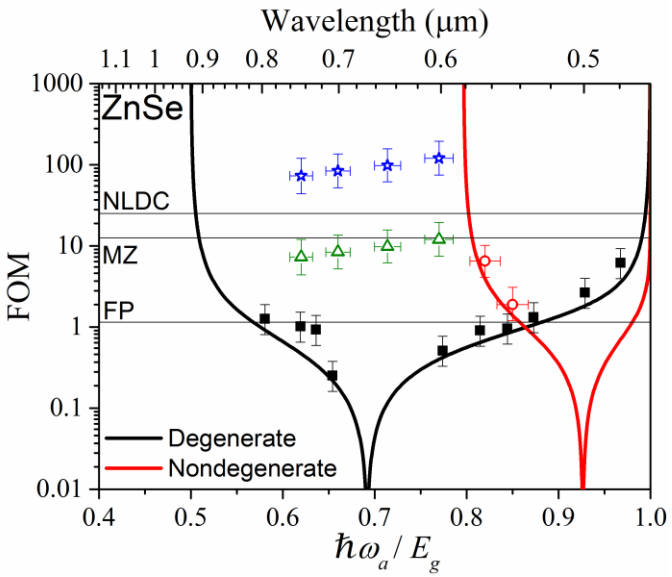

Figure 6.9 Measured FOM of ZnSe in the presence of 2PA for degenerate (black squares) and nondegenerate (red circles) NLR, as compared to theory (solid lines) [41, 45]; FOM in the presence of ND-3PA are based on I_{sw} = 10 GW/cm^2 (green triangles) and I_{sw} = 1 GW/cm^2 (blue stars). The degenerate data is from [44]. The minimum requirements for AOS geometries of a Mach-Zehnder (MZ) interferometer, nonlinear directional coupler (NLDC) and Fabry-Perot (FP) filter are included for comparison.

As an example, Figure 6.9 shows measured $\mathrm{FOM}_{2\mathrm{PA}}$ and $\mathrm{FOM}_{3\mathrm{PA}}$ of ZnSe for both degenerate and nondegenerate cases, along with theoretical curves calculated using Eq. (6.5) and $\alpha_2(\omega_a;\omega_b)$ spectra from the same two-band model [41, 45]. The degenerate data (black squares) are calculated based on the experimental results of n_2 and α_2 from [44]. Within the 2PA region, $\hbar\omega_a/E_g$> 0.5, the degenerate $\mathrm{FOM}_{2\mathrm{PA}}$ is too small to meet the criteria of all the AOS geometries,

except $\hbar\omega_a/E_g$ > 0.9 where loss from band-tail absorption increases. This essentially limits the operating wavelength of ZnSe for AOS to below half of the bandgap, λ_a> 928 nm. Such limitations may be overcome with nondegenerate enhancement of NLR. In agreement with theory, the nondegenerate $\mathrm{FOM_{2PA}}$ (red circles) near the onset of ND-2PA ($\hbar\omega_a/E_g$ ~ 81%) is measured to be ~7× larger than the degenerate $\mathrm{FOM_{2PA}}$ at the same signal wavelength of λ_a = 570 nm. The improvement over the degenerate case can become even larger with higher nondegeneracy (e.g. ~ 50× in ZnO at λ_a = 480 nm). For 0.6 < $\hbar\omega_a/E_g$< 0.8, ND-3PA becomes the dominate loss mechanism in ZnSe as ND-2PA no longer occurs since $\hbar\omega_a + \hbar\omega_b < E_g$. Based on Eq. (6.9), $\mathrm{FOM_{3PA}}$ is inversely proportional to I_{sw}. In Figure 6.9, nondegenerate $\mathrm{FOM_{3PA}}$ of ZnSe is calculated from the measured parameters in Table 6.2 using two different irradiances, I_{sw} = 10 GW/cm^2 (green triangles) and I_{sw} = 1 GW/cm^2 (blue stars), where the smaller I_{sw} results in significant improvement of $\mathrm{FOM_{3PA}}$ over the degenerate case in the same spectral region (i.e. ~ 340× at λ_a = 700 nm) and satisfies the criteria of all AOS geometries.

Table 6.4 Measured nondegenerate FOMs in 2PA and 3PA region.[a,b]

λ_a(nm)	$\mathrm{FOM_{2PA}}$ / $\mathrm{FOM_{3PA}}$		
	ZnO	ZnSe	CdS
440	6.7 (+3.8/-2.3)		
460	20.8 (+11.3/-7.6)		
480	31.4 (+18.7/-11.6)		
550	1238 (+793/-476)	1.9 (+1.2/-0.7)	1.3 (+0.7/-0.5)
570	>1286	6.5 (+3.7/-2.4)	0.37 (+0.23/-0.15)
600		120 (+75/-45)	0.88 (+0.8/-0.4)
650		98 (+60/-36)	100 (+61/-36)
700		84 (+52/-32)	99 (+61/-37)
750		73 (+47/-29)	180 (+111/-67)

[a]FOM is defined in Eqs. (6.8) and (6.9), where I_{sw} = 1 GW/cm^2 for $\mathrm{FOM_{3PA}}$.
[b]The asymmetric error bars are calculated based on the upper and lower limits of n_2, α_2 and α_3 in Table 6.1, Table 6.2 and Table 6.3.

CHAPTER 7: TWO-PHOTON PHOTOCHROMISM

As introduced in 1.2. , we are interested in investigating photochromic molecules, particularly the Spiro-type compounds, as potential materials to offer strong and broadband nonlinear absorption for ultrafast nonlinear applications. To obtain a relatively large 2PA cross section without affecting the photochromic properties, we have developed an efficient two-photon photochromic molecules by coupling a Chromene with a donating 2PA chromophore via FRET.

In this chapter, we start with a brief overview of organic photochromism. To achieve efficient two-photon photochromism, we introduce a composite molecule (denoted PC-1) in which a chromene is covalently bonded with a 2PA chromophore. Linear measurements of absorption and fluorescence spectra of PC-1 are performed, providing evidence of photochromic ring opening induced by energy transfer. By study the accumulation of open-form populations, the thermal dynamics and energy transfer processes are investigated. Finally, we present transient absorption measurements of one- and two-photon induced ring-opening, as well as ring closing dynamics.

7.1. Organic Photochromism: Molecules and Dynamics

In organic molecules, photochromism behaves as the reversible transformation within a unimolecular species activated by electromagnetic radiation [46]. Such processes lead to a cleavage and reformation of a particular chemical bond, which is referred to as ring opening and closure, respectively. Different from the photo-physical process that causes a redistribution of electronic density, a photochromic reaction, as a photo-chemical process, causes changes in the molecular levels, and atomic distances can be correlated to specific potential energy changes. Figure 7.1 (a) gives a universal description of photo-chemical reaction coordinates by using potential energy curves to represent ground and excited states for both the closed- and open-form of a photochrome. The

excited closed-form molecule can transfer with a certain quantum yield ϕ_{op} to the open-form via either a diabatic or adiabatic process, depending on whether the reaction pathway occurs within the same energy level (adiabatic) or not (diabatic). The pathway shown in Figure 7.1 (a) represents a diabatic process as an example, which is the most common one in organic photoreactions [46]. The reversing process from open- to closed-from can occur either thermally with a reversing rate k_T, or via another photochemical reaction at efficiency ϕ_{cl} by absorbing a visible photon.

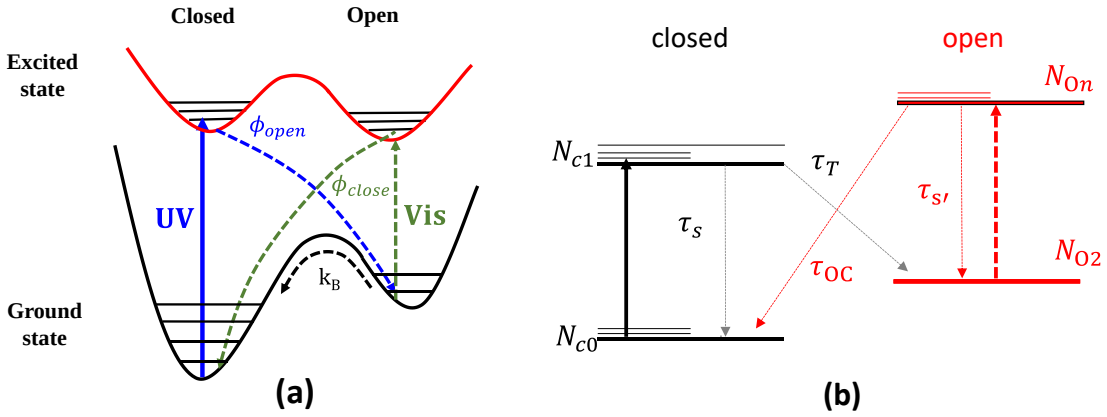

Figure 7.1 Schematic potential energy curves of general photochromic reaction (only the diabatic process is shown as an example); (b) simplified transformation diagram using molecular triplet state as an analogy.

Regardless of the fast vibrational relaxation dynamics and only taking into account the minima or maxima of both potential energy surfaces, one can treat this reversible photochromic transformation using the triplet molecular system as an analogy, as introduced in 2.3. [100, 187]. As shown in Figure 7.1 (b), the open-form, with long lifetime, is treated as the "triplet" state, where the ring opening quantum yield ϕ_{op}, defined in the same manner of the intersystem crossing rate, i.e. $\tau_s/(\tau_s + \tau_T)$. But a significant difference is there is an additional relaxation channel for the excited-state open form. Besides decaying back to its ground state, it is also possible for the open

form to transfer back to the closed form with a quantum efficiency ϕ_{cl}, i.e. $\tau_{s\prime}/(\tau_{s\prime} + \tau_{\mathrm{OC}})$. The actual photochromic reactions, e.g. τ_T and τ_{OC}, involve multiple transients (states) which may have different lifetimes and absorption cross sections. In this case, more states in Figure 7.1 (b) are needed to describe the system, as discussed in 7.4. . This methodology has been widely adopted as a phenomenological approach to describe the dynamics of photochromic ring-opening and closing reactions, and the parameters, e.g. quantum yields and absorption cross sections, can usually be determined by analyzing the experimental results from transient absorption measurements [188-190]. As opposite to thermal ring closing, the photochemically induced ring closure also occurs in only a few picoseconds, which enables the applications such as bidirectional photonic switching and erasable optical memory [58, 60, 61, 191]. However, photo reversing can be detrimental for other applications such as optical limiting [192].

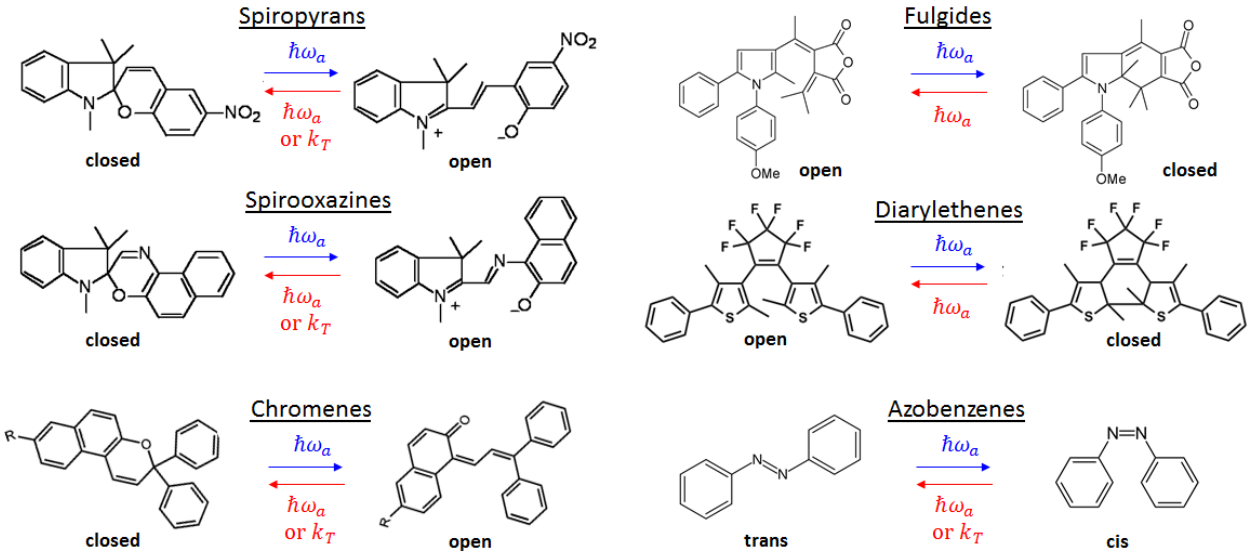

Figure 7.2 Common families of organic photochromic compounds, including both closed- and open-forms reversible transformations [46, 193].

Depending on the photo-isomerization mechanisms occurring during the ring opening process, the organic compounds can be classified into different families. Figure 7.2 shows the most universal photochromes and the associated open forms, which include Spiropyrans, Spirooxazines, Chromenes, Fulgides, Azobenzene and Diarylethenes, with photo-chemical reaction energy $h\omega_a > h\omega_b$ and thermal reversing rate k_B. Spiropyrans and related compounds such as Spirooxazines and Chromenes are probably the most intensively studied photochromic molecules and are also of the great interest to us, which, by definition, present two heterocyclic parts connected together through a typical tetrahedral Spiro-carbon atom and are undergoing a *cyclohexadiene-1,3–hexatriene-1,3,5* type photo-transformation, as shown in Figure 7.2. Note the two halves of the molecule in terms of the Spiro-carbon are orthogonal to each other, and the Benzopyran or 2H-Chromene part is the common signature of a Spiropyran type photochrome. In linear spectroscopy, Spiropyran type photochromes in the closed form usually absorb in the UV range from 200 nm to 400 nm which can lead to cleavage of the bond between the Spiro-carbon and Oxygen, and sequentially result in the open form isomer which absorbs in the visible due to the presence of the π-electron system. Note the open form isomer is also usually known as photo-merocyanine due to the Transoid (thermally stable structure) being very similar to Merocyanine [193]. Spirooxazines and Chromenes share very similar spectral and structural properties with Spiropyrans [194]. Azobenzenes are based on different photo-reaction mechanisms, because without cyclic structure they change the absorption spectrum via cis-trans isomerization. Fulgides and Diarylethenes are transparent in open-form, and upon UV radiations, the closed-form becomes absorptive in the visible spectrum. Once excited, their closed-form have extremely long lifetime, making them good candidates for optical storage memory applications [60, 193]

7.2. Two-photon Photochromism via FRET

Except for absorbing one UV photon, photochromic transformation can also be activated through absorption of two visible photons. Using 2PA instead of 1PA for inducing photochromic transformations offers tremendous advantages such as high density in three-dimensional (3D) data recording [57 , 195]. However, most of the organic photochromes have very small 2PA cross sections (δ_{2PA}), making the 2PA induced photochromic transformation inefficient. For example, a typical δ_{2PA} for a Spiropyran type photochrome is about 20 GM or less at the maximum of the 2PA spectrum [61, 196, 197]. Diarylethene derivatives show similar δ_{2PA}, i.e. 10-44 GM [62, 198]. To enhance the two-photon photochromism effect, one approach is to chemically modify the photochromic structure to achieve larger δ_{2PA}, such as attaching a molecule with the large 2PA. But usually the resulting molecule may exhibit weaker photochromic response or even lose the photochromic properties [62, 199].

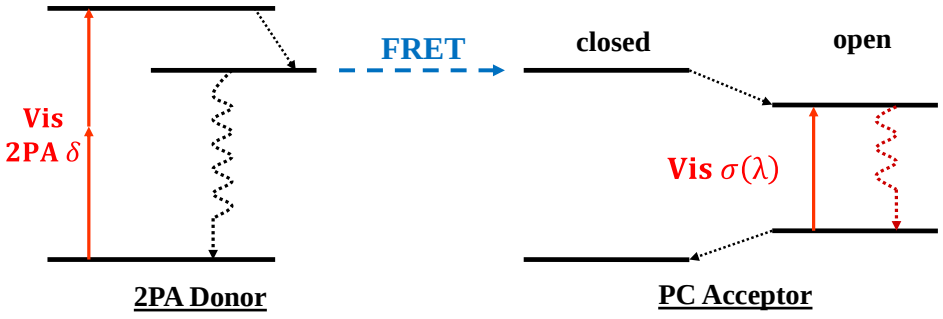

Figure 7.3 Schematic of 2PA-FRET induced photochromic ring opening mechanism.

An alternative method to achieve an efficient two-photon photochromic effect is to utilize Förster resonance energy transfer (FRET) from a donating chromophore with a large δ_{2PA} to a

photochromic acceptor. Thus the energy absorbed by the donor via 2PA is able to induce photochromic transformation by intermolecular FRET, as illustrated in Figure 7.3. Previously, we demonstrated this mechanism within a mixture of a two-photon fluorophore (4,4'- bis(2,7-dicyclohexyl-9H-carbazol-9-yl)biphenyl) and a spiroxazine-derived photochrome (2-((1,3,3-trimethylspiro[indoline-2,3'-naphtho[2,1-b][1,4]oxazine]-5'-yl)methylene)malononitrile) [200, 201]. Another experiment with mixture of diarylethene-derived photochromes with 2PA chromophores gives a two-fold enhancement in the open-form absorption induced by 2PA, compared to pure photochromic species [202]. As discussed later in 7.2.2. , FRET efficiency is strongly dependent on the separation of donor and acceptor moieties, which requires high concentration for both 2PA chromophore and photochrome in the mixture experiment.

Here, we present a newly synthesized bifunctional molecules involving a 2,7-bis(carbazolyl)fluorene-derived 2PA moiety covalently linked to a chromene-derived photochromic moiety, referred as "PC-1" [203]. Different from chemical modification of photochrome itself, this composite molecule is designed to mitigate electronic interaction between the 2PA chromophore and chromene. The samples are provided by *Aix Marseille Université* and *Soreq*.

7.2.1. Molecular Structure and Linear Characterizations

As shown in Figure 7.4 (a-c), the composite molecule PC-1 is synthesized by covalently link a photochrome, 2H-benzo[h]chromene (2H-naphtho[1,2-b]pyran), with a 2PA chromophore (denoted M-106), 9,90-(9-(3-hydroxypropyl)-9-methyl-9H-fluorene-2,7-diyl)bis-9H-carbazole. The distance between the photochromic and the 2PA moieties is about 5–6 Å, which is calculated from B3LYP/6-31G(d) geometry optimization [203]. This distance is short enough to provide efficient

FRET and, in the meantime exclude the possibility of through-bond and through-space intermolecular electronic interaction [203]. It has been shown in Ref. [203], by substituting the amino group in *para*-position of one of the phenyl groups, shorter distance between the two moieties can be obtained. Additional investigations on the thermal motion of atoms in molecules is carried out using Oak Ridge Thermal Ellipsoid Program (ORTEP) representations, as shown in Figure 7.4 (d), which indicates a distance of ~ 6.9 Å between 2PA and photochromic moieties for a "unfolded" confirmation, where the orthogonal geometry may result in negligible electronic interaction between them [203].

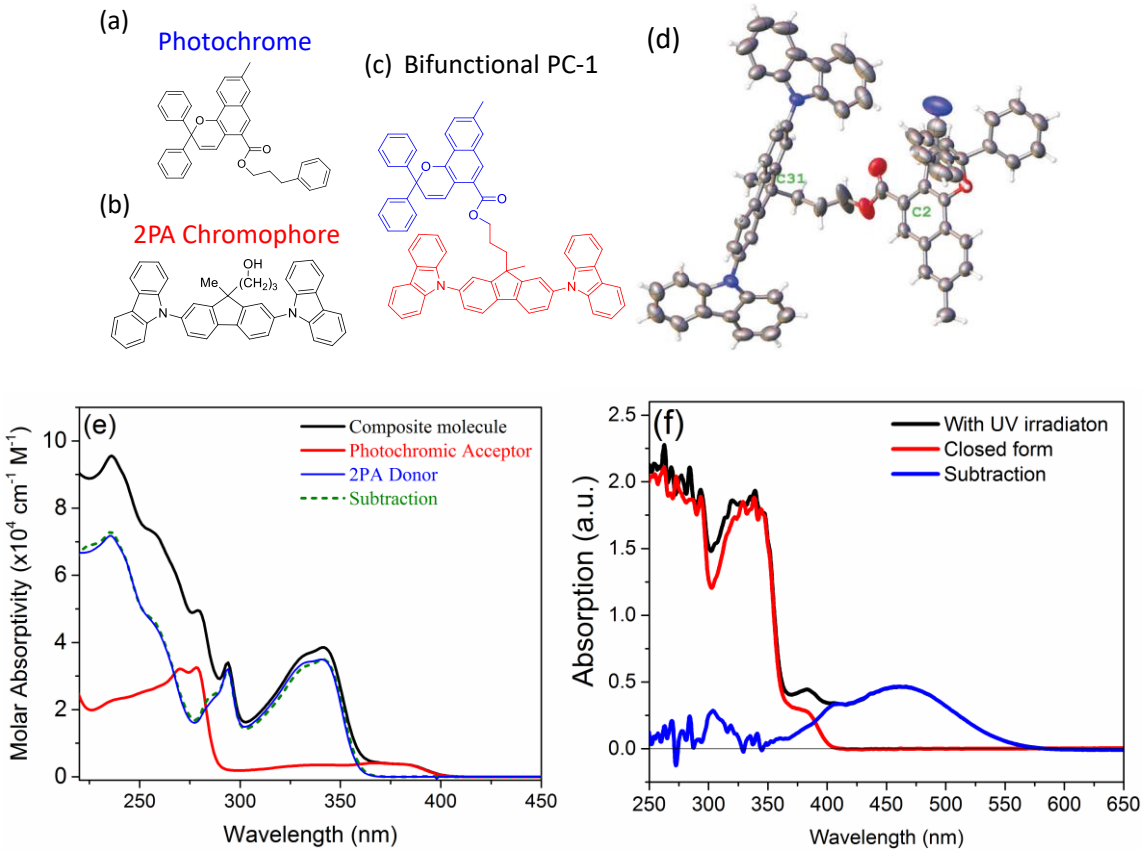

Figure 7.4 Molecular structures of (a) photochrome, (b) 2PA chromophore and (c) composite molecule PC-1; (d) ORTEP representation of the molecular structure of PC-1 with a distance between C2 and C31 of 6.923 Å [203]; (e) the linear absorption spectra in DCM of PC-1, photochrome, and their subtraction, as compared to that of the pure 2PA chromophore; (f) The absorption spectra in DCM of closed-form PC-1, after UV illumination (closed- and open-form mixture form) and the subtraction between them.

The molar absorptivity spectra of composite molecule (PC-1), M-106 and photochrome are measured in dichloromethane (DCM) solutions using Cary500 Spectrophotometer, as shown in Figure 7.4 (e). The subtraction of the absorption spectra of PC-1 and photochrome matches that of M-106, indicating negligible electronic interaction between these two moieties. The relatively weaker absorption band of the PC-1 at 370 – 400 nm originates from the photochromic moiety, and the stronger band between 300 – 370 nm is from the absorption of M-106, with a peak value of ~ 4×10^4 $M^{-1}cm^{-1}$. To show the effect from ring opening, we fill the PC-1 solution with concentration of 7.8×10^{-5} M into a 1 cm fused silica cuvette, the absorption spectrum is measured by using the Ocean Optics Spectrometer HR4000 with a focused white-light beam from a Xenon lamp as the light source. Figure 7.4 (f) shows the spectra before and after illumination by 170 μJ, 355 nm picosecond pulses for ~30 seconds, and the subtraction between them. As a results of ring opening, a broad absorption band forms in the visible spectrum, i.e. 400-600 nm. The absorption in the UV (i.e. <350 nm) remains relatively unchanged for both open and closed form, which is consistent with the results observed in [203].

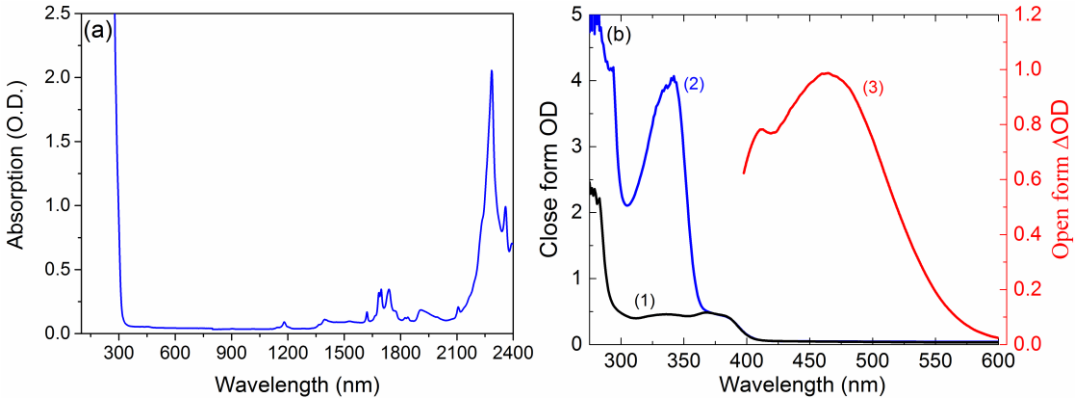

Figure 7.5 Linear absorption spectra of (a) blank and (b) dye-doped sol-gels with (1) photochrome, (2) PC-1; (3) shows the visible absorption spectrum of open-form from a PC-1 doped sol-gel.

PC-1 has also been doped into sol-gel materials [55]. Sol-gel material is a glassy inorganic-organic hybrid matrix prepared by the fast sol-gel process, which are solidified without shrinkage or formation of cracks and present promising transparency and thermal stability properties for optical applications [53]. The linear absorption spectra of a blank sol-gel is shown in Figure 7.5 (a), where the sol-gel host itself only absorbs in UV, i.e. < 300 nm, and nearly transparent in visible spectral range. The absorption peaks in infrared denote the finger prints of the sol-gel material. The linear absorption spectra of sol-gels doped with PC-1 and pure photochromes are shown in Figure 7.5 (b), which are similar with the spectra measured in DCM solutions as shown in Figure 7.4 (e). Upon excitation using a HeCd CW laser at 325 nm, the open-form PC-1 also gives a broad-band absorption spectrum in visible, centered at ~ 465 nm as observed in DCM solutions. Since molecules are localized in the sol-gel matrix without diffusion, the characterizations of thermal dynamics of photochromic molecules are convenient, as discussed in 7.3.1. .

7.2.2. Theoretical FRET Efficiency

As first recognized in 1949 [204], FRET is a rather common phenomenon. It has been widely applied in numerous applications such as optical sensors and switches [205], for tracking dynamics and understanding biological systems [206]. The main mechanism of FRET starts with a donor fluorophore being excited into an excited state, which might transfer its resonant energy to an adjacent acceptor chromophore via a non-radiative dipole-dipole interaction. The efficiency of FRET processes is very sensitive to donor-acceptor molecular pair structures, and contains a significant amount of information regarding each moiety. The FRET efficiency depends on multiple factors: 1) the spectral overlap between donor fluorescence and acceptor absorption; 2) the average

distance between donor and acceptor moieties; 3) the relative dipole orientation and 4) the fluorescence lifetime of the donor. It has been shown that the FRET efficiency ϕ_{FRET} is inversely proportional to the 6$^{\mathrm{th}}$ power of the distance r between donor and acceptor,

$$\phi_{\mathrm{FRET}} = \frac{R_0^6}{R_0^6 + r^6}, \tag{7.1}$$

where R_0 is known as the Förster radius. For $r = R_0$, the FRET efficiency is 50%. Theoretically, R_0 can be calculated from

$$R_0^6 = 8.79 \times 10^{-25}\left(\kappa^2 n^{-4} Q_D J(\lambda)\right), \tag{7.2}$$

where κ^2 is a factor describing the relative orientation of the dipoles, which is usually taken as $\kappa^2 = 2/3$ for isotopically oriented donor and acceptor molecules [200, 205]; n is the refractive index of the material, Q_D is the donor's fluorescence quantum yield, and $J(\lambda)$ is the spectral overlap integral of the donor's fluorescence emission and the acceptor's absorbance spectrum, which is given by

$$J(\lambda) = \int_0^\infty F_D(\lambda)\varepsilon_A(\lambda)\lambda^4 d\lambda, \tag{7.3}$$

where $F_D(\lambda)$ is the corrected fluorescence spectrum of the donor with the total intensity normalized to unity, and $\varepsilon_A(\lambda)$ is the molar absorptivity spectrum of the acceptor.

The fluorescence spectrum of donor from a low concentration DCM solution (2.6×10^{-6} M) M-106 is measured using the PTI Quantamaster spectrofluorometer, which shows a maximum ~ 360 nm stokes-shifted from its absorption peak (~ 340 nm), as shown in Figure 7.6 (a). The quantum yield Q_D is determined to be ~ 80%, using Rhodamine 6G in ethanol with Q_D = 95% as a reference [115, 207]. By integrating the normalized the fluorescence spectrum of M-106 with the absorption spectrum of photochrome using Eq. (7.3), we obtain the spectral integral function

$J(\lambda)$, as shown in Figure 7.6 (b), from which we determine the Förster radius as $R_0 = 0.7$ nm. With a donor acceptor distance of $r \sim 5 - 7$ Å determined from quantum chemical calculation [203], the FRET efficiency is estimated to be 50 – 88%. With better spectral overlap, i.e. larger $J(\lambda)$, the FRET efficiency can be improved.

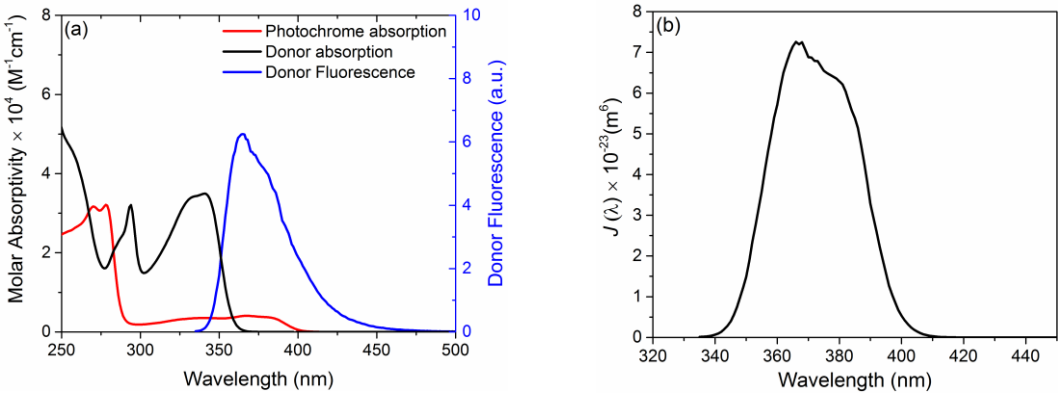

Figure 7.6 (a) Linear absorption spectra of photochrome (red) and M-106 (black), along with the fluorescence spectrum of M-106 (blue); (b) calculated spectral integral function $J(\lambda)$.

7.2.3. Experimental Evidence of FRET

The effect of FRET is investigated in detail via transient absorption measurements with a two-photon excitation, as discussed in 7.4.2. . Here, we present the results from linear characterizations using fluorescence excitation and anisotropy techniques, which serve as indirect evidence of energy transfer within the composite molecule PC-1.

The fluorescence emission spectra of PC-1 and pure photochrome are measured with excitation at 330 nm, where the spectrum from PC-1 exhibits two distinct bands, as shown in Figure 7.7 (a), coinciding with the bands observed for pure photochrome (peak at 420 nm) and M-106 (peak at 360 nm) measured in Figure 7.6 (a). By measuring fluorescence quantum yield, we notice

a strong quenching from ~ 80% in donor M-106 to ~ 1% in composite molecule PC-1, which is an indication of internal energy transfer from 2PA donor to photochromic acceptor [208].

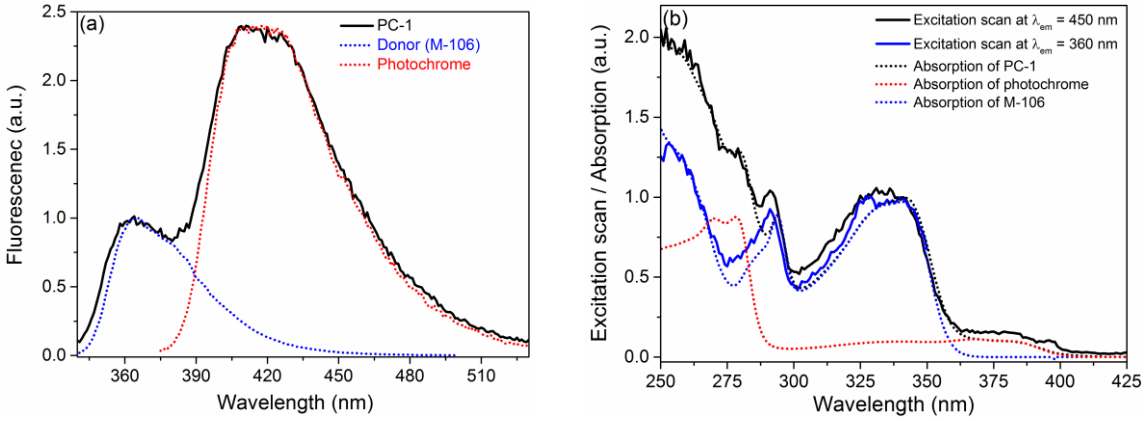

Figure 7.7 (a) Fluorescence spectra of PC-1, M-106 and photochrome in DCM; (b) excitation scans of PC-1 (solid) with fixed emission wavelength at 450 nm (black) and 360 nm (blue), in comparison to absorption spectra (dash) of PC-1 (black), M-106 (blue) and photochrome (red).

To verify the origins of the fluorescence bands, excitation scan is performed by fixing the fluorescence emission at a particular wavelength λ_{em} and monitoring the fluorescence intensity by varying the excitation wavelength [208]. Figure 7.7 (b) shows the results after correction using the spectrum of the Xenon lamp. At an emission wavelength of 360 nm, the excitation scan contour follows the absorption spectrum of M-106, further confirming its origination from the donor moiety. At λ_{em} = 450 nm where the fluorescence emission is only contributed by the photochrome (see Figure 7.7 (a)), the excitation scan contour follows the absorption spectrum of the PC-1 (black dash), which serves as another indication that the photon energy absorbed by the donor may be transferred to the acceptor, leading to fluorescence emission from photochrome. If there were no internal energy transfer between donor and acceptor, the excitation scan at 450 nm would follow

the absorption spectrum of the photochrome (red dash). Thanks to the covalent bonding between donor and acceptor moieties, FRET is able to observe in extremely diluted solutions.

Another evidence of energy transfer within the composite molecule PC-1 may be from one-photon fluorescence anisotropy measurements. As introduced in [209], anisotropy f is related with the angle between absorption transition (excitation polarization) and fluorescence emission dipole moment β by

$$f = f_0 \frac{3\cos^2\beta - 1}{2}, \tag{7.4}$$

where $f_0 = 0.4$ is the maximum of anisotropy derived from orientational averaging considering photoselection rule . For large angle of β, $f < 0.4$ corresponding to a depolarization between excitation and emission. This usually indicates higher lying excited states which are 1PA forbidden but possibly accessible through 2PA. Therefore, one of the application of anisotropy measurements is to locate possible wavelengths where 2PA occurs. An example is discussed in Figure 7.16.

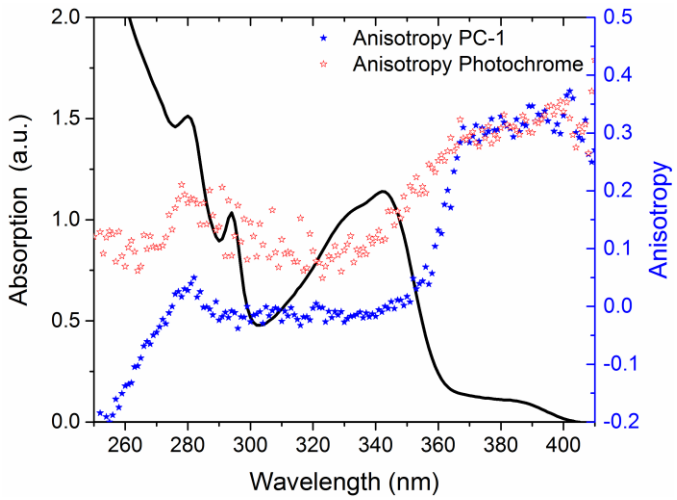

Figure 7.8 (a) Fluorescence anisotropy measurements of PC-1 (blue) and photochrome (red), as compared to the absorption spectrum of PC-1 (black) in dichloromethane.

There are other processes that may also cause depolarization within the lifetime of the excited state, e.g. nanoseconds. For example, the molecular reorientation in most solvents occurs in several picoseconds, as measured and listed in Table 4.3. Reabsorption may also result in depolarization. To mitigate these effects, highly viscous solvents, e.g. glycerol and poly-tetrahydrofuran (p-THF) with low concentration of molecules need to be used.

Alternatively, energy transfer processes may also depolarize the fluorescence from the excitation polarization. Figure 7.8 shows the fluorescence anisotropy measurements of pure photochrome (red) as well as composite molecule PC-1 with the emission wavelength of 450 nm at which only the fluorescence of photochrome contribute. Compared to the absorption spectrum of PC-1, we found within the absorption band 360 – 400 nm that originates from photochrome, both molecules show similar anisotropy, i.e. ~ 0.3, indicating small fluorescence anisotropy. However, within the absorption band that donor mainly contributes, i.e. 300 – 360 nm, the anisotropy measured from PC-1 is significantly smaller than photochrome, which is possibly because the fluorescence emitted from photochrome moiety is induced by the energy transfer from donor moiety.

7.3. Cumulative Measurements with Sol-gels

As introduced in 7.2.1. , sol-gel matrix localizes the molecules which allows measurements to be performed over a long time. This is particularly useful to study the thermal dynamics of photochrome, i.e. thermal reversing process, as the lifetime of the open form is usually too long in which diffusion in solutions may become a problem for tracking the absorption change of the molecule. In this section, the thermal dynamics are characterized from a dye-doped sol-gel. By study the dependence of open-form population accumulation on the excitation energy, we can determine the open-form molar absorptivity spectrum as well as the energy transfer efficiency.

7.3.1. Thermal Dynamics

Upon UV excitation, the open-form photochrome shows a broad absorption band (400-600nm) with a peak absorbance ΔOD at 460 nm, as discussed in Figure 7.5. Here, a chromene doped sol-gel slab with thickness of 1 mm is excited with UV radiation at 355 nm. At steady state, the UV induced ring opening and thermal reversing reach an equilibrium. The thermally reversible process of the composite sol-gel was studied by tracking the spontaneously decaying of ΔOD after the excitation is blocked at room temperature. As shown in Figure 7.9 (a) in logarithmic scale, the normalized open-form ΔOD at 460 nm decays from two initial states: with higher excitation energy, ΔOD decays from 0.9; with lower excitation energy, ΔOD decays from 0.6. Both are fitted with a triple exponential decay function with the same three time constants, i.e. 63 ± 5 s (τ_1), 530 ± 30 s (τ_2) and 24400 ± 500 s (τ_3). The results indicate that open-form isomers with different thermal stabilities are formed upon excitation [210]. However, we notice these isomers have similar spectra, as shown in Figure 7.9 (c). This was examined by comparing the normalized ΔOD spectrum at different times, i.e. 5 s and 9060 s, after blocking excitation.

We also observed that the recover process from the open form can be significantly speeded up by illuminating the sample with a CW laser light at 532 nm. As shown in Figure 7.9 (b), the UV excitation is applied at time zero, and the open-form photochrome starts to accumulate and reach a steady state after a few minutes. After the excitation is blocked at 412 s, thermal reversing occurs at first to recover the open form back to the closed form. After ~ 30 minutes, the remaining ΔOD is mainly due to those long-lived open-form isomers. At the time of 2816 s, a ~ 1 mW CW beam at 532 nm is illuminated on the sample with a spot size of ~ 0.5 mm (HW1/e^2M), which significantly speeds up the recovery, e.g. the ring closing nearly completes within only a few minutes, as shown in the inset of Figure 7.9 (b).

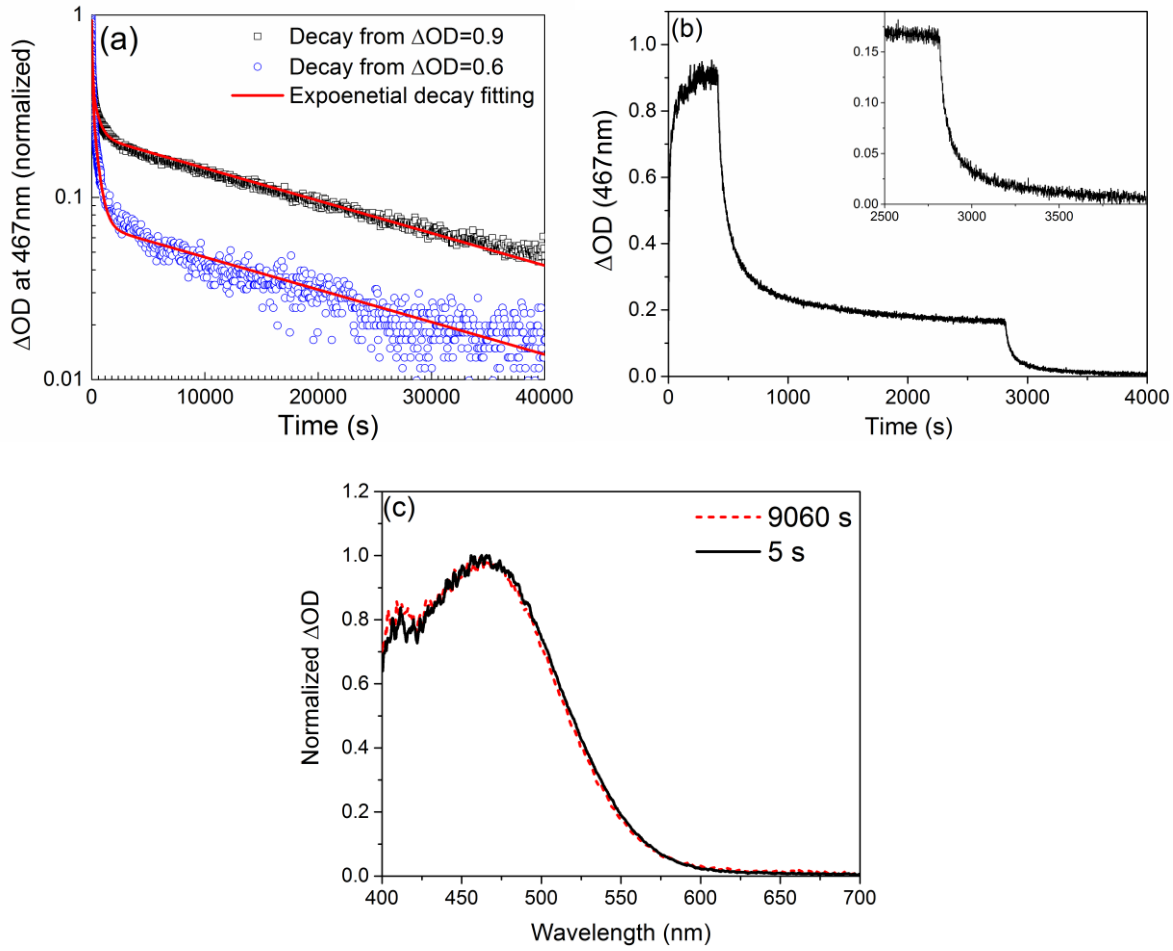

Figure 7.9 (a) Thermal reversing dynamics measured at 460 nm, recovering from two initial conditions: ΔOD=0.9 (black) and ΔOD=0.6 (blue). Both are fitted with triple exponential decay functions using same time constants. (b) thermal reversing of open form after excitation being blocked at 412 s; recovering process is speeded up by illumination of a 532 nm CW beam at 2816 s; (c) normalized ΔOD spectra at 5 s and 9060 s during thermal reversing.

7.3.2. Open-form Accumulation

Since the open-form is thermally unstable, the determination of molar absorptivity (ε_{op}) is difficult. Here, we present a methodology to measure the population accumulation of the open-form molecules in a sol-gel sample, from which the open-form molar absorptivity and ring opening efficiency can be determined with a limited accuracy. Although this approach does not provide

complete information of the photochromic reaction which usually requires transient absorption measurements, it serves an easier approach to evaluate the overall efficiency [55].

In this experiment, the sol-gel sample was excited using a HeCd laser emitted at a wavelength of 325 nm. A white-light beam from a Xenon lamp is used to probe the open-form ΔOD in visible spectral ranges. The transmission of the probe was collected into a spectrometer and the spectra of ΔOD were measured in real time. Since the closed and the open forms have very similar absorption cross section at 325nm (see Figure 7.4 (d)), the absorption at the excitation wavelength does not change during the process of ring opening. Therefore, the excitation irradiance distribution across the path length of the sol-gel sample can be treated independent of time and decays exponentially along the sample path length z, i.e. $I_e(I_0, z) = I_0 10^{-\varepsilon_c N_0 z}$, where I_0 is the input irradiance, ε_c is the molar absorptivity at excitation wavelength and N_0 is the initial population of closed form. Upon excitation, the closed form transfers to open form, and in the meantime thermal reversing acts as a competing mechanism decreasing the open-form population. Compared to the thermal reversing timescale, i.e. seconds, the transition from closed form to open form is nearly instantaneous, which allows us to evaluate this process by using a simple two-level system. By treating the closed and open forms as ground and excited states respectively, a rate equation is applied to describe closed- (N_c) and open- (N_{op}) form population changes in terms of I_0, time t and z

$$\frac{dN_{op}(I_0, z, t)}{dt} = \alpha_c(I_0, z, t)\frac{I_e(I_0, z)}{h\nu} - \frac{N_{op}(I_0, z, t)}{\tau}, \tag{7.5}$$

where $h\nu$ is the photon energy of excitation, τ is the thermal reversing time constant measured in Figure 7.9 (a) and $\alpha_c(I_0, z, t)$ is the effective absorption coefficient at 325 nm, which only accounts

for the absorption from closed-form molecules and becomes smaller as more molecules accumulate in the "open state". Here, $\alpha_c(I_0, z, t)$ is taken as

$$\alpha_c(I_0, z, t) = \Big(N_0 - N_{op}(I_0, z, t)\Big)\,\sigma_c \phi, \tag{7.6}$$

where σ_c is the absorption cross section which is related with molar absorptivity in SI units by $\sigma_c = \mathrm{Ln}[10]\varepsilon_c$; ϕ is the efficiency term. By substituting Eq. (7.6) to (7.5), $N_{op}(I_0, z, t)$ can be solved for any time t during the accumulation, which results in ΔOD due to ring opening by integrating across the sample thickness L

$$\Delta\mathrm{OD}(I_0, t) = \varepsilon_{op} \int_0^L N_{op}(I_0, z, \mathrm{t})\, dz, \tag{7.7}$$

The first sample is a 0.9 mm thick sol-gel doped with mixture of photochromes and M-106 with different concentrations. The linear absorption spectrum of this mixed sol-gel is shown in Figure 7.10 (a), from which the concentrations are found to be ~ 0.9 and 0.18 mM for photochrome and M-106 respectively, using their molar absorptivity spectra in Figure 7.4 (e). At this low concentration, the distance between them is too long for energy transfer to occur, so the energy absorbed by M-106 does not contribute to ring opening, but it is still important to consider in order to calculate the irradiance distribution across the sample pass length, i.e. $I_e(I_0, z)$. By solving Eq. (7.6) and (7.5), the accumulation of $N_{op}(I_0, z, t)$ can be calculated for any input peak irradiance I_0, at any time t after turning on the excitation and at any path length z inside of the sample. Figure 7.10 (c) shows the calculated steady state $N_{op}(I_0, z, t \to \infty)$ for various I_0 and z, from which the overall attenuation in visible (or ΔOD) due to ring opening can be found using Eq. (7.7). In practice $t \to \infty$ is not realizable, we need to estimate how long of excitation time is good for the steady-state approximation. By only considering the fast thermal reversing process, i.e. 63s (τ_1) measured

in Figure 7.9 (a), we found with a particular I_0, ring opening builds up in time and reaches an equilibrium with thermal reversing after turning on the excitation for ~ 300 s, as shown in Figure 7.9 (d). Note N_{op} shown here is averaged for entire sample thickness z.

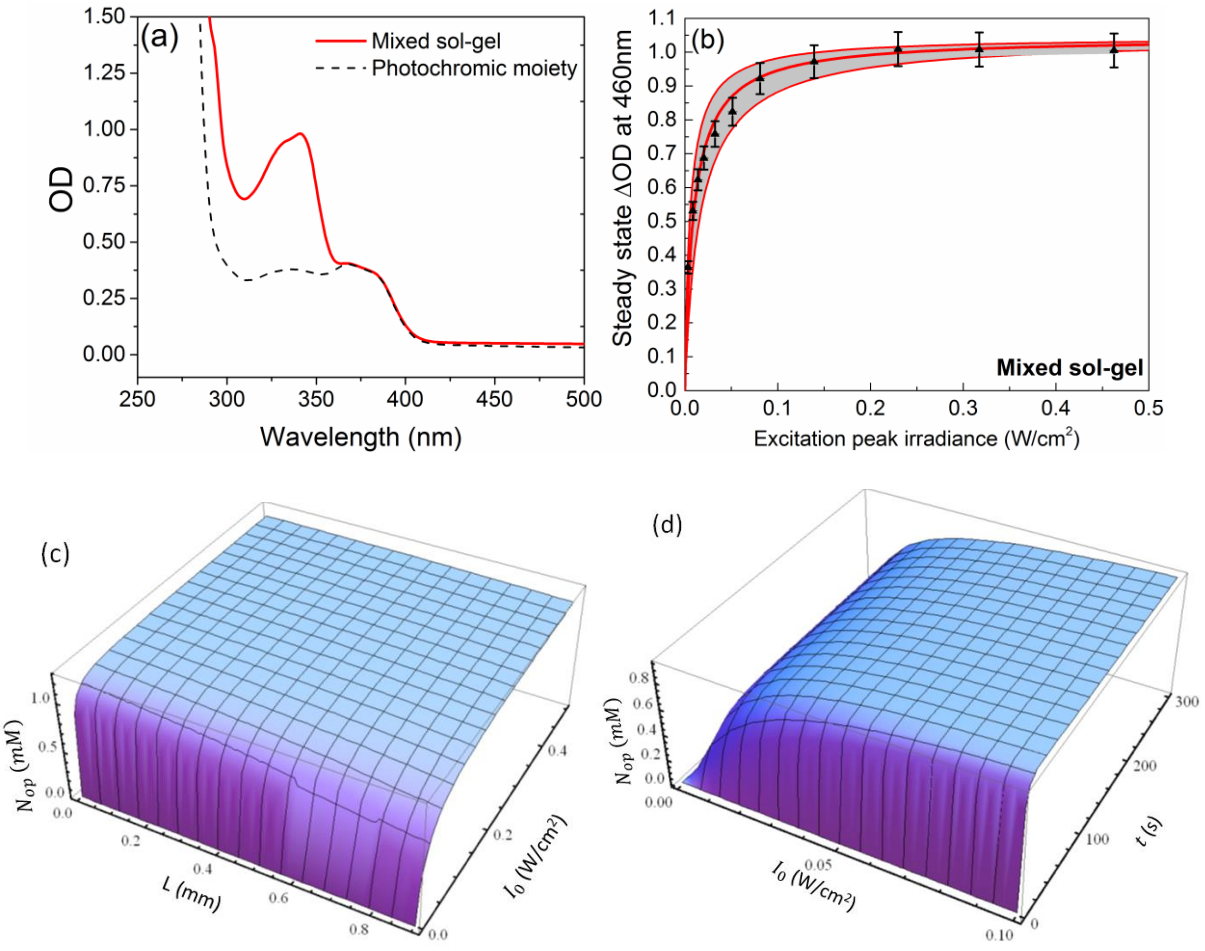

Figure 7.10 (a) Linear absorption spectrum (red) of a sol-gel doped with mixture of M-106 and photochrome with different concentration; (b) measured (black) irradiance dependence of open-form ΔOD of mixed sol-gel at 460 nm and fits (red) using $\varepsilon_{op} = 9700$ M^{-1}cm^{-1} with $\phi = 10$, 20 and 30 %, where the shaded area represents the values of ϕ in between; (c) steady-state accumulation of N_{op} for different I_0 and z; (d) accumulation build-up of a N_{op} averaged over z.

The measured steady-state ΔOD at 460 nm due to ring opening is shown in Figure 7.9 (b) with different peak excitation irradiance. A fit is applied using Eq. (7.7) by varying ε_c and ϕ. The

accumulation of open-form molecules increases for higher input irradiance, and eventually become saturated. This is consistent with the modelling in Figure 7.9 (c), where with $I_0 > 0.2$ W/cm^2 most molecules are opened and uniformly distributed across z. Therefore, the data from higher irradiance provides a good fit for $\varepsilon_{op} = 9700 \pm 500$ M^{-1}cm^{-1} from the magnitude at saturation. The lower irradiance data, where the ΔOD is rapidly changing, is more sensitive to ϕ. Here, we fit with $\phi = 20 \pm 10$ %, where the uncertainties represented as the upper and lower limits of the shaded region. Here, ϕ is the ring opening efficiency ϕ_{op}, which is more rigorously characterized in 7.4. via transient absorption measurements.

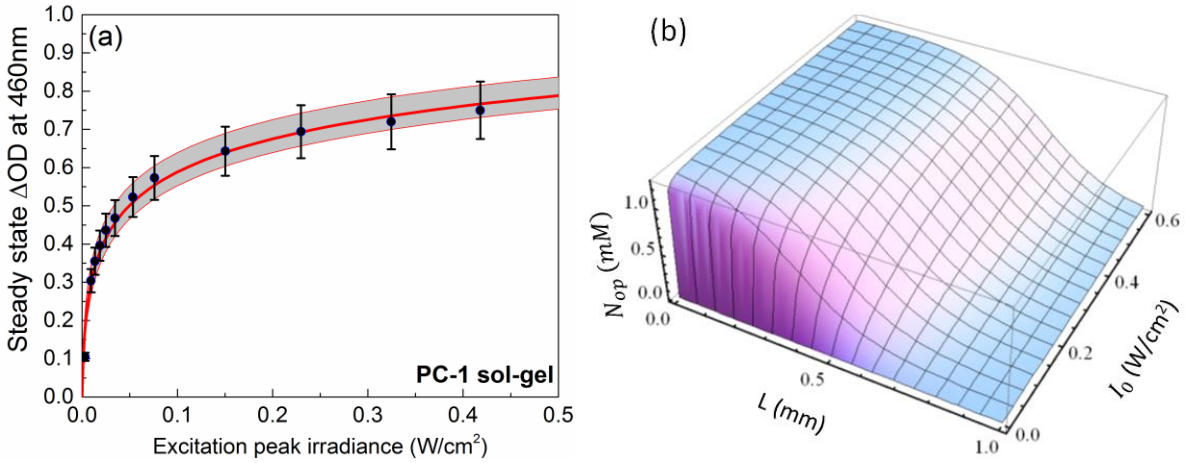

Figure 7.11 (a) Measured (black) irradiance dependence of open-form ΔOD of composite sol-gel at 460 nm and fit (red) with the same ε_{op} measured in Figure 7.10 (b) and $\phi = 8$, 10 and 12 %; (b) steady-state accumulation of N_{op} for different I_0 and z.

A similar study is applied to a 1 mm thick sol-gel slab doped with 1.2 mM composite molecule PC-1. The linear absorption spectrum is shown in Figure 7.5 (b). Due to the higher concentration of donor moiety compared to the mixed sol-gel, the excitation at 325 nm experiences significant attenuation as propagating through the material. The steady-state distribution of the opened molecules is shown in Figure 7.11(b), where the ring opening occurs mostly at front surface

of sample. Upon excitation, both donor and photochromic moieties absorbs at 325 nm, but they contribute to ring opening at efficiencies, i.e. $\phi_{FRET}\phi_{op}$ for the donor and ϕ_{op} for the photochromic acceptor. Weighted by the OD measured Figure 7.5 (b), we define a total efficiency $\phi = 0.87\phi_{FRET}\phi_{op} + 0.13\phi_{op}$, which corresponding to the results from fit using Eq. (7.7). With the same ε_{op} measured in mixed sol-gel, the fit of the measured irradiance dependence of open-form ΔOD of composite sol-gel at 460 nm results in a total efficiency of $\phi = 10 \pm 2$ %. Assuming ϕ_{op}~20% from the mixed sol-gel study in Figure 7.10. The FRET efficiency $\phi_{FRET} = 43 \pm 10$ %, which shows agreement with the theoretical prediction derived in 7.2.2. within the error bar.

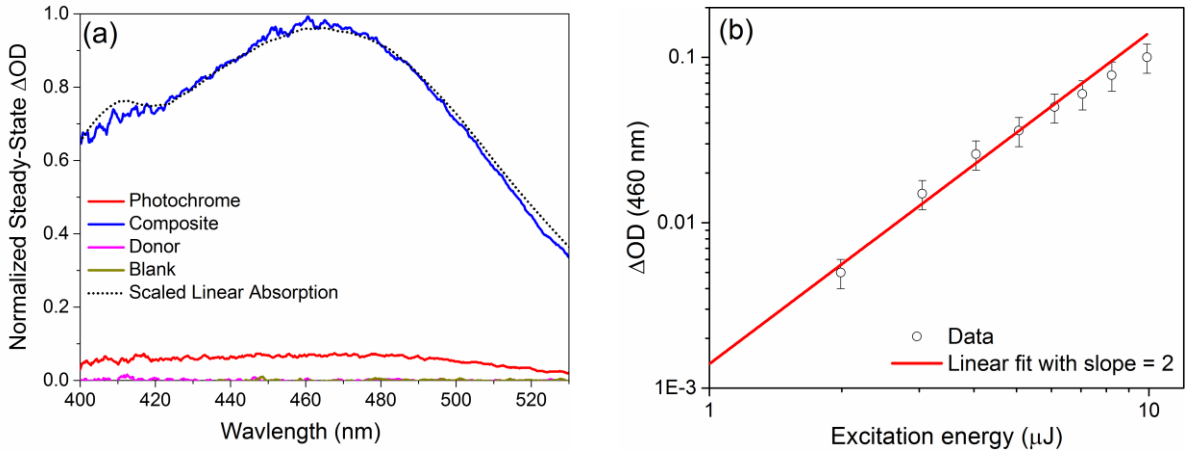

Figure 7.12 (a) Open-form absorption spectra induced by a same two-photon excitation in sol-gels doped with composite PC-1 and pure photochrome; the quadratic dependence of ΔOD at 460 nm on the excitation energy.

The steady-state open-form accumulation is also observed when excited by femtosecond pulses at 620 nm. Here, the ring opening in PC-1 is mainly attribute to 2PA of donor moiety followed by FRET. In this work, we use the TOPAS-HE to produce the 1240nm excitation pulses, which is then doubled by a 3 mm BBO. The generated SHG at 620nm was focused on the sample with spot size ~ 460μm (HW1/e^{2}M) as the two-photon excitation. As discussed later in Figure

7.16, M-106 has a relatively large 2PA absorption cross section at 620 nm, and the absorbed energy will induced ring opening of photochromic moiety via FRET. As shown in Figure 7.12, quite significant 2PA-FRET enhancement (~ 14 ×) over photochromes is observed in composite sol-ge. The donor and blank sol-gels show no change in absorption. By varying the excitation energy, ΔOD at 460 nm shows a near-quadratic dependence. This is a signature of two-photon photochromism, differing from the linear dependence observed one-photon UV-excitation measurements with small excitation energies (see Figure 7.11 and Figure 7.10).

7.4. Ultrafast Dynamics of Ring Opening and Closing

As previously discussed in 7.1. , the knowledge of the transient absorption within photochromic transformation is crucially important for ultrafast applications such as optical memory and all-optical switching. An efficient photochrome is indispensable to have large ring opening yields with small competitive sub-reaction processes. Ultrafast spectroscopy with sub-picosecond time-resolution is necessary to provide detailed information on the photochromic reaction profiles [190]. For example, time-resolved measurements such as pump-probe experiments have been used to investigate isomerization [211], bond cleavage [189], electro-cyclic reactions [212], as well as other mechanisms that occur in the most commonly used photochromes.

First, we are interested in parameters associated with ring opening process such as opening time constants, efficiencies and absorption cross sections. For composite molecule (PC-1), the ring opening can be either due to linear absorption in UV of photochrome itself or 2PA in visible of donor (M-106) moiety followed by FRET. Compared to the accumulative approach previously discussed in 7.3. with sol-gels, the pump-probe measurements allow us to evaluate the photo-

chromic reaction and FRET in a more physical level. Another interest is related to the photo reversing process, which has been qualitatively demonstrated in Figure 7.9 (b). Similar to the transient ring opening process, a pump-probe experiment on pre-opened photochromes should be able to resolve the temporal dynamics, efficiencies and absorption cross sections associated with the closing processes.

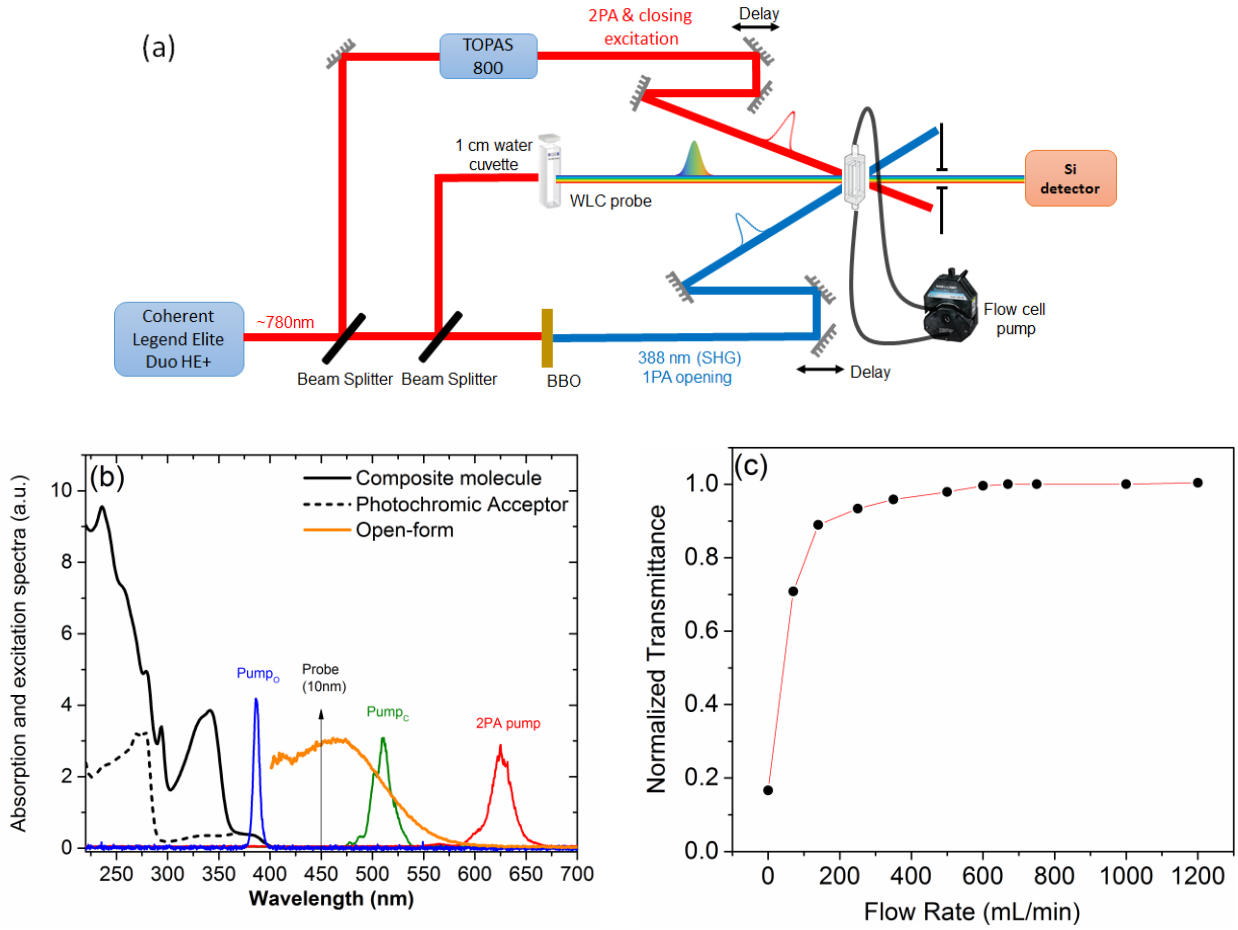

Figure 7.13 (a) experimental setup of pump-probe measurements with flowed solutions; (b) measured spectra for a near-UV pump for1PA opening (blue), a visible pump for 2PA-FRET opening (red) and a visible pump for closing (green), as compared to the absorption spectra of closed-form PC-1 (black solid), open-form PC-1 in visible (orange) and closed-form pure photochrome (black dash); the arrow indicates the probe wavelength and bandwidth; (c) measured transmission (normalized to the maximum) of the probe from Pump$_O$ excited PC-1 with various flow rate.

The configuration of the experiment, i.e. the wavelengths of pump and probe, is designed based on the absorption spectra of PC-1 and photochrome. As shown in Figure 7.13 (a-b), to measure ring opening activated by one-photon UV excitation, the $Pump_O$ is derived from the SHG of Coherent laser system at wavelength of 388 nm and spectrally filtered with 10 nm (FWHM) bandwidth. $Pump_O$ only excites the photochromic shoulder PC-1 where the donor moiety (M-106) does not affect. To measure the 2PA-FRET induced ring opening. The 2PA pump is taken from the signal beam of TOPAS-800 (OPA) and frequency doubled to 620 nm, where M-106 exhibits large 2PA (see Figure 7.16). In the closing experiment, TOPAS-800 is tuned to output at 510 nm ($Pump_C$) from the sum frequency generation between signal and 780 nm pump beam. This excites the opened molecules to induced photo reversing. The probe is chosen at the wavelength of 450 nm, which is from a filtered WLC generated from a 1 cm water cuvette pumped at 780 nm directly from the laser. By simultaneously having two pump pulses, the experimental setup is capable of measuring the ring closing dynamics of the intermediate open-form transients, which can be done by applying $Pump_C$ right after $Pump_O$ at the time delay when the molecule is not fully opened.

One difficulty encountered in the transient measurements of photochromic molecule is that the open-form lifetime is up to hours in duration (see Figure 7.9), which is much longer than the time between each coming laser pulses, i.e. 1 ms for 1kHz repetition rate. This leads to cumulative effects, making impossible to resolve the transients. To avoid this issue, we flow the solution through a spectroscopic cell, so that fresh material is replenished within the optical beam size for each laser shot. Therefore, a large amount of material is needed to be stored in a reservoir. In this work, the sample is prepared in DCM solutions with 2.6 mM concentration. A 1 mm path length flow cell is connected to a 40 mL reservoir with Viton tubing. To determine the minimum needed flow rate, the transmission of probe is measured from the sample excited by $Pump_O$. As shown in

Figure 7.13 (c), the transmission of probe is minimum with static solutions (zero flow rate), simply due to the accumulation of open-form population from each coming laser shot. Upon increasing the flow rate, the transmission increases and becomes stable for > ~ 600 mL/min, which is used for all the transient absorption measurements.

7.4.1. 1PA Ring-opening Dynamics

In this experiment, the sample is placed at the minimum beam waist of probe beam. The Pump$_O$ beam at 388 nm are focused at sample with a spot size of 230 μm (HW1/e^{2}M). The probe beam is focused into a beam waist of 25 μm (HW1/e^{2}M), and overlap with the center of Pump$_O$ beam. The crossing angle of the pump and the probe was kept small (< 2°). The two calcite polarizers are used to ensure linear polarization for both pump and probe beam, and their polarization are kept parallel in all the measurements. To measure the transient absorption due to ring opening, the probe pulse is delayed with respect to pump pulse with a motorized stage and the transmitted beam is detected using a Si detector, as shown in Figure 7.13 (a). The signal from detector is sent to a lock-in amplifier (SR830) that is sensitive at the 286 Hz modulation frequency applied to Pump$_O$ by an optical chopper. The zero-delay position of the translation stage is calibrated using the signal from nondegenerate 2PA in CS_2, and the pulsewidths of Pump$_O$ and probe are 180 and 300 fs (FWHM) respectively.

The measured normalized transmission of probe with Pump$_O$ is shown in Figure 7.14 (a). Upon one-photon excitation (388 nm) directly applied on photochromic moiety, the transmission decreases from a transparent closed-form to the absorptive open-form with multiple dynamics. The induced absorption quickly arises after zero delay in several hundreds of femtoseconds, which

reaches a maximum and becomes smaller in the next few picoseconds. This transient feature becomes obvious in a detailed scan of the first 3 ps with excitation energies of 5 and 2.5 μJ, as shown in Figure 7.14 (b). The transmission change linearly scales with the excitation energy, because the open-form population is induced by 1PA. The absorption slowly increases again in the next ~ 20 ps and reaches a long-lived excited-state absorption, indicating the completion of ring-opening process.

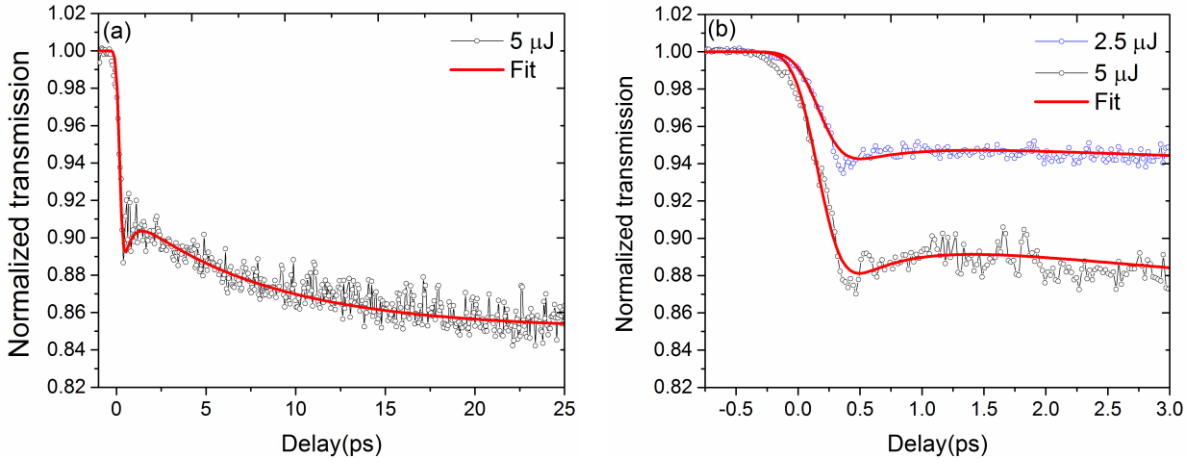

Figure 7.14 Measured transient absorption of PC-1 (circles) at 450 nm after one-photon excitation (388 nm) directly applied on photochromic moiety with a temporal delay of (a) 25 ps and (b) a detailed scan within 3 ps with two different pump energies. The fits (red) are applied using a 3-step model [188].

The transient ring-opening dynamics of spiro-type photochromic molecules have been extensively studied both theoretically and experimentally. The open-form transient absorption measured in this experiment is very similar to previous observations [188, 194, 212], which can be attributed to different physical origins during the photochromic reaction. The C-O bond cleavage between spiro-carbon and oxygen has been reported to occur on a picosecond or even sub-picosecond time scale, which produces an intermediate photoproduct, inheriting an orthogonal parental geometry. This is then followed by a geometrical change, i.e. cis-trans isomerization, to the planar

merocyanine forms [190, 213]. For example, Ref. [214] is one of the early studies using a picosecond pump-probe measurements, where the ring-opening dynamics measured from a Spiropyran derivative show a broad absorption band over the entire visible regime in the first several picoseconds, which was followed by the formation of merocyanine in the next ~ 20 ps. Another measurement on a spirooxazine with femtosecond time resolution reveals more details of ring-opening transients [215]. Similar to Ref. [214], a broadband absorption was first measured within several hundreds of femtoseconds, which is attributed to ESA of oxazine chromophore. However, in between the ESA and merocyanine formation, another intermediate open-form transient arises within the next 2 ps, which exhibits a narrowing and a blue shifting of absorption spectrum. In some spectral region, the absorption of this intermediate product could be smaller than the first occurring ESA. This intermediate transient may correspond to C-O bond cleavage, forming a cis-merocyanine with the parental orthogonal geometry. Finally, the formation of stable merocyanine is observed in the next few tens of picoseconds, which is consistent with the observations in other experiments reported in Refs. [188, 194, 212].

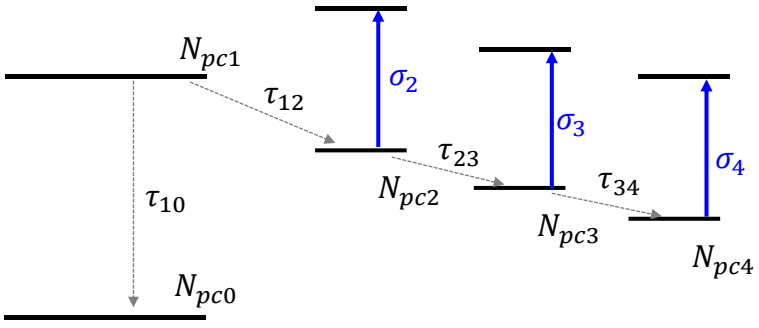

Figure 7.15 energy diagram of the “3-step” reaction model.

The measured results shown in Figure 7.14 can be interpreted by adopting the reaction scheme discussed above. Commonly, it is also recognized as a "3-step" reaction model: after the closed form being excited, it first relaxes from a higher electronic state S_2 to a vibrational state of a lower electronic state S_1, where a ESA occurs across the visible regime and contributes to absorption maximum at ~ 500 fs. Then, the vibration relaxation process overcomes the energy barrier, resulting in C-O bond breaking. The formed intermediate transient cis-merocyanine exhibits a narrowing and shifting of absorption spectrum compared to initial ESA, giving a decrease of absorption at 450 nm for the next a few picoseconds. The slowly increasing absorption in next 20 ps originates from cis-trans isomerization, forming the final open-form product trans-merocyanine. The energy diagram shown in Figure 7.15 represents the "3-step" reaction model, where ground-state N_{pc0} is the closed-form, N_{pc1}, N_{pc2}, N_{pc3} and N_{pc4} represent the populations in electronic state S_2, S_1, intermediate cis-merocyanine and stable trans-merocyanine, respectively, which have different lifetimes and absorption cross sections at the probe wavelength. The ring-opening process start with the relaxation from N_{pc1} to N_{pc2}, while a competing process occurs from N_{pc1} to N_{pc0}, from which we define the ring-opening efficiency $\phi_{op} = \tau_{10}/(\tau_{10} + \tau_{12})$.

Table 7.1 Fit parameters of ring-opening transients of photochrome

Absorption cross sections	Lifetimes
$\sigma_{01} = 1.5 \times 10^{-17}\text{cm}^2$	$\tau_{10} = 250 \pm 50\text{fs}$
$\sigma_2 = 3.5 \times 10^{-17}\text{cm}^2$	$\tau_{12} = 500 \pm 100\ \text{fs}$
$\sigma_3 = 2.5 \times 10^{-17}\text{cm}^2$	$\tau_{23} = 700 \pm 200\ \text{fs}$
$\sigma_4 = 3.7 \times 10^{-17}\text{cm}^2$	$\tau_{34} = 8 \pm 2\ \text{ps}$

By numerically solving the time evolution of the population in each state in Figure 7.15, we have a unique set of parameters to fit the measured transient absorption dynamics in Figure

7.14. From linear absorption spectrum in Figure 7.4 (e) and steady-state accumulative measurements in Figure 7.11 (a), σ_{01} and σ_4 can be calculated from known values of molar absorptivities. Since σ_4 governs the magnitude of signal at 25 ps, σ_2 and σ_3 can be found from the relative magnitudes of the minimum transmission at ~ 5 ps and the less pronounced maximum transmission appeared ~ 1 – 2 ps. The time constants are found by fit the multiple temporal dynamics, e.g. τ_{12}, τ_{23} and τ_{34} are fit from the first decreasing, the following small increasing and the last slowly decreasing of transmission. Finally, τ_{10} is varied to match the overall magnitude, as it is related with ϕ_{op}. The fit parameters are summarized in Table 7.1, which yields $\phi_{op} = 30 \pm 7$ % in agreement with the accumulative measurement on the mixed sol-gel (see Figure 7.10). Errors in fitted cross sections (20%) are estimated from the uncertainty in irradiance as well as experimental noise of the data.

7.4.2. 2PA-FRET Ring-opening Dynamics

In this two-photon excitation experiment, the same PC-1 solution is used as the previous 1PA ring-opening experiment. The only difference is the Pump$_O$ is replaced by the 2PA pump beam at 620 nm which is focused at sample with a spot size of 300 μm (HW1/e^{2}M). The pulsewidth of the 2PA pump is ~ 200 fs (FWHM) determined from the cross-correlation for 2PA signal in this measurement. Similarly, pump and probe are co-polarized and cross each other at a small angle (< 2°). The other experimental conditions, e.g. detection system, are identical with the 1PA excitation experiment.

In opposite to the 1PA excitation experiment where only the photochromic moiety is excited, the ring-opening of PC-1 under two-photon excitation involves contributions from the donor

moiety. Therefore, it is worth performing measurements on both M-106 and PC-1 molecules. With identical experimental conditions, the results will give a direct comparison which reveals the effects from FRET.

The 2PA spectrum of M-106 has been measured from 440 nm to 800 nm using two-photon induced fluorescence (2PIF) technique, as shown in Figure 7.16 (a). A Z-scan measurement at 480 nm serves as a cross check to the results obtained from 2PIF. The measured 2PA spectrum shows a maximum at 620 nm with a degenerate 2PA cross section δ_D around 70 GM. This two-photon state may be inferred from a fluorescence anisotropy measurement of M-106 in DCM solution, which shows a strong depolarization occurring ~ 300 nm. This may be corresponding to the two-photon transition at 620 nm.

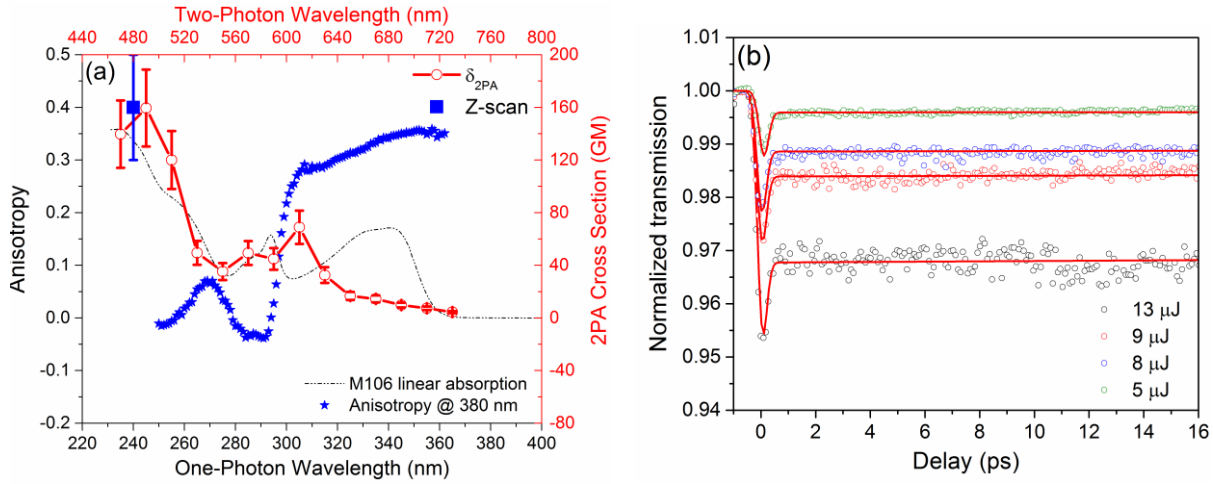

Figure 7.16 (a) 2PA spectrum of M-106 measured by two-photon induced fluorescence (red circles) and Z-scan (blue square) measurements, along with comparisons to fluorescence anisotropy (blue stars) at emission wavelength of 380nm and linear absorption spectrum (black curve); pump-probe measurements (circles) of M-106 in DCM solution with different excitation energies, along with fits (red lines) with same molecular parameters.

With the 2PA pump beam at 620 nm, the normalized probe transmission is measured with different excitation energies, as shown in Figure 7.16 (b). Here, the M-106 is made also in DCM

solution with a concentration of 3.6 mM. At zero delay, the decrease of transmission follows the cross-correlation of pump and probe, which is from the nondegenerate 2PA. The initial decrease of transmission does not return back to zero, instead we observe a long-lived signal with a decay rate much longer than the time scale of the temporal delay. It is attributed to the excited-state absorption molecules excited by the pump through degenerate 2PA, which scales quadratically with excitation energy. The data is analyzed considering a three-level system, as introduced in 2.3. , where the rate equations to describe the populations evolution and probe irradiance I_p attenuation can be written as

$$\begin{aligned} \frac{dI_p}{dz} &= -\frac{2\delta_{\mathrm{ND}} N_0 I_e}{\hbar\omega_e} I_p - \sigma_{12} N_1 I_p, \\ \frac{dN_0}{dt} &= -\frac{\delta_{\mathrm{D}} N_0 I_e^2}{2(\hbar\omega_e)^2} + \frac{N_1}{\tau_s}, \\ \frac{dN_1}{dt} &= \frac{\delta_{\mathrm{D}} N_0 I_e^2}{2(\hbar\omega_e)^2} - \frac{N_1}{\tau_s}, \end{aligned} \tag{7.8}$$

where δ_{ND} is the nondegerate 2PA cross section of excitation at 620 nm and probe at 450 nm, and the lifetime of the higher excited-state N_2 is assumed to be fast, meaning no population builds up in N_2. δ_{ND} and σ_{12} can be found by fitting the magnitudes of signals at zero delay and positive delay, respectively. Note the fluoresence lifetime τ_s is not resolved in this measurement, which requires longer delays to reveal the decay of ESA signal. The estimation from the measured fluoresence quantum yield, i.e. ~ 80 %, using Strickler-Berg's relation [209] gives 2.3 ns for τ_s. With the same parameters, the signals measured with four different energies can be fitted simultaneously, as summarized in Table 7.2.

With same experimental conditions of 9 μJ excitation, the PC-1 sample (used in 1PA experiment) is measured along with M-106. As shown in Figure 7.17 (b), the signals from PC-1

are normalized to the concentration ratio to M-106 solution to give a direct comparison. PC-1 shows almost same signal as M-106 at zero delay, because only the nondegenerate 2PA of donor contributes. However, the long-lived ESA from M-106 is not capable to remain in PC-1, which instead exhibits a decay of absorption to a smaller value in a few of picoseconds. This is because by linking M-106 with a photochrome, FRET introduces another channel for excited M-106 (N_1) to relax to, i.e. $N_1 \rightarrow N_{pc1}$ as shown in Figure 7.17 (a). Therefore, the excited electronic state S_2 of closed-form photochromic moiety is directly induced by FRET, as opposite to that induced by 1PA excitation in UV. After 2PA excitation and FRET, the ring-opening process follows previously discussed "3-step" reaction scheme (see Figure 7.15). Since physically the excited M-106 can only activate photochrome by FRET with a certain probability, we phenomenologically introduce a competing process, i.e. τ_1, to account for the possibility that the excited M-106 ends up staying at N_1 with an ESA. Therefore, the PC-1 signal measured at longer delays are essentially due to the absorption from a combination of the opened photochromic moiety and the excited M-106. In Figure 7.17 (c), by adopting the parameters for photochromic transients listed in Table 7.1, we fit the decaying dynamics using ~ 8 ps as the FRET decay constant τ_T, and the overall magnitudes is fit by adjusting the competing time constant τ_1, as summarized in Table 7.2. This yields a FRET efficiency $\phi_{FRET} = \tau_1/(\tau_1 + \tau_T)$ of 76 ± 10 %, which agrees with the theoretical prediction in 7.2.2. , but is slightly larger than that determined from accumulative studies of the composite sol-gel in 7.3.2. .

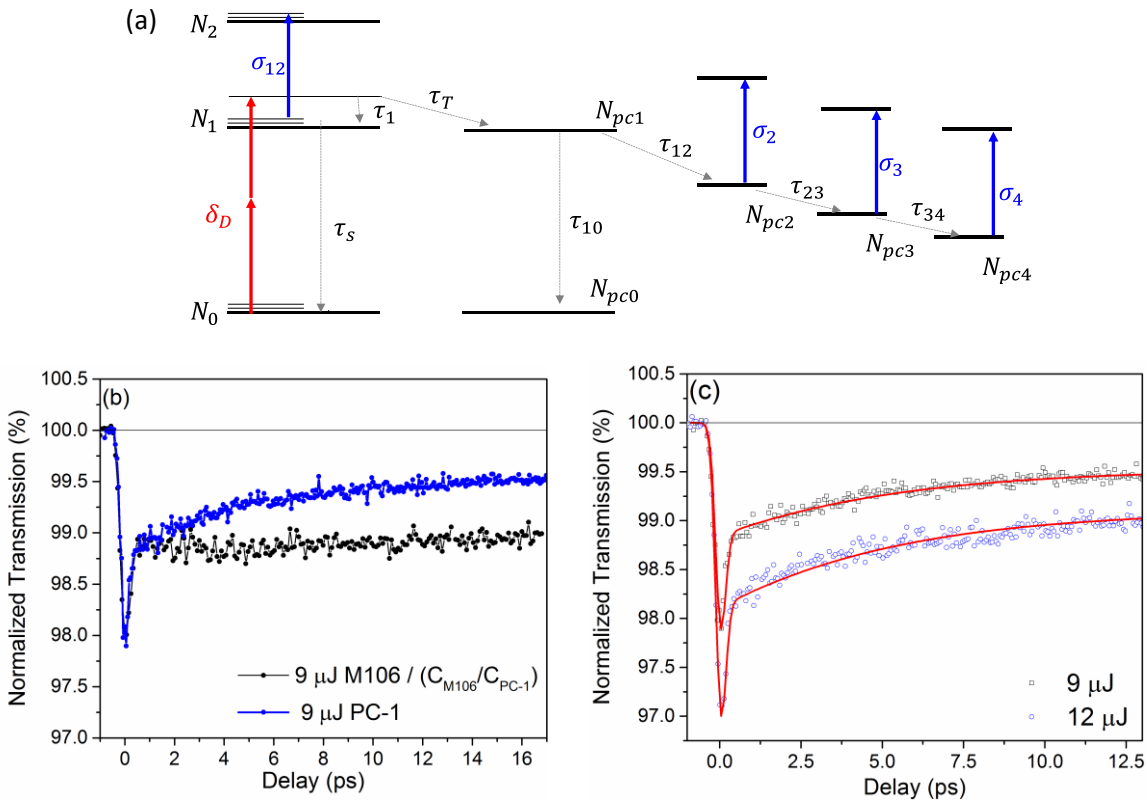

Figure 7.17 (a) energy diagram of 2PA-FRET photochromism scheme of PC-1: 2PA of donor moiety followed by FRET and the "3-step" reaction process (see Figure 7.15); a direct comparison of signals (normalized to its concentration) from PC-1 (blue) and M-106 (black) DCM solutions with identical experimental conditions; (c) measured transient absorption signals of PC-1 (circles) with two different energies, along with fits (red lines) using 2PA-FRET scheme in (a).

It must be noted that the absorption cross section of all measured open-form transients (see Table 7.1) are smaller than the ESA cross section σ_{12} of M-106 at the wavelength of 450 nm, the maximum of open-form absorption band. Therefore, the overall NLA actually decreases when photochromic molecule is involved. This manifests in Figure 7.17 (b) that a smaller absorption is observed when FRET occurs in PC-1, as compared to a larger ESA from pure M-106. For applications such as optical limiting which requires an enhanced NLA for a single shot, PC-1 may not be a good candidate at least for the wavelength of 450 nm. But 2PA-FRET induced photochromism may contribute to enhancement of NLA in other cases. For example, the open-form absorption

exhibits truly broadband, which may give NLA for other wavelengths which cannot be reached by the ESA of M-106. Also, the lifetime of open-form is extremely longer than that of the excited-state of M-106, which may benefit NLA from accumulative effects.

Table 7.2 Fit parameters of 2PA-FRET photochromism in PC-1.

Absorption cross sections	Lifetimes
$\delta_{\mathrm{ND}} = 103$ GM	$\tau_s \sim 2.3$ ns
$\delta_{\mathrm{D}} = 70$ GM	$\tau_1 = 30 \pm 6$ ps
$\sigma_{12} = 16 \times 10^{-17} cm^2$	$\tau_T = 8 \pm 3$ ps

7.4.3. Ring-closing Dynamics

The ring-closing transient dynamics are not investigated as often as that of the ring-opening for spiro-compounds, as the open-form merocyanine is not thermally stable. Precise determinations of closing quantum yield and intermediate transient closing photoproducts are critical for practical photonic devices designed to utilize the photo reversing properties such as a bidirectional photo switching [191]. In previous literatures, most transient absorption measurements are performed on metastable *trans*-merocyanine, which is optically produced, e.g. using UV illuminations [189, 191, 216, 217].

Here, to probing the transient absorption changes of ring-closing process, the solution reservoir is illuminated with a series of GaN light-emitting diodes (LEDs) at the wavelength of 365 nm with total power of 12 W, which produced open-form PC-1 in DCM solutions to flow through each laser shot. Based on the linear transmission of probe after the flow cell, the effective open-form molecule is 60 μM which remains constant during the measurements. The excitation now is

replaced with $Pump_C$ from TOPAS-800 at 510 nm with a pulsewidth of ~ 150 fs (FWHM), determined from the cross-correlation from a nondegenerate 2PA signal in CS_2. $Pump_C$ is focused at sample with a spot size of 300 μm ($HW1/e^2M$). Similarly, pump and probe are co-polarized and cross each other at a small angle (< 2°). The other experimental conditions, e.g. detection systems, are same as the previous 1PA and 2PA ring-opening experiments. This experiment is only sensitive to optically produced merocyanine moiety of open-form PC-1, the donor and closed-form photochromic moieties are transparent at both $Pump_C$ and probe wavelength, and will not affect the measurements.

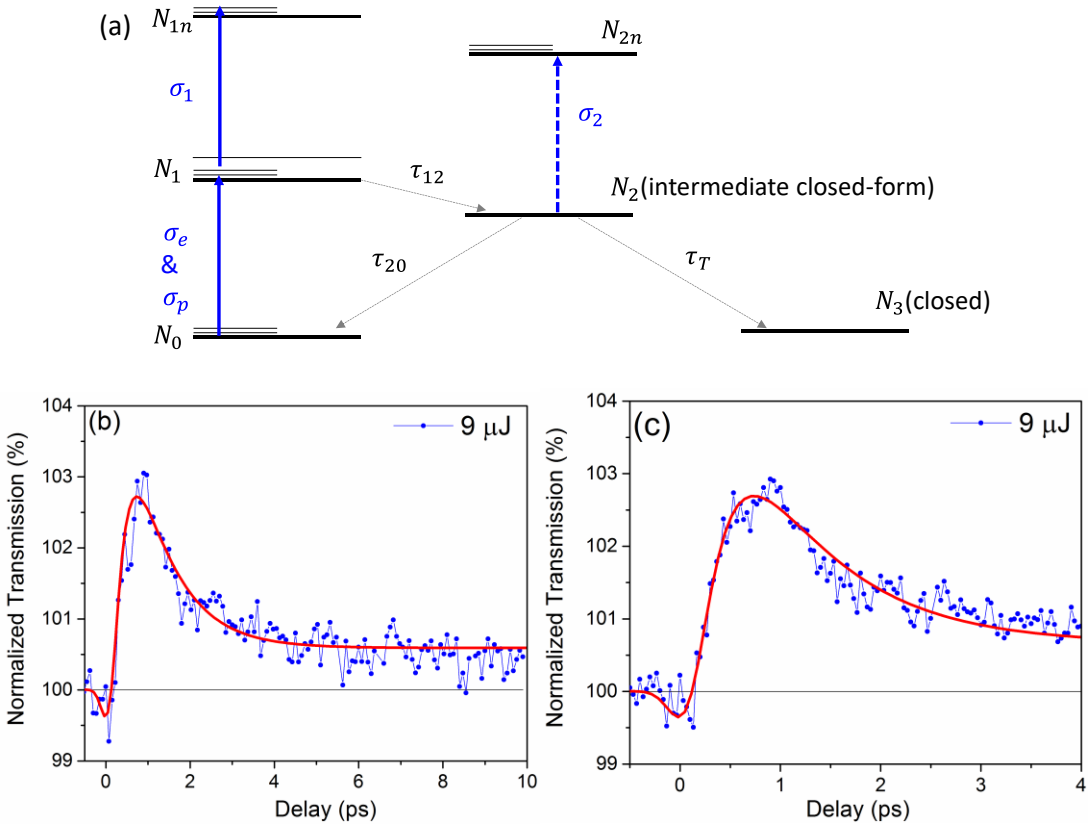

Figure 7.18 (a) Energy diagram of ring-closing reaction scheme; (b) measured (blue) normalized transmission of an optically induced *trans*-merocyanine solution, showing a transient recovery due to ring-closing; (c) measurement of ring closing dynamics within 4 ps.

Table 7.3 Fit parameters of photo-induced ring-closing.

Absorption cross sections	Lifetimes
$\sigma_e = 2.5 \times 10^{-17} cm^2$	$\tau_{12} = 300 \pm 100$ fs
$\sigma_p = 3.7 \times 10^{-17} cm^2$	$\tau_{20} = 1.1 \pm 0.3$ ps
$\sigma_1 = 6.5 \times 10^{-17} cm^2$	$\tau_T = 8 \pm 3$ ps
$\sigma_2 < 1 \times 10^{-17} cm^2$	

The transient absorption dynamics of merocyanine under visible excitation is measured in Figure 7.18 (b) for 10 ps of delay, and a detailed measurement within first 4 ps is shown in Figure 7.18 (c). Due to the low concentration of optically produced merocyanine, the S/N of closing measurements is not as good as that in the ring opening experiments. The energy diagram shown in Figure 7.18 (a) is used to describe the ring-closing dynamics. First at zero delay, a decrease of transmission is barely observed within the noise floor, which may be because at the probe wavelength the excited-state of merocyanine (N_1) has a larger absorption cross section σ_1 than the cross section σ_p of the ground-state open form. A large signal of ESA from excited-state merocyanine is observed in another measurement with a DCM solution of a commercially available chromene, 3,3-Diphenyl-3H-naphtho[2,1-b]pyran, using identical experimental conditions. Then the transmission quickly increases, indicating a fast decay of N_1 to another state N_2, where the absorption cross section σ_2 is smaller than σ_p, giving a saturation of probe absorption. Therefore, N_2 is also referred as intermediate closed form, which has certain probabilities to return back to ground-state merocyanine, i.e. $N_2 \rightarrow N_0$, giving recovery of probe absorption, or proceed to complete ring-closing by $N_2 \rightarrow N_3$, contributing signals at longer delay (> 6 ps). The parameters are determined from a fit to the different features in the measured closing dynamics, as summarized in Table 7.3, where

the values of σ_e (pump) and σ_p (probe) are from the open-form molar absorptivity measured in 7.3.2. . The ring-closing efficiency is determined as $\phi_{cl} = \frac{\tau_{20}}{\tau_{20}+\tau_T} = 12 \pm 3$ %.

CHAPTER 8: CONCLUSIONS AND FUTURE WORK

This chapter provides the conclusions on the work done on investigating the ultrafast mechanisms of nonlinear refraction for molecular liquids and gases, the measurements of dispersion of the nondegenerate nonlinear refraction of semiconductors and the characterization of the 2PA-FRET photochromic molecule PC-1. Possible future work on each subject is also discussed.

8.1. NLR of Molecular Liquids and Gases

In the study of molecular liquids, we have experimentally determined the total NLO response function for 24 selected organic solvents using the polarization-resolved Beam Deflection technique, in which bound-electronic and each nuclear contribution are explicitly separated. We found for molecules with a permanent polarizability anisotropy, the NLO response function can be decomposed into a nearly instantaneous bound-electronic response, along with three noninstantaneous nuclear contributions which are attributed to collision, libration and diffusive reorientation. With parallel polarized excitation and probe waves, the universal temporal response of these molecules exhibits an instantaneous response followed by a quickly damped librational response, and then the slow exponential decaying response from molecular reorientation dominates for longer delays. The librational and reorientational responses vanish for rotationally symmetric molecules such as carbon tetrachloride.

We found the NLO response functions are closely related with their molecular structures. For example, in benzene derivatives, the benzene moiety contributes significantly to the overall nonlinearity of the molecule. In part, this arises from the aromatic planar structure with relatively larger polarizability anisotropy, resulting in a large reorientational response. Depending on the substitution groups, the nonlinear response of benzene derivatives may be altered. For example,

we notice methyl substitutions give minor effects on both electronic and reorientational NLR. But we measured different reorientational responses in nitrobenzene and o-dichlorobenzene, and different electronic NLR in butyl salicylate.

We also found the magnitude of the reorientational contribution is dependent upon the linear polarizability anisotropy of the molecule. For example, the measured alcohols show negligible signal at longer temporal delays, which is due to its small anisotropy from the single-bonded structure. The theoretical value of the reorientation NLR coefficient, $n_{2,r}$, is derived from the linear polarizability tensors, as discussed in 4.1.2. . This theory shows good agreement with our experimental results if the Lorentz-Lorenz local field correction factor is not considered.

Therefore, this work establishes a database of NLO response functions for some common solvents based on self-consistent measurements, which can be used for predicting the outcomes of other NLR related experiments such as Z-scan. Future work on Z-scan measurements of $n_{2,\mathrm{eff}}$ will be useful to compare to the theoretical prediction as shown in Figure 4.8.

We have also demonstrated the capability of the BD technique in the measurements of NLR transients of ambient air and gaseous CS_2, where both bound-electronic and coherent rotational responses are resolved. In the air measurements, the contributions from individual constituents, i.e. N_2 and O_2, are separated. A Fourier analysis of many periods of rotational revivals reveals the rotational Raman spectrum, from which the rotational and centrifugal distortion constant of N_2 and O_2 are unambiguously determined. Using the polarizability anisotropy $\Delta\alpha$ as a self-reference, the electronic $n_{2,el}$ of air is also determined.

In the gas phase measurements of CS_2, we identify two isotopologues, i.e. $C^{32}S_2$ and $C^{32}S^{34}S$, from the half revival signal. The effects from the thermally populated system is that the first excited vibrational state and centrifugal distortion are manifest in the quarter revival signal.

Additionally, we determined the electronic second hyperpolarizability $\langle\gamma\rangle$, which coincides with the $\langle\gamma\rangle$ measured in liquid phase CS_2 (within errors) if considering the Lorentz-Lorenz local field correction factor. Experimental investigations in the future of $\langle\gamma\rangle$ for other solvent molecules (including polar molecules) in the gas phase may be compared to $\langle\gamma\rangle$ determined from liquid-phase measurements, i.e. using $n_{2,el}$ in Table 4.3., which may help further understand the Lorentz-Lorenz local field theory and reveal its limitations.

8.2. ND-NLR Dispersion of Semiconductors

We have presented experimental measurements on the dispersion of the nondegenerate nonlinear refraction of ZnO, ZnSe, and CdS using BD technique. With various values of nondegeneracy, the ND-NLR coefficient $n_2(\omega_a;\omega_b)$ is measured over a broad spectral range, along with the corresponding ND-2PA and ND-3PA coefficients. To extract the values of these nonlinear coefficients, GVM has been taken into account in the analysis of the data. Using an excitation pulse at $\hbar\omega_b$ = 0.54 eV, a positively enhanced $n_2(\omega_a;\omega_b)$ is measured in all direct-gap semiconductors with a probe $\hbar\omega_a$ near the ND-2PA resonance. In ZnO, with $\hbar\omega_b$ at 16 % of the bandgap, more than one order-of-magnitude enhancement of $n_2(\omega_a;\omega_b)$ over its zero-frequency limit is measured. In CdS, the sign change of $n_2(\omega_a;\omega_b)$ near the bandgap is also resolved. We found good agreement between experimental results and our earlier theoretical predictions using nonlinear Kramers-Kronig relations [41, 45, 105, 165, 166], in both nondegenerate enhancement and spectral dispersion shapes of n_2. We therefore confirm the theory over an extremely large range of photon energy ratios, allowing predictions of the best operating wavelengths of semiconductor devices engineered to use cross-phase modulation.

Based on time-wavelength mapping of a linearly up-chirped probe pulse, we also demonstrate the anomalously dispersive behavior of extremely nondegenerate $n_2(\omega_a;\omega_b)$ near the bandgap in ZnO, which rapidly switches sign from the enhanced positive n_2 to a large negative value over a very narrow spectral range. This strongly dispersive NLR has potential to provide not only large but ultrafast modulation of a femtosecond pulse with bandwidth centered near the zero-crossing frequency to enable new applications such as nonlinear pulse shaping.

This enhancement of NLR suggests the possibility of all-optical switching based on the nondegenerate Kerr effect. A larger $n_2(\omega_a;\omega_b)$ significantly reduces the switching energy for the required phase changes for all AOS devices. Also, the magnitude, sign, and dispersion of NLR can be significantly tailored with nondegenerate beams by selecting the appropriate excitation wavelength, which can lead to advantages over its degenerate counterpart. Operating in a nondegenerate scheme with a control beam at a (mid-) infrared wavelength, we can essentially avoid 2PA in the signal beam, leaving a relatively smaller nondegenerate 3PA as the dominant nonlinear loss, resulting in a larger FOM_{3PA}. Approximately 340× improvement of the FOM_{3PA} over the degenerate case at the same signal wavelength has been measured in ZnSe when using < 1 GW/cm^2 switching irradiance.

8.3. Two-Photon Photochromism

In order to obtain a relatively larger 2PA cross section without affecting the photochromic properties, we have synthesized a composite two-photon photochromic molecules, PC-1, by coupling a chromene with a donating 2PA chromophore via FRET. Both quantum chemical calculation and

linear absorption measurements indicate negligible electronic interaction between these two moieties. We have observed several evidence that the energy transfer occurs between 2PA donor and photochromic acceptor. This is from fluorescence characterizations of the quantum yields, excitation spectrum and anisotropy.

By doped the molecules in to a sol-gel matrix, we mitigate the diffusion problem that exists in solutions, allowing us to perform measurements over a long period of time. First, thermal reversing is characterized and reveals at least three open-form isomers are form upon UV excitation, which have different thermal stabilities, i.e. from fast decaying isomer ($\tau_1 = 63$ s) to a nearly stable isomer ($\tau_1 = 24400$ s). Based on sol-gel samples, we also developed a methodology to determine the open-form molar absorptivity and ring opening efficiency ϕ_{op} by evaluating the accumulation of open-form molecules. In this case, the ring-opening efficiency is determined from a sol-gel in which the only effective molecules are photochromes. Knowing ϕ_{op}, FRET efficiency ϕ_{FRET} is determined from a sol-gel doped by PC-1, which shows the agreement with theoretical predictions.

The transient ring opening and closing parameters of PC-1 is measured by a series of pump-probe experiments. We observed the ring opening of the photochrome occurs in picoseconds time scale with three different transients, namely excited-state closed form, *cis*-merocyanine and *tran*-merocyanine. The overall ring opening efficiency is determined to be ~ 30 %. In the experiment with two-photon excitation, the donor molecule M-106 itself exhibits a large excited-state absorption with a cross section even larger than that of all the open-form transients of photochrome. Therefore, in the two-photon experiment of PC-1 where M-106 is coupled to photochrome via FRET, we observed a decrease of NLA compared to pure M-106. From the same experiment, FRET efficiency ϕ_{FRET} is determined to be ~ 76 %. The closing dynamics is investigated by pump-probe measurements with a sample contains optically produced *tran*-merocyanines. We observe

the closing process involves an intermediate closed form, from which the efficiency to complete ring closing is ~ 12%. Note this closing dynamics is only for metastable *tran*-merocyanine. In another closing experiment performed on a commercially available chromene, 3,3-Diphenyl-3H-naphtho[2,1-b]pyran, with ring opening induced by a femtosecond UV pump pulse ($Pump_O$), we have observed that the other intermediate open-form transients, e.g. *cis*-merocyanine may have higher closing efficiency than *tran*-merocyanine.

The parameters PC-1 provides insight into photochromic ring opening and closing reaction. Current data provide the absorption cross section of different transients only at the wavelength the open-form absorption peak. Future work to map out the full transient absorption spectra would complete the understanding of this molecule, making it ready for ultrafast application of various photonic devices.

However, PC-1 does not serve the purpose of enhancing NLA, therefore may not provide strong optical limiting effect. First, the open-form cross section is smaller than M-106, which actually decrease the effective NLA of the system. Additionally, the confirmation of photo-induced ring closing accompanied by an intermediate closed form occurs in a few of picoseconds, which compete with 2PA-FRET activation, resulting in less population of open-form required for sufficient NLA.

LIST OF REFERENCES

1. Iliopoulos, K., et al., *Ultrafast third order nonlinearities of organic solvents.* Optics Express, 2015. **23**(19): p. 24171-24176.

2. Ho, P.P. and R.R. Alfano, *Optical Kerr effect in liquids.* Physical Review A, 1979. **20**(5): p. 2170-2187.

3. Sheik-Bahae, M., et al., *Sensitive measurement of optical nonlinearities using a single beam.* Quantum Electronics, IEEE Journal of, 1990. **26**(4): p. 760-769.

4. Rau, I., et al., *Comparison of Z-scan and THG derived nonlinear index of refraction in selected organic solvents.* Journal of the Optical Society of America B, 2008. **25**(10): p. 1738-1747.

5. Bala Murali Krishna, M. and D. Narayana Rao, *Influence of solvent contribution on nonlinearities of near infra-red absorbing croconate and squaraine dyes with ultrafast laser excitation.* Journal of Applied Physics, 2013. **114**(13): p. 133103.

6. Couris, S., et al., *Sub-picosecond studies of the third-order optical nonlinearities toluene solutions.* Journal of Physics B: Atomic, Molecular and Optical Physics, 1996. **29**(21): p. 5033.

7. Minoshima, K., M. Taiji, and T. Kobayashi, *Femtosecond time-resolved interferometry for the determination of complex nonlinear susceptibility.* Optics Letters, 1991. **16**(21): p. 1683-1685.

8. Zhao, F., et al., *Third-order nonlinear optical properties of an azobenzene-containing ionic liquid crystalline polymer.* Optical and Quantum Electronics, 2014. **46**(11): p. 1491-1498.

9. Kawazoe, T., et al., *Measurement of nonlinear refractive index by time-resolved z-scan technique.* Optics Communications, 1999. **160**(1–3): p. 125-129.

10. Nibbering, E.T.J., et al., *Measurement of the nonlinear refractive index of transparent materials by spectral analysis after nonlinear propagation.* Optics Communications, 1995. **119**(5): p. 479-484.

11. Levenson, M.D. and N. Bloembergen, *Dispersion of the nonlinear optical susceptibilities of organic liquids and solutions.* The Journal of Chemical Physics, 1974. **60**(4): p. 1323-1327.

12. Ganeev, R.A., et al., *Two- and three-photon absorption in CS2.* Optics Communications, 2004. **231**(1–6): p. 431-436.

13. Phu Xuan, N., et al., *Picosecond measurements of the third order susceptibility tensor in liquids.* Optics Communications, 1984. **51**(6): p. 433-437.

14. Couris, S., et al., *An experimental investigation of the nonlinear refractive index (n2) of carbon disulfide and toluene by spectral shearing interferometry and z-scan techniques.* Chemical Physics Letters, 2003. **369**(3–4): p. 318-324.

15. Albrecht, H.-S., et al., *Ultrafast beam-deflection method and its application for measuring the transient refractive index of materials.* Applied Physics B, 1993. **57**(3): p. 193-197.

16. Boudebs, G., M. Chis, and J.P. Bourdin, *Third-order susceptibility measurements by nonlinear image processing.* Journal of the Optical Society of America B, 1996. **13**(7): p. 1450-1456.

17. Reichert, M., et al., *Temporal, spectral, and polarization dependence of the nonlinear optical response of carbon disulfide.* Optica, 2014. **1**(6): p. 436-445.

18. Ferdinandus, M.R., et al., *Beam deflection measurement of time and polarization resolved ultrafast nonlinear refraction.* Optics Letters, 2013. **38**(18): p. 3518-3521.

19. Heritage, J.P., T.K. Gustafson, and C.H. Lin, *Observation of Coherent Transient Birefringence in CS_2 Vapor.* Physical Review Letters, 1975. **34**(21): p. 1299-1302.

20. Lin, C.H., et al., *Birefringence arising from the reorientation of the polarizability anisotropy of molecules in collisionless gases.* Physical Review A, 1976. **13**(2): p. 813-829.

21. Bartels, R., et al., *Phase modulation of ultrashort light pulses using molecular rotational wave packets.* Physical Review Letters, 2001. **88**(1): p. 013903.

22. Zhou, X., et al., *Molecular Recollision Interferometry in High Harmonic Generation.* Physical Review Letters, 2008. **100**(7): p. 073902.

23. Lee, K.F., et al., *Phase control of rotational wave packets and quantum information.* Physical Review Letters, 2004. **93**(23): p. 233601.

24. Korech, O., et al., *Observing molecular spinning via the rotational Doppler effect.* Nat Photon, 2013. **7**(9): p. 711-714.

25. Varma, S., et al., *Molecular quantum wake-induced pulse shaping and extension of femtosecond air filaments.* Physical Review A, 2012. **86**(2): p. 023850.

26. Marceau, C., et al., *Femtosecond filament induced birefringence in argon and in air: Ultrafast refractive index change.* Optics Communications, 2010. **283**(13): p. 2732-2736.

27. Calegari, F., C. Vozzi, and S. Stagira, *Optical propagation in molecular gases undergoing filamentation-assisted field-free alignment.* Physical Review A, 2009. **79**(2): p. 023827.

28. Zahedpour, S., J. Wahlstrand, and H. Milchberg, *Quantum control of molecular gas hydrodynamics.* Physical Review Letters, 2014. **112**(14): p. 143601.

29. Floß, J., et al., *Nuclear spin selective laser control of rotational and torsional dynamics.* The Journal of Chemical Physics, 2012. **136**(8): p. -.

30. Armstrong, J.A., et al., *Interactions between Light Waves in a Nonlinear Dielectric.* Physical Review, 1962. **127**(6): p. 1918-1939.

31. Boyd, R.W., *Nonlinear Optics*. 3 ed. 2008: Academic Press. 611.

32. Stegeman, G.I. and R.A. Stegeman, *Nonlinear Optics: Phenomena, Materials and Devices*. 2012: Wiley.

33. Bartlett, R.J. and G.D. Purvis, *Molecular hyperpolarizabilities. I. Theoretical calculations including correlation.* Physical Review A, 1979. **20**(4): p. 1313-1322.

34. Stegeman, G.I. and R.A. Stegeman, *Nonlinear Optics: Phenomena, Materials and Devices*. Wiley Series in Pure and Applied Optics, ed. G. Boreman. 2012, Hoboken, NJ: John Wiley & Sons, Inc. 488.

35. Spence, D.E., P.N. Kean, and W. Sibbett, *60-fsec pulse generation from a self-mode-locked Ti:sapphire laser.* Optics Letters, 1991. **16**(1): p. 42-44.

36. Van Stryland, E.W., et al., *Optical limiting with semiconductors.* Journal of the Optical Society of America B, 1988. **5**(9): p. 1980-1988.

37. Van Stryland, E.W., et al., *Two Photon Absorption, Nonlinear Refraction, And Optical Limiting In Semiconductors.* Optical Engineering, 1985. **24**(4): p. 244613-244613-.

38. Eisenberg, H.S., et al., *Discrete Spatial Optical Solitons in Waveguide Arrays.* Physical Review Letters, 1998. **81**(16): p. 3383-3386.

39. Stegeman, G.I. and M. Segev, *Optical Spatial Solitons and Their Interactions: Universality and Diversity.* Science, 1999. **286**(5444): p. 1518-1523.

40. Hutchings, D. and B. Wherrett, *Theory of the dispersion of ultrafast nonlinear refraction in zinc-blende semiconductors below the band edge.* Physical Review B, 1994. **50**(7): p. 4622.

41. Sheik-Bahae, M., et al., *Dispersion of bound electron nonlinear refraction in solids.* Quantum Electronics, IEEE Journal of, 1991. **27**(6): p. 1296-1309.

42. Balu, M., et al., *Dispersion of nonlinear refraction and two-photon absorption using a white-light continuum Z-scan.* Optics Express, 2005. **13**(10): p. 3594-3599.

43. Balu, M., et al., *White-light continuum Z-scan technique for nonlinear materials characterization.* Optics Express, 2004. **12**(16): p. 3820-3826.

44. Balu, M., et al., *Broadband Z-scan characterization using a high-spectral-irradiance, high-quality supercontinuum.* Journal of the Optical Society of America B, 2008. **25**(2): p. 159-165.

45. Sheik-Bahae, M., J. Wang, and E.W.V. Stryland, *Nondegenerate optical Kerr effect in semiconductors.* IEEE Journal of Quantum Electronics, 1994. **30**(2): p. 249-255.

46. Dürr, H. and H. Bouas-Laurent, *Photochromism: Molecules and Systems: Molecules and Systems*. 2003: Gulf Professional Publishing.

47. Hirshberg, Y., *Photochromie dans la serie de la bianthrone.* Compt Rend Acad Sci, 1950. **231**: p. 903-904.

48. Joseph, C. and S.S. H, *Photochromic naphthopyran compositions*. 1971, Google Patents.

49. Wardzynski, W., T. Łukasiewicz, and J. Żmija, *Reversible photochromic effects in doped single crystals of bismuth germanium (Bi12GeO20) and bismuth silicon oxide (Bi12SiO20).* Optics Communications, 1979. **30**(2): p. 203-205.

50. Araujo, R.J., W.H. Cramer, and S.D. Stookey, *Method of forming photochromic polarizing glasses*. 1972, Google Patents.

51. Crano, J.C., et al., *Photochromic compounds: Chemistry and application in ophthalmic lenses.* Pure and applied chemistry, 1996. **68**(7): p. 1395-1398.

52. Gupta, A. and R.D. Blum, *Method for manufacturing photochromic lenses*. 1996, Google Patents.

53. Levy, D., *Photochromic Sol−Gel Materials.* Chemistry of Materials, 1997. **9**(12): p. 2666-2670.

54. Smith, G.P., *Photochromic glasses: Properties and applications.* Journal of Materials Science, 1967. **2**(2): p. 139-152.

55. Zhao, P., et al. *Förster Resonance Energy Transfer within a Donor-Acceptor Composite Photochromic Molecule through One-and Two-Photon Absorption*. in *CLEO: Science and Innovations*. 2014. Optical Society of America.

56. Irie, M., *Photochromism: memories and switches introduction.* Chemical Reviews, 2000. **100**(5): p. 1683-1684.

57. Irie, M., *Diarylethenes for memories and switches.* Chemical Reviews, 2000. **100**(5): p. 1685-1716.

58. Parthenopoulos, D. and P. RENTZEPIS, *Three-dimensional optical storage memory.* Science, 1989. **245**(4920): p. 843-845.

59. Toriumi, A., J. Herrmann, and S. Kawata, *Nondestructive readout of a three-dimensional photochromic optical memory with a near-infrared differential phase-contrast microscope.* Optics letters, 1997. **22**(8): p. 555-557.

60. Belfield, K.D., *FRET-based two photon three dimensional optical data storage*. 2011, Google Patents.

61. Kawata, S. and Y. Kawata, *Three-dimensional optical data storage using photochromic materials.* Chemical Reviews, 2000. **100**(5): p. 1777-1788.

62. Ogawa, K., *Two-Photon Absorbing Molecules as Potential Materials for 3D Optical Memory.* Applied Sciences, 2014. **4**(1): p. 1.

63. Tavella, F., A. Marcinkevičius, and F. Krausz, *Investigation of the superfluorescence and signal amplification in an ultrabroadband multiterawatt optical parametric chirped pulse amplifier system.* New Journal of Physics, 2006. **8**(10): p. 219.

64. Almeida, V.R., et al., *All-optical control of light on a silicon chip.* Nature, 2004. **431**(7012): p. 1081-1084.

65. Hutchings, D.C., J.S. Aitchison, and C.N. Ironside, *All-optical switching based on nondegenerate phase shifts from acascaded second-order nonlinearity.* Optics Letters, 1993. **18**(10): p. 793-795.

66. Stegeman, G.I. *Material figures of merit and implications to all-optical waveguide switching*. 1993.

67. Stegeman, G.I., et al., *Third order nonlinear integrated optics.* Journal of Lightwave Technology, 1988. **6**(6): p. 953-970.

68. Wa, P.l.K., et al. *All optical multiple-quantum-well waveguide switch*. Electronics Letters, 1985. **21**, 26-28.

69. Zhao, P., et al. *Beam Deflection Measurements of Nondegenerate Nonlinear Refractive Indices in Direct-gap Semiconductors*. in *CLEO*. 2015. San Jose, CA: Optical Society of America.

70. Ferdinandus, M., *Techniques for Characterization of Third Order Optical Nonlinearities*, in *CREOL, The College of Optics and Photonics*. 2013, University of Central Florida. p. 207.

71. Kalpouzos, C., et al., *Femtosecond laser-induced optical kerr dynamics in CS2/alkane binary solutions.* Chemical Physics Letters, 1988. **150**(1): p. 138-146.

72. Kummli, D.S., H.M. Frey, and S. Leutwyler, *Femtosecond degenerate four-wave mixing of carbon disulfide: High-accuracy rotational constants.* The Journal of Chemical Physics, 2006. **124**(14): p. 144307.

73. McMorrow, D., W.T. Lotshaw, and G.A. Kenney-Wallace, *Femtosecond optical Kerr studies on the origin of the nonlinear responses in simple liquids.* IEEE Journal of Quantum Electronics, 1988. **24**(2): p. 443-454.

74. Peceli, D., et al. *Three-Photon Absorption of GaAs and other Semiconductors*. in *Nonlinear Optics*. 2013. Kohala Coast, Hawaii, United States: Optical Society of America.

75. Tzer-Hsiang, H., et al., *The transient optical Kerr effect of simple liquids studied with an ultrashort laser with variable pulsewidth.* Selected Topics in Quantum Electronics, IEEE Journal of, 1996. **2**(3): p. 756-768.

76. Wahlstrand, J.K., Y.H. Cheng, and H.M. Milchberg, *Absolute measurement of the transient optical nonlinearity in N${}_{2}$, O${}_{2}$, N${}_{2}$O, and Ar.* Physical Review A, 2012. **85**(4): p. 043820.

77. Agrawal, G.P., *Nonlinear Fiber Optics*. 3 ed. Optics and Photonics, ed. P.L. Kelly, I.P. Kaminow, and G.P. Agrawal. 2001, San Diego, GA: Academic Press.

78. Paufler, P., *P. N. Butcher, D. Cotter The elements of nonlinear optics. Cambridge University Press. Cambridge 1990, XIV + 344p. Preis £ 30.00, ISBN 0-521-34183-3.* Crystal Research and Technology, 1991. **26**(6): p. 802-802.

79. Hecht, E., *Optics, 4th.* International edition, Addison-Wesley, San Francisco, 2002.

80. Saleh, B.E. and M.C. Teich, *Fundamentals of Photonics*. 2nd ed. 2007: Wiley Series in Pure an Applied Optics. ISBN.

81. Kaplan, A.E., *"External" self-focusing of light by a nonlinear layer.* Radiophysics and Quantum Electronics, 1969. **12**(6): p. 692-696.

82. Falcão-Filho, E.L., et al., *Robust Two-Dimensional Spatial Solitons in Liquid Carbon Disulfide.* Physical Review Letters, 2013. **110**(1): p. 013901.

83. Kovsh, D.I., et al., *Nonlinear Optical Beam Propagation for Optical Limiting.* Applied Optics, 1999. **38**(24): p. 5168-5180.

84. Pricking, S. and H. Giessen, *Generalized retarded response of nonlinear media and its influence on soliton dynamics.* Optics Express, 2011. **19**(4): p. 2895-2903.

85. Zel'Dovich, B.Y., N.F. Pilipetsky, and V.V.e. Shkunov, *Principles of phase conjugation*. Vol. 42. 2013: Springer.

86. Cirloganu, C.M., et al., *Three-photon absorption spectra of zinc blende semiconductors: theory and experiment.* Optics Letters, 2008. **33**(22): p. 2626-2628.

87. Cirloganu, C.M., et al., *Extremely nondegenerate two-photon absorption in direct-gap semiconductors [Invited]*. Opt. Express, 2011. **19**(23): p. 22951-22960.

88. Ensley, T.R., et al., *Quasi-three-level model applied to measured spectra of nonlinear absorption and refraction in organic molecules.* Journal of the Optical Society of America B, 2016. **33**(4): p. 780-796.

89. Bräunlich, P., R. Hall, and P. Lambropoulos, *Laser-Induced Quenching of Metastable Deuterium Atoms. Singly Stimulated Two-Photon Emission and Anti-Stokes Raman Scattering.* Physical Review A, 1972. **5**(3): p. 1013-1025.

90. Hoskins, L.C., *Pure rotational Raman spectroscopy of diatomic molecules.* Journal of Chemical Education, 1975. **52**(9): p. 568.

91. Ensley, T.R., *White-Light Continuum for Broadband Nonlinear Spectroscopy*, in *CREOL, The College of Optics and Photonics*. 2015, University of Central Florida.

92. Steffen, T., N.A.C.M. Meinders, and K. Duppen, *Microscopic Origin of the Optical Kerr Effect Response of CS2−Pentane Binary Mixtures.* The Journal of Physical Chemistry A, 1998. **102**(23): p. 4213-4221.

93. Zhao, P., et al. *Nonlinear refraction dynamics of solvents and gases*. 2016. Proc. SPIE 9731, Nonlinear Frequency Generation and Conversion: Materials, Devices, and Applications XV, 97310F

94. Ziólek, M., M. Lorenc, and R. Naskrecki, *Determination of the temporal response function in femtosecond pump-probe systems.* Applied Physics B, 2001. **72**(7): p. 843-847.

95. Reichert, M., et al. *Nondegenerate two- and three-photon nonlinearities in semiconductors*. 2016.

96. Göppert-Mayer, M., *Über Elementarakte mit zwei Quantensprüngen.* Annalen der Physik, 1931. **401**(3): p. 273-294.

97. Hellwarth, R., *Third-order optical susceptibilities of liquids and solids.* Progress in Quantum Electronics, 1977. **5**: p. 1-68.

98. Prior, Y., *A complete expression for the third-order susceptibility (χ⁽³⁾) - Perturbative and diagrammatic approaches.* IEEE Journal of Quantum Electronics, 1984. **20**(1): p. 37-42.

99. Cacciari, I., *Third-order optical susceptibility: A comparison among various terms.* Optik - International Journal for Light and Electron Optics, 2010. **121**(1): p. 94-96.

100. Peceli, D., *Absorptive and Refractive Optical Nonlinearities in Organic Molecules and Semiconductors*, in *CREOL, The College of Optics and Photonics*. 2013, University of Central Florida. p. 210.

101. Xia, T., et al., *Optimization of optical limiting devices based on excited-state absorption.* Applied Optics, 1997. **36**(18): p. 4110-4122.

102. Kedenburg, S., et al., *Linear refractive index and absorption measurements of nonlinear optical liquids in the visible and near-infrared spectral region.* Optical Materials Express, 2012. **2**(11): p. 1588-1611.

103. Van Stryland, E.W., et al., *Characterization of nonlinear optical absorption and refraction.* Progress in Crystal Growth and Characterization of Materials, 1993. **27**(3): p. 279-311.

104. Sheik-Bahae, M., A.A. Said, and E.W. Van Stryland, *High-sensitivity, single-beam n2 measurements.* Optics Letters, 1989. **14**(17): p. 955-957.

105. Sheik-Bahae, M., et al., *Sensitive measurement of optical nonlinearities using a single beam.* IEEE Journal of Quantum Electronics, 1990. **26**(4): p. 760-769.

106. Sato, Y., R. Morita, and M. Yamashita, *Study on Ultrafast Dynamic Behaviors of Different Nonlinear Refractive Index Components in CS_2 Using a Femtosecond Interferometer.* Jpn. J. Appl. Phys., 1997. **36**(Part 1, No. 4A): p. 2109-2115.

107. Purwar, H., et al., *Collinear, two-color optical Kerr effect shutter for ultrafast time-resolved imaging.* Optics Express, 2014. **22**(13): p. 15778-15790.

108. Steffen, T. and K. Duppen, *Time resolved four- and six-wave mixing in liquids. II. Experiments.* The Journal of Chemical Physics, 1997. **106**(10): p. 3854-3864.

109. Ferdinandus, M.R., et al., *Dual-arm Z-scan technique to extract dilute solute nonlinearities from solution measurements.* Opt. Mater. Express, 2012. **2**(12): p. 1776-1790.

110. Xia, T., et al., *Eclipsing Z-scan measurement of $\lambda/104$ wave-front distortion.* Optics Letters, 1994. **19**(5): p. 317-319.

111. Wang, J., et al., *Time-resolved Z-scan measurements of optical nonlinearities.* Journal of the Optical Society of America B, 1994. **11**(6): p. 1009-1017.

112. Sheik-Bahae, M., et al., *Nonlinear refraction and optical limiting in "thick" media.* Optical Engineering, 1991. **30**(8): p. 1228-1235.

113. Ensley, T.R., et al. *Nonlinear Characterization of Thin Films by the Dual-Arm Z-scan Method*. in *Frontiers in Optics 2013*. 2013. Orlando, Florida: Optical Society of America.

114. Siegman, A.E., *Lasers*. 1986, University Science Books: Mill Valley, CA. p. 1283.

115. Hu, H., *Third Order Nonlinearity of Organic Molecules*, in *CREOL, The College of Optics and Photonics*. 2012, University of Central Florida. p. 250.

116. Jackson, W.B., et al., *Photothermal deflection spectroscopy and detection.* Applied Optics, 1981. **20**(8): p. 1333-1344.

117. Spear, J.D. and R.E. Russo, *Transverse photothermal beam deflection within a solid.* Journal of Applied Physics, 1991. **70**(2): p. 580-586.

118. Reichert, M., et al., *Beam deflection measurement of bound-electronic and rotational nonlinear refraction in molecular gases.* Optics Express, 2015. **23**(17): p. 22224-22237.

119. Reichert, M., et al., *Beam deflection measurement of bound-electronic and rotational nonlinear refraction in molecular gases: erratum.* Optics Express, 2016. **24**(17): p. 19122-19122.

120. Milam, D., *Review and Assessment of Measured Values of the Nonlinear Refractive-Index Coefficient of Fused Silica.* Applied Optics, 1998. **37**(3): p. 546-550.

121. Negres, R.A., et al., *Experiment and analysis of two-photon absorption spectroscopy using a white-light continuum probe.* Quantum Electronics, IEEE Journal of, 2002. **38**(9): p. 1205-1216.

122. Malitson, I.H., *Interspecimen Comparison of the Refractive Index of Fused Silica*,†.* Journal of the Optical Society of America, 1965. **55**(10): p. 1205-1209.

123. Kampfrath, T., K. Tanaka, and K.A. Nelson, *Resonant and nonresonant control over matter and light by intense terahertz transients.* Nat Photon, 2013. **7**(9): p. 680-690.

124. Fleischer, S., et al., *Molecular Orientation and Alignment by Intense Single-Cycle THz Pulses.* Physical Review Letters, 2011. **107**(16): p. 163603.

125. McMorrow, D., et al., *Analysis of Intermolecular Coordinate Contributions to Third-Order Ultrafast Spectroscopy of Liquids in the Harmonic Oscillator Limit.* The Journal of Physical Chemistry A, 2001. **105**(34): p. 7960-7972.

126. Friedman, J.S. and C.Y. She, *The effects of molecular geometry on the depolarized stimulated gain spectra of simple liquids.* The Journal of Chemical Physics, 1993. **99**(7): p. 4960-4969.

127. Dogariu, A., et al., *Purely refractive transient energy transfer by stimulated Rayleigh-wing scattering.* Journal of the Optical Society of America B, 1997. **14**(4): p. 796-803.

128. Constantine, S., et al., *A Novel Technique for the Measurement of Polarization-Specific Ultrafast Raman Responses.* The Journal of Physical Chemistry A, 2001. **105**(43): p. 9851-9858.

129. Fecko, C.J., J.D. Eaves, and A. Tokmakoff, *Isotropic and anisotropic Raman scattering from molecular liquids measured by spatially masked optical Kerr effect spectroscopy.* The Journal of Chemical Physics, 2002. **117**(3): p. 1139-1154.

130. Xu, Q.-H., Y.-Z. Ma, and G.R. Fleming, *Heterodyne detected transient grating spectroscopy in resonant and non-resonant systems using a simplified diffractive optics method.* Chemical Physics Letters, 2001. **338**(4–6): p. 254-262.

131. Miller, K.J., *Calculation of the molecular polarizability tensor.* Journal of the American Chemical Society, 1990. **112**(23): p. 8543-8551.

132. Shelton, D.P. and J.E. Rice, *Measurements and calculations of the hyperpolarizabilities of atoms and small molecules in the gas phase.* Chemical Reviews, 1994. **94**(1): p. 3-29.

133. Willetts, A., et al., *Problems in the comparison of theoretical and experimental hyperpolarizabilities.* The Journal of Chemical Physics, 1992. **97**(10): p. 7590-7599.

134. Kajzar, F. and J. Messier, *Third-harmonic generation in liquids.* Physical Review A, 1985. **32**(4): p. 2352-2363.

135. Applequist, J., J.R. Carl, and K.-K. Fung, *Atom dipole interaction model for molecular polarizability. Application to polyatomic molecules and determination of atom polarizabilities.* Journal of the American Chemical Society, 1972. **94**(9): p. 2952-2960.

136. Miller, K.J. and J. Savchik, *A new empirical method to calculate average molecular polarizabilities.* Journal of the American Chemical Society, 1979. **101**(24): p. 7206-7213.

137. Bogaard, M.P., et al., *Rayleigh scattering depolarization ratio and molecular polarizability anisotropy for gases.* Journal of the Chemical Society, Faraday Transactions 1: Physical Chemistry in Condensed Phases, 1978. **74**(0): p. 3008-3015.

138. Bridge, N.J. and A.D. Buckingham, *The Polarization of Laser Light Scattered by Gases*. Vol. 295. 1966. 334-349.

139. Chen, Y.H., et al., *Single-shot, space- and time-resolved measurement of rotational wavepacket revivals in H_2, D_2, N_2, O_2, and N_2O.* Optics Express, 2007. **15**(18): p. 11341-11357.

140. Reichert, M., *Nonlinear Optical Response of Simple Molecules and Two-photon Semiconductor Lasers*. 2015, University of Central Florida Orlando, Florida.

141. Chen, Y.H., et al., *Direct Measurement of the Electron Density of Extended Femtosecond Laser Pulse-Induced Filaments.* Physical Review Letters, 2010. **105**(21): p. 215005.

142. Stapelfeldt, H., et al., *Time-resolved Coulomb explosion imaging: A method to measure structure and dynamics of molecular nuclear wave packets.* Physical Review A, 1998. **58**(1): p. 426-433.

143. Hishikawa, A. and K. Yamanouchi, *Coulomb Explosion Imaging of Molecular Dynamics in Intense Laser Fields*, in *Progress in Ultrafast Intense Laser Science II*. 2007, Springer Berlin Heidelberg. p. 1-24.

144. Townes, C.H. and A.L. Schawlow, *Microwave spectroscopy*. 2013: Courier Corporation.

145. Miller, D.A.B., *Quantum Mechanics for Scientists and Engineers*. 2008: Cambridge University Press.

146. Bitter, M. and V. Milner, *Rotational excitation of molecules with long sequences of intense femtosecond pulses.* Physical Review A, 2016. **93**(1): p. 013420.

147. Milner, V. and J.W. Hepburn, *Laser Control of Ultrafast Molecular Rotation.* Advances in Chemical Physics, 2016. **159**.

148. Atkins, P. and J. De Paula, *Elements of physical chemistry*. 2012: Oxford University Press.

149. Diels, J.-C. and W. Rudolph, *Ultrashort laser pulse phenomena*. 2006: Academic press.

150. Wall, K.F. and A. Sanchez, *Titanium sapphire lasers.* The Lincoln Laboratory Journal, 1990. **3**(3): p. 447-462.

151. Ciddor, P.E., *Refractive index of air: new equations for the visible and near infrared.* Applied Optics, 1996. **35**(9): p. 1566-1573.

152. La Fontaine, B., et al., *Filamentation of ultrashort pulse laser beams resulting from their propagation over long distances in air.* Physics of Plasmas (1994-present), 1999. **6**(5): p. 1615-1621.

153. Weber, A., *High-resolution rotational Raman spectra of gases*, in *Raman Spectroscopy of Gases and Liquids*. 1979, Springer. p. 71-121.

154. Milner, A.A., et al., *Effects of ultrafast molecular rotation on collisional decoherence.* Physical review letters, 2014. **113**(4): p. 043005.

155. William, D.R., *"Earth Fact Sheet," (NASA, 2013)*. May 25, 2015: http://nssdc.gsfc.nasa.gov/planetary/factsheet/earthfact.html.

156. Dooley, P.W., et al., *Direct imaging of rotational wave-packet dynamics of diatomic molecules.* Physical Review A, 2003. **68**(2): p. 023406.

157. Hartmann, J.-M. and C. Boulet, *Quantum and classical approaches for rotational relaxation and nonresonant laser alignment of linear molecules: A comparison for CO2 gas in the nonadiabatic regime.* The Journal of chemical physics, 2012. **136**(18): p. 184302.

158. Larsen, J.J., et al., *Aligning molecules with intense nonresonant laser fields.* The Journal of chemical physics, 1999. **111**(17): p. 7774-7781.

159. KoosC, et al., *All-optical high-speed signal processing with silicon-organic hybrid slot waveguides.* Nat Photon, 2009. **3**(4): p. 216-219.

160. Villeneuve, A., et al., *Ultrafast all-optical switching in semiconductor nonlinear directional couplers at half the band gap.* Applied Physics Letters, 1992. **61**(2): p. 147-149.

161. Nakamura, S., K. Tajima, and Y. Sugimoto, *Experimental investigation on high-speed switching characteristics of a novel symmetric Mach–Zehnder all-optical switch.* Applied Physics Letters, 1994. **65**(3): p. 283-285.

162. Nozaki, K., et al., *Sub-femtojoule all-optical switching using a photonic-crystal nanocavity.* Nat Photon, 2010. **4**(7): p. 477-483.

163. Pelc, J.S., et al., *Picosecond all-optical switching in hydrogenated amorphous silicon microring resonators.* Optics Express, 2014. **22**(4): p. 3797-3810.

164. Van, V., et al., *All-optical nonlinear switching in GaAs-AlGaAs microring resonators.* IEEE Photonics Technology Letters, 2002. **14**(1): p. 74-76.

165. Hutchings, D.C., et al., *Kramers-Krönig relations in nonlinear optics.* Optical and Quantum Electronics, 1992. **24**(1): p. 1-30.

166. Sheik-Bahae, M., *Nonlinear Optics of Bound Electrons in Solids*, in *Nonlinear Optical Materials*, J.V. Moloney, Editor. 1998, Springer New York: New York, NY. p. 205-224.

167. Aversa, C., et al., *Third-order optical nonlinearities in semiconductors: The two-band model.* Physical Review B, 1994. **50**(24): p. 18073-18082.

168. Ensley, T.R., et al., *Energy and spectral enhancement of femtosecond supercontinuum in a noble gas using a weak seed.* Optics Express, 2011. **19**(2): p. 757-763.

169. Pattanaik, H.S., et al., *Three-dimensional IR imaging with uncooled GaN photodiodes using nondegenerate two-photon absorption.* Optics Express, 2016. **24**(2): p. 1196-1205.

170. M. Reichert, A.L.S., G. Salamo, D. J. Hagan, E. W. Van Stryland, *Observation of Nondegenerate Two-Photon Gain in GaAs.* arXiv:1602.05912, 2016.

171. Cirloganu, C.M., et al., *Extremely nondegenerate two-photon absorption in direct-gap semiconductors [Invited]*. Optics Express, 2011. **19**(23): p. 22951-22960.

172. Mizrahi, V., et al., *Two-photon absorption as a limitation to all-optical switching.* Optics Letters, 1989. **14**(20): p. 1140-1142.

173. Shima, H. and T. Nakayama, *Higher mathematics for physics and engineering*. 2010: Springer Science & Business Media.

174. Van Stryland, E.W., et al., *Energy band-gap dependence of two-photon absorption.* Optics Letters, 1985. **10**(10): p. 490-492.

175. Bolger, J.A., et al., *Nondegenerate two-photon absorption spectra of ZnSe, ZnS and ZnO.* Optics Communications, 1993. **97**(3): p. 203-209.

176. Hutchings, D.C. and E.W. Van Stryland, *Nondegenerate two-photon absorption in zinc blende semiconductors.* Journal of the Optical Society of America B, 1992. **9**(11): p. 2065-2074.

177. Naumov, A.N. and A.M. Zheltikov, *Frequency–time and time–space mappings with broadband and supercontinuum chirped pulses in coherent wave mixing and pump–probe techniques.* Applied Physics B, 2003. **77**(2): p. 369-376.

178. Solli, D.R., ChouJ, and JalaliB, *Amplified wavelength-time transformation for real-time spectroscopy.* Nat Photon, 2008. **2**(1): p. 48-51.

179. Chou, J., Y. Han, and B. Jalali, *Time-wavelength spectroscopy for chemical sensing.* IEEE Photonics Technology Letters, 2004. **16**(4): p. 1140-1142.

180. Kelkar, P.V., et al., *Time-domain optical sensing.* Electronics Letters, 1999. **35**(19): p. 1661-1662.

181. Reichert, M., et al. *Nondegenerate two- and three-photon nonlinearities in semiconductors*. in *Ultrafast Bandgap Photonics*. 2016. Proc. SPIE 9835.

182. Bond, W.L., *Measurement of the Refractive Indices of Several Crystals.* Journal of Applied Physics, 1965. **36**(5): p. 1674-1677.

183. Tatian, B., *Fitting refractive-index data with the Sellmeier dispersion formula.* Applied Optics, 1984. **23**(24): p. 4477-4485.

184. Gomez, M.S., J.M. Guerra, and F. Vilches, *Weighted nonlinear regression analysis of a Sellmeier expansion: comparison of several nonlinear fits of CdS dispersion.* Applied Optics, 1985. **24**(8): p. 1147-1150.

185. Kang, J.U., et al., *Limitation due to three-photon absorption on the useful spectral range for nonlinear optics in AlGaAs below half band gap.* Applied physics letters, 1994. **65**(2): p. 147-149.

186. DeLong, K., K. Rochford, and G. Stegeman, *Effect of two-photon absorption on all-optical guided-wave devices.* Applied Physics Letters, 1989. **55**: p. 1823-1825.

187. Peceli, D., et al., *Optimization of the Double Pump–Probe Technique: Decoupling the Triplet Yield and Cross Section.* The Journal of Physical Chemistry A, 2012. **116**(20): p. 4833-4841.

188. Antipin, S.A., et al., *Femtosecond transient absorption spectroscopy of non-substituted photochromic spirocompounds.* Chemical Physics Letters, 2000. **331**(5–6): p. 378-386.

189. Hobley, J., et al., *Ultrafast photo-dynamics of a reversible photochromic spiropyran.* The Journal of Physical Chemistry A, 2002. **106**(10): p. 2265-2270.

190. Miyasaka, H. and M. Irie, *Ultrafast Dynamics of Photochromic Systems*, in *Femtosecond Technology*. 1999, Springer Berlin Heidelberg. p. 389-400.

191. Buback, J., et al., *Ultrafast Bidirectional Photoswitching of a Spiropyran.* Journal of the American Chemical Society, 2010. **132**(46): p. 16510-16519.

192. Feneyrou, P., et al., *Photochromic compounds as optical limiters in the nanosecond time range: the example of mercury dithizonate complex.* Photochemical & Photobiological Sciences, 2003. **2**(3): p. 195-202.

193. Crano, J.C. and R.J. Guglielmetti, *Organic Photochromic and Thermochromic Compounds: Volume 1: Photochromic Families*. 1999: Springer.

194. Paramonov, S.V., V. Lokshin, and O.A. Fedorova, *Spiropyran, chromene or spirooxazine ligands: Insights into mutual relations between complexing and photochromic properties.* Journal of Photochemistry and Photobiology C: Photochemistry Reviews, 2011. **12**(3): p. 209-236.

195. Berkovic, G., V. Krongauz, and V. Weiss, *Spiropyrans and Spirooxazines for Memories and Switches.* Chemical Reviews, 2000. **100**(5): p. 1741-1754.

196. Matczyszyn, K., et al., *One- and Two-Photon Absorption of a Spiropyran–Merocyanine System: Experimental and Theoretical Studies.* The Journal of Physical Chemistry B, 2015. **119**(4): p. 1515-1522.

197. Tian, H. and Y. Feng, *Next step of photochromic switches?* Journal of Materials Chemistry, 2008. **18**(14): p. 1617-1622.

198. Saita, S., et al., *Two-Photon Photochromism of Diarylethene Dimer Derivatives.* ChemPhysChem, 2005. **6**(11): p. 2300-2306.

199. Mikhailov, I.A., K.D. Belfield, and A.E. Masunov, *DFT-Based Methods in the Design of Two-Photon Operated Molecular Switches.* The Journal of Physical Chemistry A, 2009. **113**(25): p. 7080-7089.

200. Fardad, S., et al. *Förster Energy Transfer to a Spirooxazine Photochromic Molecule through One- and Two-Photon Absorption*. in *Conference on Lasers and Electro-Optics 2010*. 2010. San Jose, California: Optical Society of America.

201. Gvishi, R., et al. *Resonance energy transfer in a novel two-component system: two-photon fluorophore and a photo-chromic acceptor molecule*. 2005.

202. Belfield, K.D., et al., *Two-Photon Photochromism of a Diarylethene Enhanced by Förster Resonance Energy Transfer from Two-Photon Absorbing Fluorenes.* ChemPhysChem, 2006. **7**(12): p. 2514-2519.

203. Bekere, L., et al., *Chromenes involving a two-photon absorbing moiety: photochromism via intramolecular resonance energy transfer.* New Journal of Chemistry, 2016. **40**(2): p. 1143-1148.

204. Főrster, T., *10th Spiers Memorial Lecture. Transfer mechanisms of electronic excitation.* Discuss. Faraday Soc., 1959. **27**: p. 7-17.

205. Becker, K., et al., *Electrical control of Forster energy transfer.* Nat Mater, 2006. **5**(10): p. 777-781.

206. Stephens, D.J. and V.J. Allan, *Light Microscopy Techniques for Live Cell Imaging.* Science, 2003. **300**(5616): p. 82-86.

207. Kubin, R.F. and A.N. Fletcher, *Fluorescence quantum yields of some rhodamine dyes.* Journal of Luminescence, 1982. **27**(4): p. 455-462.

208. Hu, H., et al. *Energy Transfer within a Donor-Acceptor Photochromic Molecule*. in *Frontiers in Optics 2013*. 2013. Orlando, Florida: Optical Society of America.

209. Lakowicz, J.R., *Principles of fluorescence spectroscopy*. 2013: Springer Science & Business Media.

210. Favaro, G., et al., *Kinetic analysis of the photochromic behavior of a naturally occurring chromene (lapachenole) under steady irradiation.* Molecular Crystals and Liquid Crystals, 1997. **298**(1): p. 137-144.

211. Lednev, I.K., et al., *Femtosecond time-resolved UV-visible absorption spectroscopy of trans-azobenzene in solution.* The Journal of Physical Chemistry, 1996. **100**(32): p. 13338-13341.

212. Miyasaka, H., et al., *Picosecond laser photolysis studies on photochromic reactions of 1,2-bis(2,4,5-trimethyl-3-thienyl)maleic anhydride in solutions.* Chemical Physics Letters, 1994. **230**(3): p. 249-254.

213. Klajn, R., *Spiropyran-based dynamic materials.* Chemical Society Reviews, 2014. **43**(1): p. 148-184.

214. Ernsting, N.P. and T. Arthenengeland, *PHOTOCHEMICAL RING-OPENING REACTION OF INDOLINOSPIROPYRANS STUDIED BY SUBPICOSECOND TRANSIENT ABSORPTION.* Journal of Physical Chemistry, 1991. **95**(14): p. 5502 - 5509.

215. Tamai, N., T. Asahi, and H. Masuhara, *Intersystem crossing of benzophenone by femtosecond transient grating spectroscopy*. Chemical physics letters, 1992. **198**(3): p. 413-418.

216. Gómez, I., M. Reguero, and M.A. Robb, *Efficient Photochemical Merocyanine-to-Spiropyran Ring Closure Mechanism through an Extended Conical Intersection Seam. A Model CASSCF/CASPT2 Study*. The Journal of Physical Chemistry A, 2006. **110**(11): p. 3986-3991.

217. Kumar, R.S.S., et al., *Primary photo-events in a metastable photomerocyanine of spirooxazines*. Optical Materials Express, 2011. **1**(2): p. 293-304.